University of Strathclyde Engineering

Applications of Programmable MEMS Micromirrors in Laser Systems

Ralf Bauer

Department of Electronic and Electrical Engineering
Centre for Microsystems & Photonics

A thesis submitted to the Department of Electronic and Electrical Engineering at the University of Strathclyde for the degree of Doctor of Philosophy

June 2013

Declaration of Authenticity & Author's rights

This thesis is the result of the author's original research. It has been composed by the author and has not been previously submitted for examination which has led to the award of a degree.

Signed:

Date:

Acknowledgements

The work in this thesis could not have been done without the support, guidance and contribution of a large number of people. First of all I want to express my gratitude to Deepak Uttamchandani who has taken me on this PhD journey without hesitation and by organising funding for me and this project solely based on a couple of emails and phone calls we had. There was always an open door for discussions and questions and I very much appreciate the guidance and discussions of ideas and possibilities we had throughout these last years. His enthusiasm, insight and knowledge about some of the intricate parts of the MEMS world were truly inspiring and helped shape parts of this project to the point where they are now.

I would also like to express my thanks and gratitude to Walter Lubeigt who became my second supervisor soon after him joining CMP and who's experience, knowledge and assistance in so many parts of this project were invaluable. There have been points where quite some late nights or even weekend days were spent by both of us working on some of the problems or planning the next steps forward and I am very grateful for the always open door for discussions. It also has been immense fun working in the lab together, from the exciting scientific experiments to the choice of music.

From the point I started Li Li was my first point of contact at CMP and helped getting me started and find my way around the University system, which I am still very thankful for. As our projects shared quite some common grounds there were many enjoyable discussions, banter and stories we shared over the three years of sitting back to back as well as a lasting friendship. Our conference trip to Istanbul will always stay in good memory and the amazing time we had there during and after the conference.

Ian Armstrong also deserves a special mentioning for all the little help on some data and image processing suggestions, for his guidance through some of the first TA labs I did, as well as for all the countless funny moments, inside jokes and great friendship we share from within the office to the regular trips to the climbing centre.

The whole atmosphere within CMP was one of the great things throughout this PhD and beyond, as the solidarity, helpfulness and sheer fun of everyone involved has made it a place that can only be described as a thoroughly enjoyable work environment that can hardly be surpassed. I am very grateful to everyone in the group making it to this amazing place. All the academic staff who are providing valuable guidance and enthusiasm, Walter, George and Brian who have all steered and helped steering this group where it is now, Michele and Gordon who are providing some of the broad width of research making this group so versatile and diverse, Mick whose optical sensing and Matlab expertise as well as his stories from Chorley and beyond always provide good entertainment. I also want to thank the researchers I have had the pleasure to work with over the time, Gordon, Euan and Bob who all provided helpful and diverse inputs to my work.

The whole group of PhD students have made CMP such a joy to work in and with a group so helpful, inspiring, cheerful and social I felt like having exactly the right balance to get through this PhD journey the best way one can imagine. Some have been with me along the way for quite a while: Cameron, Ran, Ania, Graham, Jamie and Barbara whose introduction of the group to Boteco has led to many fun occasions, while for others it feels like they have been here the whole time although they joined only recently: Kay, Carlota, Gordon, Thomas. I am very grateful to every single one of you shaping this wonderful work environment.

Finally I would also like to thank my family for all the support they have given me and am very grateful how this influenced everything from the decision of doing a PhD in Scotland to the overall PhD journey.

Abstract

The use of optical microelectromechanical systems (MEMS) as enabling devices has been shown widely over the last decades, creating miniaturisation possibilities and added functionality for photonic systems. In the work presented in this thesis angular vertical offset comb-drive (AVC) actuated scanning micromirrors, and their use as intra-cavity active Q-switch elements in solid-state laser systems, are investigated.

The AVC scanning micromirrors are created through a multi-user fabrication process, with theoretical and experimental investigations undertaken on the influence of the AVC initial conditions on the scanning micromirror dynamic resonant tilt movement behaviour. A novel actuator geometry is presented to experimentally investigate this influence, allowing a continuous variation of the initial AVC comb-offset angle through an integrated electrothermal actuator. The experimentally observed changes of the resonant movement with varying initial AVC offset are compared with an analytical model, simulating this varying resonant movement behaviour.

In the second part of this work AVC scanning micromirrors are implemented as active intra-cavity Q-switch elements of a Nd:YAG solid-state laser system. The feasibility of achieving pulsed laser outputs with pulse durations limited by the laser cavity and not the MEMS Q-switch is shown, combined with a novel theoretical model for the Q-switch behaviour of the laser when using a bi-directional intra-cavity scanning micromirror. A detailed experimental investigation of the pulsed laser output behaviour for varying laser cavity geometries is presented, also discussing the influence of thin film coatings deposited on the mirror surfaces for further laser output power scaling.

The MEMS Q-switch system is furthermore expanded using a micromirror array to create a novel Q-switched laser system with multiple individual controllable output beams using a common solid-state gain medium. Experimental results showing the simultaneous generation of two laser outputs are presented, with cavity limited pulse durations and excellent laser beam quality.

Table of Contents

List of Symbols

α	Absorption coefficient
ϵ	Dielectric constant
ϵ_e	Surface emissivity
η_s	Slope efficiency
γ	Power loss per round trip
κ	Curvature
λ	Wavelength
μ	Damping factor
ν	Poisson's ratio
ω_0	Angular frequency
ϕ	Photon density
ρ	Density
ρ'	Radius of curvature
σ	Stimulated emission cross section
σ'	Thin film stress
σ'_{SOI}	Bending stress of silicon
τ	Pulse duration
τ_c	Cavity life time
τ_f	Fluorescence life time
θ	Tilt angle
ξ	Damping coefficient
A	Area
A'	Fitting parameter
$\vec{B}$	Magnetic field
b	Side length of mirror
C	Capacitance
c	Speed of light
C_0,C_1,C_2,...	Capacitance fit constants
C_h	Specific heat capacity
C_p	Coefficient of thermal expansion

$c_{n,x}$	Zernike coefficient
D	Damping coefficient
d	Height separation / Distance
D'	Distance
D_s	Stiffness matrix
$\vec{E}$	Electric field
E	Young's modulus
E_{pulse}	Pulse energy
F	Force
f	Frequency
f'	Focal length
G	Shear modulus
g	Gain coefficient per unit length
G'	Gain within cavity
h	Device thickness
I	Current
I_θ	Torsional moment of inertia
K	Spring constant
k'	Fitting factor
k^*	Zernike normalisation factor
k_0,k_1,k_2,...	Nonlinear spring constants
k_t	Thermal conductivity
k_θ	Torsional spring constant
L	Round trip loss in resonator
l	Length
$\vec{M}$	Magnetisation
$\vec{m}_{coil}$	Magnetic moment
m	Mass
M^2	Beam quality factor
N	Population
n	Population density
N'	Number of comb gaps
n'	Refractive index
O	Output coupling fraction
P	Power
P_p	Pump power
R	Reflectivity
r	Radius

r_s	Resistivity
S_0	Initial stress
$\vec{T}'_y$	Torque around y-axis
T	Temperature
t	Time
T'	Torque
t_d	Pulse delay time
t_r	Cavity round trip time
V	Voltage
V'	Volume
V_{FEM}	Voltage of the FEM simulation
w	Width
w'	Laser beam radius
w_e	Energy density
W_p	Pump rate
x	Position
y	Distance
z	Height difference
z'	Propagation direction

1 Introduction

The use of microelectromechanical systems (MEMS) as sensors or actuators in commercial products has increased significantly over the last couple of decades, with current market analyses showing MEMS as a greater than 10 bn US dollar market in the year 2012 [1]. MEMS are used in a wide variety of sensor applications such as accelerometers [2] and microphones [3] and as actuators, e.g. as enabling elements in projector systems [4]. The increase is currently driven by demands especially from consumer products, with advantages of miniaturisation, added functionalities and cost reductions due to batch fabrication, enabling smaller packaging and the move towards the next generation of devices. In this thesis the sub-category of micro-opto-electromechanical systems (MOEMS) and specifically the theoretical and experimental investigation and application of scanning micromirror MEMS as intra-cavity elements in a solid-state laser system are studied. This is a novel application of scanning MEMS micromirrors, with only a proof of concept shown previously [5], as scanning micromirrors are currently primarily applied in imaging [6–8] and projection systems [9, 10]. In this work the feasibility and performance of a scanning micromirror as an active Q-switch in solid-state laser systems is investigated. The novel aspects of the work are to be seen as creating added functionality to the laser system due to the application of MEMS, as well as a new device design which permits further basic investigation of the electrostatic microscanner characteristics and performance of the specific microscanner design used inside the laser system.

The rest of this introductory chapter will give a short overview of the current MEMS technology, especially in the context of scanning micromirrors and the state of the art of these devices, as well as the application of MEMS in laser systems. The rest of this thesis is structured as followed:

In chapter 2 an analytical hybrid model for the prediction of the scanning behaviour of an electrostatic MEMS micromirror with angled vertical initial offsets of the comb-drive actuators is presented and verified. Chapter 3 investigates the specific case of a MEMS scanning micromirror with variable initial offset comb-actuators and the influence of this initial offset on the scanning behaviour of the mirror. The offset change is achieved by means of (a) an electrical actuator and (b) mechanical displacement. The application of the analytical model from chapter 2 confirms the experimental behaviour, with higher initial offsets leading to higher scan angles. In chapter 4 the use of a scanning micromirror as an active Q-switch element and end mirror of a Nd:YAG solid-state laser system is investigated. The Q-switched laser performance using gold coatings and a test dielectric coating on the micromirrors is evaluated using several laser setups. A novel simulation model for determining the Q-switched laser output using MEMS scanning micromirrors as active Q-switch elements is also presented in chapter 4 and verified for one of the experimental investigated laser setups. Chapter 5 introduces the novel concept of using an array of scanning micromirrors to create multiple individual temporal controlled laser outputs through a single solid-state laser gain medium. A dual output laser system is presented with maximum pulse energies of almost $8\,\mu$J. Chapter 6 summarises the findings in the thesis and gives an overview of the challenges and outlook for future work.

1.1 MEMS technology

MEMS are, as the name states, devices with functional parts of dimensions in the micrometre range using electrical actuation or readout to excite or measure mechani-

cal movements. The microscale definition of the functional parts leads to fabrication requirements with alignment tolerances and accuracy in the single micrometre range. To achieve these requirements, MEMS have built on and benefited from the development of the integrated circuit (IC) technology, which started from the 1960s. The use of silicon as material of choice for a majority of MEMS devices originates from this background, as reliable and cost-effective fabrication technologies were developed and adapted from the IC sector and extended to allow for the specifics of MEMS, particularly having thicker functional structures and sometimes requiring full thickness etching of substrates. The specific advantages of MEMS are therefore partly achieved through this combined origin of the fabrication processes, with batch fabrication possibilities leading to low device costs, ease of integration due to the small feature sizes, low power consumption and the possibility for novel applications and concepts due to novel sensing or actuation possibilities.

1.1.1 Common MEMS fabrication processes & materials

MEMS fabrication processes can be classified in general, and especially for silicon based fabrication, in the two categories of surface micromachining and bulk micromachining [11]. Both processes use a combination of photoresists, photolithography and etch steps to define the device geometries, plus material deposition of functional materials including metals, piezoelectric film layers, magnetic film layers or even biological or chemical layers. Surface micromachining uses the deposition and patterning of thin films on top of a substrate, including sacrificial layers which are used for releasing functional structures through etching. A wide variety of materials can be used with poly-silicon being a common material. The substrate is in this case not patterned, and released structures are therefore suspended above a relatively thin air cavity. Bulk micromachining is used especially for single crystal silicon (SCS), with the substrate not only being the mechanical base but also a part of the device, e.g. as proof mass for accelerometers. The substrate is in this case also undergoing a patterning and etch step,

with non-liquid based etching being done in the form of a deep reactive ion etch (DRIE) step to achieve as close as possible vertical sidewalls throughout the substrate. Alternative fabrication processes, especially for applications in bio-compatible MEMS and microfluidics, are based on forming a mould and reforming the features in the desired material, with processes like LIGA (Lithographie, Galvanoformung und Abformung, German) [12] or similar fabrications using SU-8 and PDMS [13].

The most common material used for MEMS devices is nevertheless silicon, especially SCS [14], due to its availability through IC fabrication and the related reliable small feature size fabrication capabilities. SCS has a hardness above iron ($850\,\mathrm{kg\,mm^{-2}}$) and tensile yield strength values of a multiple of stainless-steel ($7.0 \cdot 10^5\,\mathrm{N\,cm^{-2}}$), combined with a maximum possible value of the Young's modulus close to it (190 GPa) [15], leading to more reliable devices due to the single crystal structure and these strength values. Silicon in the form of poly-silicon is used for surface micromachining and exploits material properties that maintain some of SCS advantageous properties [16]. Polysilicon is deposited as a thin film with process temperatures in excess of 500°C and has no homogeneous crystal lattice but crystal grains, leading to variations of the material parameters and possible high stress concentrations and gradients [16]. The advantage of polysilicon is an easy integration into the CMOS processes as an additional layer. Nevertheless, the high deposition temperatures restrict possible additional functional materials. Recently MEMS devices were also investigated with ceramic materials as functional parts, especially using carbides and nitrides like SiC [17], SiN [18] or AlN [17], which are integrated with common SCS process steps.

The MEMS devices designed, characterised and applied in this thesis are all fabricated using a multi-user silicon on insulator process, SOIMUMPs, offered commercially by the foundry MEMSCAP Inc. with well investigated material parameters [14, 19]. This process uses doped SCS device layers with 10 μm or 25 μm thickness and will be described in detail in section 3.2.

1.1.2 MEMS sensing and actuating principles

Historically MEMS sensors are more advanced than actuators due to the easier integration and coupling to the macroworld [11]. Sensing principles can be roughly classified by their physical principle with displacement, inertia or pressure most commonly sensed by piezoresistive or capacitive sensors. Piezoresistive sensors are built on the principle of changing resistance due to strain in the material [20], while the changing distance or overlap area of capacitor electrodes change the measured capacitance [21]. Magnetic fields can be detected with Hall [22] or Lorentz-force [23] sensors, measuring an induced current or displacement due to the presence of a magnetic field. For chemical sensing conductive polymers or impedance based sensors can be used amongst others. A capacitance change of an polymer coated electrode based sensor can be measured, due to swelling and changes of the dielectric constant of the polymer when specific chemicals are absorbed [24]. For metal oxide based impedance chemical sensors the conductivity also changes when a chemical reaction takes place, which requires in general the metal oxide to be heated [25]. Further chemical sensors include surface acoustic wave (SAW) sensors, where the resonance frequencies of the SAWs change with chemicals binding to the used substrates [26], or electrochemical sensors where current or potential changes due to chemical reactions on electrodes are measured [27]. Biological sensors can use molecular-specific reactions which can be very specific but are generally irreversible [28], or even cell-based sensors where living cells can detect and amplify chemical signals [29].

Actuator principles for MEMS are generally classified into four categories. (I) Electrothermal devices using Joule heating to create displacements, (II) piezoelectric devices using piezoelectric forces in specific materials like PZT, ZnO or AlN, (III) electromagnetic devices using Lorentz forces or magnetostatic forces and, lastly, (IV) electrostatic devices using the electrostatic force created between capacitive electrodes. In the next section, examples will be presented how the above mentioned micro-actuation techniques are implemented in MEMS scanning mirrors.

1.2 MEMS scanning mirrors

MEMS scanning micromirrors were one of the first applications of actuated structures in the field of optical MEMS, with a first device demonstrated by Petersen in 1980 [30] and built using a SCS device layer in combination with a manually aligned glass substrate incorporating backside electrodes for the actuation. Since then scanning micromirrors have been widely investigated using a variety of actuation principles and have been applied to a variety of application areas and commercial products. Generic advantages of scanning micromirrors are the possibility of a high angular range (above 80° optical scan range) combined with a frequency actuation in the kHz range, the high reliability due to the use of SCS, an easy integration possibility for position sensor principles and the general advantages of MEMS including their miniaturisation potential and batch fabrication possibility. In the rest of this section the mentioned application areas and actuation principles will be reviewed and introduced.

1.2.1 Application areas of scanning mirrors

MEMS scanning micromirrors have application possibilities in a wide variety of areas, with a general classification being possible as projection systems, imaging systems, sensing applications and application for laser beam manipulation. For projection systems, commercially available systems can be found, like Microvisions pico-projector [31], as well as laboratory-based systems for displays [32, 33]. Imaging system based applications of microscanners have also been demonstrated in a variety of fields, with barcode scanner systems commercially available and single pixel cameras having been demonstrated in a laboratory environment [34]. MEMS microscanners in biomedical applications enable integration in endoscopic probes for in-vivo imaging and include optical coherence tomography [35], reflectance and fluorescence confocal microscopy [36,37] and multi-photon microscopy [38, 39]. For sensing applications scanning mirrors have, for example, been demonstrated in a Fourier transform infra-red spectrometer [40]. Laser

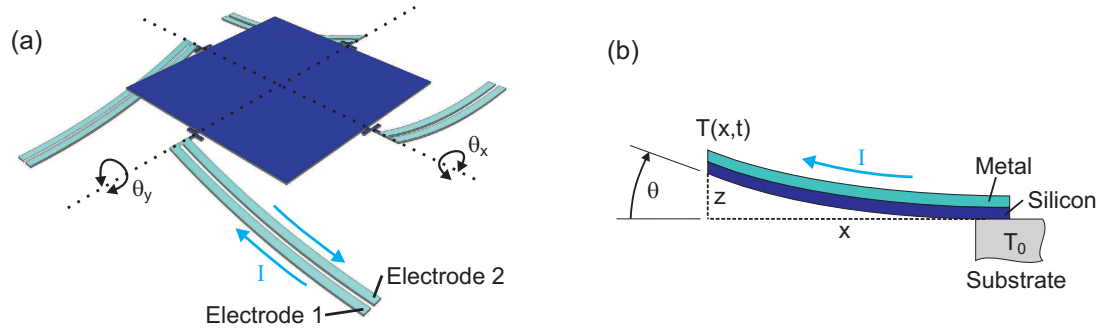

Figure 1.1: (a) Schematic of a 2D electrothermal scanner with (b) parameter definitions for a bimorph actuator model.

beam manipulation with scanning micromirrors is done in the context of variable optical attenuators [41] and has also been demonstrated in a first test as an intra-cavity element in a laser system for obtaining Q-switched laser output [5]. The actuation principles for the enabling scanning mirrors of these applications will be described in the following sections, starting with electrothermal actuation followed by electromagnetic actuation, electrostatic actuation and piezoelectric actuation.

1.2.2 Electrothermal actuation

Electrothermal actuation schemes for scanning micromirrors are generally split into two groups, one of which uses the bimorph effect between two materials with different coefficients of thermal expansion (CTE) to generate an out-of-plane movement, and the other one using a geometric constrain to generate the out-of-plane movement. Thermal actuators were first used by Riethmüller and Benecke in 1988 [42] to build a microactuator based on a bimaterial transducer element which can be used for scanning micromirrors. The thermal expansion of materials due to Joule heating is in this case used to generate the movement. The thermal time constants of these movements, usually lying in the range of tens of milliseconds, limit the actuation speed for static displacements, which is the desired operation regime for this actuation concept. A general schematic of an electrothermal actuated micromirror and a cross section view of a generic bimaterial actuator can be seen in Fig. 1.1(a) and Fig. 1.1(b) respectively. When applying a poten-

tial difference $V(t)$ between electrode 1 and 2 the resulting current I will generate heat in the actuator. The temperature distribution $T(x,t)$ along the actuator, in respect of the position x and time t, is then mainly governed by the heat generated by the current and by the loss due to heat conduction through the material to the substrate. This can be described by the one-dimensional heat equation [43]:

$$\frac{\partial T(x,t)}{\partial t} = \frac{V^2(t)}{C_h \rho\, r_s\, l^2} + \frac{k_t}{C_h \rho} \frac{\partial^2 T(x,t)}{\partial x^2}. \tag{1.1}$$

In this case heat conduction through air to the surrounding substrate, convective cooling through air flow and radiative heat losses are often neglected [44]. C_h is the effective specific heat of the material combination, ρ is the effective density, r_s is the resistivity, l the length of the actuator loop and k_t the effective thermal conductivity. The increased temperature generates an elongation of the actuator beams, which is translated into an out of plane movement by the previously mentioned mechanisms of bimorph actuation or geometric constraint.

In the bimorph case, the temperature change will create a change in the stress distribution between the two material layers due to different CTEs of these materials. This leads to an out of plane bending of the beam. Metals generally used for bimorph actuators include gold [42], nickel [45] or aluminium [8, 46–48] and have a higher CTE than the substrate layer, which consists of silicon or silicon-dioxide. This leads to a downward bending movement with increasing temperature when the metal layer is deposited on top of the silicon.

In the case of geometric restraints leading to an out of plane actuator motion, a combination of "hot" and "cold" beams is used to generate the movement. These beams share typically a common connection point to the micromirror, with a "cold" beam implying that no current is present through this beam and therefore no *active* Joule heating. A temperature change still occurs due to heat conduction through the connection to the "hot" beam, which experiences Joule heating. Some of the geometrical

layouts presented so far centre around a two layer beam structure. A step between single or multiple inner unheated and outer heated beams [49, 50] has been shown as well as two beams located on top of each other with a connection point only at the top end of the beams [51]. A single layer structure has also been used with a single unheated inner beam where the displacement direction is induced by an intrinsic stress in the silicon layer [43]. The deflection using geometrical constraints is in general an upward bending movement, but depends on the initial configuration of the mechanical connection.

The general advantage of electrothermal actuators can be seen in their possibility to create displacements with low, single digit, driving voltages compared to higher required voltage levels of electrostatic actuators. Additionally the possibility of static displacements allows not only dynamic beam scanning but also beam steering applications, with the acting force being independent of the position of the actuator. Limitations of thermal actuators can mainly be seen in the thermal time constants of the actuation, limiting the usage to mostly lower frequencies in the range of tens of Hertz. The thermal heat limits also constrict the maximum actuator displacements, with an additional disadvantage being the power consumption in the tens to hundreds of milliwatt range compared to other driving principles with orders of magnitude lower power consumption.

Electrothermal actuators with bimorph actuation have mostly been used so far for scanning micromirror, especially in systems having the possibility of static displacement. Inverted in series connected bimorph actuators have been used [48,52] to generate a tip-tilt-piston movement, with an example shown in Fig. 1.2(a). The use of four actuators symmetrically placed around the mirror plate allows a pure piston movement with a displacement of up to 480 μm. Static tilt angles of up to 60 $^\circ$ total optical scan angle (TOSA) at 8 V are possible with dynamic actuation at the resonance frequency of 490 Hz almost doubling the angle, albeit by introducing a slight mode coupling between the two tilt axes. A similar connection concept for the actuators has also been used with folded bimorph actuators [35], achieving static TOSA values of 62 $^\circ$ with 5.5 V dc and

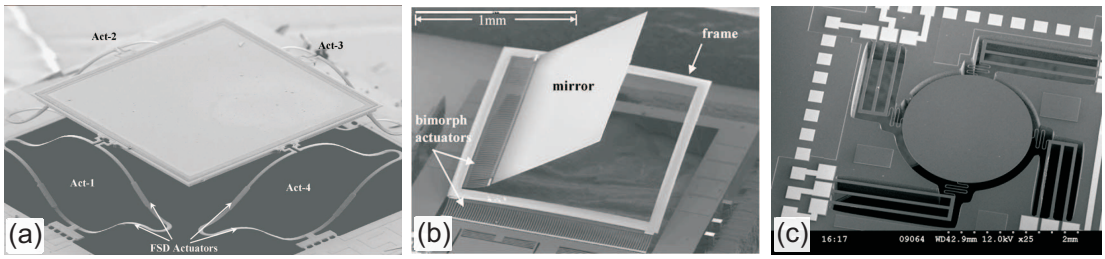

Figure 1.2: Examples of electrothermal scanning mirrors: (a) use of inverted in series connected actuators [52], (b) use of a linear array of bimorph actuators [46], (c) micromirror using geometric constraints [34].

piston displacements of more than 600 μm. The general concept of this actuator is a linear array of bimorph cantilevers connected in parallel to generate the displacement. Similar actuators have also been shown without the folding structure for 1D [53, 54] and 2D [46,55,56] tilt operation (see Fig. 1.2(b)). The disadvantage of these structures is the loss of the rotation axis at the mirror centre. A maximum static 1D mechanical scan angle of 124° was shown [53] without heat failure of the device. The use of a single bimorph actuator instead of an array has also been shown in variations with a one dimensional tilt through a single connection [45] and with connections to the mirror plate designed using serpentine springs to allow a plane mirror surface despite the angled actuators [8, 47, 57]. The tilt angles of these devices were shown to be around 20° TOSA with actuation voltages as low as 1.4 V. The use of geometric constrained actuators in scanning micromirrors follows a similar connection scheme as the single bimorph actuators, by using serpentine springs as connections to the mirror plate [34] (see Fig. 1.2(c)). The geometric constrain is hereby achieved by an unheated middle beam and an initial upward out-of-plane bending curvature of the actuator due to intrinsic stress distributions resulting from the fabrication. The tilt angles are considerably lower than the ones observed with bimorph actuators with angles of 3° TOSA, but allowing the usage of simpler fabrication processes.

Additionally to the purely electrothermal actuation described so far, there have also been device investigations using hybrid actuation schemes, combining electrothermal actuation with electrostatic or electromagnetic actuation, whose basic principles will be

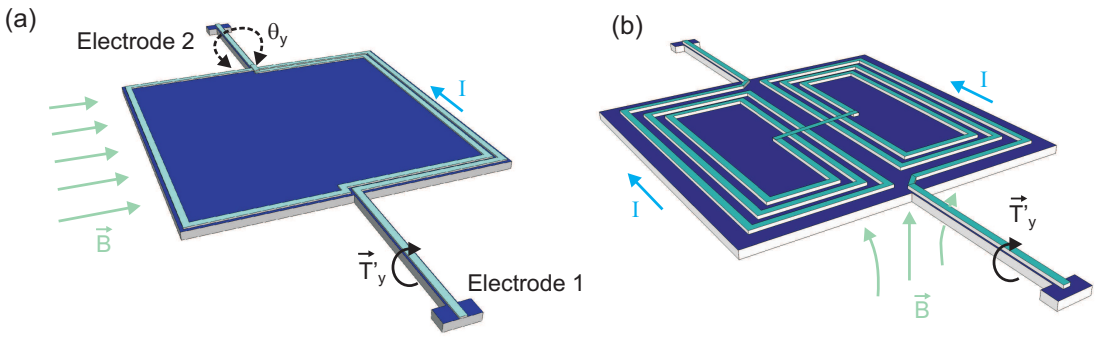

Figure 1.3: Schematic of electromagnetic scanners with permanent magnets placed (a) at the side of the mirror surface or (b) underneath it.

described in the following sections. The combination of electrothermal and electrostatic actuation for generating one "slow" thermal axis, in the movement frequency range of tens of Hertz, and one "fast" electrostatic axis, in the kilohertz range, shows the possibility of 2D raster scan patterns with more than 10 ° TOSA in both axes and a fast scan axis with resonant frequencies of 1.6 kHz [7]. The same combination principle has also been used combining electrothermal and electromagnetic actuation [58], with the slow electrothermal axis allowing scan angles of up to 3 ° TOSA and the electromagnetic axis of up to 6 ° TOSA with 10 V actuation each. The thermal axis drives in this case a frame structure on which the magnetic actuator is fixed in a gimbal configuration. The combination of electrothermal actuation and electromagnetic actuation within the same actuator has also been shown [59] with the actuation current through the thermal beam working at the same time as the origin of the electromagnetic force. The advantage of this combination is the use of the high force electrothermal actuation when operating at a relative low frequency range and the use of the electromagnetic actuation for high angle driving at resonances above 10 kHz.

1.2.3 Electromagnetic actuation

Electromagnetic actuation for a scanning micromirror can also be split into two design groups. Either a conductor coil on the mirror is used in a static external magnetic field to generate the mirror movement torque (see Fig. 1.3), or a ferromagnetic layer on

the mirror is used in an external magnetic field which controls the mirror displacement by its orientation and strength. The governing principle of the mirror coil actuation is the Lorentz force acting on moving charges in a static magnetic field. Placing the micromirror in a static, homogeneous magnetic field $\vec{B}$ created by permanent magnets placed on the non-anchored sides of the mirror will create a torque $\vec{T}_y'$ when a current I is flowing through the conductor loop on the mirror surface (see Fig. 1.3(a)). The torque can be expressed as:

$$\vec{T}_y' = \vec{m}_{coil} \times \vec{B}, \tag{1.2}$$

with $\vec{m}_{coil}$ being the magnetic moment of the coil which can be expressed as $m_{coil} = I \cdot A_{total}$, where A_{total} is the area enclosed by the coil turns [60]. Reversing the current flow in the coil will create a torque in the opposite direction. This allows a bidirectional static tilt actuation which is controlled by the current. The magnitude of the current is limited by the heat induced damage to the metal tracks, which sets the requirement for relatively large external magnetic fields to create large movement angles. Most presented devices use permanent magnets with magnetic fields in the range of 0.5 T. Instead of using two permanent magnets on the side of the chip it is also possible to use a single magnet below the chip [61–63]. In this case two coils with opposing spiral direction need to be placed on each side of the mirror surface, with the dividing line along the desired torsion axis (see Fig. 1.3(b)). To generate the required torque a non uniform magnetic field with a field gradient is needed, which generally is the case for a small magnet having a similar footprint as the mirror surface. A detailed investigation of the influence of the magnet shape and size is presented in [63].

When using a ferromagnetic layer on the mirror surface, a magnetostatic force can be induced by the interaction of an external magnetic field with the magnetization $\vec{M}$ of the ferromagnetic layer (see Fig. 1.4). The external magnetic field is created by a coil structure allowing the control of the mirror tilt. It needs to act with an angle on the ferromagnetic layer, similar to the single backside permanent magnet case discussed previously. The tilted magnetic field creates a magnetization $\vec{M}$ in the ferromagnetic

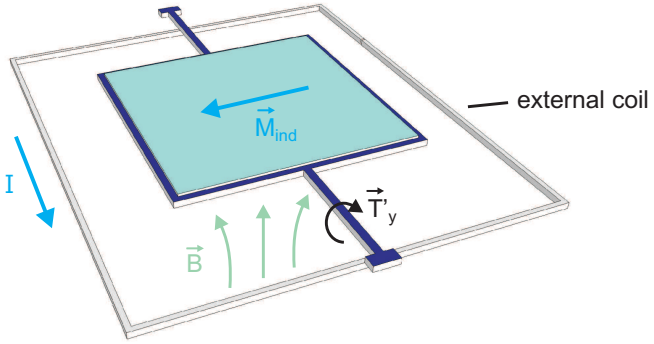

Figure 1.4: Schematic of an electromagnetic scanner with an external coil driving the micromirror.

layer, which then tries to align with the inducing field and therefore creates the driving torque $\vec{T}'_y$ for the mirror. This can be expressed as [64]:

$$\vec{T}'_y = V'_{mag} \cdot \vec{M} \times \vec{B}, \tag{1.3}$$

with V'_{mag} being the volume of the ferromagnetic material. The magnetization $\vec{M}$ depends in this case on the inducing external magnetic field $\vec{B}$, the angle between the original mirror surface position and the external field, as well as material and geometry parameters of the ferromagnetic layer. Additional to the torque created by the magnetization of the ferromagnetic material a second torque can be created on the mirror surface due to eddy currents in the mirror plate, which are induced by a time varying magnetic field when driving the external coil magnet with an AC signal [65]. The induced eddy currents create a Lorentz force when placing the chip in between permanent magnets, which adds a torque component for the movement of the scanning mirror.

The first demonstrated magnetic mirror-like tilt actuator consisted of a permanent magnet mounted on a movable silicon plate with a planar gold coil structure surrounding the actuator [66]. Rotation angles of up to 15 ° TOSA were achieved with drive currents of 235 mA. Since then both previously discussed driving principles have been used to create scanning micromirrors.

Using a ferromagnetic layer on the backside of the mirror surface and the backside of the torsion springs allows actuation with an in-plane or out-of-plane magnetic field [67]. The in-plane magnetic field uses magnetostrictive actuation of the torsion bar to create a torque, while the out-of-plane field acts on the full backside layer creating an electromagnetic torque due to the change of magnetization in the magnetic layer. TOSAs of up to 25 ° are shown at resonance with a resonance frequency of 55 Hz. The use of magnetostatic actuation using a permalloy film deposited on the mirror has also been shown with a non-symmetric magnetic field created by an offset located bottom coil with [64, 68] and without [69] a side-mounted permanent magnet. The permanent magnet on the side ensures a constant magnetization of the ferromagnetic layer. The results without the permanent magnet show a maximum TOSA of 25 ° while with the permanent magnet TOSAs of 88 ° are shown [68]. Applying an in-plane magnetization with 45 ° orientation to the scan axes allows the simultaneous actuation of both axes by creating 2D scan patterns using both resonance modes of a gimbal structure (see Fig. 1.5(c)) actuated at the same time [64]. A scan field of 13 ° x 11 ° with resonant frequencies of 584 Hz and 11.15 kHz has been shown with this. The general advantage of using ferromagnetic layers is seen in easier fabrication processes as no additional layers for coil isolation are needed on the mirror.

When looking at the two discussed possibilities for using coils on the mirror surface, the use of a bottom permanent magnet allows a more compact setup and higher fill factors when using multiple mirrors. By using the discussed 2 counter propagating coils on two sides of a desired torsion axis, a simple spreading magnetic field from a permanent magnet underneath the mirror generates a torsional torque. Four coils on the backside of the mirror surface [61] or two coils each on the frame and the mirror surface [62] have been used for generating 2D scanning patterns. The size of the frame of the gimbal mounted mirrors can be reduced by using coils only on the mirror surface which allows a higher fill factor. A 16 x 20 mirror array has been shown with this principle with mirror diameters of 1.4 mm and scan angles of more than 24 ° TOSA

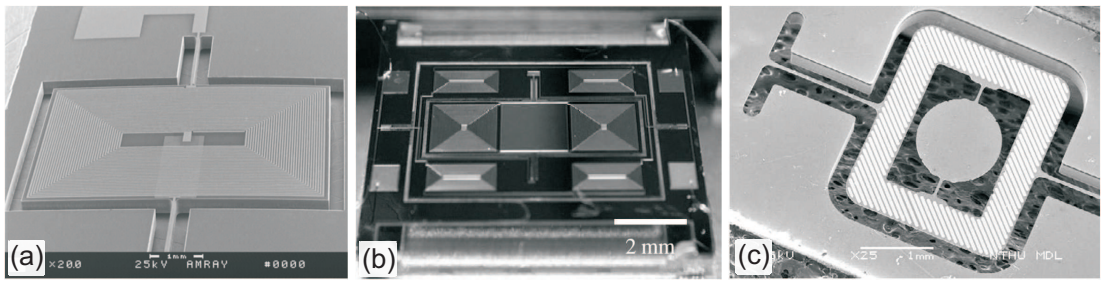

Figure 1.5: Example of electromagnetic actuated scanning mirror: (a) with single coil actuation [71], (b) with dual coil and single permanent magnet [62] and (c) with ferromagnetic layer on mirror [64].

for static displacement in both axes. The resonance frequencies in this case are quite low with 96 Hz and 135 Hz. Using the frame as substrate for one of the coil pairs (see Fig. 1.5(b)) allows static torsion angles of 16° TOSA for a mirror surface with 2 mm diameter and also low resonance frequencies of 106 Hz and 80 Hz. 1D scanners with permanent magnets placed at the side of the mirror were shown with TOSAs of 16° at 4 kHz resonant frequency including an actuation and a sensing coil on top of each other [70] as well as mirrors with large size of $6 \times 4\,\mathrm{mm}^2$ which showed maximum TOSA values of 30° at 0.8 kHz resonant frequency (see Fig. 1.5(a)) [71]. The use of similar devices for 2D scanning has also been presented by actuating a torsion and flexing mode of the mirror simultaneously in resonance [72]. The in-plane magnetic field needs to be orientated at 45° to the torsion axes in this case. A 2D scanning mirror which allows a raster scan pattern has also been shown by using a gimbal structure with a driving coil located at the frame only [33]. In this case the driving signal is a combination of the resonance actuation of the inner mirror at 21.3 kHz, which is coupled from the frame to the gimbaled mirror, and a quasi static raster scan of the frame. TOSA values of 65° and 58° are achieved in this case. A complete decoupling of both axes has also been achieved by using a gimbal structure with separate coils placed on the backside of the frame and the mirror [73]. This allows static tilt in both axes with TOSA of 4.6°. To avoid any coil connections on the torsion beams, two additional principles have been investigated: the use of an induced current in a closed loop coil on the mirror surface [74] and the use of eddy currents excited by an AC magnetic field in a

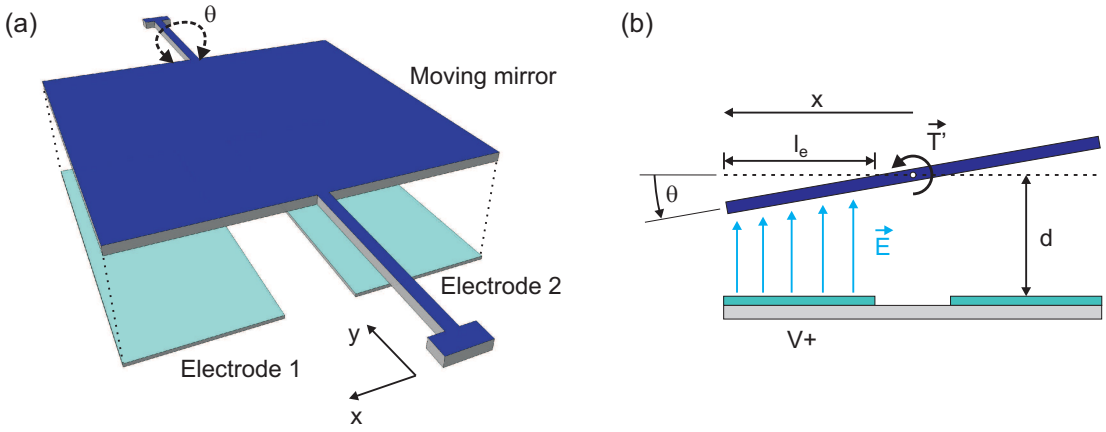

Figure 1.6: (a) Schematic view of an electrostatic parallel plate actuated mirror and (b) definitions for the torque and actuation calculations.

metal layer on the mirror [65]. The general advantages of electromagnetic actuation lie in the possible static actuation with linear forces and a lower power consumption than thermal actuated mirrors. But the need of permanent magnets or driving coils introduces a constraint on the size requirements.

1.2.4 Electrostatic parallel plate actuation

Electrostatic actuation has been the most popular actuation scheme so far for scanning micromirror, from the first device shown in 1980 [30] up to the present day. General advantages are a low power consumption (in the range of μW) due to only parasitic current flow and the possibility of using simple fabrication processes. The category can also be split into two distinctive designs: electrostatic parallel plate actuation and comb-drive actuation. The first principle will be discussed in this section with comb-drive actuation featuring in the two subsequent sections.

The movement of a scanning micromirror with electrostatic parallel plate actuation is based on the attracting force between two electrodes when applying a potential difference. Two electrodes placed underneath a suspended mirror plate (as seen in Fig. 1.6) can then generate a static or dynamic tilt movement of the mirror plate around the connection axis y. When applying a voltage V at one of the electrodes and grounding

the moving mirror, an electric field $\vec{E}$ is created between the electrode and the mirror plate, which will create the attracting force F [75]:

$$F = \frac{1}{2}\frac{\mathrm{d}C}{\mathrm{d}z}V^2 = \frac{1}{2}\varepsilon\frac{A}{d^2}V^2 \tag{1.4}$$

where C is the capacitance between electrode 1 and the moving mirror, A is the area of the electrode, d is the height separation between the mirror and the bottom electrode, ε is the dielectric constant and V is the applied potential difference. The torque T', responsible for the mirror movement, depends on the distance of the acting force to the mirror rotation axis and can then be calculated by [30]:

$$\begin{aligned} T' = \int_{b/2-l_0}^{b/2} F(x)\cdot\frac{x}{b}\,\mathrm{d}x &= \frac{1}{2}\,\varepsilon\,V^2\,b\int_{b/2-l_0}^{b/2}\frac{x}{d(x)^2}\,\mathrm{d}x \\ &= \frac{1}{2}\,\varepsilon\,V^2\,b\int_{b/2-l_0}^{b/2}\frac{x}{(d-\theta x)^2}\,\mathrm{d}x. \end{aligned} \tag{1.5}$$

b is in this case the side length of the mirror, l_0 the distance of the start of the bottom electrode from the mirror rotation axis and θ the tilt angle of the mirror. At static displacements this torque equals the restoring torque of the two torsion bar springs, through which it is possible to calculate the static mirror angle. Dynamic actuation is also possible with an increased angular response at the mechanical resonance of the mirror. To form a 2D scanning mirror with a similar combination of static and dynamic driving possibilities the bottom electrodes need to be separated into 4 quadrants and a gimbal frame added around the mirror surface [76]. Sensing of the mirror position can be achieved by reading out the capacitance of the unused electrodes.

The attractive possibilities of the combination of 2D static scanning with low power consumption, fast response times and high fill factors are counterbalanced by the disadvantages of a multi-layer fabrication process, a limiting scan angle defined by the distance between the mirror plate and the bottom electrodes and the drop of actuation force with increasing electrode distance to the mirror. Additionally, pull-in behaviour

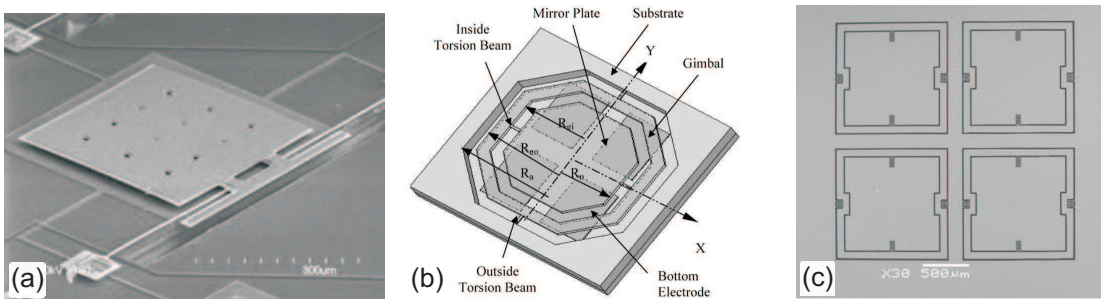

Figure 1.7: Examples of electrostatic parallel plate scanning mirrors: (a) 1D switching mirror with 90° rotation [80], (b) 2D scanning mirror [81], (c) 2x2 array of 2D mirrors with side wall electrodes [82].

can be observed at higher angles which creates the necessity to design a physical stop or appropriate driving schemes to avoid this. Pull-in describes the snapping of the mirror plate to the ground electrodes due to the increased electrical field strength.

The very first demonstrated scanning micromirror used parallel plate actuation by assembling the moving part, defined by etching of a silicon chip, on top of a glass substrate with the bottom electrodes [30]. Scan angles of 2° TOSA at 15 kHz resonant frequency were shown. Several modification schemes to the actuator were used over the years to lower the necessary actuation voltages, improve the linearity of the scanner and avoid pull-in phenomena. One of these is the use of inclined bottom electrodes [77] to reduce the required driving voltage. Scan angles of 43° TOSA at a resonance frequency of 925 Hz were shown. To avoid pull-in behaviour closed-loop control can be used with online measurement of the mirror displacement on a position sensitive detector [78] or by mechanical means, for example with using a comb-structure on the side of the mirror [79]. In this case the combs hit the substrate next to the electrodes and prevent a short between the mirror surface and the bottom electrodes. A 1D switching mirror with static tilt angles of up to 90° TOSA has also been reported by using a non-symmetric mirror with a short actuator side which gets pulled into a trench area by horizontal and vertical electrodes [80].

Two dimensional scanning mirrors have been presented by adding a gimbal frame structure and either using 4 bottom electrodes underneath the mirror or 2 electrodes

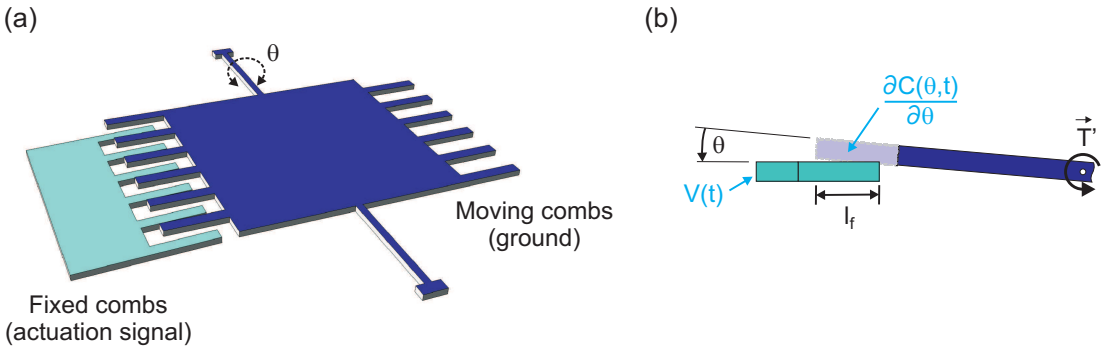

Figure 1.8: (a) Schematic of electrostatic comb-drive actuation and (b) definitions for in-plane vertical actuator calculations.

each placed under the mirror and under the frame. In the first case a higher active mirror area is present with scan angles of 6° TOSA [81] or 3° TOSA [76]. Modelling and linearisation of the driving of these type of devices has been shown with multiple approaches [83,84] to reach a linear static scan field of the mirror. The second case uses a wider frame to accommodate the bottom electrodes underneath it [85,86], which enables an easier decoupling between the two scan axes. To increase the electrostatic force for 2D scanning micromirrors added side wall electrodes next to the bottom electrode actuation have been investigated [87], which allow static rotation angles of up to 20° TOSA. Due to the placement of the actuators underneath the mirror surface, arrays with high fill factors can be achieved. For one dimensional scanners a linear array with elongated mirrors and scan angles of up to 6° TOSA was shown [88], while two dimensional scanners in a 2x2 array with a fill factor of 56 % were also demonstrated [82].

1.2.5 Electrostatic comb-drive actuation

The use of electrostatic comb-drive actuators for fast scanning micromirrors has become very popular over the last decade due to their higher actuation forces with lower required voltage levels compared to parallel plate actuators, and the fact that no external components are needed as is the case for electromagnetic scanner. A schematic of a comb-drive actuated scanning mirror can be seen in Fig. 1.8(a). The higher actuation forces are achieved due to a greatly reduced distance between the driving electrodes

compared to the distances for parallel plate actuation. This leads to an increased overall capacitance and therefore to the possibility of reduced driving voltages. A direct torque T' is created by the capacitance change between the comb electrodes (e.g. see [89]):

$$T'(\theta, t) = \frac{1}{2} \frac{\mathrm{d}C(\theta)}{\mathrm{d}\theta} V(t)^2 \tag{1.6}$$

with $C(\theta)$ being the overall capacitance between the comb fingers, which changes with the scanner rotation angle θ, and $V(t)$ being the excitation voltage (see Fig. 1.8(b)). As the torque always acts to maximize the capacitance and therefore the comb overlap, no static displacements are generally possible, apart from schemes where high initial offsets between the combs exist. Due to this, resonant driving schemes are used for this type of scanning mirror with the resulting scanner dynamics and rotation angles being determined through the general Duffing type movement equation [90]:

$$I_\theta \ddot{\theta} + D \dot{\theta} + K \theta = T'(\theta, t). \tag{1.7}$$

I_θ is the torsional moment of inertia of the moving part of the scanner, D is the damping coefficient, K the spring constant determined by the two torsion beams and $T'(\theta, t)$ the already mentioned electrostatic torque created by the applied voltage. Solutions to this equation have a sinusoidal form and show high scan angles only around the mechanical resonance frequencies, which are determined by the mechanical properties and dimensions of the scanner. Two main philosophies were followed so far for creating vertical comb drive scanning mirrors. Number one tries to align the combs perfectly in-plane, whilst number two tries to create a vertical or angled offset between the fixed and moving combs.

In-plane vertical comb-drive actuators

In-plane comb-drive actuators were first used in 1989 to create resonant structures in poly-silicon, with the movement confined in the device layer plane [91]. To modify these

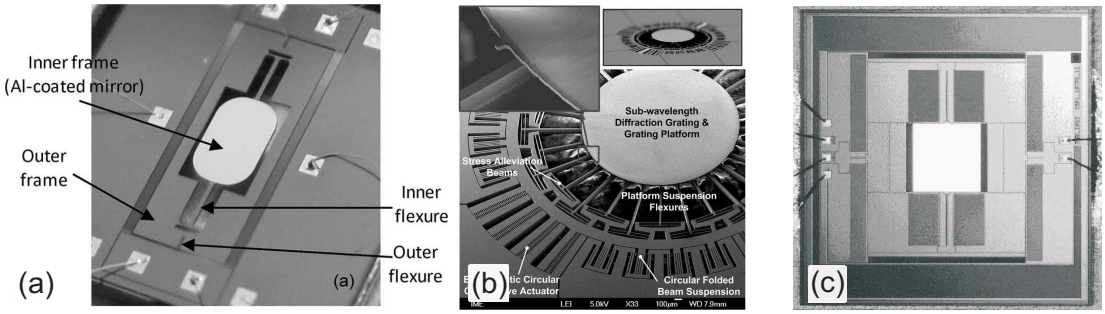

Figure 1.9: Examples of in-plane vertical comb-drives: (a) 1D scanner with magnification of inner mirror movement [90], (b) rotating grating scanner [92], (c) 2D scanning mirror [93].

structures for achieving a torsional movement a modified spring structure is needed, with no direct modification of the comb-drive being necessary as small imbalances created through the fabrication are sufficient to allow the start of a torsional resonance movement, provided the actuator is driven around the torsional resonance frequency of the scanning mirror. The advantage of this type of comb-drive is that no additional fabrication steps are required to align or offset the comb fingers. A perfect flatness of the combs also leads to flat mirror surfaces due to fabrication in the same device layer, which is one of the important considerations for scanning mirrors in projection and imaging systems.

One dimensional scanning mirrors have been investigated in terms of their damping [94], phase control for stable driving [95] and their dynamic flatness behaviour. Distributed spring connections to the mirror surface with multiple joints [10, 96] and the additional use of a backside reinforcement structure underneath the mirror surface have shown to reduce the dynamic deformation of the mirror surface with scan angles of 40 ° TOSA at resonance frequencies of 30.8 kHz, also by using a double frame structure [97]. The inclusion of a frame structure adds the additional advantage of a possible magnification of the tilt movement, excited by the combs located at the outside of the frame, in respect to the mirror part connected with a second, thinner torsion beam which is set in line with the original torsion axis (see Fig. 1.9(a)) [90]. TOSA of 72 ° at a resonance frequency of 22.1 kHz with 190 V_{p-p} actuation have been shown in this

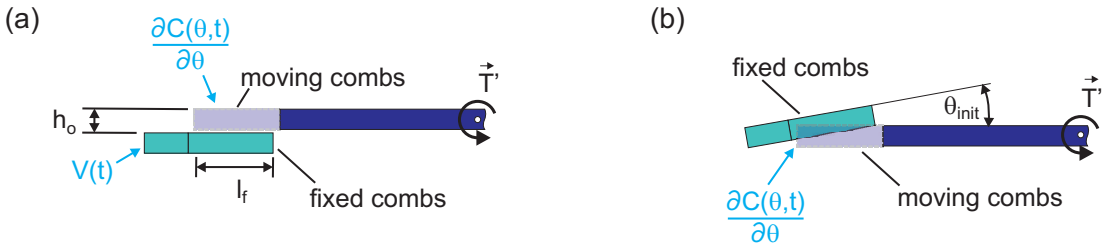

Figure 1.10: Initial positions of (a) staggered vertical comb-drives (SVC) and (b) angular vertical comb-drives (AVC).

case using an out-of-phase movement between the frame and mirror parts. A further concept for one dimensional scanning mirrors with in-plane comb-drives has been developed using an in-plane rotating grating, which scans the first order diffraction of an incident beam [98] (see Fig 1.9b)). By using a multi-layer approach and fabricating the diffraction grating platform separately from the circular comb-drive actuators scan angles of 33 °TOSA at 23.4 kHz were demonstrated with this technology [99].

Two dimensional scanning is generally achieved by implementing a gimbal-frame structure with separate comb-drive actuators for both scanning axes. In this case extra effort needs to be undertaken to electrically isolate the two sets of comb-drives by using oxide filled trenches. The first demonstration of this (see Fig. 1.9(c)) showed scan angles of 22 °TOSA at 0.72 kHz with 16 V actuation for the mirror axis and 8 ° TOSA at 0.9 kHz with 22 V actuation for the frame axis [93, 100]. Improvements to the angular range can be shown by modifying the mirror towards a more elliptical shape [101] and also by an adapted spring design for linearising the spring behaviour [102]. This lead to an optical scan range of up to 112 ° x 84 ° TOSA at resonance frequencies of 1 kHz and 16 kHz respectively, with also including a piezo-resistive sensor for integrated measurement of the instantaneous angular position of the mirror.

Offset vertical comb-drive actuators

Two different schemes are generally used to create an initial offset between the fixed and moving combs, allowing the possibility of static scan angles with comb-drive actuators:

staggered vertical comb-drives (SVC) and angular vertical comb-drives (AVC).

SVC actuators have moving and fixed combs which are in their rest position parallel but show a vertical offset (see Fig. 1.10(a)), generally created by using several different device layers during fabrication. A summary of current fabrication processes for this type has recently been published by Gallagher et al. [103]. The first actuator of this type was shown by Selvakumar et al. [75] using several polysilicon layers and allowing vertical deflection. The use of polysilicon allows in this case multiple device layers and a step by step structuring, which also enables the fabrication of movable combs underneath the mirror surface [104] (see Fig. 1.11(b)) at the cost of reduced quality of the material properties and thinner device layers compared to single crystal silicon devices. With these designs, 2 degrees of freedom joints can be implemented to allow 2D scanning mirrors with static displacements of 26.8 ° TOSA in both axes [105]. The alignment between fixed and moving combs is important to avoid a sidewards pull-in of the comb-drive. This alignment accuracy requirement leads to several demonstrated fabrication steps to ensure the alignment. Fabrication with etch steps from only the front-side of the chip have been shown with two device layers and an oxide etch stop for the moving combs [106, 107]. This leaves the fixed combs made up of two electrically separated parts which can be used for combined piston and tip/tilt actuation. Static scan angles of 11 ° TOSA and 7 ° TOSA for a 2D scan have been demonstrated with devices having resonant deflection angles of 23 ° TOSA at 1.18 kHz and 17 ° TOSA at 2.76 kHz [107]. Variations of this use a rough backside etch for removing the lower device layer part of the moving combs to achieve SVC without overlap [108] or wafer bonding of the two device layers with a rough front side etch underneath the moving combs and alignment of the comb-drive through a final front side etch step [109, 110]. Recently, direct alignment of front and backside etch steps has also been used with high fabrication precision to allow single etch steps for both moving and fixed combs [111, 112]. A 2D scanner with this comb fabrication was shown combining a slanted comb-drive design to increase the static displacement over a common rectangular comb-

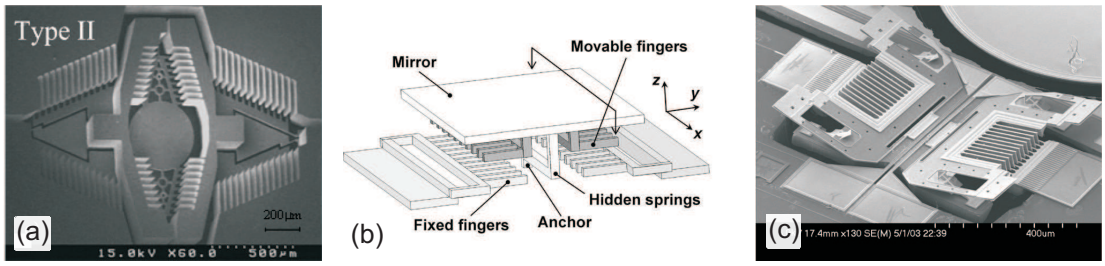

Figure 1.11: Examples of offset vertical comb-drive actuators: (a) 2D scanner with slanted SVC comb-drive [111], (b) polysilicon scanner with SVC comb-drives underneath mirror surface [104], (c) AVC with tilted moving combs [89].

drive [113](see Fig. 1.11(a)). Additional functionality for scanning mirrors with SVC was also recently presented by including a deformable mirror on the SVC actuated device through electrostatic actuation of a ring electrode underneath the mirror plate [112].

AVC actuators have their fixed or moving combs angled in their initial rest position to create the possibility of static displacements (see Fig. 1.10(b)). To create the initial angle between the combs three routes have been exploited so far: pre-tilting the whole mirror, tilting the moving combs or tilting the fixed combs. To tilt the whole mirror a frame around the mirror anchors can be used and tilted by 45° through reflow of photoresist at the hinges between frame and substrate [114, 115] with achievable scan angles of 19° TOSA at 1.1 kHz resonant actuation. Alternatively the mirror can also be pre-tilted by a thermal actuator connected to the torsion bar in combination with a latch mechanism [116] or by plastic deformation of the torsion beam using a lid wafer to statically tilt the mirror in an oven heat cycle [117]. To change the angle of the moving combs a hinge on the connection between the mirror anchors and the moving combs is used which can be angled with the reflow of a photoresist deposited on the hinge [89, 118, 119](see Fig. 1.11(c)). A 2D scanner using this approach shows static rotation angles of 24° TOSA and 16° TOSA for the inner and outer gimbal actuator with possible resonance movement frequencies of 315 Hz and 144 Hz. The most common approach to create an AVC device is by tilting the fixed combs. This can also be done

by using the reflow of a resist on hinges on the combs [120], by using capillary forces during drying to pull down an anchor pad of the fixed combs [121], by using a constant mechanical displacement of a pad connected to the fixed combs [122] or by using a non-actuated thin bimorph structure between the substrate anchor of the fixed combs and the combs themselves, which curls due to heat cycles during fabrication [123, 124]. Optical scan angles for an example using the mechanical displacement have shown static tilts of 28 ° TOSA for the outer part of a gimbal 2D structure and 40 ° TOSA resonant movement at 23.5 kHz for the inner part.

1.2.6 Piezoelectric scanning mirror

A further actuation mechanism for inducing tilt movements of scanning micromirrors is the inverse piezoelectric effect, which describes a mechanical strain in the crystal structure of a piezoelectric material induced by an applied voltage difference. This strain can lead to bending of the actuators, similar to the induced displacements in thermal actuators, which can be used to drive static or resonance tilt movements of microscanners. The most common piezoelectric materials used in MEMS systems are lead zirconate titanate (PZT), barium titanate (BTO), zinc oxide (ZnO) and aluminium nitride (AlN). So far demonstrated MEMS scanners are using PZT as the active piezoelectric material, while ZnO has been a common material for MEMS microphones and BTO having been mostly replaced by PZT. AlN has only recently been commercially available for thin films with accurate fabrication [125] and has so far been shown in MEMS microphones, but not in scanning mirrors.

Piezoelectric actuation in MEMS scanning mirrors has the advantages of low actuation voltages in the single digit voltage range combined with a possibility for static displacement as well as dynamic resonant movement in the tens of kHz range. The fabrication and integration possibilities in silicon fabrication processes have only recently allowed investigations with a variety of device designs.

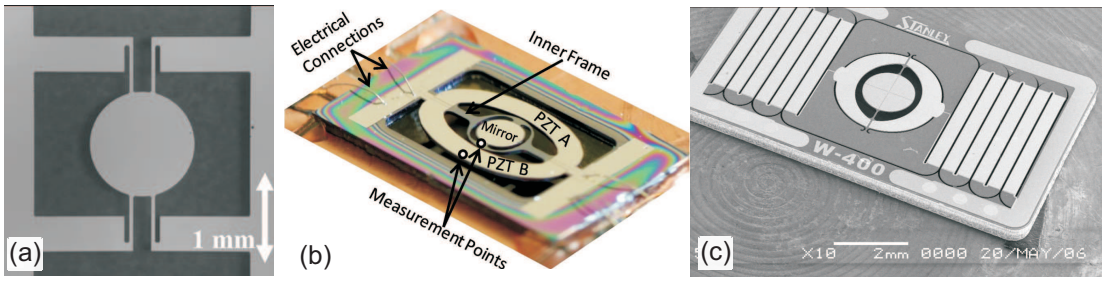

Figure 1.12: Piezoelectric actuated scanning mirrors with (a) external PZT stack as actuator [126], (b) PZT film deposited on frame around 2D scanning mirror [127] and (c) 2D scanning mirror with meander PZT springs for slow scan and PZT film on mirror frame for resonant fast scan [128].

Piezoelectric actuated microscanners have been shown with two generic actuation principles, a scanning mirror structure combined with an external stack of PZT layers [126,129] or scanning mirrors where in general a single PZT layer has been integrated in a frame or anchor structure of the mirror [58,127,128,130,131] to create the scanning movement actuation. By using an external PZT stack only resonant actuation of the scanner can be achieved, with the vibration of the PZT coupled to the micromirror via the anchor beams [126]. An example for this type of mirror is shown in Fig. 1.12(a) where optical scan angles of 50° at resonance frequencies around 30 kHz are shown for actuation voltages as low as 2 V. With the possibility of integrating piezoelectric layers into a silicon or metal based MEMS micromirror fabrication process, the active layers can be integrated directly with the micromirror structure on an external frame for creating a resonance actuation with minimal surface deformation of the mirrors [127] (see Fig. 1.12(b)). This device shows optical scan angles of up to 38.5° at a resonance frequency around 40 kHz, with actuation voltages of 25 V [127]. A 2D scanning mirror including a slow and fast scan axis with individual PZT actuators has also been demonstrated [128]. In this case a PZT layer at a mirror frame creates a fast resonant scan, while PZT layers deposited on serpentine springs allow a slow orthogonal scan axis with a frequency of 60 Hz (see Fig. 1.12(c)). The fast scan is set at a resonance frequency of 11.2 kHz leading to optical scan angles of 39° with an applied voltage of 40 V, while the slow scan leads to an optical scan angle of 29° for the same applied voltage. A 2D

raster scan projection was demonstrated with perfect rectangular shape.

1.3 MEMS in laser systems

The use of MEMS in laser systems has first found interest during the telecommunications boom in the late 1990s, where notably tunable diode-lasers and widely tunable filters using MEMS technology were investigated for their prospects of miniaturization, cost-effective fabrication and added functionality. More recently the use of MEMS devices as active elements for generating pulsed laser outputs has also seen increased research interest. In this section an overview of MEMS demonstrated so far as active elements in laser cavities will be given.

1.3.1 Spectral tuning of the laser output

Tuning of the output wavelength of a microchip laser, a fibre laser or a vertical cavity surface emitting laser (VCSEL) is of high interest in the telecommunication industry, as it enables the possibility to create flexible optical networks. The two main principles used for spectral tuning are a change of the laser cavity length and the combined use of a grating and tilting mirror. A change of the cavity length will change the spacing of the longitudinal laser modes and, if the initial spacing is large enough, shift the wavelength of a single mode laser output through this. The use of a grating as tuning element works by diffracting different wavelength under different angles on the grating and using a rotating mirror to select which wavelength is fed back to the system.

Wavelength tuning using MEMS in VCSEL systems was demonstrated in the 1990s with increased research interest in applications in the telecommunications industry during that time. An overview of early tuning schemes was presented by Chang-Hasnain [132]. In MEMS VCSEL systems the cavity length is tuned by electrostatic actuation between the semiconductor gain structure and a cantilever or membrane distributed Bragg reflector (DBR) [133], or by electrothermal actuation of the supports of

the output DBR [134]. This leads to a change in the distance between the gain medium and reflector and therefore the tuning of the emission wavelength of the VCSEL. Recently a membrane DBR with four support beams with electrothermal actuation was shown to achieve a tuning range of 20 nm with the dielectric layers of the DBR being doped with silicon to enable electrical conductivity for the thermal actuation [134]. A similar approach using tuning contacts on the top dielectric layer has also shown a singlemode tuning range of 50 nm [135]. To avoid current flow through the top DBR a single cantilever support structure for the DBR has also been shown recently to achieve tuning of the output, albeit by a reduced tuning range of around 5 nm [136].

Different approaches for spectral tuning of microchip laser by means of MEMS mirrors are reviewed by Liu and Zhang [137]. Tuning the cavity length was, for example, achieved with an in-plane comb-drive actuated curved mirror with a laser output wavelength tuning range of 13.5 nm [138]. The use of a grating for wavelength discrimination has also been shown with a rotating MEMS mirror in combination with an etalon as a wavelength selective element and a tuning range of 40 nm with a lasing linewidth smaller than 50 kHz [139].

For a fibre laser, the approach of a grating-based wavelength tuning can also be used and has been shown by using a commercially available digital micromirror device (DMD) from Texas Instruments to select individual wavelengths [140]. Alternatively a tunable Fabry-Perot cavity inside a fibre ring laser can be used, which has shown a tuning range of 35 nm with a spectral width smaller than 0.06 nm [141].

1.3.2 Adaptive optics in laser systems

Intra-cavity tuning of the spatial properties of a laser changes the mode structure of the laser resonator and can be used to stabilize a cavity under load. Especially in higher power solid-state lasers, where thermal distortion created by the laser within its gain medium limits power scaling of the output, possible applications for tuning the spatial

profile of the laser can be seen. Spatial tuning of the intra-cavity electromagnetic field of the resonator can, in principle, be applied from changing the curvature of a cavity mirror to a multi-actuator adaptive optics mirror for an in-depth tuning of the cavity mode shape. A stepping stone for using adaptive optics MEMS mirrors was the commercial availability of an electrostatic actuated membrane deformable mirror fabricated by OKO Flexible Optical from 1997 onwards [142, 143]. This mirror was available at the fraction of the price of other commercially available systems at the time due to advantages of MEMS bulk fabrication processes. This enabled easy access to adaptive optics for a multitude of research fields. The specific mirror consisted of a silicon nitride membrane suspended above an array of 37 actuators in a honeycomb arrangement, which deform parts of the membrane due to the electrostatic force created by an applied voltage to the actuators.

Using an adaptive optics mirror allows for the correction of higher order aberrations (introduced by the thermal load inside the gain medium) with a higher accuracy and can therefore be used, in cooperation with a feedback loop, for real time optimisation of the intra-cavity optical field of solid-state lasers with high thermal defocusing and birefringence effects [144]. The adaptive optics mirror consists in this case of a deformable membrane mirror with a circular array of actuators which change the overall shape of the mirror surface. Similar adaptive optics mirrors using piezoelectric unimorph actuators underneath a glass membrane to generate the mirror deformation were also shown for continuous wave intra-cavity laser use. High reflective coatings applied to the glass membrane allowed in this case power handling capabilities of about 500 W of a 1030 nm laser output [145]. These mirror types were initially developed for astronomy applications to correct for the disturbance of earth's atmosphere [146] as well as in medical applications for improved image quality in microscopy systems [147].

Changing the spatial profile of the cavity can also be used for creating a pulsed laser output if the cavity is designed at a point close to the stability limit. Further definition of the cavity stability will be given in chapter 4. A change in the mirror curvature

will therefore change the cavity quality to allow or hinder the propagation of a stable intra-cavity optical field, which creates a pulsed output when repeatedly switching the mirror curvature between these two states. Pulsed output with pulse durations in the range of 25 μs has been demonstrated with this technique [148].

1.3.3 Temporal tuning of the laser output

The use of MEMS as intra-cavity temporal tuning elements in solid-state and fibre laser systems has only recently started to attract attention, with MEMS devices being investigated to replace common bulk switches like acousto-optic modulators (AOM) or electro-optic modulators (EOM). Using MEMS reflective devices can reduce intra-cavity losses due to the removal of an additional optical element in the cavity. Further advantages are the less demanding electrical driving requirements of the MEMS devices, as no high voltage radio-frequency driving components are needed as is the case for AOM or EOM.

In general, temporal tuning of the laser output can be achieved with three different methods: gain-switching, Q-switching and mode-locking. Gain-switching creates output pulses with a fast modulation of the gain via the pump power of the laser, for example by inserting a short current pulse for a diode laser or by short pulsed optical pumping. MEMS devices are not suitable for this method as they modulate the loss of the laser and not the gain directly. The generation of pulsed outputs with MEMS devices for Q-switching and mode-locking will be discussed in the two following sub-sections.

Q-switched pulse operation

Q-switch operation of lasers works by using a modulation of the losses of the laser cavity to achieve a pulsed output. Initially the losses are set to a high value during which the laser pump builds up a high inversion density inside the gain medium which is above

the threshold density required for lasing. When the cavity losses are switched to a low value, this high inversion density creates a fast build up of laser radiation from noise, which is amplified over multiple cavity round trips. Due to an inversion level well above threshold a high intra-cavity power is present, which therefore depletes the upper laser level well below the threshold inversion density and ends the pulse. After this point the losses in the cavity are switched to a high value again to allow the pump build up of the upper laser level for the next pulse. A more detailed description will be given in chapter 4.

So far, MEMS devices have been demonstrated as active Q-switches for microchip, fibre and solid-state laser. A piezoelectric actuated polymer mirror was used in a Nd:YVO_4 microchip laser to generate Q-switched output pulses by vibration of the mirror surface [149]. Pulse durations of 16 ns with an average output power of 1.1 mW were achieved with this setup. The unimorph piezoelectric mirror consisted in this case of layer pairs of different polymers, creating an inherent reflectivity of 87 % at the lasing wavelength of 1064 nm. The combination of an active MEMS Q-switch scheme with a passive saturable absorber Q-switch was also demonstrated for a microchip laser [150]. The short pulse duration of 565 ps was generated by the saturable absorber while the repetition rate of 1.7 kHz was determined by the MEMS cantilever and achieved an average output power of 3.24 mW. The MEMS cantilever is similar to the device shown in Fig. 1.13(a) and consists of a metallic stack of gold and chrome layers suspended above a SiO_2 layer on top of a silicon substrate. The cantilever is actuated using an electrostatic force due to a potential difference applied between the actuator and substrate.

The use of MEMS as active Q-switches in fibre laser systems has been demonstrated with several MEMS mirror concepts. A polysilicon electrostatic parallel-plate actuated mirror was used in a Nd-fibre laser system allowing pulse durations of 2 μs at repetition rates of 20 kHz and average output powers < 200 mW [151]. Metallic membrane mirrors were also presented as active Q-switches for Er-doped fibre laser with 320 ns pulse

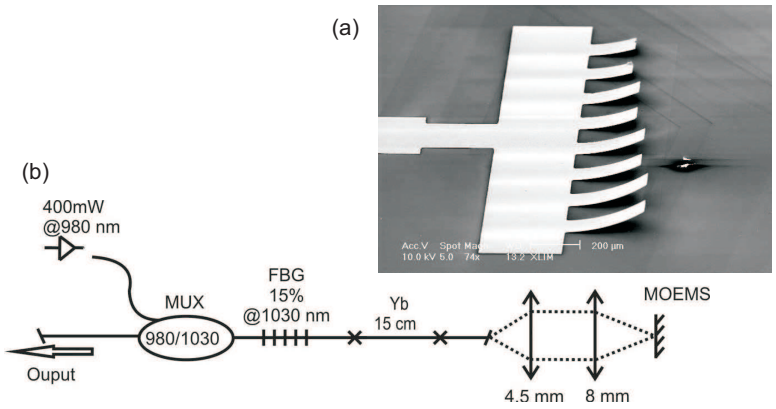

Figure 1.13: (a) Electrostatic metallic MEMS cantilever used for creating Q-switch actuation in a (b) fibre laser setup by focusing the output of an open fibre end onto the cantilever [153].

duration and 30 mW average power as well as for a combined Yb- and Er-fibre laser setup [152]. The combination of the two fibre lasers is realised within the fibre with a wavelength division multiplexer (WDM) to direct both lasing wavelengths on the same membrane mirror. The laser outputs were then amplified by a ytterbium and erbium doped fibre amplifier, respectively, which created average output powers of 250 mW per fibre at 1.9 μs pulse durations. A further MEMS device demonstrated as an active Q-switch for fibre lasers is a metal cantilever structure (see Fig. 1.13) which has shown pulse durations of 20 ns with 80 mW output power in a single Yb-fibre laser [153]. The cantilever is 1.1 μm thick with a top and bottom gold layer surrounding a thin chrome layer to gain an initial curvature of the cantilever. The electrostatic actuation of the cantilever allows movements up to about 200 kHz between the curved rest position and the position of the cantilever attracted to the substrate. The Q-switched laser output of maximum 80 mW average power was achieved with a repetition rate of 200 kHz and pulse durations of 20 ns, with the open side of the fibre laser output focused down to a 8 μm spot size on the MEMS. An array of similar cantilevers has recently also been shown for synchronization of multiple fibre laser with pulse durations of 400 ns and pulse energies of 25 nJ at repetition rates of 20 kHz [154]. Multiple fibre lasers were in this case arranged in a parallel alignment to guide the individual fibre outputs on the electrostatic cantilever array. Multiplexing of the individual laser outputs was

then achieved through a wavelength division multiplexer to combine the laser outputs with slightly different wavelength, defined by the fibre Bragg gratings used as output couplers of each laser. MEMS active Q-switching in solid-state lasers has also been presented with a silicon scanning micromirror operated at its mechanical resonance, with achieved pulse durations of 220 ns and an average output power of 20 mW in a Nd:YLF laser cavity [5]. The investigations in this thesis are based on this work using scanning micromirrors of a generic similar design.

Mode-locked pulse operation

Mode-locked operation of laser systems can create even shorter pulses than Q-switching and is based on locking the longitudinal modes in the laser resonator with a fixed phase. This leads to a periodic constructive interference of the modes which creates a pulse train. The fixed phase is created by modulating the cavity losses with a frequency equal to the inverse of the cavity round-trip time. The pulse duration is then determined by the number of interfering longitudinal modes, with a higher number of modes (wider bandwidth of the laser) leading to shorter pulse durations.

The use of a MEMS membrane mirror with a high vibration frequency was recently presented as an active mode locking element for an erbium based fibre-laser system [155]. Parts of the membrane were vibrating at a frequency of 4.96 MHz with quality factor changes of the laser cavity in the single percent range, which created a pulse train with 1 ns pulse duration and average power of 100 mW. A pulsed output was only achieved when the membrane vibration frequency matched the cavity free spectral range, which is the inverse of the cavity round-trip time, confirming the operation in the mode-locked regime.

1.4 Summary

In section 1.1 commonly used MEMS fabrication processes and materials were reviewed combined with some of the most common sensing and actuation principles employed using MEMS. Section 1.2 reviewed actuation principles and application areas of MEMS scanning micromirror, with emphasis on electrostatic actuated scanning micromirror, which is the device category investigated and used in the further presented work. In the final section 1.3 the integration of MEMS in laser systems was reviewed, showing spatial, spectral and temporal tuning applications.

2 Theoretical model of an electrostatic resonant scanning micromirror

In this chapter a theoretical model describing the dynamic motion of electrostatic comb-drive actuated scanning micromirrors is presented and discussed. The special case of angled vertical offset comb-drive (AVC) actuators is used, as all following investigations in further chapters will use this type of device. This geometry is resulting from the used SOIMUMPs multi-user fabrication process which creates an intrinsic stress in the single-crystal silicon (SCS) device layer [156] leading to an intrinsic AVC geometry. Comb-drive actuated microscanners are chosen due to their possibility for a high optical angular displacement range of $> 90°$ at resonant actuation and low power consumption in the μW range, as the desired application, namely the use as intra-cavity Q-switch elements in laser systems, requires fast movement speeds in the range of $1{\cdot}10^4\,\mathrm{rad\,s^{-1}}$ for the angular velocity. Another possible scanning mirror choice could have been the use of electromagnetic actuated microscanners, but the available fabrication process for the mirror designs, namely SOIMUMPs, does not allow multi-loop tracks or ferromagnetic layers on the mirror surface, therefore limiting the range of designs of this class of devices.

Previous investigations of theoretical models for electrostatic AVC actuated micromirrors have focused on expressions for static tilt displacements, using for example analytical expressions without the consideration of electrical fringe fields [123, 157]. As

fringe fields can play an important role for the angled offset comb-drives, a hybrid approach combining FEM simulations for the electrical field distribution and analytical expressions for the static tilt motion has also been shown [119] and was applied to several mirror geometries [89, 120]. For the description of the dynamic resonance motion of an AVC, a model using fit parameters to experimentally obtained results has been presented so far [115]. The methodology followed in this chapter is combining the two last mentioned approaches and is using a hybrid approach of FEM simulations for determining the electrical field distribution and analytical expressions for the dynamic motion equation. In this case, only the damping related factor needs to be determined experimentally, as a closed analytical description for the damping of a microscanner is outside the scope of this thesis. All other parameters can be defined prior to fabrication of the scanning micromirror.

In the following section the theoretical basics of the motion equation and its parameters will be explained, followed by an introduction to nonlinear effects and their inclusion in the described simulation model, which can have an influence on the displacement behaviour of the micromirrors. As the comb-drive actuators will have vertical height offsets in the range of up to 50 μm during the resonance movement, fringe field effects have to be considered for determination of the applied electrostatic torque. This will be discussed in the next section including the model description. The chapter will finish with a verification of the developed model using experimental data from an exemplar fabricated scanning micromirror.

2.1 Movement equation for resonant behaviour

The tilting electrostatic scanning micromirrors used for the work described in this thesis can be categorised as damped forced oscillators with a single degree of freedom, the tilt angle θ. A linear motion of these can be modelled in the case of a single frequency

excitation and linear viscous damping with the general motion equation [158]:

$$\ddot{x} + 2\,\mu\,\dot{x} + \omega_0^2\,x = F, \tag{2.1}$$

where x is the movement parameter, μ is a factor related to the damping, ω_0 is the angular eigenfrequency of the system and F is the external excitation force. For the specific case of the tilt movements used in this work the equation can be adapted to [115]

$$\ddot{\theta} + 2\,\xi\omega_0\,\dot{\theta} + \omega_0^2\,\theta = \frac{T'(\theta,t)}{I_\theta}\,. \tag{2.2}$$

$\theta\,[\mathrm{rad}]$ is here the mechanical tilt angle of the mirror surface, ξ is the damping coefficient, $T'(\theta,t)$ [Nm] is the time- and angular-dependent external applied torque and $I_\theta\,[\mathrm{kg\,m^2}]$ the torsional moment of inertia of the microscanner.

The viscous damping of the movement, represented by the term $2\,\xi\omega_0\,\dot{\theta}$, occurs due to air damping on the mirror surface and possible squeeze film damping between the combs of the electrostatic comb-drive actuators. Exact modelling of these effects is a complex task especially due to large movements combined with small feature sizes and gaps and is therefore not pursued in this work. An alternative way to estimate the damping coefficient ξ requires the prior knowledge of the Q-factor of the frequency response curve as these two parameters are related via [115]

$$\xi = \frac{1}{2\,Q}. \tag{2.3}$$

The Q-factor itself is defined as

$$Q = \frac{f_0}{f_2 - f_1}, \tag{2.4}$$

with the centre resonant frequency f_0 and the bandwidth $f_2 - f_1$, where f_2 and f_1 are the movement frequencies at which the angular response of the mirror has dropped to $1/\sqrt{2}$ times the maximum angle. This approach of estimating the damping coefficient is also used by some of the simulation models referenced in the previous section.

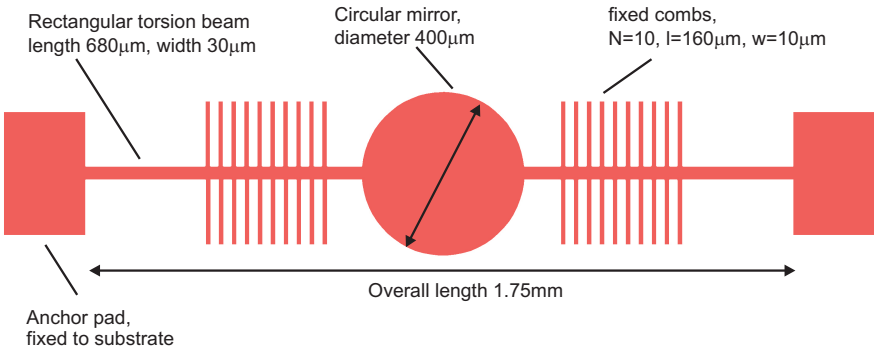

Figure 2.1: Top view layout of an exemplar comb-drive actuated SOI (silicon on insulator) resonant scanning micromirror with circular mirror surface and rectangular torsion beams.

The angular eigenfrequency $\omega_0 = 2\pi f_0$ of the device is part of the damping representation and also used for the spring related part of the motion equation, represented by the term $\omega_0^2\,\theta$. It can be calculated through

$$\omega_0^2 = k_\theta / I_\theta, \tag{2.5}$$

which is the ratio of the torsional spring constant k_θ and the already mentioned torsional moment of inertia I_θ. Both these parameters can be calculated using the geometry definitions and material properties of the micromirror. I_θ of an exemplar micromirror structure, as shown in Fig. 2.1, can be approximated in first instance with the combination of the moments of inertia of a disc $I_{disc} = \frac{1}{12}\,m_{disc}\left(3\,r^2 + h^2\right)$ and two rectangular beams with $I_{beam} = \frac{1}{12}\,m_{beam}\left(h^2 + w^2\right)$, neglecting the influence of the combs attached to the torsion beams. m_{disc} and m_{beam} are the mass of the disc and beam respectively, r is the radius of the disc, h is the device thickness and w is the width of the torsion beams. With this, the overall torsional moment of inertia can be estimated as

$$I_\theta = \frac{1}{12}\,\rho\,h\left[2\,w\,l\left(h^2 + w^2\right) + r^2\,\pi\left(3\,r^2 + h^2\right)\right]. \tag{2.6}$$

The parameter ρ is the density of single crystal silicon and l the length of the two identical torsion beams. For more complex shapes and a higher accuracy determination

of the moment of inertia a geometric eigenfrequency FEM simulation can be used. As FEM tool the software COMSOL Multiphysics is used here in which the torsional moment of inertia for a simulated geometrical structure can be determined by using a volume integration over the expression "solid.rho*(Yˆ2+Zˆ2)" of the simulation results. In this case the considered torsion axis for the moment of inertia has to be aligned with the x-axis of the simulation.

The spring constant k_θ is defined mainly by the two torsion beams whose contribution can each be calculated for constant cross-section rectangular beams, where the width w is bigger or equal to the thickness h, with [159]

$$k_{\theta,beam} = \frac{G\,wh^3}{l}\left[\frac{1}{3} - 0.21\left(\frac{h}{w}\right)\left(1 - \frac{h^4}{12w^4}\right)\right]. \tag{2.7}$$

G is in this case the shear modulus of silicon. The results of the already mentioned eigenfrequency FEM simulation can be used for a more accurate representation in equation (2.2) instead of the analytical calculated combination of spring constant and torsional moment of inertia. For an accurate FEM result the anisotropic material properties of the single crystal silicon used for the MEMS micromirrors need to be considered in this case, which are shown in table 2.1 later in this chapter.

The external torque $T'(\theta, t)$ inducing the movement is created by electrostatic comb-drive actuators and can therefore be expressed by the change of the capacitance between the comb electrodes $\frac{\mathrm{d}C}{\mathrm{d}\theta}$ and the applied voltage $V(t)$ in the form [89]:

$$T'(\theta, t) = N'\,\frac{1}{2}\,\frac{\mathrm{d}C}{\mathrm{d}\theta}\,V(t)^2. \tag{2.8}$$

N' represents in this case the number of gaps between the moving and fixed combs in which the electrical field is present. The time dependent components of this torque are the applied voltage, which is in general a sine-wave or square-wave signal with a frequency around the mechanical resonant eigenfrequency of the mirror or a harmonic of it, and the differential capacitance, which depends on the overlap of the comb fingers

which changes in time. The exact determination of this differential capacitance distribution and its implementation in the theoretical model is shown at a later stage in this chapter.

The mentioned case of excitation signals taking the form of higher harmonics of the device resonance frequency is originating from the nonlinearities in the motion equation which are discussed in section 2.2. In this case the steady state oscillation of the device is adjusted through the nonlinearities to result in a movement around the device resonance, even though the excitation is at the harmonic. If the excitation frequency is an integer multiple of the device oscillation these are called sub-harmonic resonances while an excitation with a harmonic frequency having the form of an inverse integer multiple of the device oscillation is called super-harmonic resonance. A detailed analysis and discussions of these effects can be found in [158]. For the devices used in this thesis a sub-harmonic driving is partly used in the application of MEMS scanning mirrors in laser systems, but is not relevant in this chapter or the investigation of general properties of AVC actuated micromirrors discussed in the following chapter.

With the above discussed parameters a solution to the second order ordinary differential equation (ODE) in (2.2) can be calculated using a numerical approach. This is done with the software Matlab using an in-built function ODE45 which is a generic solver for first order ODEs. The equation

$$\ddot{\theta} = -2\,\xi\,\omega_0\,\dot{\theta} - \omega_0^2\,\theta + \frac{1}{2}\,\frac{\mathrm{d}C}{\mathrm{d}\theta}\,\frac{V(t)^2}{I_\theta} \tag{2.9}$$

therefore needs to be reduced from its second order form to a first order description. This can be done by splitting it into a system with two first order equations using two variables for θ in the form [115]

$$\begin{aligned} \dot{\theta}_1 &= \theta_2 \\ \dot{\theta}_2 &= -2\,\xi\,\omega_0\,\theta_2 - \omega_0^2\,\theta_1 + \frac{1}{2}\,\frac{\mathrm{d}C}{\mathrm{d}\theta_1}\,\frac{V(t)^2}{I_\theta} \end{aligned} \tag{2.10}$$

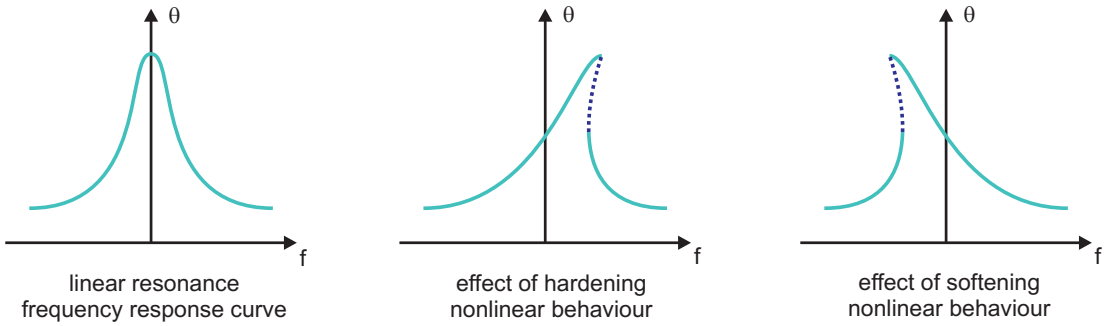

Figure 2.2: Effect of nonlinearities in the motion equation on the frequency response curve of an oscillator with no effective nonlinearity, spring hardening behaviour and spring softening behaviour; dotted parts can not be achieved in physical system.

θ_1 represents the original tilt angle θ, with θ_2 being the first time derivative of the angle $\dot{\theta}$. To solve this system of ODEs the initial conditions for both variables θ_1 and θ_2 need to be defined, as well as a time span for which a solution is sought. The resulting solution of the ODE45 function is the time response of θ_1 and θ_2 from which a scan angle for the defined input parameters can be determined after the system has settled to a stable resonance.

2.2 Nonlinearities

Nonlinearities will start playing a role in the movement behaviour of the microscanner for actuation cases reaching tilt angles or displacements above a certain threshold which varies depending on the design and materials of the chosen scanner. These nonlinearities originate from two different effects. First the electrostatic excitation, as the differential capacitance includes higher order terms of θ, and secondly a mechanical related nonlinearity in the torsion springs which are used to suspend the mirror structure.

The nonlinearities result in an effective "softening" or "hardening" behaviour of the frequency response curve (see Fig. 2.2), with the spring related nonlinearity being in general responsible for the hardening behaviour and the electrostatic force nonlinearity being responsible for the softening behaviour [160]. Nonlinear softening behaviour is

related to the frequency response curve showing a tilt of a previously symmetric resonance curve towards lower frequencies, up to the point where multiple stable solutions exist for one particular excitation frequency and therefore jump discontinuities and hysteretic behaviour will occur. Nonlinear hardening behaviour will on the other hand lead to a tilt of the frequency response curve towards higher frequencies with the same possible effects as mentioned for the softening behaviour. In the nonlinear behaviour schematic graphs in Fig. 2.2 the dotted lines represent non-existing solutions, as these parts can not be achieved through a frequency up- or down-sweep of the excitation signal. In the case of nonlinear hardening behaviour a frequency up-sweep will lead to a jump from the highest oscillation amplitude to the point on the lower light curve with equal frequency while a frequency down-sweep will lead to a jump from the lowest point on the dotted line to the higher light curve with again equal frequency. Therefore no point on the dotted line can be created as it represents an unstable frequency response. The effect of these nonlinearities needs to be considered when the respective device should be operated at its highest possible tilt angle.

2.2.1 Electrostatic nonlinearity

The electrostatic excitation introduces a nonlinear forcing term due to the dependency of the differential capacitance on higher order terms of the tilt angle θ, which can in general be written in the form of a power series [115]

$$\frac{\partial C}{\partial \theta} = C_0 + C_1\,\theta + C_2\,\theta^2 + C_3\,\theta^3 \ldots \tag{2.11}$$

where $C_1, C_2, C_3, ...$ are constants to fit to the physical capacitance dependence. C_1 will change the effective resonant frequency of the scanning mirror as it modifies the spring related part of the motion equation (2.9) to $-\omega_0^2 + C_1\,\frac{V(t)^2}{2I_\theta}$. This modification combined with the effect of the higher order terms will lead to the influence of the nonlinear softening behaviour.

2.2.2 Mechanical nonlinearities

The mechanical nonlinearities present in the scanning mirrors have two origins with a material related factor due to nonlinearities in the material parameters, especially the Young's modulus, and a geometry related factor which originates from the deformation of the physical shape of the torsion bars during the movement. The nonlinearity in the Young's modulus has hereby a strain dependency whose effect is showing an influence during higher angular movements [161]. For both origins of the mechanical nonlinearities an accurate and complete mathematical description is beyond the scope of this section, especially with accurate nonlinear material parameters missing so far in the literature. To nevertheless include the effects in the mathematical description of the motion equation a nonlinear spring constant can be assumed in the form

$$k_\theta = k_0 \left(1 + k_1\,\theta + k_2\,\theta^2 + k_3\,\theta^3 + \ldots\right) . \tag{2.12}$$

k_0 is hereby the linear spring constant, which has been defined analytically above and $k_1, k_2, k_3, ...$ are the nonlinear spring constants for the quadratic, cubic, etc. nonlinearities introduced by the mentioned mechanical effects. Approaches to determine these constants are possible in the form of fits to FEM simulations [43] or by fitting to experimentally obtained data [162]. For resonator structures which are designed to be symmetric in their displacement, which is the case for the tilt resonances discussed in this thesis, the quadratic nonlinear spring constant term $k_1\,\theta$ can be neglected [162]. The cubic nonlinearity $k_2\,\theta^2$ is therefore the governing mechanical nonlinear factor in this case.

2.3 Fringe fields and differential capacitance

The differential capacitance $\frac{\partial C}{\partial \theta}$, governing the torque factor in the motion equation, is determined by the electrostatic comb-drive actuator shown in Fig. 2.3, which is used

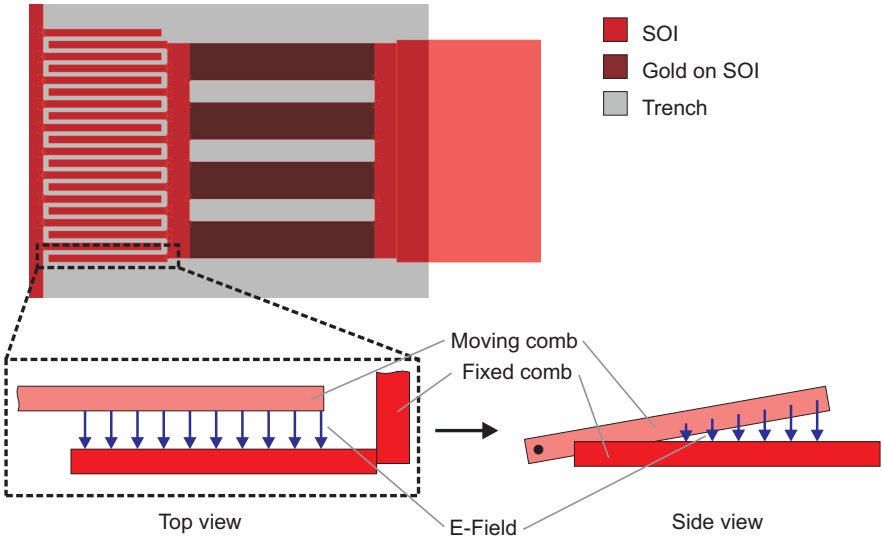

Figure 2.3: Schematic of the used comb-drive actuators with all functional parts defined in the silicon-on-insulator (SOI) device layer.

for the devices discussed here. The comb-drive consists of finger electrodes connected to the torsion beam of the microscanner, therefore classed as moving combs, which are interlaced with finger electrodes connected to the substrate, therefore classed as fixed combs. The substrate connection of the fixed combs is created, for the devices discussed here, by a group of four connection beams coated with a 1.1 μm thick gold layer. This will create an out-of-plane curvature, due to intrinsic stress in the SOI layer and thin film stresses introduced by the gold layer, that leads to an initial tilt angle between the two comb categories. The actuator is therefore classified as angled vertical comb-drive (AVC) whose influence will be investigated in detail in the next chapter. The fixed and moving parts of the comb-drive have the same thickness, with the tilt movement of the actuated micromirror changing the instantaneous overlap of each comb-pair. This movement offset combined with the initial offset leads to the necessity to consider the vertical fringe fields of the electrical field created between the comb electrodes when a potential difference is present between them.

To accurately determine the electrical field distribution of the comb-drive which is governing its capacitance, a 2D FEM simulation is used. This is similar to the work presented in [119], with the aim to reduce computational requirements and increase the

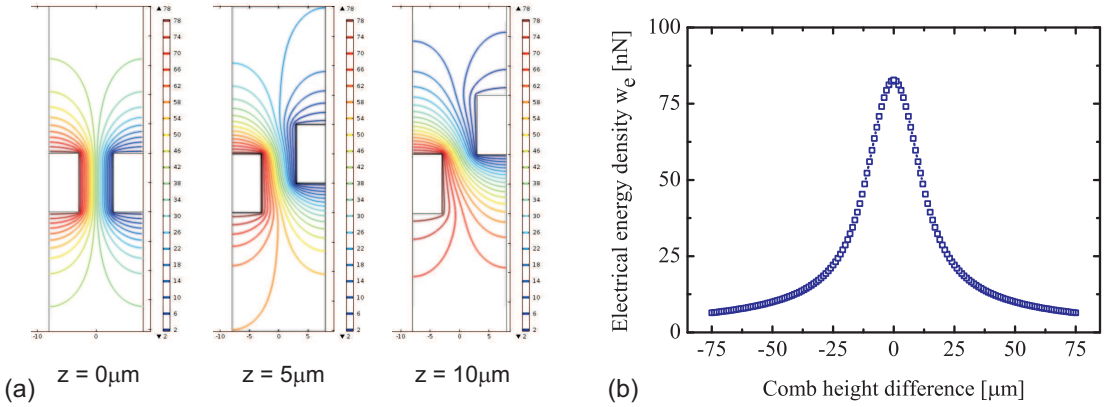

Figure 2.4: (a) Electrical potential distribution of a unit comb-drive cell for varying height differences and (b) resulting electrical energy density distribution of a unit cell for varying height difference.

simulation speed. For the FEM simulation of the electrical field a unit cell between two comb-fingers with 10 μm thickness is used, consisting of the cross-section of half a moving finger and half a fixed finger (see Fig. 2.4(a)). The simulation is built-up using the FEM tool COMSOL Multiphysics. The geometry of the unit cell needs to be defined to solve the electrical field distribution, with the two rectangular electrodes modelling the cross-section of the half-combs and a surrounding box modelling the air surrounding the combs. The vertical position of one of the half combs is defined via a variable to allow a parametric sweep in the solver, generating the electrical field distributions of the varying offsets over the length of a comb. The material properties of the half-combs are set to the single crystal silicon properties defined in Table 2.1, with the applied potential difference being modelled with a voltage terminal of 80 V at the circumference of the fixed comb and a voltage terminal of 0 V at the circumference of the moving comb. The resulting electrical potential distribution of the electrostatic simulation for each comb-offset is used to calculate the electrical energy density w_e using a surface integration over the full air cavity. The resulting dataset is shown in Fig. 2.4(b) with the influence of the fringe fields clearly visible with a non-zero energy density for height difference values larger than the comb-finger height of 10 μm.

To calculate the capacitance of the whole comb-drive from these 2D FEM results an

integration of the energy density needs to be conducted over the length of the moving comb, taking into account the changing height between the moving and fixed combs due to the AVC actuator geometry. In this case the curvature along the combs, which results from the chosen fabrication process, is neglected and the combs are assumed to be straight. The capacitance calculation can then be done in the form [163]

$$C(\theta) = N' \cdot \frac{2}{V_{FEM}^2} \int_0^{l_1} w_e \left(z(l,\theta)\right) \mathrm{d}l \,. \tag{2.13}$$

For the distribution of the energy density w_e a 8th order Fourier fit to the graph in Fig. 2.4(b) is used for the calculation in Matlab. $C(\theta)$ is the capacitance of the whole comb-drive for a specific tilt angle θ of the micromirror, N' is the number of gaps between the comb fingers, V_{FEM} is the voltage used to create the potential difference in the FEM simulation of the electric field, l_1 is the length of the comb overlap and $z(l,\theta)$ is the function of the height difference between a moving and fixed comb, dependent on the micromirror tilt angle and the integration variable l along the moving combs. For an AVC actuator this height difference takes the form

$$z(l,\theta) = l \cdot \sin(\theta - \theta_i) + z_1 + l_2 \cdot \sin(\theta) \tag{2.14}$$

with the variable definitions shown in Fig. 2.5. l is the length variable for the integration along the moving comb, θ_i the initial angle between the moving and fixed combs in their rest position, z_1 the vertical offset at the end of the fixed combs and l_2 the distance between the tilt axis of the micromirror and the end of the fixed combs. The values for these parameters are calculated from measurements of the actual height distribution after fabrication of the actuators.

To gain the capacitance distribution over the whole angular movement range equation (2.13) is evaluated for varying tilt angles between ±22.5°. With this distribution a differential capacitance can be determined over the same movement range by using the

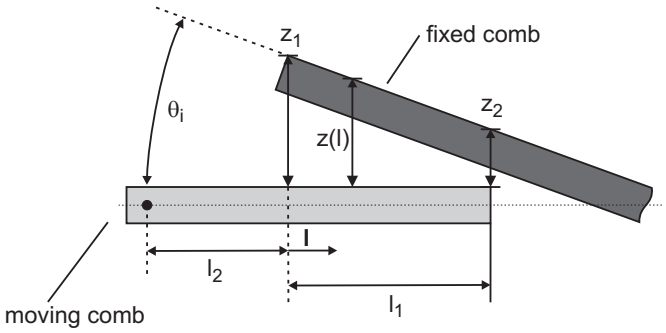

Figure 2.5: Schematic side view of a comb pair with parameter definitions for the calculation of the height difference function $z(l, \theta)$.

approximation of a difference quotient in the form of

$$\frac{\partial C(\theta)}{\partial \theta} \approx \frac{C(i) - C(i-1)}{\theta(i) - \theta(i-1)}. \tag{2.15}$$

The values of this approximation are then fitted with a 20th order Fourier series that can be used for the numerical solution of the system of first order ODEs in (2.10).

2.4 Model verification with example scanner

In the following section the described simulation approach will be implemented using experimentally obtained data of an example scanning micromirror.

2.4.1 Design parameters

The design of the used micromirror is shown in Fig. 2.6. The mirror surface has a diameter of 400 μm with rectangular torsion beams with a length of 675 μm and width of nominally 30 μm as anchor connections to the substrate. Four comb-drives are symmetrically distributed around the torsion beam with the 160 μm by 10 μm fixed combs of the comb drive having a closest distance to the mirror of 90 μm and a lateral spacing between two combs of 6 μm. The fixed combs are anchored using the already mentioned four connection beams having a 1.1 μm gold coating on them. All parts are designed

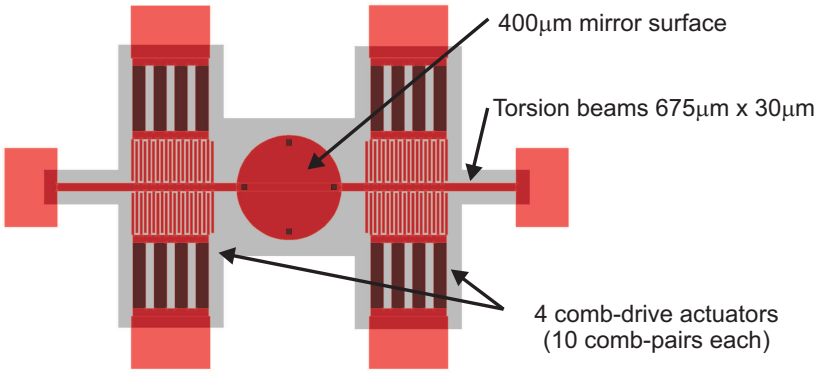

Figure 2.6: Design layout of the exemplar used SOI scanning micromirror to verify the simulation approach.

in the same device layer, which is made up of 10 μm thick doped single crystal silicon. The moving parts and connection beams of the fixed combs are all fully released using a backside etch step on the substrate used as handle wafer for the device. The fabrication of the device is done by using a multi-user silicon-on-insulator process (SOIMUMPs) offered by the company MEMSCAP Inc. An AVC actuator geometry is in this process intrinsically created through a doping related stress in the 10 μm device layer as well as through thin film stresses resulting from gold coating layers on the fixed comb anchors. These stresses lead to an out-of-plane bending, creating an angled vertical offset of the comb-drive in its rest position. The overall fabrication and design process for similar micromirrors will be shown in more detail in sections 3.1 and 3.2.

2.4.2 Experimental results

After fabrication of the devices the surface profile and height steps between the fixed and moving combs were measured using a Veeco NT1100 optical white light interferometer profiler. An overview of the comb-drives of one side of the exemplar scanner is shown in Fig. 2.7 using a 10x magnification lens combination and the VSI (vertical scanning interferometry) measurement mode of the profiler due to the occurring height steps in the range of 10 μm. To determine the maximum (z_1) and minimum (z_2) vertical comb-offsets of the comb-drive chosen for actuation, a 2D line scan evaluation is

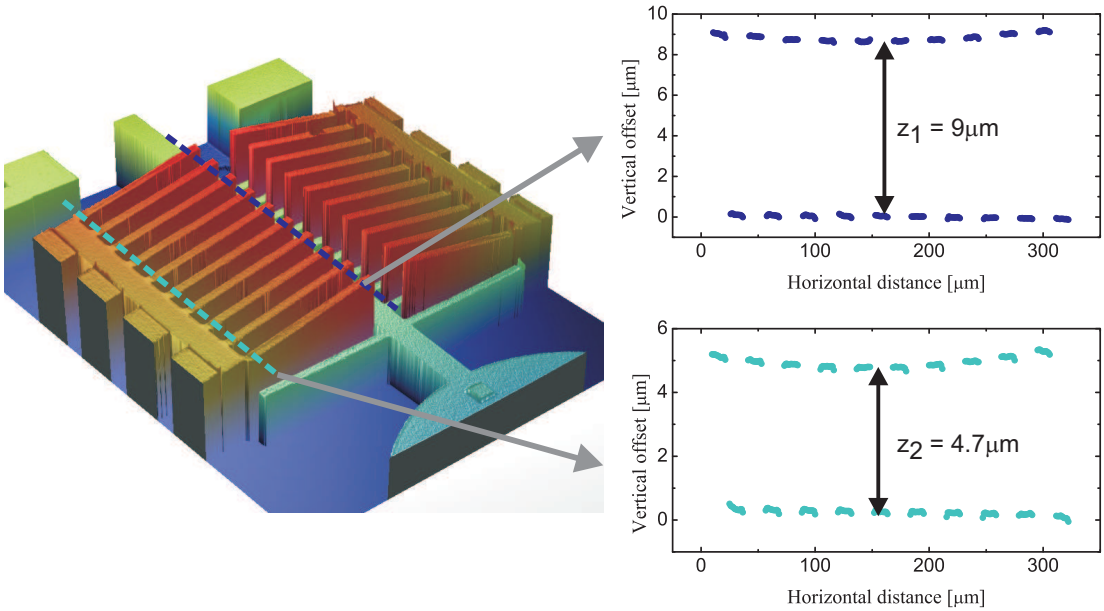

Figure 2.7: 3D representation of the measured height difference distribution of 2 comb-drive actuators with the distribution of the maximum (z_1) and minimum (z_2) height difference of the experimentally used comb-drive.

performed on the measured profile along the end positions of the moving combs and fixed combs. The resulting height steps are shown in Fig. 2.7 with the average offsets between neighbouring combs being $z_1 = 9\,\mu$m and $z_2 = 4.7\,\mu$m.

The fabricated devices were experimentally actuated to obtain a value for the damping factor ξ of the motion equation using the Q-factor of the frequency response curves obtained during actuation. To actuate the devices the fabricated chips are mounted on a custom PCB using $25\,\mu$m thick aluminium wire bonds. To induce the desired tilt scanning movement of the micromirror a sine-wave voltage signal with nominal amplitudes of 40 V, 50 V and 70 V and a driving frequency corresponding to half the mechanical movement frequency was used. To create the driving signal an Agilent 33250A arbitrary waveform generator (AWG) in combination with a FLC A400 twenty times amplifier is used (see Fig. 2.8(a)). A $10\,\text{k}\Omega$ resistor is connected in series between the amplifier and the PCB to limit the current through the system in the case of a shorting of the comb-drive electrodes. This short would create a current loop through the device which can potentially fuse individual comb-pairs together due to excessive

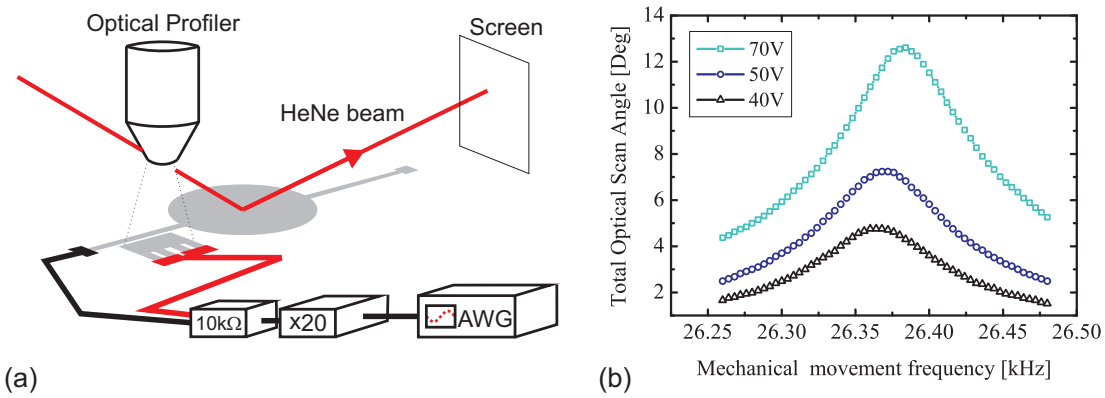

Figure 2.8: (a) Schematic of the experimental measurement setup for resonant actuation of the microscanner and (b) experimentally obtained frequency response curves of the tilt resonance movement.

heat created by the electrical current. The series resistor will limit the created electrical current in this case and therefore the induced heat in the combs. The active signal is connected to the fixed comb-electrodes with the moving combs being connected to the ground line of the actuation output. To measure the angular response of the applied signal a HeNe probe laser is directed onto the mirror surface and the displacement of the reflection is measured on a screen. The scanning tilt movement results in a line scan on the screen through which the total optical scan angle (TOSA) can be determined. The measurement schematic for this is also shown in Fig. 4.15.

The resulting frequency response curves for the tilt around the torsion beam axis are shown in Fig. 2.8(b) for the three mentioned actuation voltages. For all three a symmetric frequency response curve is obtained around the respective peak resonance frequency. With increased actuation voltage the peak shifts towards higher frequencies due to the influence of the electrostatic induced nonlinearities [115]. For the 40 V actuation a resonance peak of $\theta_{40} = 4.8°$ at 26.364 kHz is visible with the increased sine-wave driving amplitude of 50 V leading to $\theta_{50} = 7.2°$ at 26.370 kHz and 70 V leading to $\theta_{70} = 12.6°$ at 26.384 kHz. The Q-factors for these resonances, calculated from the frequency response curves, are then 320, 320 and 350 respectively. This leads to a damping factor of $\xi = 0.0016$ for the exemplar mirror used here. It has to be mentioned that the effective amplitude of the sine-wave signal at the comb-drive is reduced from the

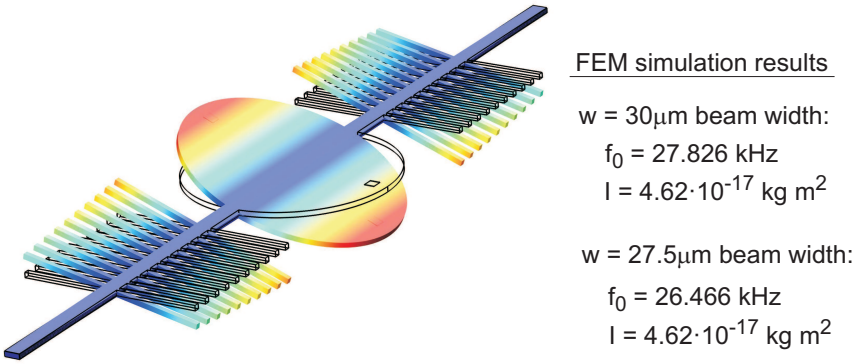

Figure 2.9: 3D FEM modal simulation of the tilt resonance movement including the obtained resonance frequencies and torsional moments of inertia for the two discussed torsion beam width cases.

nominally set voltage level at the signal generator as the series resistor and additional parasitic resistances on the device tracks will reduce the effective available voltage.

2.4.3 Model parameter

With the experimental data for the damping coefficient and initial comb offsets and angles obtained, the rest of the parameters for an analytical solution of the motion equation can be calculated using a FEM modal analysis and calculations in Matlab. To obtain values for the resonant eigenfrequencies of the micromirror a 3D layout of the moving parts of the mirror is constructed in the FEM software (see Fig. 2.9). Single crystal silicon was chosen for the material properties using several adaptations to the inbuilt properties in the COMSOL library. The specific material properties for the used fabrication process of the devices show an orientation dependent behaviour [19] of the Young's modulus and therefore anisotropic material properties need to be used. Table 2.1 shows a summary of the used material properties with the parameters of the stiffness matrix D_s used for the Young's modulus E defined as [14]:

Table 2.1: *SOI material properties used in COMSOL.*

Symbol	Description	Value
ρ	Density	$2329\,\mathrm{kg/m^3}$
c_{11}	Elastic constant 11	$165.7\,\mathrm{GPa}$
c_{12}	Elastic constant 12	$63.9\,\mathrm{GPa}$
c_{44}	Elastic constant 44 / Shear modulus	$79.6\,\mathrm{GPa}$
C_p	Coefficient of thermal expansion	$2.5 \cdot 10^{-6}\,1/\mathrm{K}$
$S_{0,xx}$	Initial stress in x-direction	$15 \cdot 10^6\,\mathrm{N/m^2}$
$S_{0,yy}$	Initial stress in y-direction	$15 \cdot 10^6\,\mathrm{N/m^2}$

$$\sigma' = D_s \cdot \epsilon = \begin{bmatrix} c_{11} & c_{12} & c_{12} & 0 & 0 & 0 \\ c_{12} & c_{11} & c_{12} & 0 & 0 & 0 \\ c_{12} & c_{12} & c_{11} & 0 & 0 & 0 \\ 0 & 0 & 0 & c_{44} & 0 & 0 \\ 0 & 0 & 0 & 0 & c_{44} & 0 \\ 0 & 0 & 0 & 0 & 0 & c_{44} \end{bmatrix} \begin{bmatrix} \epsilon_1 \\ \epsilon_2 \\ \epsilon_3 \\ \epsilon_4 \\ \epsilon_5 \\ \epsilon_6 \end{bmatrix} \tag{2.16}$$

with σ' being the stress vector and ϵ the strain vector in the material. If the device is fabricated along the x-axis of the SOI wafer an in-plane rotation by 45° of the overall device layout has to be performed in COMSOL to align to the correct material properties [14]. An anisotropic linear elastic material model has to be chosen for the solid mechanics physics settings with fixed constraints at the end of the torsion beams. To perform the FEM analysis a tetrahedral mesh with the setting of an extra fine element size leading to 30441 elements was chosen and automatically created in COMSOL. The eigenfrequency study leads to the mode-shape shown in Fig. 2.9 for the tilt movement with a simulated resonance frequency of $f_0 = 27.826\,\mathrm{kHz}$. This frequency is obtained by using not the nominal thickness of the device layer but a measured thickness value of $9.2\,\mu\mathrm{m}$. The thickness was measured by breaking a sample chip and investigating its cross-section with a Hitachi S3000N scanning electron microscope (SEM). The side-view of the tip of a comb-drive is shown in Fig. 2.10 on which the thickness of $9.2\,\mu\mathrm{m}$ was determined. The simulated resonance frequency overestimates the measured frequency by about $1.5\,\mathrm{kHz}$ or $6\,\%$. To obtain a good match between the simulated and measured

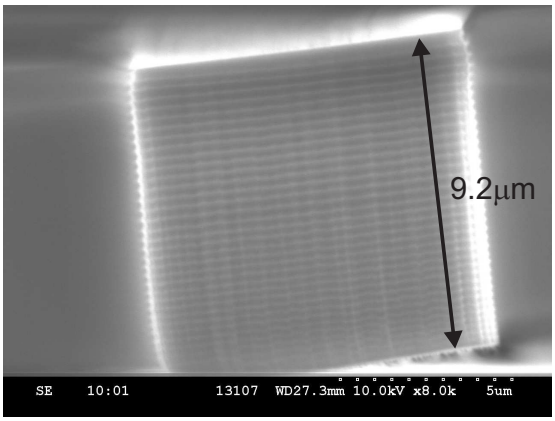

Figure 2.10: SEM image of the side-view of the front facet of a comb on the chip used for the example scanning mirror investigation.

tilt resonance frequency the width of the torsion beam has to be reduced to a value of 27.5 μm leading to a simulated resonance frequency of $f_0 = 26.466\,\text{kHz}$. Similar FEM simulation results were obtained using a further FEM software tool (CoventorWare).

The centre of the torsion beam axis has to be aligned with the x-axis of the simulation program for the calculation of the torsional moment of inertia I_θ using the FEM simulation. Using the already described volume integration a value of $I_\theta = 4.62 \cdot 10^{-17}\,\text{kg m}^2$ is obtained for both torsion beam widths discussed above.

Using the analytical calculation of the spring constant in (2.7) and expression (2.5) an estimation of the tilt (i.e. torsional) resonance frequency can also be obtained, which should underestimate the resonance frequency as the stiffening effect of the combs attached to the torsion beams is neglected. Using the torsion beam length of 675 μm and width of 30 μm, combined with the device thickness of 10 μm and a shear modulus of $G = 50.9\,\text{GPa}$ leads to a spring constant of $k_{analytical} = 9.477 \cdot 10^{-7}\,\text{Nm rad}^{-1}$. With this and the moment of inertia obtained from COMSOL the resonance frequency can be calculated as

$$f_{analytical} = \frac{1}{2\pi}\sqrt{\frac{k_{analytical}}{I_\theta}} = 22.79\,\text{kHz}. \tag{2.17}$$

This underestimates the measured frequency due to the neglecting of the stiffening effect of the moving combs. When adapting the torsion beam width to 27.5 μm, as used for

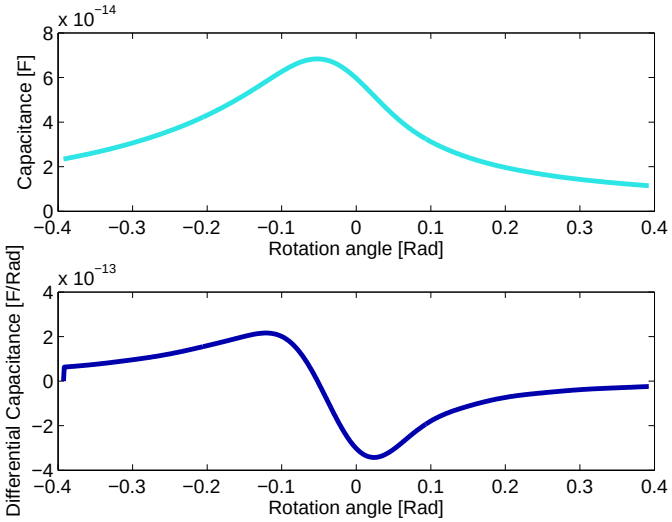

Figure 2.11: Simulated capacitance (top) and differential capacitance (bottom) distribution for one of the comb-drive actuators of the example microscanner.

the fitting FEM simulation, a spring constant of $k_{analytical,0} = 8.499 \cdot 10^{-7}\,\mathrm{Nm\,rad^{-1}}$ is calculated which leads to an analytical calculated resonance frequency of

$$f_{analytical,0} = 21.59\,\mathrm{kHz}. \tag{2.18}$$

This frequency shows the expected underestimation of the measured value as discussed earlier. For the further calculations the resonance frequency value obtained in COMSOL with the 27.5 μm wide torsion beam is used to gain a possible comparison between the simulation and measurements.

The angular behaviour of the capacitance C and differential capacitance $\partial C/\partial\theta$ is calculated using the measured initial comb-offset values and the method described in section 2.3. With the maximum and minimum average initial comb-offset of $z_1 = 9\,\mu$m and $z_2 = 4.7\,\mu$m an initial comb-offset angle of $\theta_i = 1.66°$ is used for the evaluation of the instantaneous height difference between the moving and fixed combs, leading to the capacitance distributions shown in Fig. 2.11. The Matlab program used to determine these distributions can be found in Appendix A resulting in a maximum capacitance of 68 fF at a mechanical rotation angle of −3° due to the AVC geometry of the comb-drive

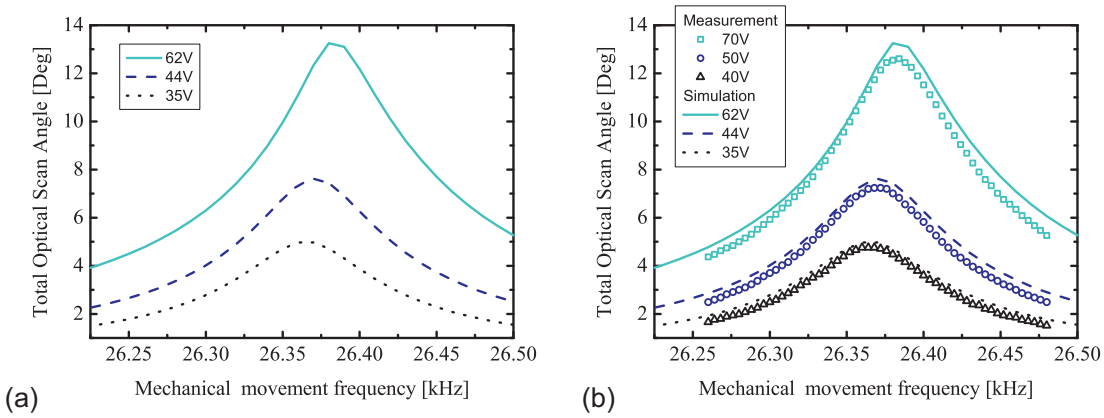

Figure 2.12: (a) Simulated frequency response curves using the determined parameters and (b) overlap of simulated (lines) and measured (dots) frequency response curves.

actuators. A fit to the differential capacitance distribution is then used in the Matlab solution of the ODE motion equation of the device.

2.4.4 Results

With the parameters discussed in the previous sections the motion equation for the device can be solved using the Matlab program described in this chapter (see Appendix A). The amplitude of the voltage signal is used as input parameter, with values of 62 V, 44 V and 35 V to confirm the simulation accuracy with the measurements obtained previously. The voltage levels are lower than the nominal values of the signal generator/amplifier combination of the experiment due to the already described series resistor and parasitic track resistance on the device. For the frequency and resistor combination used here the nominal voltage amplitude is reduced to a value of 88 %. The resulting simulated frequency response curves for a sweep of the actuation frequency f from 13.1 kHz to 13.3 kHz in 5 Hz steps is shown in Fig. 2.12(a). Similar to the experimentally obtained frequency response curves an increase of the peak resonance frequency, with increasing driving voltage is present with peak resonance frequencies of 26.365 kHz, 26.370 kHz and 26.380 kHz for the 35 V, 44 V and 62 V actuation respectively. The maximum simulated TOSA values for these cases are 5.0°, 7.6° and 13.3°.

The comparison between the simulated and experimentally obtained frequency response curves is show in Fig. 2.12(b). An excellent agreement between the measured and simulated results can be seen with a matching peak resonance frequency shift and matching motion amplitudes. The resulting angular range is small enough to not cause any nonlinear spring softening or hardening effects and therefore no bend in the frequency response curve. Also no nonlinear spring constant factors had therefore to be considered in the description of the torsion beam springs. For different scanning micromirror designs with higher angular range these nonlinear factors have to be considered, leading to a balancing or increase of the electrostatic induced nonlinearities.

2.5 Conclusions

A hybrid simulation model for dynamic resonant motions of AVC actuated scanning micromirrors was shown in this chapter, including the possibility to address nonlinear motion behaviour caused by a nonlinear spring constant. The model requires a prior knowledge of the damping coefficient which was only experimentally obtained as an analytical expression for the damping of microscanners is outside the scope of this thesis. Apart from the damping description all other simulation parameters are obtained from the geometrical layout and material properties as basis of the hybrid model. The model verification using an example scanning micromirror showed excellent agreement between the model and experimentally obtained frequency response curves, which were all without nonlinearities. The model is used in the next chapter for a further scanning micromirror design investigating a continuously variable AVC actuator.

3 Variable offset angular vertical comb-drive scanning mirror

The use of angled vertical comb-drives (AVC) as actuators of micromirrors has already been discussed in the previous chapters, with mentioning of their specific advantages for static displacements and the investigations of the influence of initial comb-offsets on the static displacement [89, 119, 120, 123]. This investigation of the initial comb-offset dependency has not been performed for the dynamic scanning movement at the mechanical resonance of the micromirrors, which is the topic of this chapter.

The angular offset of the AVC actuator used in this thesis originates from the fabrication process used for the micromirrors and is intrinsic to the generic mirror design developed at the Centre for Microsystems and Photonics. To investigate to which extent the AVC initial conditions like the comb rest-angle and the comb-offsets influence the angular performance of the devices at resonance, an AVC geometry is developed which can create varying initial comb-offsets by using an additional electrothermal actuator. In this chapter the experimental investigation on the performance of the actuator and its influence on the resonant movement is presented, along with a theoretical investigation based on the analytical hybrid model for the micromirror motion, which was built up in the previous chapter.

Section 3.1 introduces the design of the micromirror followed by the used fabrication process and its properties. Section 3.3 focuses on the design and performance of the

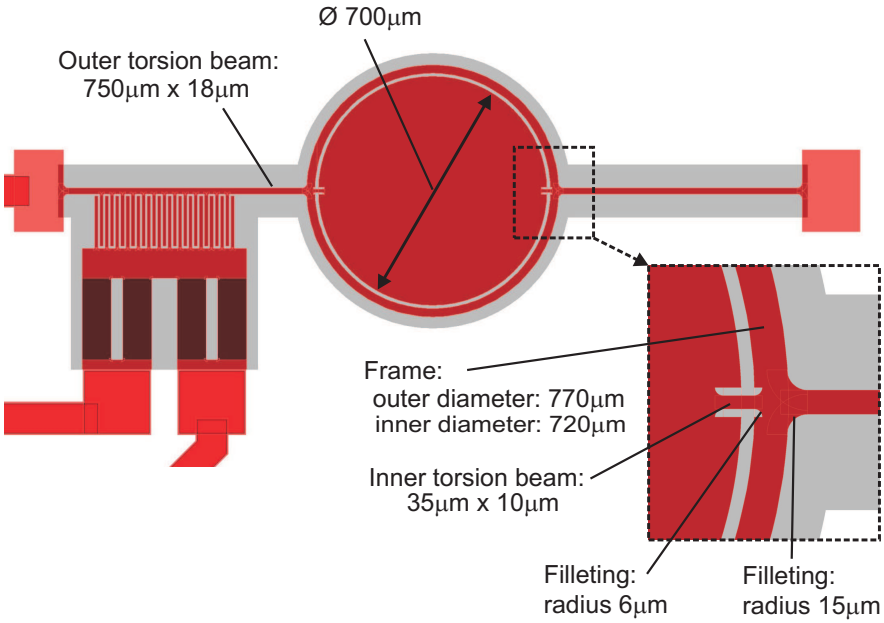

Figure 3.1: Design of the AVC scanning micromirror including inset of the frame/inner mirror connection.

electrothermal actuator used to change the AVC offset, with sections 3.4 and 3.5 showing the experimental investigation of the influence of the initial vertical AVC offset by using the thermal actuator and a mechanical adjustment of the comb-offset. Section 3.6 uses the hybrid model from the previous chapter to simulate the experimentally observed behaviour, followed by a discussion of the resulting performance and agreement between the experimentally and theoretically obtained data.

3.1 Design of scanning mirror

The silicon scanning micromirror design shown in Fig. 3.1 is used as a basis to investigate the influence of the AVC actuator initial conditions on the resonant movement behaviour of the device. The design is based on previously investigated devices with the generic layout of a circular mirror surface and rectangular torsion beams as spring elements and suspension with the design choices influenced by the used multi-user SOIMUMPs fabrication process. The mirror surface has a diameter of 700 μm, with the main outer

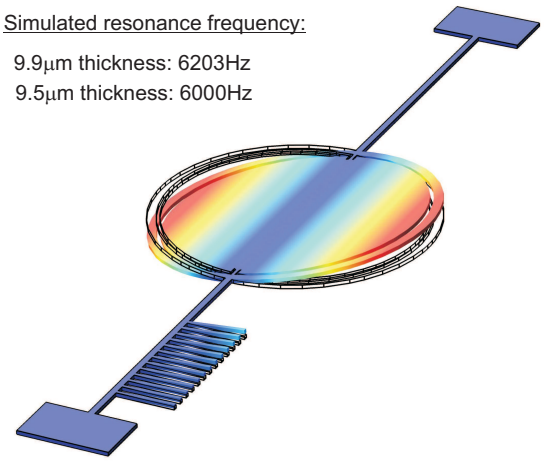

Figure 3.2: Simulated FEM modeshape for the tilt resonance movement mode of the AVC microscanner.

torsion beams having a length of 750 μm and a width of 18 μm. The end facets of the beams are connected to the anchor points and frame using fillets with a 15 μm radius to reduce the occurring stress concentration at sharp edges. A frame with a width of 25 μm was placed around the mirror surface with the aim of achieving a magnification of the tilt movements between the rotation of the combs and the rotation of the mirror surface [90]. A second set of torsion springs, having a length of 35 μm, a width of 10 μm and connecting the frame and the mirror surface, was inserted in line with the main torsion springs for this magnification to occur. The achieved movement magnification factor is only in the range between 1 and 2, as the length of the inner torsion beams was limited in order to still allow a large continuous mirror surface. This is needed for the application of this type of scanning micromirror in laser systems.

A single side comb-drive actuator is used as electrostatic actuator, with its moving combs connected to one of the torsion beams. The 160 μm long and 10 μm wide moving combs are placed at a minimum distance of 238 μm from the frame. 13 moving combs are used with a lateral centre to centre distance of 22 μm. The corresponding fixed combs and their anchor mechanism is described in further detail in section 3.3.

A modal FEM simulation is built up to evaluate the movement modeshapes and

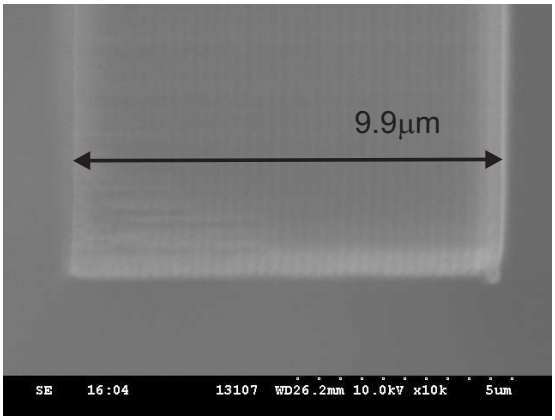

Figure 3.3: SEM measurement of the chip cross-section for the device layer thickness determination.

eigenfrequencies of the micromirror design. The model is built up using the commercially available FEM software COMSOL Multiphysics, with the overall design of the moving parts of the mirror being replicated using basic geometry building blocks within COMSOL. The SOI parameters already introduced in the previous chapter are used as material properties, which can be found in table 2.1. The definition of the material properties requires an in-plane rotation of the geometry by 45 degrees in the simulation tool to align the silicon crystal axes. The boundary conditions for the simulation are fixed constraints at the anchor end of the torsion beams and a linear elastic material model set to an anisotropic description to take the anisotropy of the silicon on insulator (SOI) material into account. The mesh required to solve the FEM is constructed of six parts, a triangular mesh for each of the outer torsion beams, the frame, the mirror surface and the inner torsion beams and a quad type mesh for the moving combs. For the entire geometry a swept mesh with three layers through the device thickness is used leading to a total of 7809 elements. The FEM model is solved using a direct eigenfrequency solver to gain the first six eigenfrequencies and modeshapes of the structure. The mode of interest for the use as a scanning micromirror is the tilt mode shown in Fig. 3.2, which is the second movement mode located at a simulated resonance frequency of 6203 Hz. Similar to the modal FEM simulation used in the previous chapter the measured thickness of the device of 9.9 μm was used for the simulation. The thickness was again determined

by using a SEM image of the chip cross-section (see Fig. 3.3) with a side-view of a comb structure consisting of only the device layer. The movement magnification between the mirror surface and frame is shown in the FEM with a resulting magnification factor of 1.09. It will be shown in a later part of this chapter that the experimentally determined movement frequency of the device is 5990 Hz, which leads to an overestimation of the resonance frequency by the FEM by 210 Hz, i.e. around 3.5 %. To achieve matching movement frequencies between the experimental and simulated data a device thickness of 9.5 μm is needed for the FEM simulation, which is within the device layer thickness tolerances specified for the nominal 10 μm thick fabrication process used.

3.2 Fabrication process

The scanning micromirror devices are fabricated using a commercially available multi-user foundry process provided by the company MEMSCAP Inc. A multi-user silicon-on-insulator process SOIMUMPs was chosen due to the cost effective fabrication possibilities and the material property advantages of the single crystalline silicon used in a SOI process. The fabricated MEMS designs are returned on 1 by 1 mm^2 chips with 15 dies shipped for each design run.

3.2.1 MEMSCAP process steps

A schematic of the fabrication process used for the scanning mirror devices is shown in Fig. 3.4. It consists of four mask steps, with a single frontside etch step defining the device geometry. The initial wafer consists of a SOI wafer with a 400 μm thick n-doped silicon substrate and a 10 μm thick top silicon layer, which are separated by a 1 μm thick oxide layer. The top silicon device layer is phosphorous doped to increase its conductivity, enabling the creation of actuator and sensor designs. The doping in this case is shown to have a non-uniform vertical doping concentration, which will lead to stress induced curvatures when the device layer is released from the backside [156]. The

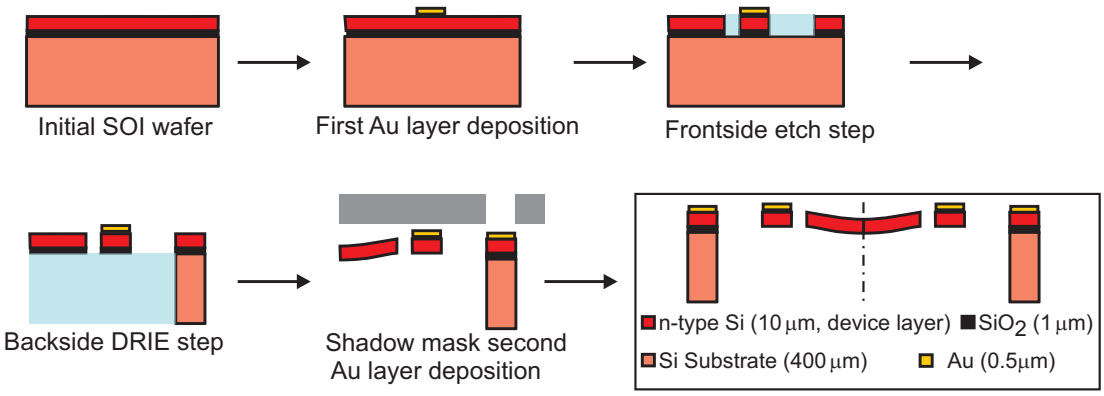

Figure 3.4: SOIMUMPs fabrication process steps used by MEMSCAP Inc.

first step after doping is the deposition and patterning of a pad metal layer consisting of 500 nm gold on top of 20 nm chrome for adhesion purposes. A following mask and frontside deep reactive ion etch (DRIE) step is used to define the device geometry and connection lines. The release of the moving structures is created by a following backside DRIE step through the whole substrate wafer in combination with a wet etch step of the backside to remove the oxide layer from the released parts. A second metal layer can be applied at the end of the fabrication to create a thicker metallisation by using a shadow mask process of a 600 nm thick gold layer deposition in combination with 50 nm of chrome for adhesion. The released device parts will show an out-of-plane curvature due to the already mentioned intrinsic stress originating from the inhomogeneous doping [156].

A SEM image of the fabricated devices is shown in Fig. 3.5. The aluminium wire-bond connections shown at the top side of the overview image are used for electrical connection of the mounted chip to a custom PCB used for testing. The tracks from the bond pads to the actuators and mirror anchors are covered with a pad metal layer to reduce parasitic resistances. The inset of Fig. 3.5 shows the fabricated comb-drive which will be further discussed in section 3.3.

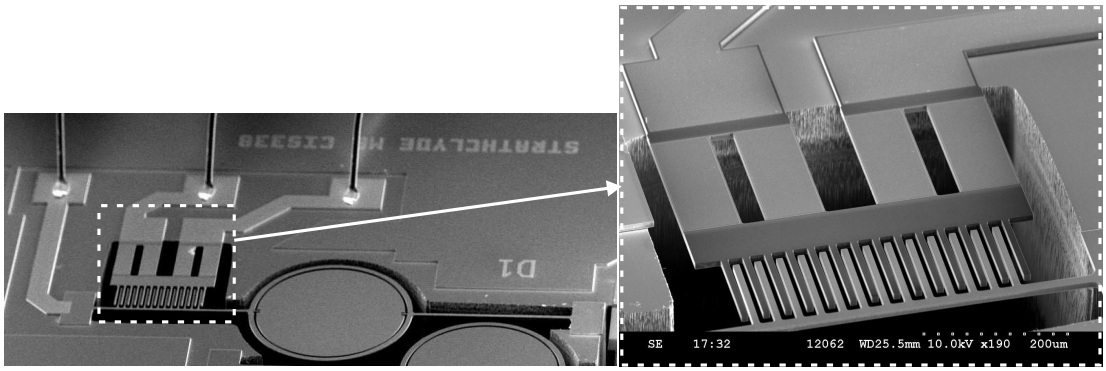

Figure 3.5: SEM image of the fabricated AVC scanning micromirror, including focus on the AVC actuator.

3.2.2 Verification of stress gradient

Intrinsic stress gradients in the silicon device layer and thin film stresses introduced by the gold layers will lead to a curvature in single-side clamped beams and will also introduce a curvature or buckling on double-side clamped released structures. These effects are used to create the angular offset of the AVC geometry, but also need to be considered for distortions of the mirror surface. To estimate the influence and relative magnitude of introduced stresses a series of height scans using an optical white light interferometer profiler was performed on a set of cantilevers with different coatings. The cantilevers were 600 μm long with a width of 50 μm and a nominal thickness of 10 μm. The analysis of the optical profiler images shows a homogeneous curvature along the cantilevers, introduced by the mentioned stress effects, with different radius of curvature (ROC) values for the three cases of a cantilever consisting of solely the SOI device layer, a cantilever consisting of the SOI device layer and a 500 nm thick pad metal layer, and a cantilever consisting of the SOI device layer and both metal layers with a combined thickness of 1.1 μm. The measured ROC for these cases are $0.09\,\mathrm{m} \pm 0.004\,\mathrm{m}$, $0.034\,\mathrm{m} \pm 0.0006\,\mathrm{m}$ and $0.019\,\mathrm{m} \pm 0.0002\,\mathrm{m}$ respectively, when assuming a curvature measurement error of $0.5\,\mathrm{m}^{-1}$ due to possible errors in the spherical fit and measurement tolerances of the optical profiler. Using these measured values a maximum intrinsic stress level for the SOI layer can be determined, as well as the thin

film stresses introduced by the gold coatings. For the SOI layer the maximum bending stress can be calculated with [156]

$$\sigma'_{soi} = -E \cdot \frac{y}{ROC}, \tag{3.1}$$

where E is the Young's modulus of silicon, y is the distance from the centroid axis to the edge and ROC is the measured radius of curvature. Using a Young's modulus of 169 GPa and a centroid distance of $5\,\mu\text{m} \pm 0.5\,\mu\text{m}$ (due to the thickness tolerance specified for the fabrication process) therefore leads to a maximum bending stress in the SOI of $\sigma'_{soi} = -9.4\,\text{MPa} \pm 1.0\,\text{MPa}$ due to intrinsic stresses. The negative sign denotes hereby the compressive nature of the stress.

For the used gold layers the additional introduced stress can be calculated using Stoney's thin film equation [29] in the form

$$\sigma' \approx -\frac{E_s}{1-\nu_s} \cdot \frac{h_s^2}{6\,h_f} \cdot \Delta\kappa. \tag{3.2}$$

The subscripts f and s denote the thin film layer and the substrate, respectively, with E being the Young's modulus, ν is the Poisson's ratio with a value of 0.28 for SOI and h the thickness of the gold layer or substrate. To estimate the influence of the gold layer stress the change of the curvature κ between a bare SOI cantilever and a coated cantilever needs to be considered as $\Delta\kappa$ in the equation, which leads to a stress value of $\sigma'_{pad} \approx -143\,\text{MPa} \pm 33\,\text{MPa}$ when assuming a 50 nm thickness tolerance of the gold layers as well as the already mentioned SOI and curvature tolerances. Similarly the thin film stress of the combined gold layers is calculated as $\sigma'_{pad+blanket} \approx -148\,\text{MPa} \pm 33\,\text{MPa}$.

These compressive stresses lead to an out-of-plane curvature, which is dominated by the influence of the gold layer when present. To therefore create an angled comb-drive geometry the use of anchor beam structures with gold coatings is chosen for the connection of the fixed combs of the investigated AVC structures.

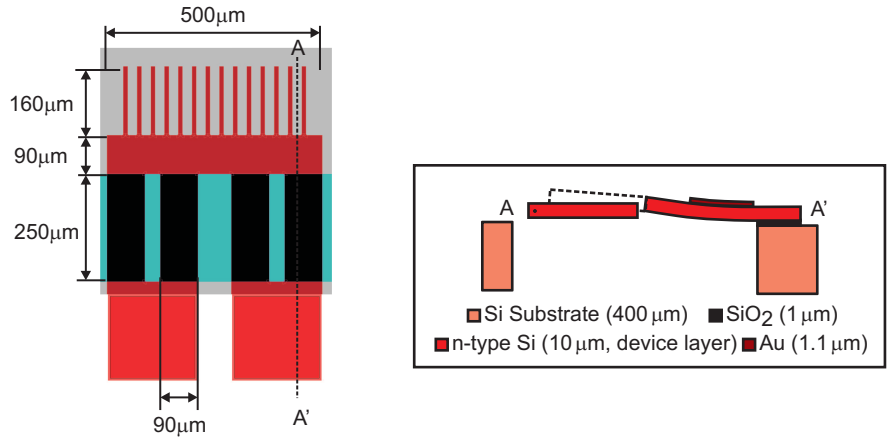

Figure 3.6: Design of the thermal actuator of the AVC fixed combs, including cross-section and layer structure.

3.3 Design of comb-drive actuator

To experimentally investigate the influence of the AVC initial offset between the moving and fixed combs on the resonance behaviour of the above discussed scanning micromirror, a possibility for continuous variation of the initial offset and cross-over angle is needed for using a single device for the investigation. A continuous variable initial AVC offset has, to the best of the author's knowledge, not been demonstrated previously, with only a step-wise and irreversible initial offset change shown and it's influence on the static mirror displacement [116]. The chosen continuous control consists in the here presented work of electrothermal bimorph actuators used as anchor points for the fixed combs of the AVC.

3.3.1 General design considerations for thermal actuator

The design of the thermal actuator structure used as anchor connection for the fixed combs of the AVC is shown in Fig. 3.6. Two silicon anchor pads are used as connection to the substrate and as ports for the current loop of the thermal actuation. Each anchor pad connects to two 250 μm long and 90 μm wide bimorph beams, consisting of the 10 μm thick silicon device layer and the gold layers with a combined thickness

of 1.1 μm. All four bimorph beams are connected using a 90 μm long and 500 μm wide horizontal silicon cross-beam, closing the current loop for the electrothermal actuator and simultaneously working as fix point for the 14 fixed comb-fingers. Each fixed comb-finger has a length of 160 μm and width of 10 μm, with a lateral centre to centre distance of 22 μm, similar to the moving combs. This will lead to horizontal gaps of the self assembled comb-drive of 6 μm.

The electrothermal actuator works on the basic principle of Joule heating in the bimorph and silicon beams. An electric current passing through the beams will create heat through the electrical resistance within the beams which causes an expansion of the beams corresponding to their coefficients of thermal expansion (CTE) and a change of the out-of-plane curvature originating from the bimorph effect in the respective beams. This bimorph effect is in this case created due to a mismatch of the coefficients of thermal expansion between gold (CTE = $14.2 \cdot 10^{-6}$ 1/K) and the used single crystal silicon (SCS) (CTE = $2.5 \cdot 10^{-6}$ 1/K) which will create a tensile stress under heating and reduces the initial curvature which exists after fabrication of the actuator beams. This will translate to a lower initial vertical offset between the fixed and moving combs of the AVC. The limiting factor for the actuator movement is governed by the onset of thermal damage in the actuator due to heating. Gold experiences in this case a lower melting point (1064°C) than SCS (1414°C), which therefore leads to an actuation limit before the highest temperature in the bimorph beams reaches the gold melting point. The highest temperature in the actuator is expected to be towards the middle of it as the main effect of heat removal will be through heat conduction through the anchor connections, with radiative heat transfer and convection negligible in first approximation.

3.3.2 FEM simulation of thermal behaviour

To model the possible displacement range of the fixed combs of the AVC design a combined thermal and mechanical simulation using the FEM software CoventorWare

Table 3.1: *Material properties used for the CoventorWare thermal FEM model [164].*

Symbol	Description	SOI value	Gold value
E	Young's modulus in [100]	130 GPa	57 GPa
ν	Poisson's ratio	0.28	0.42
CTE	Coefficient of thermal expansion	$2.5 \cdot 10^{-6}\,\mathrm{K}^{-1}$	$1.4 \cdot 10^{-5}\,\mathrm{K}^{-1}$
k_t	Thermal conductivity	$150\,\mathrm{Wm}^{-1}\mathrm{K}^{-1}$	$317\,\mathrm{Wm}^{-1}\mathrm{K}^{-1}$
ϵ_e	Surface emissivity	0.6	0.02
C_h	Specific heat capacity	$755\,\mathrm{J\,kg}^{-1}\mathrm{K}^{-1}$	$129\,\mathrm{J\,kg}^{-1}\mathrm{K}^{-1}$

was built-up. This behaviour investigation was conducted by a colleague, Dr. Li Li, and is therefore only briefly summarised in this section for completeness. To optimise the possible movement range of the vertical comb-offset, with the aim of reaching a highest possible change in vertical offset while maintaining a small actuator footprint, multiple design variations of the final AVC thermal actuator were simulated. The parameter variations were the width of the bimorph and connection beams. The chosen design discussed so far in this section showed hereby the best compromise between the temperature distribution in the gold layer and the possible vertical displacement of the comb-tips.

The boundary conditions for the FEM simulation are an applied potential difference between the two anchor pads, which is varied between a value of 0 V and 3.5 V, a reference temperature of 20°C, which is assumed at the connection between the actuator anchors and the substrate, and the material properties shown for SOI in the previous chapter. The additionally needed material properties related to the thermal simulation are shown in Table 3.1 for both the SOI and gold layer. The FEM software first solves the temperature distribution in the actuator using Joule heating as basis and then couples the resulting temperature profile to a mechanical deformation. The temperature model considers the heat loss due to thermal conduction through the actuator, heat convection and radiative heat transfer. A value of $150\,\mathrm{Wm}^{-2}\mathrm{K}^{-1}$ is assumed as an air convection coefficient for the actuator surfaces. For the mechanical deformation the

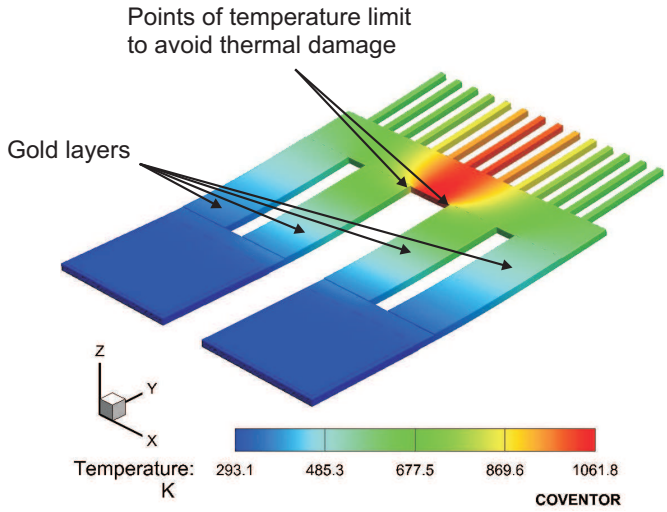

Figure 3.7: FEM results of temperature distribution of AVC thermal actuator with V_{DC} = 3.5 V.

influence of the temperature model is combined with the initial deformation due to the intrinsic stresses in the material layers. The intrinsic stresses of the SOI and gold layer without actuation are assumed to be a stress gradient of 2.4 MPa/μm for the SOI layer and a residual stress in the gold layer of 300 MPa.

The simulation result of the temperature distribution for an applied DC voltage of 3.5 V is shown in Fig. 3.7. A maximum temperature of 893 K is present at the marked temperature limiting points, with an overall maximum temperature of 1062 K at the middle comb fingers. The average vertical displacement of the actuator comb finger tips is hereby changed from an initial value of 10.8 μm to a value of 5.0 μm with respect to the vertical position of the anchor. To compare the simulation results with the experimental data discussed in the next section, the average vertical offset values of the comb finger-tips (z_1) are required for the potential difference sweep, as well as the vertical offset set back 152 μm from the finger-tips (z_2), which marks the end of the moving comb finger in case of the interdigitated assembled AVC. The summary of the simulated data for these measurement points is shown in Fig. 3.8. An increase in applied voltage will lead to the shown temperature increase for the maximum actuator temperature, which in itself leads to the reduction of the vertical comb-offsets z_1 and

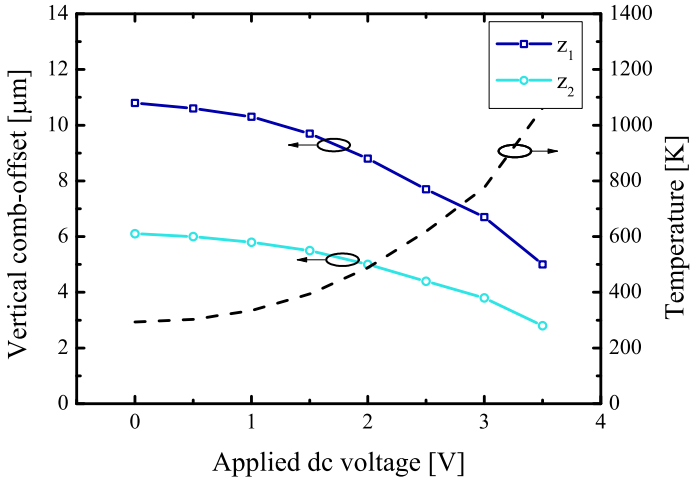

Figure 3.8: Simulated AVC comb-offset variation and maximum actuator temperature with applied DC voltage of electrothermal actuator.

z_2. The maximum applied dc voltage in the simulation was 3.5 V, reaching the thermal damage limit of the actuator.

3.3.3 Experimental results of electrothermal comb-offset variation

The vertical offset variation of the AVC actuator was experimentally determined after fabrication by using height profiles of the comb-drive during and before actuation. These were obtained by a Veeco NT1100 optical white light interferometer. A 10 times magnification lens combination was used to measure the vertical profiles of the overall comb-drive using the VSI measurement mode of the profiler. The offset of the thermal actuator was controlled using a SkyTronic DC power supply with a current limit of 3 A.

The comb-offset values z_1 and z_2 for each actuation point are evaluated using the respective profiler measurement with two 2D line-scans at the tip of the moving and fixed combs, as can be seen for an example offset of $z_1 = 5\,\mu$m in Fig. 3.9. This is the maximum possible displacement through electrothermal actuation, while avoiding thermal damage. The fixed combs are in this case in a vertical higher position than the moving combs. The vertical displacement introduced by the electrothermal actuation shows a

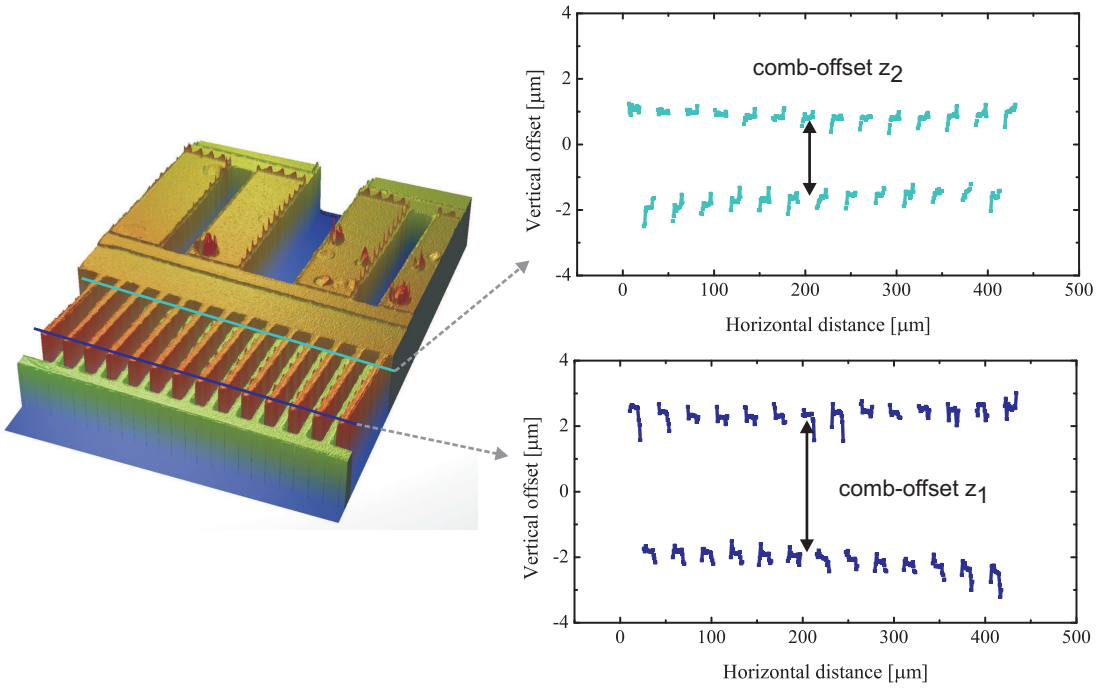

Figure 3.9: AVC offset at $z_1 = 5\,\mu$m with 2D linescans and positions for z_1 and z_2.

mostly homogeneous offset of the individual comb-pairs, with slight variations with a maximum range of $0.9\,\mu$m for the $5\,\mu$m offset case, due to a downward bending ROC of $-0.16\,$m of the torsion beam towards the mirror surface and a higher displacement of the thermal bimorph actuators in the middle of the anchor structure.

The summary of the measured experimental average vertical comb-offsets during electrothermal actuation are shown in Fig. 3.10. The maximum applied electrical power was limited to a value of 510 mW, calculated by measuring the applied DC voltage and current through the electrothermal actuator, to avoid possible thermal damage to the gold coatings of the bimorph actuators. This was necessary as earlier tests have shown a surface change of the gold layer at the expected highest temperature point during actuation with higher electrical powers. The resulting offset change for the maximum applied electrical power is a reduction of the vertical offset from $10.4\,\mu$m in the non-actuated state to $4.9\,\mu$m for z_1 and a reduction of the second vertical offset position from $6.1\,\mu$m in the non-actuated state to $2.7\,\mu$m for z_2.

The simulated and measured vertical offset changes show a good agreement, with a

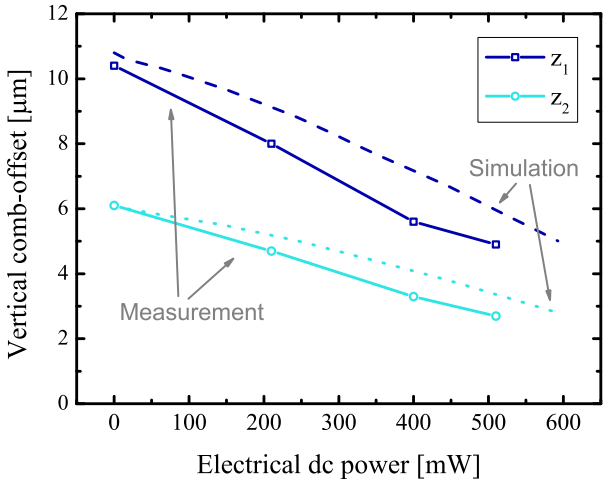

Figure 3.10: Experimental and simulated comb-offset values during electrothermal actuation of the fixed comb anchor.

reduction of the offset by half for around 500 mW electrical actuation and similarly a reduction of the initial comb cross-over angle, which is indicated by the smaller offset difference between z_1 and z_2 in both the measurement and simulation results. The underestimation of the simulated vertical offset reduction can be explained by general rough assumptions for the heat loss that were necessary to model the actuator. No perfect in-plane configuration of the comb-drive is possible using this actuator due to the thermal damage limit of the electrothermal actuator.

3.4 Experimental investigation of electrical variable comb-offset influence

With the possibility of a continuous variation of the AVC initial offset through the above discussed electrothermal actuator, an investigation of the initial offset influence on the dynamic resonance driving performance of the scanning micromirror is shown in this section.

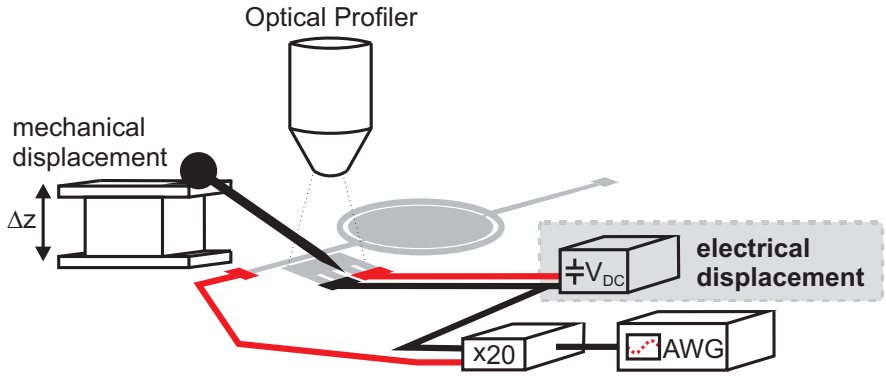

Figure 3.11: Measurement setup determining the initial offset influence on the scanning resonance movement, using the electrothermal comb displacement.

3.4.1 Experimental methodology

The setup shown schematically in Fig. 3.11 is used for both the electrically controllable initial AVC offset variation as well as the later discussed mechanical initial AVC offset variation to simultaneously evaluate the initial comb-offset of the AVC actuator and the scanning micromirror performance. The tested mirror is placed under the measurement optics of the previously introduced optical profiler to verify the comb-offset, with the two electrical driving circuits for the electrothermal comb-offset variation and the excitation of the electrostatic tilt resonance movement sharing a common ground line. The potential difference for the electrothermal actuator is created using the DC power supply and the common ground line as connections to the thermal actuator anchors. For the electrostatic comb-drive actuation the ground state at the fixed combs leads to the voltage driving signal being applied to the moving combs and therefore the whole moving structure. As only one comb-drive exists on the device no parasitic influence is to be expected through this. The investigated electrostatic driving signal amplitudes are 80 V and 120 V which shows that the applied DC voltage with a maximum of 1.5 V is negligible for the analysis. The driving signal for the resonant actuation consists of an offset square-wave voltage signal and is created using an Agilent 33250A arbitrary waveform generator (AWG) in combination with a FLC A400 times twenty amplifier.

For each targeted initial offset step the respective dc voltage level is set first and

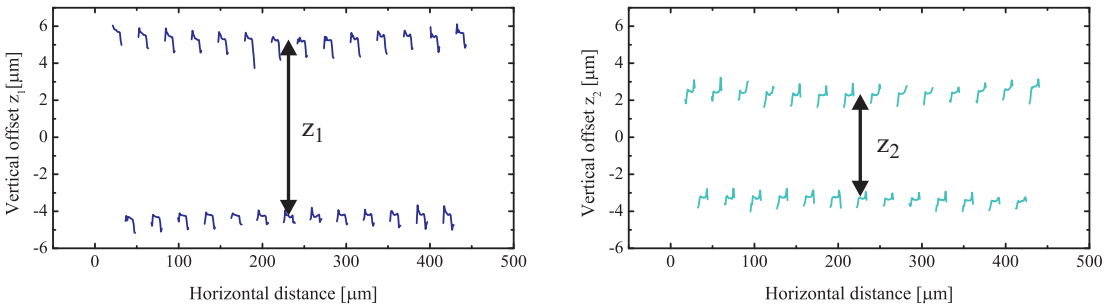

Figure 3.12: 2D linescans of AVC offsets z_1 and z_2 for the non-displaced actuator.

an optical white light profile of the comb structure is taken to verify the offset. The scanner is then actuated using the square-wave driving signal and a frequency sweep around the tilt resonance frequency. The resulting scan angles are determined using the reflection of a HeNe probe laser beam on a screen. The incident angle of the laser on the mirror surface is constrained to an angle of about 45° due to the profiler optics and their working distance.

3.4.2 Resonant behaviour without thermal actuation

No thermal actuation is required to evaluate the scanning micromirror response for the highest possible AVC offset in the used design. The measured 2D height profiles along the tips of the moving and fixed combs are shown in Fig. 3.12 for this case. The offset values are hereby $z_1 = 10.4\,\mu$m and $z_2 = 6.1\,\mu$m, both having a standard deviation of $0.2\,\mu$m. This leads to an initial AVC comb-angle between the respective comb-pairs of 28 mrad (1.6°).

The tilt movement frequency response of the scanning mirror is measured for an actuation with offset square-wave driving signals with an amplitude of 80 V and 120 V, using an actuation frequency between 5.94 kHz and 6.06 kHz for the 80 V actuation and an actuation frequency between 5.96 kHz and 6.08 kHz for the 120 V actuation. In both cases frequency steps of 5 Hz are used. The resulting total optical scan angles (TOSA) are shown in Fig. 3.13. Both actuation voltages show a symmetric frequency response curve with no visible onset of a nonlinear behaviour. The 80 V actuation leads to a

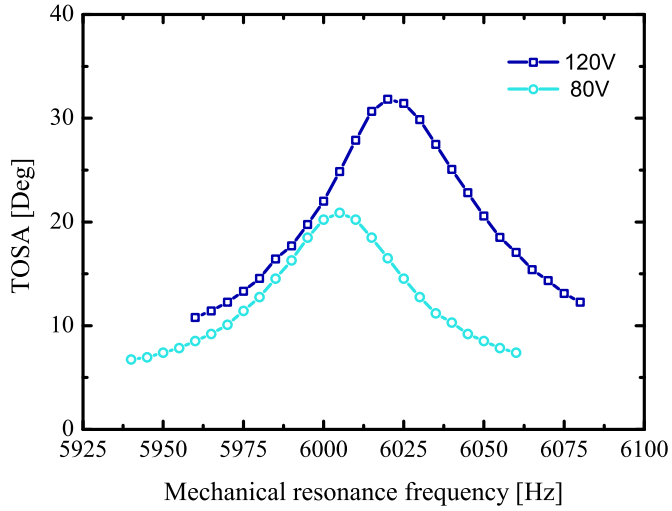

Figure 3.13: Frequency response curves for the non-displaced AVC actuator with z_1 = 10.4 μm.

maximum TOSA of 20.9° at 6005 Hz while the 120 V actuation results in a TOSA of 31.8° at 6020 Hz. These scan angles are corresponding to the tilt of the mirror surface, which is magnified in respect to the tilt of the frame, as can be seen in the earlier shown FEM simulation of the tilt movement mode shape. To evaluate the magnitude of the magnification for the as fabricated initial conditions a microscope coupled laser vibrometer was used for the 80 V actuation case. The vibrometer measurement spot was placed on the edge of the mirror surface and on the frame, in both cases at the furthest point from the rotation axis. The vibrometer feeds back a voltage level dependent on the vertical displacement and corresponding to a set scaling factor (in this case 20 μm/V). The resulting calculated tilt angles for both the mirror surface and the frame lead to a scaling factor for the tilt movement of about 1.15 between the mirror and the frame.

3.4.3 Resonant behaviour changes with comb-angle variation

The influence of the AVC initial offset change through the electrical actuation is evaluated for three additional offsets next to the non-actuated state. Vertical offset values z_1 of 8.0 μm, 5.6 μm and 4.9 μm were used for the investigation, leading to necessary

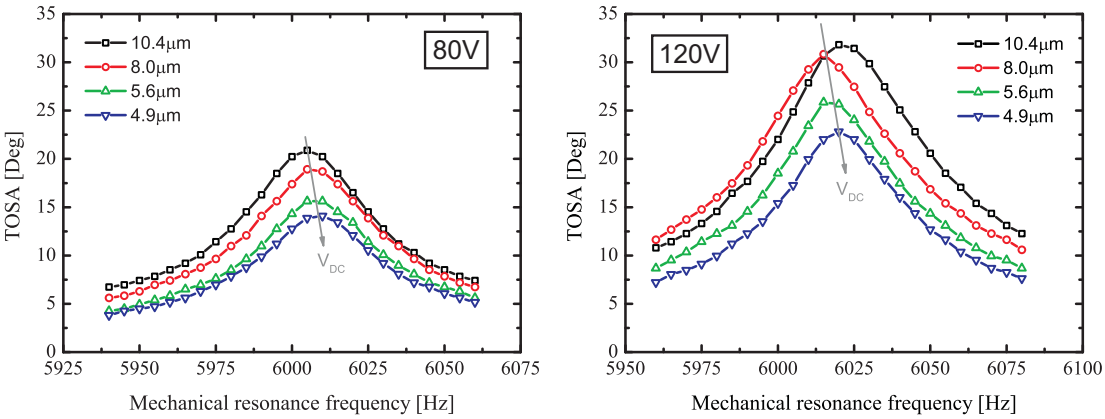

Figure 3.14: Frequency response curves for changing the AVC initial offset through the electrothermal actuator.

electrical DC actuation powers of 210 mW, 400 mW and 510 mW, respectively. The electrostatic actuation signals are identical to the ones used for the maximum offset, with an offset square-wave voltage with amplitudes of 80 V and 120 V. The resulting frequency response curves, measured using the HeNe probe laser, are shown in Fig. 3.14 for both actuation voltages. The graphs also include the already previously shown maximum offset case with a z_1 value of 10.4 μm.

For the actuation amplitude of 80 V all frequency response curves have a symmetric behaviour with no apparent nonlinearities and a reduction of the maximum resonance TOSA with reduced initial comb-offset. The maximum TOSA of 20.9° for the 10.4 μm offset reduces down to 14.1° for the 4.9 μm offset. At the same time the frequency of the resonance peak shifts to slightly higher values with a 5 Hz shift between the maximum and minimum offset case achievable by the electrical controlled AVC offset. This shift originates from the change of differential capacitance which is part of the electrostatic torque description. The change introduces in this case a variation in the spring softening behaviour, which shifts the peak resonance frequency to lower values for higher angles.

The same trends are present for the 120 V actuation case. A maximum TOSA of 31.8° at the initial offset of 10.4 μm reduces to 22.8° for the 4.9 μm offset. A frequency

shift is also present, albeit the frequency response curve with no electrical comb-offset variation has a higher peak resonance frequency then would be expected following the trend of the other three offset cases. From a comb-tip offset of 8 μm to the offset of 4.9 μm a frequency shift from 6015 Hz to 6020 Hz is present, with the peak resonance of the maximum offset also being at 6020 Hz.

The frequency shifts present in both actuation voltage cases have their possible origin in the change of the differential capacitance distribution associated with a change of the initial comb-offset. As the differential capacitance depends in a nonlinear manner on the instantaneous mirror tilt-angle a change to its distribution will change the electrostatic nonlinearity with otherwise constant electrical driving conditions. These lead to the frequency shift of 15 Hz between the 80 V and 120 V actuation. The reduction of the TOSA values for reduced AVC comb-offsets has its possible origin in the change of the capacitance distribution over the angular movement range of the scanner. To verify the behaviour an analytical simulation based on the model discussed in the previous chapter will be used in section 3.6.

3.5 Experimental investigation of mechanical variable comb-offset influence

To achieve an as close as possible comparison between the frequency response of the maximum possible AVC offset and an in-plane comb-drive configuration for the presented AVC scanning micromirror, a second mechanism to change the comb-offsets is required due to the limits of the thermal actuator discussed in the previous section. The chosen offset mechanism is for this case a careful mechanical displacement of the fixed comb-anchor using the tip of a needle in combination with multiple micrometre translation stages.

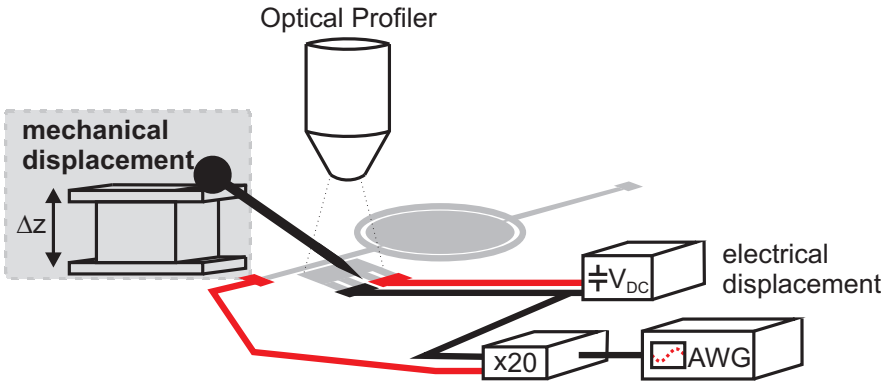

Figure 3.15: Measurement setup for determining the initial offset influence using a mechanical displacement of the fixed comb-drive anchor.

3.5.1 Experimental methodology

The experimental setup and methodology for the investigation of bigger changes of the initial AVC offset is almost identical to the previously discussed electrical offset change (see Fig. 3.15). The change of the comb-offsets is in this case performed by aligning a needle tip in the middle of the electrothermal actuator, using a set of lateral, rotational and vertical micrometre translation stages on which a needle with a tip width of approximately 100 μm is fixed. The change of the comb-offset is achieved by a vertical displacement of the needle. The needle itself needs to be angled towards the AVC as the experimental setup is fixed underneath the microscope optics of the scanning white light interferometer. As the mechanical displacement of the fixed combs creates less accurate offset steps then the electrical displacement, a measurement of the frequency response for both 80 V and 120 V electrostatic actuation signals is conducted without changing the needle position for each offset step. The chosen offset steps using the mechanical displacement are an offset with the comb-tip displacement z_1 around half-way between the initial offset and an in-plane alignment (z_1 = 3.9 μm), an offset as close as possible to an in-plane configuration (z_1 = 0.5 μm) and a negative offset at which the fixed combs initial position is lower than the moving combs (z_1 = −1.7 μm). For each configuration the frequency response curves are measured using again a HeNe probe laser aligned on the mirror surface of the scanning micromirror. The electrical

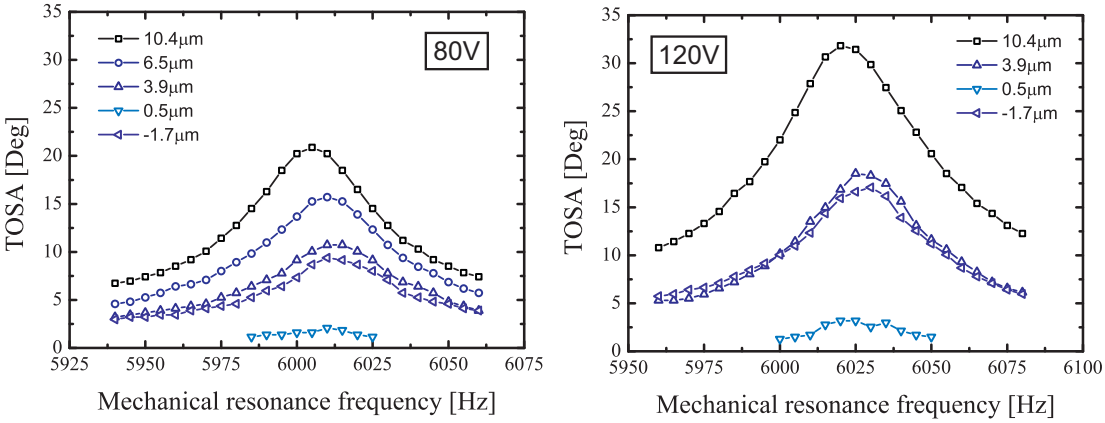

Figure 3.16: Frequency response curves for mechanical changes of the AVC initial offset, including an as close as possible in-plane configuration.

connections for the electrostatic actuation remain the same as in the electrical AVC offset investigation.

3.5.2 Resonant behaviour changes with comb-angle variation

The frequency response curves for mechanical variation of the initial AVC offsets were again measured using an offset square-wave driving signal with electrical excitation frequencies matching the mechanical movement frequencies. The maximum offset of 10.4 μm shows again the non-actuated case, which is identical to the frequency response curve obtained for the electrical AVC changes. The mentioned mechanical offset steps have initial comb-offsets at the fixed comb-tips z_1 of 3.9 μm, 0.5 μm and $-1.7\,\mu$m with corresponding vertical offsets at the moving comb tips z_2 of 1.6 μm, $-0.9\,\mu$m and $-2.5\,\mu$m, respectively. For the 80 V actuation an additional step at $z_1 = 6.5\,\mu$m was included.

The frequency response curves for both actuation voltages and all offset steps are shown in Fig. 3.16. The 80 V actuation shows a reduction of the maximum TOSA at resonance for a reduction of the initial vertical offset until an as close as possible in-plane configuration is reached. With a negative comb displacement the peak TOSA is rising again. For the 3.9 μm initial offset a maximum TOSA of 10.7° is shown, which

is close to the maximum TOSA for the $-1.7\,\mu$m initial offset. In both cases the peak resonance has shifted by 5 Hz to 6010 Hz with maximum TOSA values of 10.7° and 9.4° respectively. The as close as possible in-plane behaviour shows a further reduction of the frequency response which will be described in further detail in the next subsection.

For the 120 V actuation a similar trend is visible with again a roughly 5 Hz shift of the peak resonance frequency for the $3.9\,\mu$m and $-1.7\,\mu$m case to a peak resonance of 6025 Hz. The TOSA values for this case are 18.5° and 17.1°.

The behaviour follows the trend shown by the electrical AVC initial comb-angle variation, with higher initial comb-offsets having higher TOSAs at resonance. The observed frequency shift has again a possible origin in the nonlinear spring constants of the scanning micromirror torsion beams.

3.5.3 Behaviour around zero-position

The frequency response behaviour for an initial AVC comb offset of an as close as possible in-plane configuration is examined in more detail due to the observed lowest angular frequency response. The measured optical profile of the AVC offsets for this case is shown in Fig. 3.17. The measured 3D representation on the left shows the close height overlap between the moving and fixed combs as well as the imprint of the needle tip used to change the vertical offset. This imprint is in the form of a missing data pattern as the light reflected from the needle will not be collected back by the optical profiler optics and therefore will show a blank data area. The 2D vertical height line scans for z_1 and z_2 show a bent profile for the fixed combs at both positions. This bend with a maximum height difference of $1\,\mu$m originates from the mechanical displacement of the fixed comb anchor, where the needle tip is smaller than the overall actuator and therefore a slight non-uniform pressure is applied to generate the reduction of the vertical offset of the AVC. The profiles also show a change in offset between the tips of the moving and fixed combs, with the fixed combs being higher than the moving combs

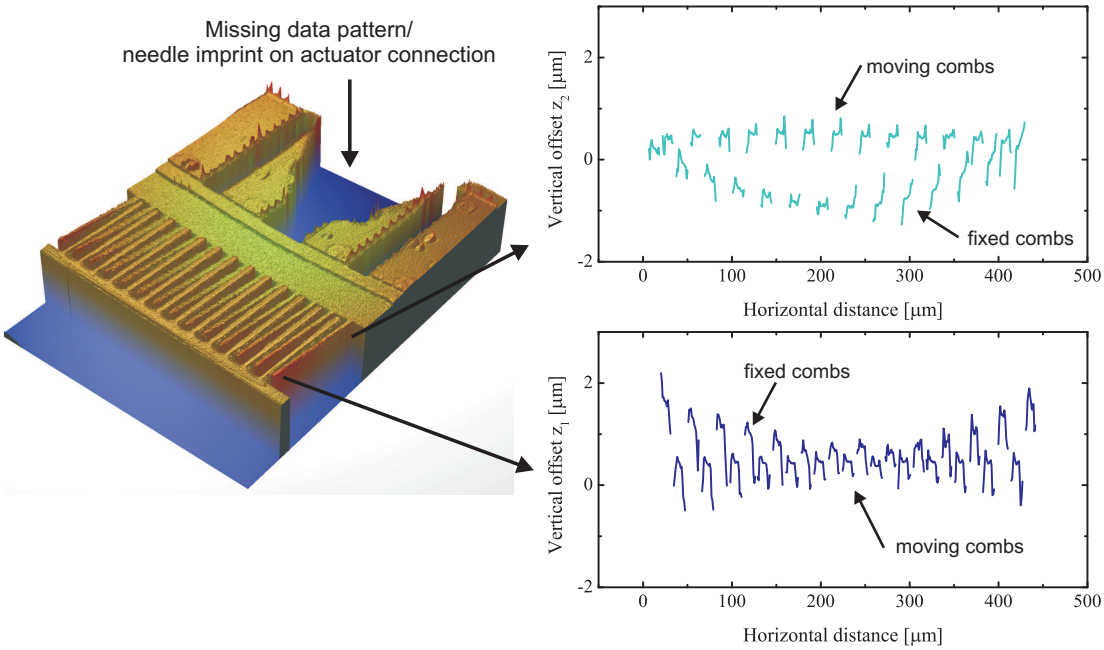

Figure 3.17: Measured AVC profile for in-plane configuration with $z_1 = 0.5\,\mu$m and $z_2 = -0.9\,\mu$m.

at $z_1 = 0.5\,\mu$m and respectively lower at $z_2 = -0.9\,\mu$m. This offset change contributes to the low angular frequency response for this driving case.

The frequency response curves shown in Fig. 3.16 show for both actuation amplitudes the lowest measured response with a TOSA of 2° and 3.2° respectively. Changing the actuation frequency to a subharmonic or superharmonic excitation of factors 2 and 1/2, respectively, leading to electrical driving frequencies of 12 kHz and 3 kHz did not show any identifiable movement response for both the actuation with 80 V and 120 V.

3.6 Analytic model of variable AVC behaviour

The analytical hybrid simulation model built-up in the previous chapter is adapted for the presented device design to theoretically model the experimentally observed frequency response behaviour for the variable AVC offset scanning micromirror. The influence of the initial vertical comb-offset on the dynamic resonance behaviour of the microscanner is again the focus of interest.

The basis of the simulation model is the numerical solution of the ordinary differential equation (ODE) systems of the scanner movement equation, using Matlab's in-built ODE45 solver. The system of two first order ODE's can be written, as shown in the previous chapter, in the following form:

$$\begin{aligned} \dot{\theta_1} &= \theta_2 \\ \dot{\theta_2} &= -4\,\pi\,\xi\,f_0\,\theta_2 - \frac{k_\theta}{I_\theta}\,\theta_1 + \frac{1}{2\,I_\theta}\,\frac{\mathrm{d}C}{\mathrm{d}\theta_1}\,V(t)^2 \end{aligned} \tag{3.3}$$

θ_1 is the tilt angle and θ_2 the first time derivative of the tilt angle. The further parameters are corresponding to the overall damping of the device, with the damping factor ξ defined through the Q-factor of the resonance motion, the limiting resonance frequency f_0 which would occur for small movements without the influence of electrostatic or mechanical nonlinearities, the torsional moment of inertia of the overall device I_θ and the overall spring constant of the device k_θ. The spring constant does, in this case, include a second order nonlinearity whose influence will be investigated later on. k_θ can therefore be written as

$$k_\theta = k_0\left(1 + k_2\,\theta_1^2\right) \tag{3.4}$$

as discussed in the previous chapter. k_0 is in this case the basic spring constant of the system with k_2 being the cubic nonlinear spring constant. The differential capacitance $\mathrm{d}C/\mathrm{d}\theta_1$ and driving voltage $V(t)^2$ are part of the electrostatic torque description and will be discussed in more detail in the following section.

The motion description with two first order ODE's in (3.3) includes the assumption that the mirror and frame have a rigid connection. This assumption is in a first approximation valid as the measured angular magnification between the mirror surface and the frame (see section 3.4.2) is a factor of only 1.15. If this assumption would not be used a further two first order ODE's would be necessary to describe the mirror movement and its coupling to the frame [90]. In addition, the spring constants and damping coefficients would need to be calculated for each part, the inner mirror and the outer

frame and suspension, separately which would raise the question how to determine the correct ratio of damping coefficient from only the overall resonance frequency response curve measurement. With the assumption of a rigid connection between the mirror and frame an overall damping coefficient can be assumed which is directly calculated from an exemplar measurement.

3.6.1 Electrostatic torque model

To model the differential capacitance distribution necessary for the torque term of the motion equation the approach described in the previous chapter is taken, using an FEM simulation of the 2D electrical field distribution of a unit cell of the comb-drive (see Fig. 2.4). With this field distribution it is possible to calculate the capacitance of each AVC configuration for each possible tilt angle θ of the moving structure, depending on the specified initial comb-offsets of the AVC. This calculation is possible using the definitions from Fig. 2.5 with

$$z(l,\theta) = l \cdot \sin(\theta - \theta_i) + z_1 + l_2 \cdot \sin(\theta) \tag{3.5}$$

as the instantaneous height offset along a comb-pair. Through this it is possible to calculate the overall instantaneous capacitance of the comb-drive throughout the mirror movement cycle according to equation (2.13). This distribution varies with the initial AVC offsets through the parameters z_1 and θ_i.

Four offset cases are chosen for the theoretical investigation of the influence of these offset changes. A maximum AVC offset with $z_1 = 10.4\,\mu$m, an offset created by the maximum electrical displacement of the AVC fixed combs with $z_1 = 4.9\,\mu$m, a closest measured in-plane AVC offset with $z_1 = 0.5\,\mu$m and a negative offset with $z_1 = -1.7\,\mu$m. The Matlab code calculating the capacitance and differential capacitance distributions for these offset cases can be found in Appendix A. The resulting distributions for the maximum AVC offset case and the closest in-plane AVC offset are shown in Fig. 3.18.

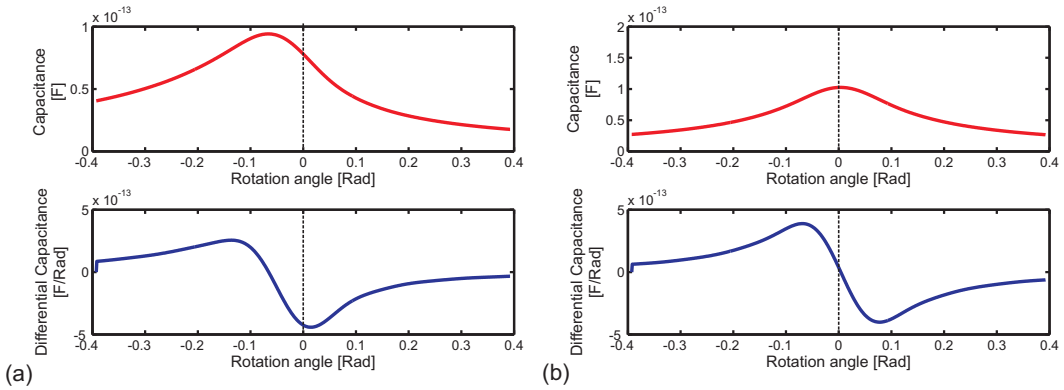

Figure 3.18: Capacitance and differential capacitance distribution for (a) $z_1 = 10.4\,\mu$m AVC offset and (b) $z_1 = 0.5\,\mu$m AVC offset.

The closest in-plane configuration shows an expected symmetrical behaviour around the mirror midpoint for both the capacitance $C(\theta)$ and differential capacitance $\partial C/\partial\theta$, while the highest offset configuration clearly deviates from this symmetry.

The second part necessary for the torque description is the applied excitation voltage signal $V(t)$ which is for all discussed cases in this chapter an offset square-wave signal that can be described as:

$$V(t)^2 = \frac{1}{4} V_0^2 \left(1 + square(2\pi f t)\right)^2, \tag{3.6}$$

where V_0 is the amplitude of the square-wave and f is the electrical excitation frequency. Similar to the experimental investigation discussed earlier in this chapter the frequency of the excitation signal is identical to the excited mechanical movement frequency.

3.6.2 Analytic model results using torque behaviour

The Matlab code to solve the motion equation for each chosen initial comb-offset step is similar to the one described in the previous chapter, with the call of the solver ODE45 for each frequency point of interest. In each step the solver uses the equations (3.3) with a 20th order Fourier series fit of the differential capacitance, the definition for the applied voltage and the definition for the nonlinear spring constant. For each frequency step the

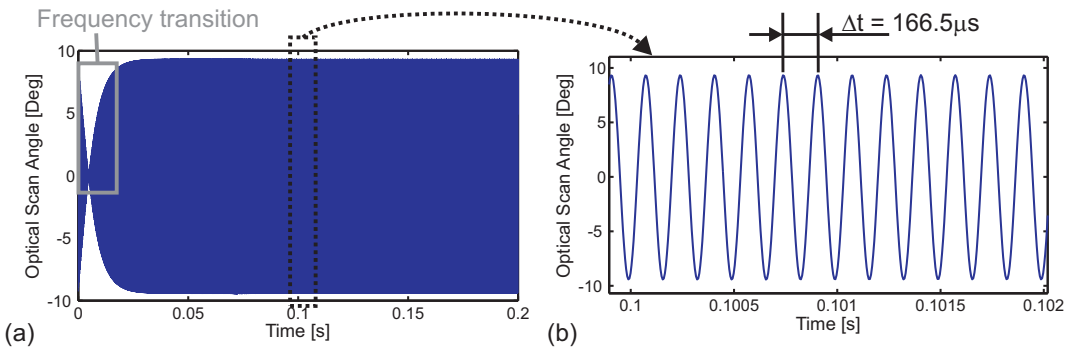

Figure 3.19: Simulation output of the time-dependent optical scan angle of the z_1 = 10.4 μm offset case with an excitation of V_0 = 56 V and f = 6006 Hz.

solver returns a time-dependent solution of both the tilt angle θ_1 and its time derivative θ_2 over the time range specified when calling the solver. This timebase needs to be long enough for the oscillation to reach a stable output, which is for the here discussed cases reached within the first 200 ms of a change to the mirror driving conditions. An exemplar output of the ODE function can be seen in Fig. 3.19 for the maximum comb-offset case around its resonance peak. The excitation parameters for this output are a voltage amplitude of V_0 = 56 V and a frequency of 6006 Hz, with the rest of the parameters taken from the z_1 = 10.4 μm offset case. The simulation result of the time dependent optical scan angle shows a decrease of the scan angle in the first 5 ms after start of the simulation, followed by a rise to the stable resonance movement (see marked part in Fig. 3.19(a)). This is the transition time between the previous movement of the mirror with a 2 Hz higher frequency, used as boundary condition for the ODE solver, and the new excited movement. A magnified image of the stable movement oscillation can be seen in Fig. 3.19(b), showing the movement period of 166.5 μs corresponding to a resonance frequency of 6006 Hz. To determine the maximum TOSA at each excitation frequency a peak search is conducted on the simulated data for the last 200 time points prior to the 0.2 s simulation end time.

The simulated frequency response curves for the four chosen comb-offset cases using this simulation approach are shown in Fig. 3.20. For all simulation cases a frequency down-sweep is chosen. The input parameters for the simulation are shown in Table

Table 3.2: *Input parameters for AVC motion equation simulation.*

Symbol	Value	Symbol	Value
I_θ	$3.963 \cdot 10^{-16}\,\mathrm{kg\,m^2}$	N	26
k_0	$5.61 \cdot 10^{-7}\,\mathrm{Nm/rad}$	V_0	56 V
k_2	0.33	z_1	"10 μm": 10.4 μm
f_0	5990 Hz		"5 μm": 4.9 μm
Δf	5 Hz		"0 μm": 0.5 μm
f_{min}	5920 Hz		" − 2 μm": −1.7 μm
f_{max}	6120 Hz	z_2	"10 μm": 6.1 μm
ξ	$3.0 \cdot 10^{-3}$		"5 μm": 2.7 μm
t	[0 s, 0.2 s]		"0 μm": −0.9 μm
			" − 2 μm": −2.5 μm

3.2, including a cubic nonlinear spring constant k_2 whose estimation and influence will be discussed in the next section. The torsion moment of inertia I_θ is an input from the modal FEM shown earlier in this chapter. The limiting resonance frequency f_0 was obtained by using the measurement data shown in Fig. 3.13 and approximating the evaluation of the maximum TOSA for actuation voltages reaching 0 V. The estimated value for this is 5990 Hz. The spring constant k_0 is calculated using this two parameters, while the damping coefficient ξ is obtained using the frequency response measurement of the 10.4 μm offset case which shows a Q-factor for the resonance movement of 166. The further input parameters of the simulation are a time interval between 0 s and 0.2 s for which the ODEs are to be solved and a frequency sweep of the excitation frequency between 6120 Hz and 5920 Hz in 5 Hz steps. As voltage amplitude for the excitation signal a value of V_0 = 56 V is chosen, as the effective voltage at the AVC actuator is reduced in respect to the amplifier output voltage of 80 V in the measurements due to a voltage drop at the 10 kΩ series resistor and a parasitic resistance in the connection lines.

The resulting frequency response curves in Fig. 3.20(a) show a highest frequency response for the maximum comb-offset case of 10.4 μm with a simulated maximum

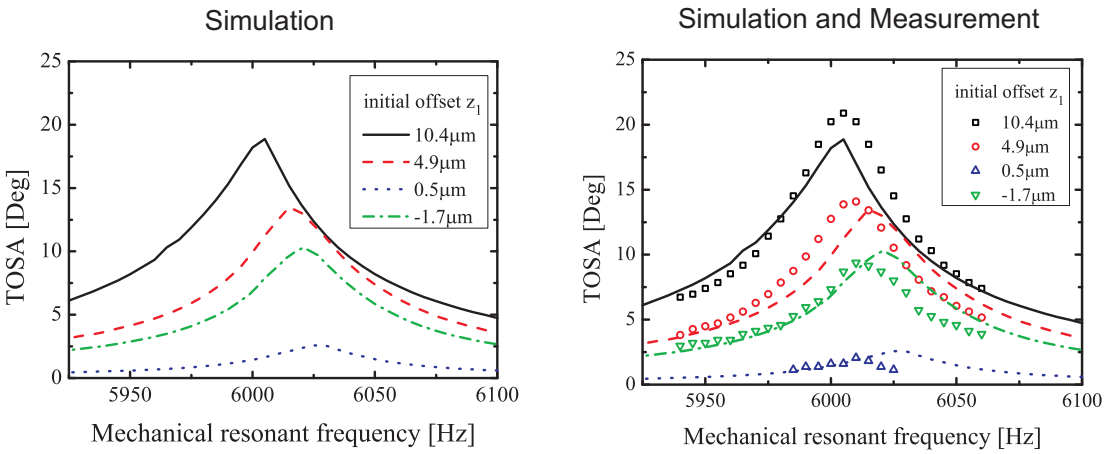

Figure 3.20: (a) Simulated frequency response curves for the 4 chosen AVC offsets with actuation of V_0 = 56 V and (b) overlap of measured and simulated frequency response curves.

TOSA of 18.9° at a resonance frequency of 6005 Hz. The lower offset cases of 4.9 μm and −1.7 μm show a frequency shift of 15 Hz and 20 Hz, respectively, to higher peak resonance frequencies with a reduced angular response of 13.5° and 10.2° respectively. The frequency response results of the closest in-plane configuration show within the chosen simulation cases a lowest angular deflection with a maximum TOSA of 2.6° at a resonance frequency of 6025 Hz. The overlap between the simulation results and the measurements is shown in Fig. 3.20(b), presenting a good agreement between both. Both trends of lower resonant scan angles and higher peak resonance frequencies for lower comb offsets are shown in the simulated and measured results. All four simulated frequency response curves show a symmetric behaviour, with the 10.4 μm case starting to show a tendency towards bending of the frequency response curve through the electrostatic induced nonlinearities. The frequency shift between the limiting resonance frequency of 5990 Hz and the respective resonance peaks is overestimated by about 10 Hz for the 4.9 μm, 0.5 μm and −1.7 μm cases for the simulation in respect to the measured behaviour.

Reasons for this slight deviation in the frequency and angular response can originate from the assumptions made for the simulation. The movement between the inner mirror and frame structure is assumed stiff to reduce the number of required ODEs to solve

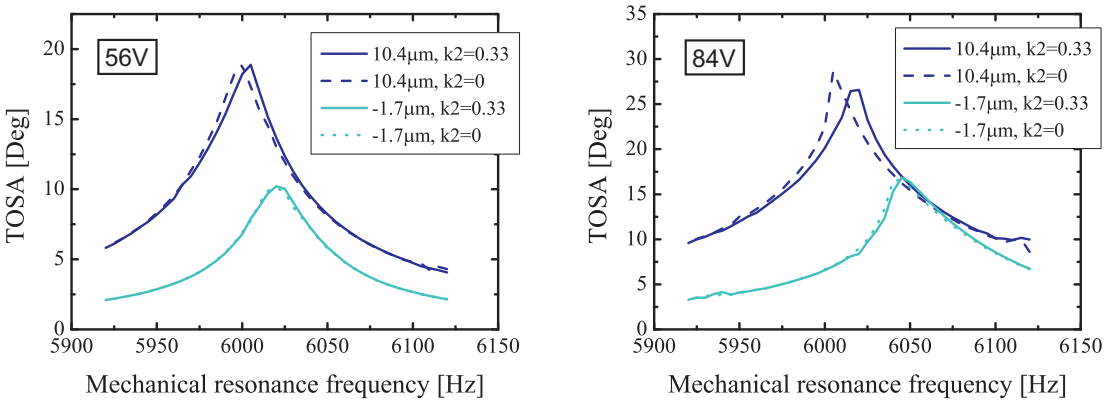

Figure 3.21: Simulated frequency response curves for 56 V and 84 V actuation with and without the influence of the nonlinear spring constant k_2.

for. This assumption was also used as no direct measurement of the individual damping factors for the moving frame and inner mirror are available and a coupled ODE system considering both structures independently would require these individual damping factors. Additionally only the average vertical offset value of the comb-drives are used for calculating the capacitance distribution, which is especially for the mechanical AVC offset changes a very approximate assumption as line scan profiles of the comb-drives shown earlier in this chapter prove. Nevertheless, the overlap between the simulated and measured behaviour is in good agreement, justifying the choice of assumptions and the chosen simulation model.

3.6.3 Model results with and without mechanical nonlinearities

The simulation model used in the previous section utilises a cubic nonlinear spring constant of $k_2 = 0.33$ for its solution. This factor was included in an attempt to map the measurement results for 80 V and 120 V actuation, as these show symmetric frequency response curves with no visible onset of nonlinearities. The value for k_2 was estimated using an adaptive step by step approach with the symmetry of the frequency response curve for $V_0 = 84$ V at the maximum offset of $z_1 = 10.4\,\mu$m as quality factor. To show the influence of the resulting nonlinear factor, Fig. 3.21 displays the frequency response curves for the maximum initial and negative comb-offsets with an actuation of 56 V

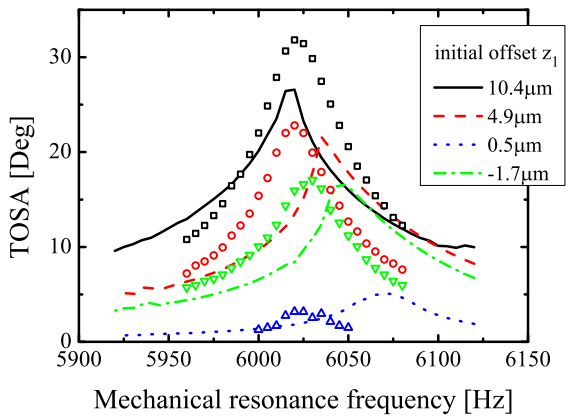

Figure 3.22: Comparison of simulated and measured frequency response curves for 120 V actuation case.

and 84 V, with and without including k_2. For the lower actuation voltage both the results with and without inclusion of the nonlinear spring constant show a symmetric frequency response curve with the positive k_2 value shifting the top of the curve to higher frequencies. At a simulation voltage of 84 V the behaviour without the nonlinear spring constant factor at the maximum initial comb-offset shows a jump discontinuity from the maximum TOSA at resonance to the angular response at a lower actuation frequency. This jump originates from the electrostatic actuation which introduces a nonlinear behaviour at higher electrical field strength. With inclusion of the k_2 factor this nonlinear response is balanced to avoid any jump discontinuity in the simulated frequency response curve.

The frequency response curves of a simulation actuation voltage of 84 V, corresponding to an applied voltage of 120 V in the measurements due to the already mentioned losses in a series resistor in the measurement setup, shows some of the limits of the current simulation tool for the scanning micromirror discussed in this chapter. Fig. 3.22 shows the overlap between the measured and simulated frequency response curves for this actuation for the four chosen offset cases described earlier. The simulation result of the z_1 = 10.4 μm offset underestimates the maximum TOSA value by 17%, or 5.2°, while the further offsets are showing a closer match of the measured and simulated

maximum TOSA values. The other three offset cases all show an overestimation in the frequency shift of the simulation with the simulated and measured resonance points deviating by as much as 45 Hz. The offset cases of 4.9 μm and $-1.7\,\mu$m additionally show a tilt of their frequency response curves at resonance towards lower frequencies, which is caused by the influence of the electrostatic induced nonlinearity.

This shows the limitation of the current simulation model for the here discussed mirror structure, as the different nonlinear effects in the outer and inner torsion springs seem to be not sufficiently covered at higher angles by the assumption of a single equivalent torsion spring. At the higher angular responses present for the 84 V actuation the damping effects for the frame and mirror may also differ from the assumed single value description, possibly contributing to the mismatch. Nevertheless the overall trend of a lower angular response for a reduced initial comb-offset is still captured using the simulation tool with all its assumptions defined earlier.

3.7 Discussion

The measurements and experimental investigations presented in this chapter show for all used actuation cases a general trend of higher achievable TOSA values for higher initial vertical offsets of the AVC actuator. The continuously variable offset changes introduced by the thermal actuator and the mechanical displacement allowed in this case the offset investigation on a single device to avoid changes introduced by fabrication variations between devices or other experimental variations. The highest actuation results are in this investigation seen for offset square-wave actuation signals with actuation frequencies matching the mechanical movement frequencies.

The simulation model adapted from the previous chapter shows a good agreement to the measurement results for lower actuation voltages, with both the variation in TOSAs and the frequency shifts seen in the measurements also visible in the simulation results. For higher actuation voltages, and therefore higher angular response of the

scanning micromirror, the overlap between measured and simulated frequency response results degrades. The general trends of the influence of the initial AVC offset are still present, but the simulation results tend to include a higher nonlinear behaviour then shown by the experiments. Possible reasons for this degradation in the simulation fit were mentioned in this chapter and are based on the assumptions taken to construct the simulation model. A simplification of the device by assuming a rigid connection between the frame and mirror surface of the used design allows the analytical description with a single damping coefficient which can be obtained through measurements. The more accurate description of the device through a coupled system of differential equations for the mirror and frame would require knowledge of the individual damping coefficients for both the mirror and the frame structure, which is not experimentally accessible. A theoretical investigation in such a matter has, to the knowledge of the author, not been undertaken either so far. Therefore a use of a coupled ODE system for the analytical description of the used devices was not followed but could be a point for future work to gain a more accurate description and better overlap between measurement and simulation results at higher actuation voltages.

Despite these limitations both the experimental and simulated results have shown an improved mirror angular response for higher AVC initial offsets, where the maximum investigated offset was limited by the fabrication process.

4 MEMS Q-switched solid-state laser

The application of MEMS devices in laser systems has recently seen some increased research interest with MEMS as intra-cavity elements for spectral and temporal control of lasers, which was reviewed in chapter 1.3.3. The temporal control is achieved by changing the quality (Q) of a laser cavity, which is related to the losses inside the cavity, between a high and low value. The spectral control as well as mode-locking, a special case of temporal control, are not considered in this thesis and will not be discussed further. The aim of the discussed Q-switching temporal control through MEMS is to achieve fast switching times to compete with currently mainly used crystal modulators using the electro-optic or acousto-optic effect. In this chapter the theoretical background for generating a pulsed laser output by using a MEMS scanning micromirror as intra-cavity active device of a solid-state laser will be presented, as well as the experimental procedure and results. The use of a solid-state laser instead of a fibre laser (which was used in most of the recently published work on this topic [151–155]) was chosen to aim for highest possible pulse energies instead of shortest pulse durations, with solid-state gain media offering easy access to high average output power in the multi Watt regime.

In section 4.1 and 4.2, the theoretical background of solid-state lasers and especially their Q-switch behaviour is reviewed, as this will be used in section 4.3 for building up an analytical model of the laser output behaviour. Next the MEMS scanning micromirrors are introduced in section 4.4, including their experimental characterisation with a

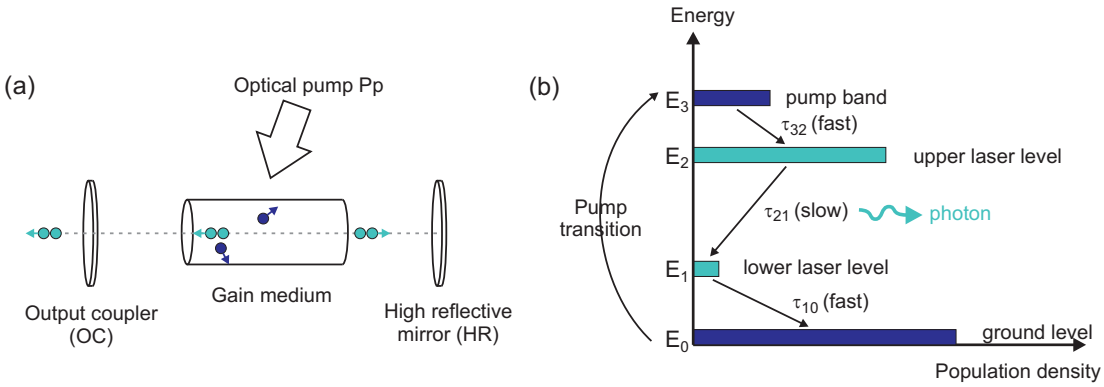

Figure 4.1: (a) Basic laser schematic with pump, gain medium and laser resonator, (b) energy diagram for 4-level laser system including energy state lifetimes.

special consideration of high reflective (HR) dielectric coatings and their influence on the mirror structure discussed in section 4.5. Section 4.6 will show the theoretical and experimental investigation of a 2-mirror laser cavity using the described intra-cavity MEMS micromirror as cavity end-mirror. Section 4.7 extends the investigation to a 3-mirror cavity including the use of a dielectric coated micromirror. A following discussion and conclusions will be presented at the end of the chapter.

4.1 Solid-state laser background

The definition of a solid-state laser used here requires the laser to have a gain medium with a crystalline or glass substrate, external resonator mirrors which create the laser cavity and optical pumping through flashlamps or diodes (see Fig. 4.1(a)). Microchip laser, which have also a solid gain medium, are not considered here as their resonator end mirrors are in general the coated surfaces of the gain chip. Common gain media used for solid-state lasers are neodymium (Nd) or erbium (Er) doped glass rods or YAG (ytterbium-aluminium-garnet), YLF (yttrium-lithium-fluoride) or Vanadate crystals, all with a fundamental output in the near infrared. Additional to these, one of the most widely used solid-state laser crystals is Ti:sapphire with applications as ultra-fast laser gain medium and in optical parametric oscillators [165, 166].

In the following sections the background for the specific case of a Nd:YAG gain medium is discussed as this is used for the experimental investigations. The description of the relevant theoretical background for an analytical model of the laser Q-switching will focus on the rate equation model of the laser system and the description of the laser cavity using geometrical optics for the spatial cavity analysis. Additional detailed background information on laser systems can be found for example in the textbooks by Svelto [167] and Koechner [168], both giving a very detailed description.

4.1.1 Rate equations

A set of coupled rate equations can be used to describe the temporal dynamics within the laser cavity, based on several generally used approximations [168]: the longitudinal and radial variations within the laser medium are ignored and only one electromagnetic (em) field cavity mode is present. Additionally the decay times of the laser gain medium energy levels (see Fig. 4.1(b)) of the pump band τ_{32} and the lower laser level τ_{10} are assumed to be very fast, leading to the approximation of $N_3 \cong N_1 \cong 0$ for the population of the pump level N_3 and lower laser level N_1. The necessary population inversion N for laser actuation is therefore simplified to $N = N_2 - N_1 = N_2$, which is the population of the upper laser level. The population is further on described as population density n [cm^{-3}] and the coupled rate equations of the laser actuation can be described with the following two equations [168]:

$$\frac{\mathrm{d}n}{\mathrm{d}t} = W_p(n_{total} - n) - n\,\sigma\,\phi\,c - \frac{n}{\tau_f} \tag{4.1}$$

$$\frac{\mathrm{d}\phi}{\mathrm{d}t} = \frac{V_a'}{V'}\,n\,\sigma\,\phi\,c - \frac{\phi}{\tau_c} \tag{4.2}$$

The temporal change of the population inversion density in equation (4.1) consists of three parts. Part one is an increase of the population inversion density by pumping, where W_p [s^{-1}] is the pump rate and n_{total} [cm^{-3}] is the overall population density. Part two is a reduction due to stimulated emission, where σ [m^2] is the stimulated

emission cross section, ϕ [m^{-3}] is the photon density in the cavity and c [$m\,s^{-1}$] is the speed of light in the medium. The final part of (4.1) describes a further reduction due to spontaneous emission, where τ_f is the fluorescent lifetime of the upper laser level. The rate equation for the photon density ϕ consists itself of two parts, with an increase in photon density due to stimulated emission and a decrease due to losses within the cavity. V_a' [m^3] is in this case the mode volume in the active medium and V' [m^3] the mode volume in the overall cavity with τ_c [s] being the photon cavity life-time. The inclusion of the factor V_a'/V' notices the fact that the photon density is defined over the whole resonator while stimulated emission only occurs within the active medium. As the initial approximation of ignoring any radial or transversal variations within the cavity was used we can replace V_a/V with the ratio of the length of the active medium l_a and the length of the cavity l_c, which modifies equation (4.2) to

$$\frac{\mathrm{d}\phi}{\mathrm{d}t} = \frac{l_a}{l_c}\, n\, \sigma\, \phi\, c - \frac{\phi}{\tau_c}. \tag{4.3}$$

By using the rate equations several dynamic characteristics of solid-state laser systems can be found, including the threshold condition or the average and peak power of the laser output. The rate equations will be used in a later part of this chapter to obtain a theoretical model for the temporal behaviour of the laser during Q-switching.

4.1.2 Laser resonator

To obtain a stable laser output, the em field in the laser cavity needs to replicate itself upon multiple reflections on the resonator mirrors. The cavity mirrors have to exhibit a curvature matching the wavefront of the propagating laser beam at the respective point in the resonator to gain a stable cavity and to support the back and forth propagation of Gaussian beams, which are a description of the solution of the em-field in the laser cavity. As Gaussian beams have a spherical wavefront at a sufficient large distance from the beam waist, the mirror surface needs to be spherical as well. The radius of

curvature (ROC) of the wavefront at a distance z' from the beam waist w_0' can be described by [168]:

$$ROC(z') = z'\left[1 + \left(\frac{\pi\, w_0'^2}{\lambda\, z'}\right)^2\right], \tag{4.4}$$

with λ being the wavelength of the propagating em-wave. With the em-distribution of the beam in a laser resonator known one can determine the beam propagation within the cavity and the cavity stability. Both can be derived using the geometrical optics ABCD-matrix formalism which relates the incident and exiting beams of an optical element by using a transfer matrix describing the optical properties of the element, as described in the work by Kogelnik et al. [169]. The incoming and exiting beam are described respectively with their distance from the cavity axis x and the angle θ towards the cavity axis, which leads to

$$\begin{bmatrix} x_{out} \\ \theta_{out} \end{bmatrix} = \begin{bmatrix} A & B \\ C & D \end{bmatrix} \cdot \begin{bmatrix} x_{in} \\ \theta_{in} \end{bmatrix}. \tag{4.5}$$

For the resonator to be stable the rays after a complete round trip need to be identical to the input rays, which leads to the condition of the determinant of the ABCD-matrix having a unit value. By using Sylvester's theorem of matrix calculus and an expansion to n' cavity round trips it can be shown that the ABCD-matrix needs to satisfy the condition [167]

$$-1 < \left(\frac{A+D}{2}\right) < 1 \tag{4.6}$$

to obtain a stable cavity. For the simplest form of a resonator, a 2-mirror cavity, this condition can be expressed in terms of the cavity length l_c and the ROCs ρ_1' and ρ_2' of the two mirrors. The ABCD-matrix of the system consists in this case of a matrix multiplication of the respective ABCD matrices of a reflection on a curved surface with ROC ρ_1', a free-space propagation over the length l_c, a reflection on a curved surface with ROC ρ_2' and a further free-space propagation over the length l_c. This leads with

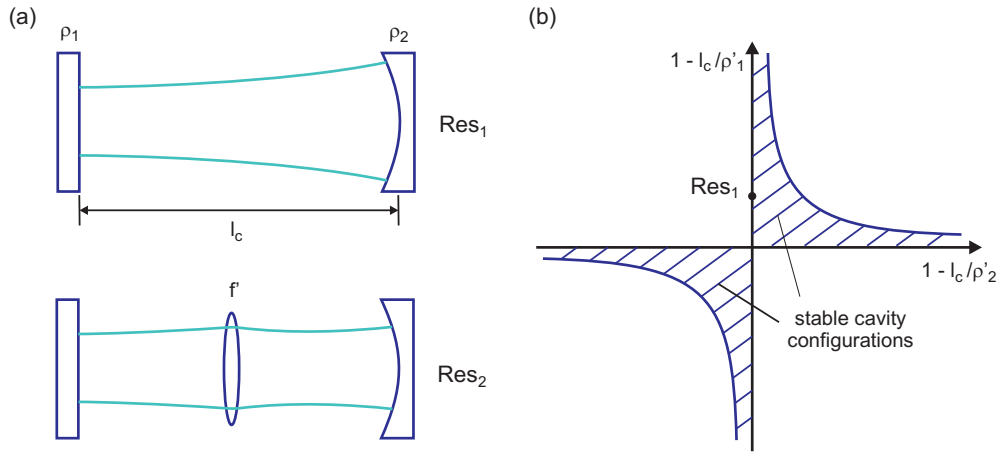

Figure 4.2: (a) Schematic of plane-concave resonator Res_1 and resonator including a thermal lens Res_2, (b) resonator stability diagram for 2 mirror cavities.

equation (4.6) to the stability condition:

$$0 < \left(1 - \frac{l_c}{\rho_1'}\right) \cdot \left(1 - \frac{l_c}{\rho_2'}\right) < 1 \tag{4.7}$$

With using both factors in this equation as parameters for a two dimensional stability diagram, it can be shown that the stable cavity configurations for a 2-mirror resonator will lie within the marked part of the diagram shown in Fig. 4.2(b). For the simple plane-concave 2-mirror configuration shown in Fig. 4.2(a) the first factor will be simplified to 1 which leads to a required ROC of mirror 2 between $\rho_2' = l_c$ and $\rho_2' = \infty$. The cavities used later in this chapter have additional optical elements inserted which can be modelled as insertion of thin lenses (as shown in Fig. 4.2(a)). Their stability will be discussed in more detail when the resonators are introduced.

Laser actuation can be achieved when the gain over a resonator round-trip equals or is bigger than the cavity losses. With the losses described as a combination of the mirror reflectivities R_1 and R_2 and the dissipative losses within the absorption coefficient per unit length α this threshold expression can be written as [168]:

$$R_1 \cdot R_2 \cdot \exp\left(2\, l_a\, (g - \alpha)\right) = 1 \tag{4.8}$$

where g is the gain coefficient per unit length of the active medium with length l_a. Within the rate equation description of the laser process the losses have been described with the photon cavity lifetime τ_c, which is the ratio of the cavity round-trip time t_r and the power loss per round-trip γ [168]:

$$\tau_c = \frac{t_r}{\gamma} \tag{4.9}$$

When rewriting equation (4.8) as

$$2\,g\,l_a = -\ln\left(R_1 R_2\right) + 2\,\alpha\,l_a \tag{4.10}$$

one can see that the right-hand side equals the losses γ in the cavity during a round-trip which leads to an expression for the photon cavity lifetime in the form of

$$\tau_c = \frac{2\,l_c}{c}\left(-\ln\left(R_1 R_2\right) + L\right)^{-1}. \tag{4.11}$$

The round-trip time has been expressed using the cavity length l_c and the speed of light c, and the absorption coefficient has been expressed using the optical round-trip losses L within the resonator.

Both the rate equation description and the theory for the spatial laser beam description inside the resonator will be used in section 4.3.

4.2 Q-switching of solid-state laser

Q-switching is a technique to generate pulsed laser output with high energy short pulses by means of rapidly changing the quality of the laser cavity. The quality of the cavity is defined as the ratio of the stored energy in the resonator to the energy losses per round-trip [168]. By therefore modulating the losses in the cavity a change of the Q-factor can be achieved. This change has to occur in a short time scale, preferably in the

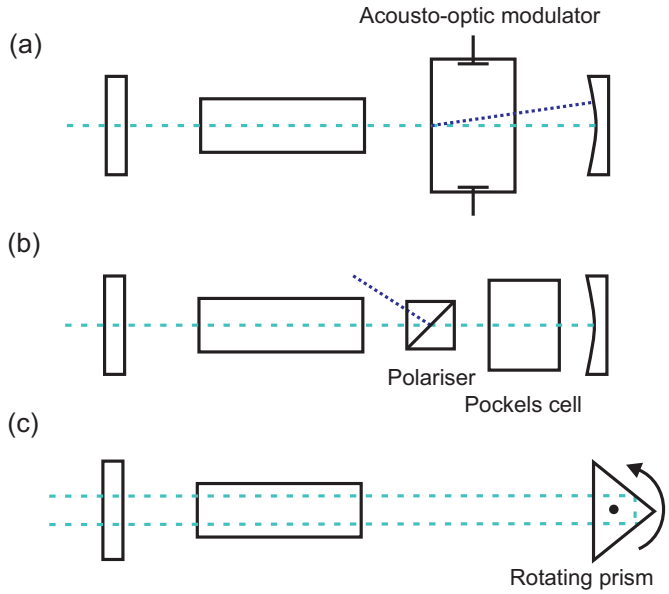

Figure 4.3: Commonly used Q-switch elements: (a) acousto-optic modulator changing the beampath through the resonator with acoustic waves in the modulator, (b) electro-optic modulator changing the beampath of polarised light, (c) rotating prism with circular cavity and two simultaneous output spots.

nanosecond range, to enable the creation of pulses with peak powers several order of magnitudes higher than the possible output for continuous laser operation. For active Q-switching a change of the losses of the cavity translates to a misalignment of the cavity. Common techniques for achieving this are shown in Fig. 4.3.

Using an acousto-optic modulator (AOM) as active Q-switch (see Fig. 4.3(a)) makes use of the diffraction encountered by an em-wave when an acoustic wave is present in the modulator. The acoustic wave will create a periodic refractive index change which creates the diffraction and changes the beam path, therefore switching the cavity to a low Q state. During this state the optical pumping of the gain medium builds up a high population inversion level. When switching the AOM off the cavity returns to its previous alignment, which is equal to a high Q state, and will therefore resume laser operation in form of a pulse. Switching times of the AOM are generally fast, in the order of several nano-seconds.

For faster modulation speeds, electro-optic modulators (EOM) in the form of a Pock-

els cell (see Fig. 4.3(b)) can be used to create Q-switched or mode-locked pulsed outputs. The Pockels cell changes the polarisation of the passing em-wave due to an induced birefringence in an optical medium by an applied electric field. When using an additional polariser in the cavity only one polarisation state exhibits low losses and therefore a high Q in the cavity. When applying an electrical signal to the modulator, it will rotate the incoming polarised light, which therefore will exhibit only a part transmission on the next polariser pass and therefore a low Q.

A third method for Q-switching lasers is a mechanical Q-switch in the form of a rotating prism or mirror (see Fig. 4.3(c)). In this case, the tilt of the prism or mirror will increase the losses of the cavity and set it to a low Q. The rotation usually takes place at a constant angular speed in a single direction, which allows a low Q during most of the rotation period and a high Q only during the pass through alignment. The use of a prism reflector instead of a mirror will reduce alignment requirements as an incoming beam will be reflected back in the same direction over a range of angles. This also leads to the build-up of a ring cavity as two discrete points on the output coupler will reflect the intra-cavity beam back to the prism (see Fig. 4.3(c)).

For an ideal fast Q-switch the change between low and high Q in the cavity is considered to occur instantaneously (see Fig. 4.4(a)). This can be assumed for EOM and AOM Q-switching. In this case a pulse starts to build up from noise when the quality is switched to a high state, with the photon density rising exponentially. The maximum of the emitted pulse is not reached until a delay time t_d during which the photon density build-up occurs. The initial population inversion density n_i is above the threshold density n_t and monotonously decreasing to a level of n_f after the pulse, which is below the threshold population density for cw laser output. In this and all other relevant Q-switch cases the time evaluation of the pulse is short enough so that both the effects of pumping and spontaneous emission, which are present in the general rate equations (4.1) and (4.3), can be neglected as their time constants are considerably longer than the Q-switching time.

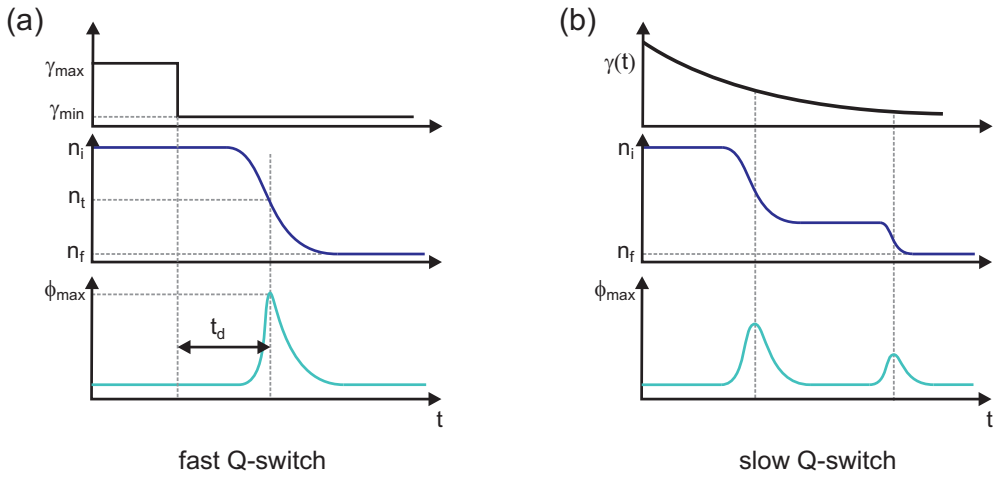

Figure 4.4: Loss γ, population density n and photon density ϕ for the Q-switch cases of (a) fast Q-switching and (b) slow Q-switching.

In the case of slow Q-switching the change of losses in the cavity is not occurring instantaneously but has a time dependent component. This is present for rotating mirror or rotating prism Q-switches, where the end-reflector rotates unidirectionally and moves through the cavity alignment position. This case will also be applicable for the micromirror Q-switch developed in this thesis. In this case the loss curve follows a shape similar to the one shown in Fig. 4.4(b). The build-up of a pulse starts when the gain, which is related to the population inversion density, in the cavity equals the decreasing loss function $\gamma(t)$. After a delay-time, similar to the fast Q-switch case, the pulse reaches its maximum when the gain drops to the instantaneous loss value due to saturation. If the gain is high enough so that the gain-loss equality occurs at a relatively high loss, it can occur that the population inversion and therefore the gain after the first pulse will be high enough to equal the instantaneous losses a second time and a second pulse can be emitted. The second pulse has a lower energy due to a lower initial population inversion density. If the loss change is fast and the pulse build-up time is therefore longer than the time needed for the loss function to rise again, a pulse will be emitted after the minimum loss point was reached. The pulse energy in this case is relatively low as the maximum of the pulse will be emitted at a time when again higher losses are present in the cavity. To achieve optimum switching in the case of a

slow Q-switch, the maximum of the pulse needs to be emitted at the point of lowest losses. This means the instantaneous losses need to equal the gain in the cavity at a time point before the lowest losses, which is equal to the pulse delay time t_d.

The MEMS scanning micromirrors used in this work as active Q-switches are similar to rotating mirror Q-switches and fall in the slow Q-switch category. The difference to a rotating mirror, apart from size, driving principle, fabrication and material properties, is a bidirectional movement of the mirror through the alignment position. This will not change the general temporal progression discussed above but a difference in the spatial distribution will have to be taken into account, which will be discussed later in this chapter. General requirements for MEMS micromirrors as Q-switch elements are movement speeds, which are fast enough to avoid multiple pulsing and enable short pulse durations, a mirror surface that shows a flat enough curvature to build-up a stable short cavity, coatings that have a reflectivity high enough to allow lasing and a movement stability that reproducibly moves the mirror surface through the cavity alignment point. These range of factors are considered in detail in section 4.4 and following.

4.3 Theoretical model for Q-switching with MEMS scanning mirrors

The theoretical laser model developed in this section is based on similar models developed for rotating prism Q-switch actuation [170,171]. However, in the presented work a novel approach using the bidirectional movement of the scanning mirror and the associated non-constant angular velocity through the alignment is required rather than using the constant angular velocity and unidirectional movement from the previous models.

The schematic for a scanning mirror Q-switched laser can be seen in Fig. 4.5 where the mirror scans through the cavity alignment position, which coincides with the mirror rest position at $\theta = 0\,\text{mrad}$. To obtain an insight in the behaviour of a solid-state

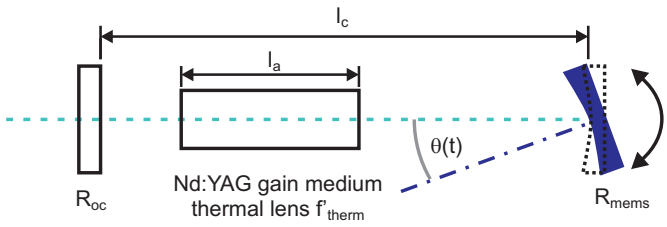

Figure 4.5: Schematic cavity layout for MEMS scanning mirror Q-switching including parameters used for the theoretical model.

laser Q-switched by a MEMS scanning micromirror a theoretical model for the time dependent behaviour of the laser output and the related spatial distribution is developed. The model discussed here is based on the coupled rate equation system of the population inversion density and the photon density (see section 4.1.1). Similar models were developed for rotating mirror Q-switched lasers [170,172] where the unidirectional constant rotation of the mirror was considered in the rate equations using a varying loss function. For the bidirectional rotation with varying angular speed occurring with the scanning mirror, a similar approach will be taken. This will give an estimation of the pulse timing and temporal build-up of the pulse. The time dependent behaviour will be used to estimate the spatial output of the MEMS Q-switched laser by using an ABCD matrix calculation model, which has the occurring pulse timing as input. The evaluation of the output behaviour in a full em field simulation, as for example performed in [173] for a rotating mirror Q-switch, is in a first approximation not essential and not considered in this case, but could be of interest for a future approach looking at the spatial intra-cavity field distribution during the pulse development.

4.3.1 Temporal model for MEMS scanning mirror Q-switching

The basis for the temporal simulation model has already been discussed in section 4.1.1 with the general description of the rate equations. Certain further approximations can be made to apply them for the description of Q-switching. The time duration for the whole Q-switch pulse description is considered a lot faster than the timings for optical pumping and spontaneous emission so that the two corresponding terms in equation

(4.1) can be neglected. This leaves the two coupled rate equations from (4.1) and (4.3) in the form:

$$\frac{\mathrm{d}n}{\mathrm{d}t} = -n\,\sigma\,\phi\,c \tag{4.12}$$

$$\frac{\mathrm{d}\phi}{\mathrm{d}t} = \phi\left(\frac{l_a}{l_c}\,n\,\sigma\;c - \frac{\gamma(t)}{t_r}\right) \tag{4.13}$$

The cavity decay time τ_c was in this case replaced by the ratio between the losses per round-trip $\gamma(t)$ and the cavity round-trip time t_r as $\tau_c = t_r/\gamma(t)$.

As the MEMS Q-switch is considered a slow Q-switch, the cavity losses will not take the form of a step function but will be an explicit function of time in the form of [168]:

$$\gamma(t) = \ln\left(\frac{1}{R_{oc}}\right) + \gamma_0 + \gamma_1(t) \tag{4.14}$$

where R_{oc} is the reflectivity of the output coupler (OC), γ_0 includes the intrinsic optical losses at perfect alignment of the scanning micromirror, also including the reflectivity R_{mems} of the MEMS micromirror, and $\gamma_1(t)$ represents the time dependent losses due to the rotation of the mirror through the alignment throughout the laser pulse development. This time dependent loss factor has been assumed in previous publications arbitrarily as a cosine-function [168, 172] or as a linear fit to measured values around the midpoint [170]. In the model presented here, it will be described in the form of a cosine-function based on a fit to the angular dependent losses obtained from a Caird-analysis [174] for a 3-mirror cavity set-up. This fit does not directly depend on the time evaluation but on the mechanical scan angle $\theta(t)$ of the MEMS mirror and takes the form

$$\gamma_1(t) = 1 + \cos\left(A' \cdot \theta(t) + \pi\right) \tag{4.15}$$

where A' is a fitting parameter. The time dependent scan angle of the mirror also takes the form of a cosine-function as

$$\theta(t) = \cos\left(2\pi f \cdot t\right) \tag{4.16}$$

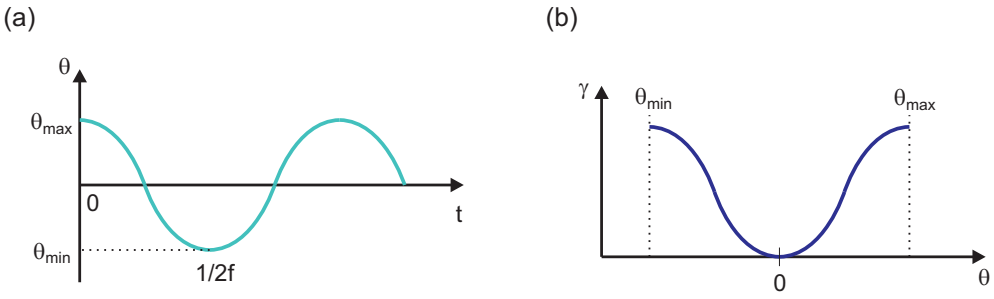

Figure 4.6: Exemplar description of (a) MEMS angular position over time and (b) loss variation over mirror angle.

with the time origin being defined at the maximum angular deflection point of the mirror (see Fig. 4.6(a)) and f being the mechanical movement frequency of the scanning mirror. An example for both the loss variation over the scan angle and the mirror angular timing can be seen in Fig. 4.6.

With the losses as additional time dependent factor in the rate equation system of (4.12) and (4.13), this ordinary differential equation (ODE) system will be solved numerically using a Runge-Kutta method implemented in the Matlab function "ODE45". For this numerical approach it is necessary to define the boundary conditions for the initial photon density ϕ_0 and the initial population inversion density n_0. As the laser output is off before the Q-switch build-up, $\phi_0 = 1$ can be assumed, which represents the noise from which the pulse will build-up. The initial population inversion density can be calculated using the critical inversion density n_{ic} at threshold, with the Q-switch open and operation in cw mode, and the ratio between the pump power P_p and the pump power at the laser threshold for cw output P_{pc}. With the pump power being proportional to the pump rate this ratio can be expressed for the initial population inversion density n_0 as [167]

$$n_0 = \frac{P_p}{P_{pc}} \cdot n_{ic} \tag{4.17}$$

with n_{ic} being defined as

$$n_{ic} = \frac{-\ln R_{oc} + \gamma_0}{\sigma\, l_a}. \tag{4.18}$$

With the parameters for the boundary system and the rate equations defined, the

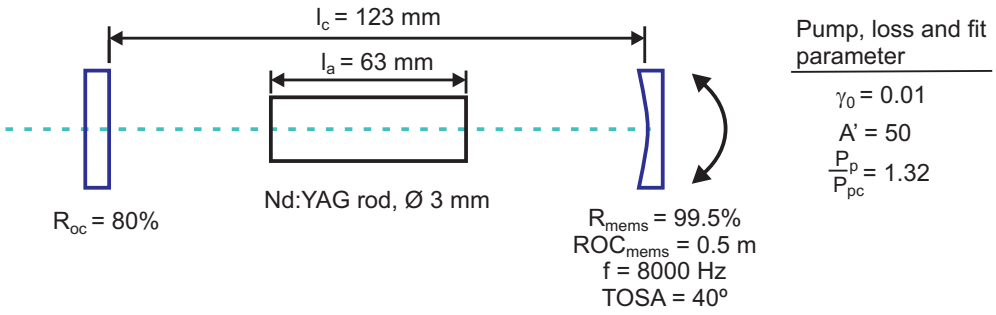

Figure 4.7: Schematic of example laser cavity used for the simulation description.

Matlab code (shown in Appendix B) will output the time development of the inversion density and the photon density in the cavity. Using the parameters of the cavity described in Fig. 4.7, a simulation output as seen in Fig. 4.8(b) will be achieved. The relevant parameters used are an overall cavity length $l_c = 123\,\text{mm}$ with a length of the Nd:YAG gain medium of $l_a = 63\,\text{mm}$, a MEMS total optical scan angle of $TOSA = 40°$ at a mechanical movement frequency of $f = 8\,\text{kHz}$, intrinsic optical cavity round-trip losses of $\gamma_0 = 0.01$, a fitting parameter $A' = 50$ for the time dependent losses and a power ratio of $\frac{P_p}{P_{pc}} = 1.32$. Using these parameters the time dependent cavity losses $\gamma(t)$ take the form displayed in Fig. 4.8(a). The time origin of this figure was formatted after solving the ODE system to coincide with the zero crossing of the moving mirror, which is the point of lowest losses during the Q-switch pulse cycle. The output laser pulse is shown to occur after the crossing of the mirror through the midpoint alignment, with a maximum of the intra-cavity photon density ϕ occurring at a delay of 492 ns after the midpoint alignment. The full width half maximum (FWHM) pulse width is $\tau = 77\,\text{ns}$. The population inversion will drop from an initial value of $9 \cdot 10^{22}\,\text{m}^{-3}$ to a final value of $6.4 \cdot 10^{22}\,\text{m}^{-3}$. After the pulse this level will increase to the initial value again due to constant pumping of the gain medium.

To show the influence of some changeable parameters of the example laser cavity, the rate equation system was simulated for changing OC reflectivities R_{oc} (see Fig. 4.9(a)), varying initial losses γ_0 which can be caused by varying the MEMS mirror reflectivity R_{mems} (see Fig. 4.9(b)), and varying pump power P_p (see Fig. 4.9(c)). In each case all

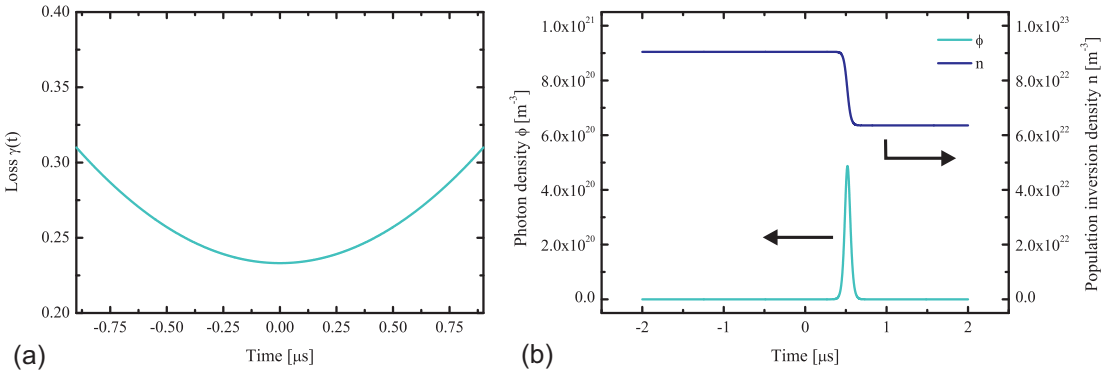

Figure 4.8: (a) Time dependent cavity losses used for the example and (b) simulation outputs of the inversion density and the photon density showing a pulse delay of $\approx 0.5\,\mu$s.

other parameters described in the previous paragraph were kept constant. It can be seen that a reduction of the OC reflectivity from the originally used value of 80 % will lead to a reduced pulse duration and also to a reduction in the pulse delay time. OC values of 85 % and higher will lead to a vanishing output pulse as the pulse delay is high enough so that the pulse would occur while the cavity would not be aligned through the transverse profile of the gain medium. At a reflectivity of roughly $R_{oc} = 71\,\%$, an optimal pulse timing will be achieved with zero delay between the peak of the output pulse and the crossing of the midpoint alignment position. For lower reflectivities, the pulse will be emitted before reaching the midpoint position. The reduction of the delay time can be explained due to the present higher pumping level and therefore higher initial inversion density as the increased losses due to the higher output coupling require a higher pump power to reach the same ratio of pump power to threshold power P_p/P_{th}. A similar effect can be seen for a variation of the initial losses γ_0, where an increase of initial losses lead to a reduction of the pulse duration and pulse delay time. For a variation of the initial losses, a zero delay pulse output can be achieved for the here presented cavity with a value of roughly $\gamma_0 = 0.13$. For a variation of the pump power level, a reduced pulse duration and pulse delay can be achieved with an increase of the ratio of pump power to threshold power P_p/P_{th}. Up to a ratio of 1.35 the pulse duration shows a faster reduction with increased pump power which can be explained

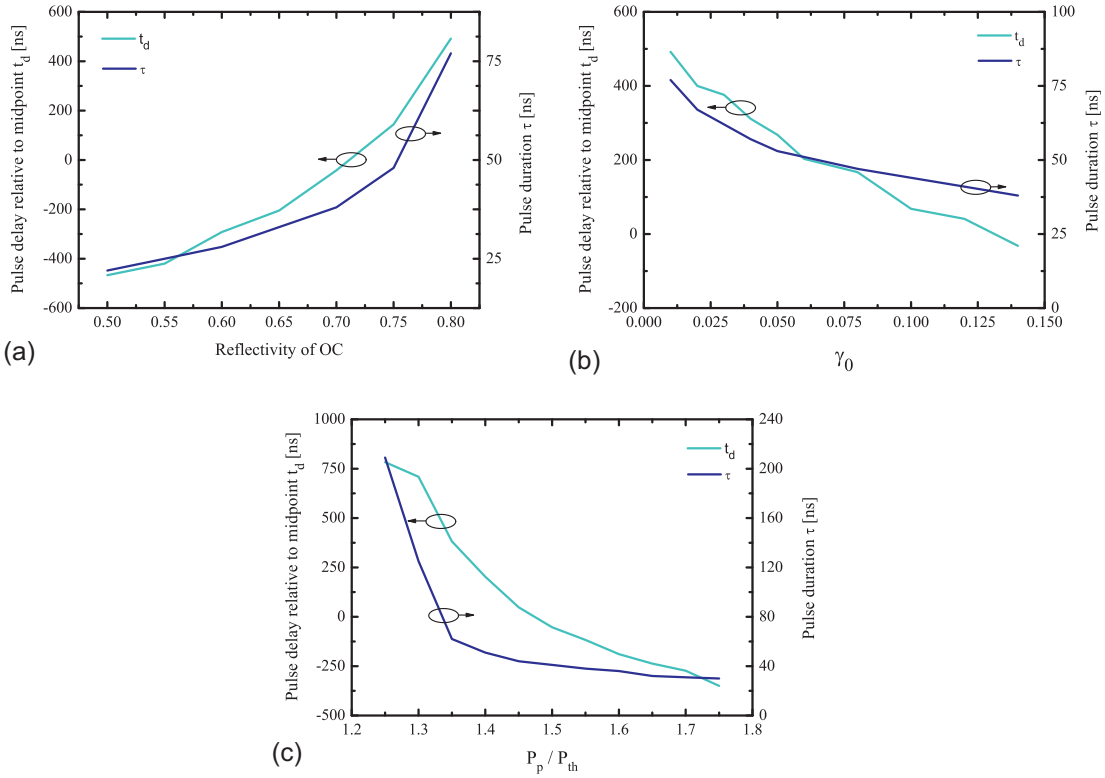

Figure 4.9: Simulated parameter variations of (a) output coupler reflectivity R_{oc}, (b) initial loss γ_0 and (c) pump power ratio $\frac{P_p}{P_{th}}$.

by an operation just above threshold. A zero pulse delay is reached in this case for a pump power ratio of P_p/P_{th} = 1.47.

The simulated temporal behaviour, showing a pulse timing dependent on the initial inversion density, is similar to results obtained by a full em field simulation demonstrated for a rotating mirror Q-switch with constant angular velocity [173]. A positive pulse delay time is also shown for lower inversion densities, equivalent to lower P_p/P_{th} ratios, and is moving to negative pulse delays for higher inversion densities.

4.3.2 Spatial model for MEMS scanning mirror Q-switching

The spatial simulation of the laser output is based on an evaluation of the ray-propagation through the laser cavity using the ABCD matrix formalism, which was already used in chapter 4.1.2 for deriving an expression for the laser cavity stability. For the spa-

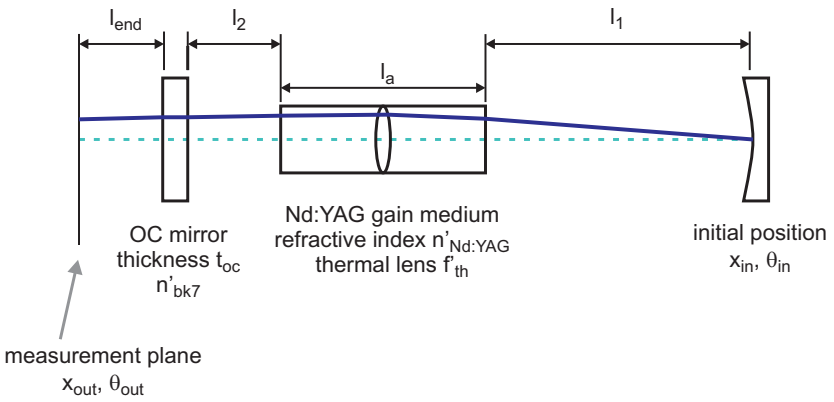

Figure 4.10: Example laser cavity for spatial simulation including characteristic parameters.

tial simulation of the laser output a ray is assumed to leave the MEMS mirror at the transversal position x_{in} with an angle θ_{in} to the cavity centre axis. This angle matches the instantaneous mirror angle at the time when the simulated output pulse from the temporal model has reached its maximum. With the ABCD formalism we can then calculate the transversal position x_{out} and angle θ_{out} at any point through the cavity and after the OC. The relationship between the output and input can be written as in chapter 4.1.2 in the form

$$\begin{bmatrix} x_{out} \\ \theta_{out} \end{bmatrix} = \begin{bmatrix} A & B \\ C & D \end{bmatrix} \cdot \begin{bmatrix} x_{in} \\ \theta_{in} \end{bmatrix} \tag{4.19}$$

with the ABCD matrix defined by the optical system through which the beam is propagating. This matrix can be written as a combination of matrices defining individual optical elements in the propagation path by using matrix multiplications with the order of the multiplications running from the output back to the start point. A list of the used matrices for individual optical elements can be found in table 4.1.

For an exemplar 2-mirror laser cavity, as shown in Fig. 4.10, we can then write for the transversal beam position x_{out} and beam angle θ_{out} at a measurement plane at distance

Table 4.1: *ABCD matrices for individual optical elements [169].*

Element	ABCD-matrix	Describing parameter
Free space propagation	$\begin{bmatrix} 1 & l \\ 0 & 1 \end{bmatrix}$	length l
Refraction at index change	$\begin{bmatrix} 1 & 0 \\ 0 & \frac{n'_{in}}{n'_{out}} \end{bmatrix}$	n'_{in} original and n'_{out} following refractive index
Thin lens	$\begin{bmatrix} 1 & 0 \\ -\frac{1}{f'} & 1 \end{bmatrix}$	focal length f'
Reflection at curved surface	$\begin{bmatrix} 1 & 0 \\ -\frac{2}{ROC} & 1 \end{bmatrix}$	radius of curvature ROC

l_{end} from the OC:

$$\begin{bmatrix} x_{out} \\ \theta_{out} \end{bmatrix} = \begin{bmatrix} 1 & l_{end} \\ 0 & 1 \end{bmatrix} \cdot \begin{bmatrix} 1 & 0 \\ 0 & n'_{bk7} \end{bmatrix} \cdot \begin{bmatrix} 1 & h_{oc} \\ 0 & 1 \end{bmatrix} \cdot \begin{bmatrix} 1 & 0 \\ 0 & \frac{1}{n'_{bk7}} \end{bmatrix} \cdot \begin{bmatrix} 1 & l_2 \\ 0 & 1 \end{bmatrix} \cdot \begin{bmatrix} 1 & 0 \\ 0 & n'_{Nd:YAG} \end{bmatrix} \cdot \begin{bmatrix} 1 & l_a/2 \\ 0 & 1 \end{bmatrix} \cdot \begin{bmatrix} 1 & 0 \\ -1/f'_{th} & 1 \end{bmatrix} \cdot \begin{bmatrix} 1 & l_a/2 \\ 0 & 1 \end{bmatrix} \cdot \begin{bmatrix} 1 & 0 \\ 0 & \frac{1}{n'_{Nd:YAG}} \end{bmatrix} \cdot \begin{bmatrix} 1 & l_1 \\ 0 & 1 \end{bmatrix} \cdot \begin{bmatrix} x_{in} \\ \theta_{in} \end{bmatrix} \tag{4.20}$$

The dielectric layers of the OC mirror have been omitted in this case, as well as the anti-reflection coatings on the laser rod, and the used parameters as defined in Fig. 4.10 are: the axial distance l_1 between the MEMS mirror and the Nd:YAG rod, the length l_a of the gain medium, the axial distance l_2 between the Nd:YAG rod and the OC, the thickness h_{oc} of the OC, the refractive index $n'_{Nd:YAG}$ of the gain medium and n'_{bk7} of the OC and finally the focal length f'_{th} of the thermal lens in the gain medium. This thermal lensing effect is caused by a non-homogeneous radial heat distribution in the laser rod which leads to a variation of the refractive index due to the thermooptic effect [168]. The gradient of refractive index along the transverse profile of the rod will act as a positive lens with the focal power dependent on the heat gradient and therefore also on the optical pump power. As approximation the effect is assumed to be equivalent to a thin lens with equivalent focal length which is located at the axial

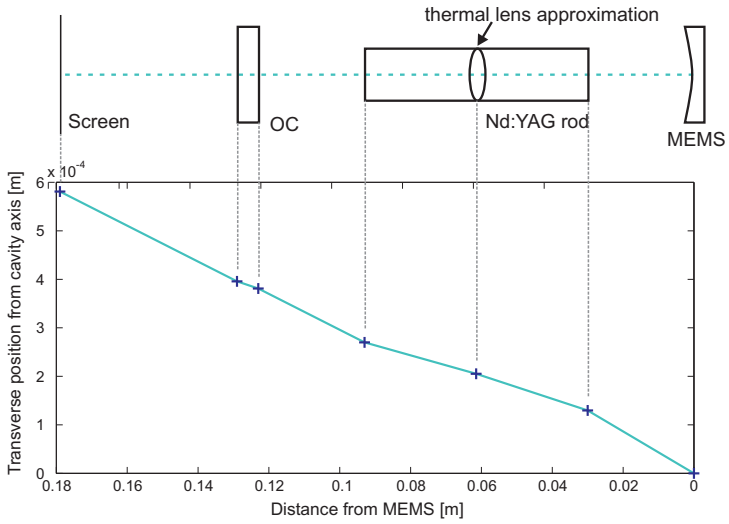

Figure 4.11: Midpoint pulse propagation through the example 2-mirror laser cavity.

midpoint of the gain medium.

For the example used earlier, the temporal behaviour can now be expanded with a spatial description. The pulse delay time of 492 ns leads to a MEMS mirror angle of 4.32 mrad which is set to be the input angle θ_{in}. When assuming that the output beam will originate at the MEMS midpoint with $x_{in} = 0$ the spatial midpoint position at a measurement plane 50 mm from the OC can be calculated as 581 μm. A thermal lens of the gain medium with a focal length of 600 mm is in this case assumed, which is in the range of values present for the experimentally observed driving conditions using an OC with $R = 80\,\%$. As this spatial midpoint offset of the output pulses will apply to both movement directions of the scanning mirror, a dual spot output with midpoint separation of 1.16 mm is expected when the outputs originate from the MEMS mirror midpoint. The overall spatial pulse propagation through the example 2-mirror laser cavity is shown in Fig. 4.11.

Both the temporal and spatial model developed over the last sections will be used in section 4.7.3 to model the experimentally investigated laser behaviour. The presented model shows similar to the later presented experimental data a dual spot output behaviour, originating from the non-optimum pulse delay times in combination with

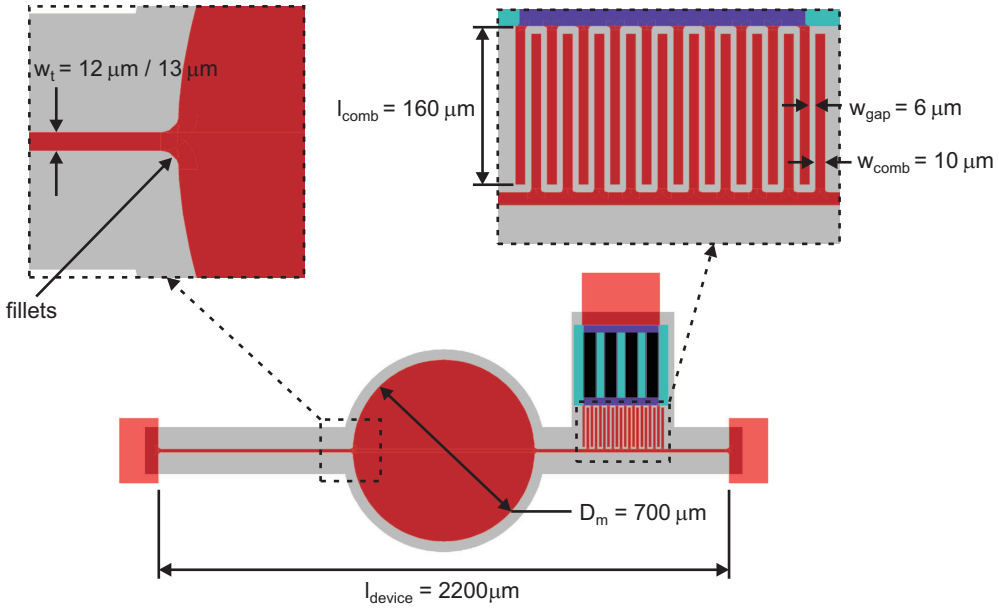

Figure 4.12: Schematic of the scanning mirror design used as Q-switch including filleting at beam connections and an inset of the comb-drive structure.

the bidirectional mirror movement. This behaviour is not observed for other slow Q-switches such as rotating prisms. In the following sections 4.4 and 4.5 the scanning micromirror used for this investigation is introduced together with the necessary HR coatings for the mirror surfaces for the device to be used as intra-cavity laser element.

4.4 MEMS mirror design

The MEMS micromirrors used to obtain Q-switching actuation of a Nd:YAG laser are based on a similar design to the one discussed in chapter 3. An electrostatic comb-drive actuation was chosen to allow high movement speeds through the alignment, which are created by a combination of resonance frequencies in the multiple kilohertz range and total optical mirror scan angles (TOSA) of several tens of degrees. A design overview of the MEMS mirror can be seen in Fig. 4.12. The single side comb-drive consists of 12 pairs of combs with 160 μm length and a width of 10 μm. The use of a comb-drive on only one side was due to design constraints for an array configuration which is discussed in chapter 5. The size of the 700 μm diameter round mirror surface was

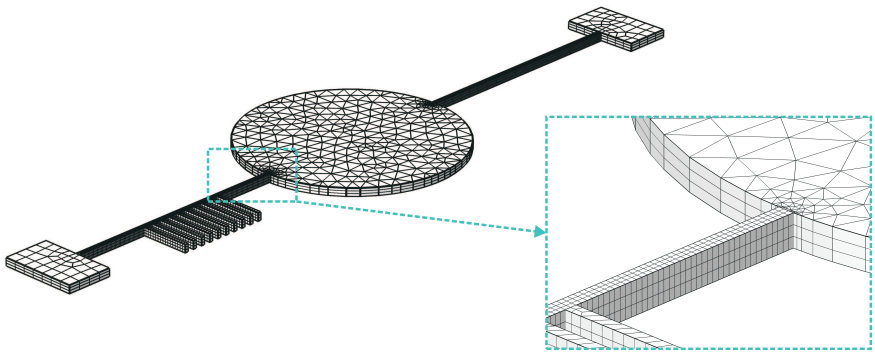

Figure 4.13: Overall mesh and inset with detailed mesh at the torsion beam - mirror connection for the FEM simulation using brick layout for torsion beams and a prism layout for the mirror surface.

chosen to balance the requirement of a mirror size large enough to accommodate the full laser mode and a size small enough to achieve resonant frequencies in the high single digit kilohertz range with scan angles of multiple tens of degrees. The second factor influencing the movement frequencies and angular range is the spring connection, which is made up of two torsion beams with 750 μm of length and a width of 12 μm. The connections to the mirror and the anchor pads are filleted with a radius of 11 μm to avoid increased stress concentrations. As the device was fabricated with MEMSCAP's SOIMUMPs process discussed in chapter 3.2, a choice of 10 μm or 25 μm thickness for the device layer was available, with 25 μm chosen for increased initial flatness of the mirror surface and a reduced surface deformation after coating of the mirror.

The mechanical behaviour of the mirror was simulated using the FEM software COMSOL Multiphysics similar to the calculations used in previous chapters. The simulation aimed to evaluate possible resonant movement modes of the device and the associated eigenfrequencies of these modes. With these FEM simulations the torsion spring width and length were adapted to their final value to try to avoid cross talk between the mirror tilt movement mode and in-plane movement modes (see Fig. 4.14). Cross talk can in this case occur when the in-plane mode frequency is an integer multiple of the tilt mode frequency, or vice versa, as a sub- or super-harmonic excitation can occur, coupling the external actuation energy not only in the tilt resonance movement but

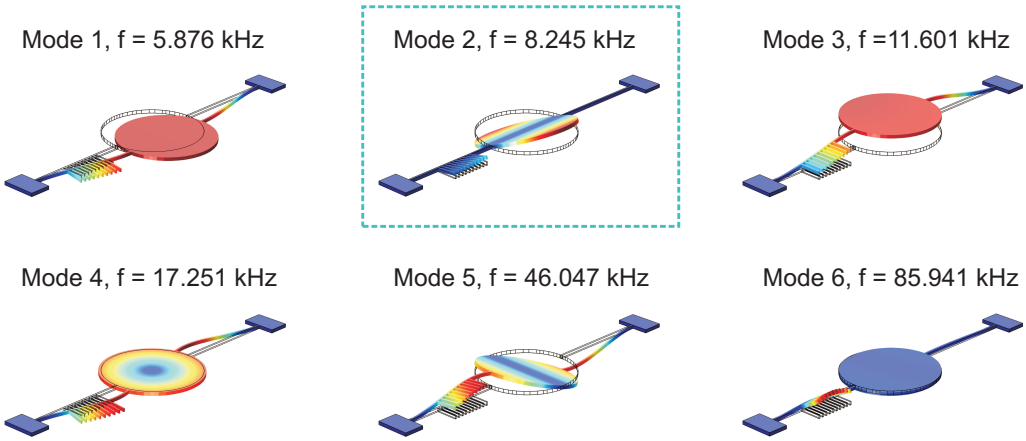

Figure 4.14: FEM simulation results of the first six mirror eigenmodes with their respective resonance frequency (with the used tilt mode highlighted).

also in the in-plane movement. The avoidance of cross talk to the in-plane mode is especially considered, as a parasitic in-plane movement will reduce the lateral gap between the fixed and moving combs of the actuator structure and therefore lead to a pull-in behaviour with sticking of the comb structure and subsequent annihilation of the mirror movement.

The simulation inputs are the device dimensions and anisotropic material properties for the silicon used in the fabrication process, as summarised in table 3.1. The orientation of the fabricated torsion beam connection is along the x-axis of the ⟨100⟩ silicon wafer which requires a 45° in-plane rotation of the model to align the given material properties with the used silicon crystal axis. The solid physics settings of the simulation need to be adjusted to anisotropic material properties and fixed boundary conditions need to be set at the bottom of the anchor pads for the eigenfrequency evaluation. The required meshing of the device for the FEM simulation was split into two parts, a brick type mesh for the combs as well as for the torsion beams and a prism type mesh for the mirror structure, both with three layers through the device thickness. The resulting mesh structure can be seen in Fig. 4.13. An in COMSOL built-in direct MUMPS solver has been used to evaluate the first six resonance movement modes which are shown with their associated eigenfrequencies in Fig. 4.14. The relevant tilt movement mode used

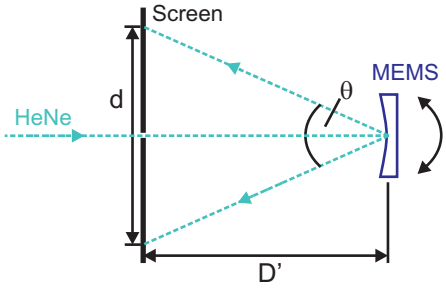

Figure 4.15: Schematic to determine the TOSA θ from a displacement of a HeNe guidance beam on a screen.

in this chapter is highlighted and shows a simulated mechanical movement frequency of 8.25 kHz.

4.4.1 Resonance frequency and angular behaviour

The angular frequency response of the fabricated device was tested reflecting a HeNe laser guidance beam from the mirror surface and evaluating the resulting scan lines on a screen. The MEMS chip was mounted on a custom built PCB board with the electrical pad connections on the chip being wire bonded to the PCB tracks to allow electrical connection via the PCB. To minimise possible errors due to angled reflections, the guidance laser is directed through a hole in the screen with the reflection on the non-actuated mirror hitting the screen about 5 mm below the incident beam hole. The scan angle under actuation is evaluated by measuring the length d of the scan line on the screen (see Fig. 4.15). The TOSA θ can then be calculated with the distance D' between the MEMS mirror and the screen using

$$\theta = 2 \cdot \arctan\left(\frac{d}{2 \cdot D'}\right). \tag{4.21}$$

The use of a vibrometer setup for a more accurate and automated determination of the frequency response is not possible in this case, as the scan angles are larger than the collection angle of the microscope lens used in these setups. In a vibrometer setup the actual movement frequency would be directly detected. To confirm the movement

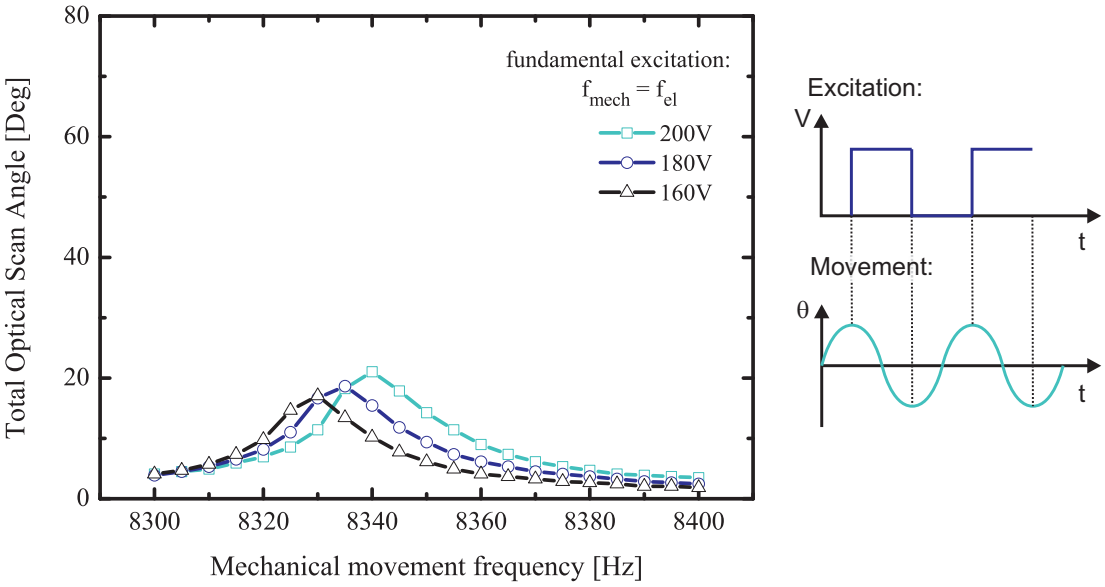

Figure 4.16: Frequency response curve for fundamental square-wave actuation of the MEMS mirror, including the temporal excitation and movement schematic.

frequency for the screen measurement a photodiode was inserted at the edge of the scan line with the repetition rate of the received signal showing the mechanical movement frequency.

The actuation of the tilt resonance mode of the mirror is obtained using an Agilent 33250A signal generator with a square-wave output signal with 50 % duty cycle combined with a FLC A400 times 20 high voltage amplifier. The active part of the driving signal is connected to the fixed combs of the actuator with the moving structure connected to the ground. A 10 kΩ resistor is connected in series between the amplifier output and the connection to the MEMS to avoid thermal destruction of the actuators in the case of a short between the moving and fixed combs. Actuation with a square-wave signal and an electrical frequency matching the mechanical movement frequency is shown in Fig. 4.16. The device was actuated using unipolar voltage steps between 0 V and 160 V, 180 V or 200 V, with the highest TOSA response of 21° at the 200 V actuation. The corresponding excitation and mechanical movement frequency is 8.34 kHz, which shows a good match between the simulated eigenfrequency of 8.25 kHz in the previous section. With a reduction of the actuation voltage a shift towards lower

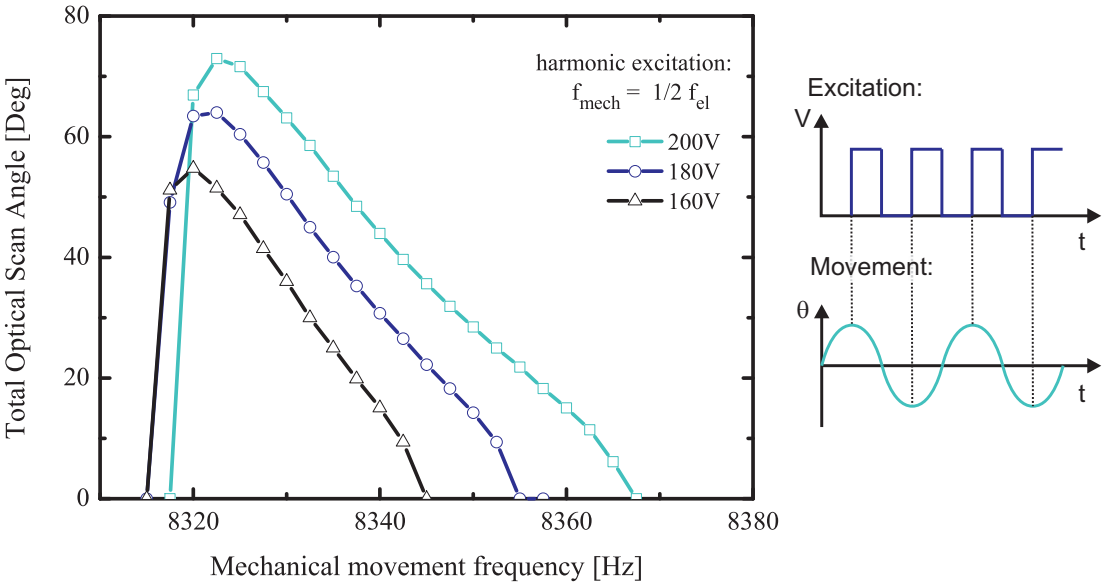

Figure 4.17: Frequency response of harmonic square-wave actuation of MEMS including the temporal excitation and movement schematic.

resonance frequencies can be seen with a 5 Hz drop for each shown step. The reason of this frequency shift can be found in the nonlinear behaviour associated with the electrostatic driving as discussed in chapter 2. The shape of the individual frequency response curves shows only a negligible asymmetry but no tilt associated with spring softening or hardening nonlinear behaviour.

A higher angular response of the device can be achieved when using an electrical square-wave actuation signal with a frequency double of the mechanical resonance frequency. In this case the on part of the signal will correspond with the part of the movement cycle having a mirror movement from the maximum angle to the centre position. As the electrostatic actuation only consists of an attracting force this leads to a synchronisation between the actuation and movement where the force is only applied at the movement parts from the maximum positions to the mirror rest position (see right side of Fig. 4.17). The frequency response curve for this harmonic excitation is shown in Fig. 4.17 with a maximum TOSA for the 200 V actuation of 73° at a mechanical movement frequency of 8.323 kHz. In this actuation case, a clear spring softening nonlinear behaviour is observable with annihilation of the movement shortly after the

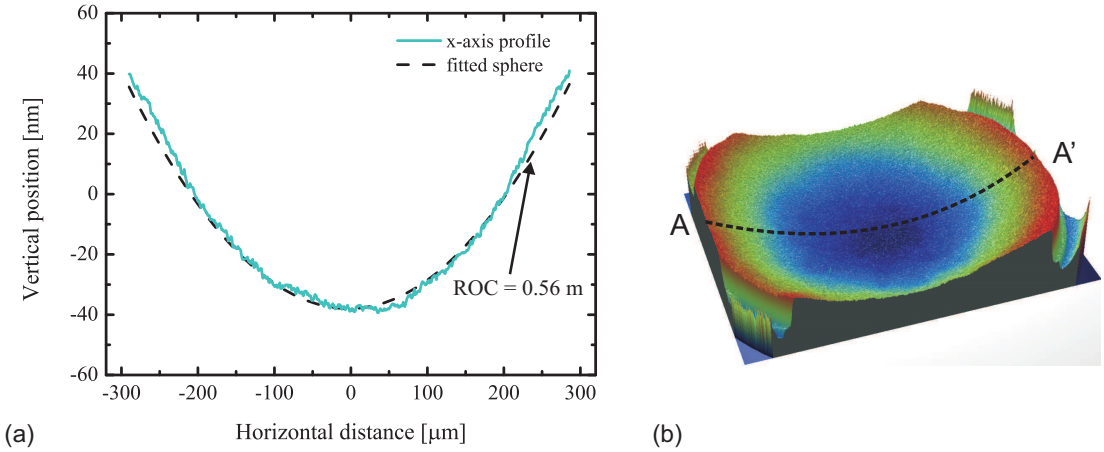

Figure 4.18: ROC measurement for the uncoated mirror surface with (a) x-axis scan including a spherical fit and (b) 3D profile.

maximum angular response on a frequency down-sweep. A similar behaviour is visible for the two other actuation voltages used, with a slight reduction of resonance frequency by a couple of Hertz and a reduced angular response of 63° TOSA for 180 V actuation and 55° TOSA for 160 V actuation.

4.4.2 Radius of curvature

The surface curvature of the fabricated mirrors was measured using a Veeco NT1100 optical white light interferometer, using a ten fold magnification with a lens combination of a x20 objective lens with NA of 0.4 and a x0.5 imaging lens. The uncoated mirror surface shows a spherical concave shape due to intrinsic stresses in the device layer, originating from the non-uniform doping concentration through the thickness of the device layer during fabrication. The measured 3D profile and scan-line along the torsion beam axis (denoted "x-axis") is shown in Fig. 4.18. The average ROC of 7 fabricated mirrors along the x-axis is 0.56 m which is fitted to the measurement graph with good agreement. From the ROC one can calculate the stress in the device layer along this axis as [156]

$$\sigma' = -\frac{E \cdot \frac{h}{2}}{ROC} \tag{4.22}$$

with the device layer thickness h, the Young's modulus E and the measured ROC. For the 25 μm thick device discussed this leads to a residual stress of −4.34 GPa in the device layer after fabrication and release of the mirror when using the Young's modulus values from chapter 3.

4.5 Coatings for high reflective mirrors

The scanning micromirrors require a thin film coating of their surface to enhance their reflectivity at the lasing wavelength of λ = 1064 nm, as the inherent reflectivity of silicon is only about ≈ 30 % for this wavelength. HR coatings are desired as they reduce the losses inside the laser cavity and therefore increase the slope efficiency and reduce the threshold of the laser actuation. Additionally, HR coatings will reduce the absorption of intra-cavity optical power on the mirrors and therefore increase the power handling.

To increase the reflectivity of the single crystal silicon mirror surface at the desired lasing wavelength of λ = 1064 nm, a metallic or dielectric coating has to be applied. The active MEMS Q-switch and mode-locking elements published so far are either directly constructed of a metallic cantilever or membrane structure [150,152–155,175] or incorporate a HR gold or dielectric coating [5,176]. Only Inoue et al. [149] demonstrated a Q-switched microchip laser using a piezoelectric vibrating MEMS mirror without metallic or dielectric layers, but by using a polymer layer structure which reached a reflectivity of up to 87 % at their lasing wavelength of 1064 nm.

For the experiments discussed in this work both a gold coating and a stack of dielectric coating layers has been applied to the micromirror surface, with their characteristics and influences on the mirror structures described in the following two sections.

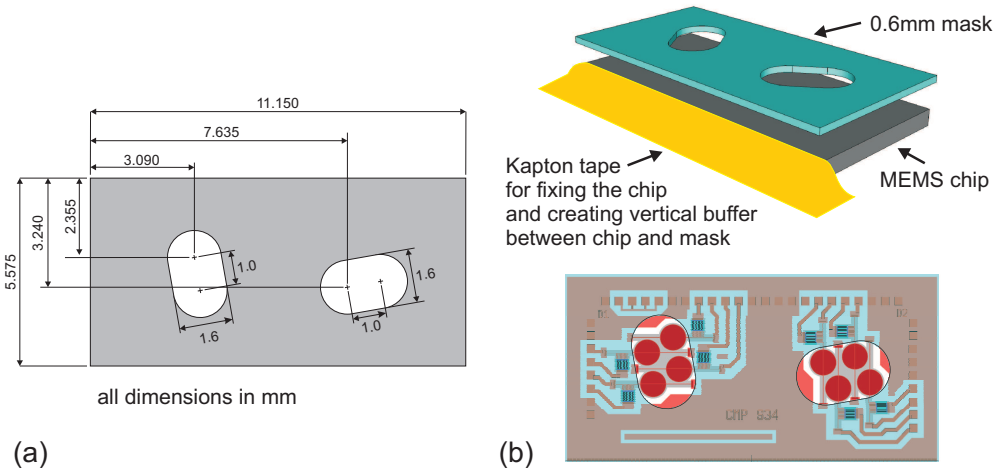

Figure 4.19: (a) Design layout of the coating mask and (b) masking layers and overlap of the coating mask relative to the used MEMS chip.

4.5.1 Gold coatings

The use of gold as an HR coating layer offers a broadband reflectivity over a wide range in the near infrared (NIR) spectrum with usual reflectivity levels as high as 96 % [177] for incident light with a wavelength between 800 nm and 20 μm. The coatings used here have been applied using an in-house post-fabrication process by thermal evaporation of the metallic layers onto the MEMS scanning mirror surfaces. The thermal evaporation was conducted by Dr. John Mackersie from the Centre for Ultrasonic Engineering of the University of Strathclyde. The chosen layer structure consisted of a thin chromium layer of around 10 nm thickness, to increase the adsorption of gold on the silicon surface, and a gold layer with a targeted thickness of around 250 nm. A variation of the layer thickness can occur as the coating chamber only used a single measurement point for the thickness estimation during the coating. The deposited overall metal thickness was measured as 240 nm after the coating process by using a Dektak Series 6M contact stylus profiler at edges of the metal coating on a microscopy slide used as holder.

The MEMS chips for coating have to be fixed on a microscopy slide as holder and need to be masked, to only coat the mirror surfaces. Without masking, a conducting coating layer deposited over the whole chip would short the comb-drive actuation electrodes

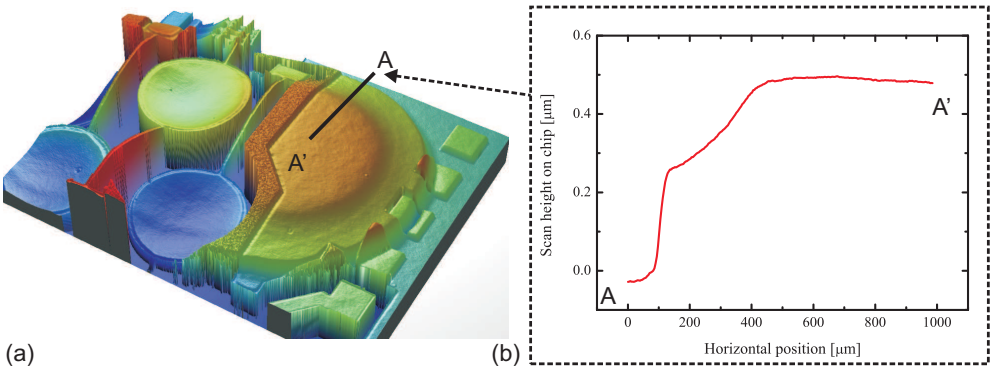

Figure 4.20: Whitelight interferometer measurement of parts of the coated micromirror array, with (a) 3D image of the measured area and (b) line scan of the coating edge on the substrate.

and hinder any movement actuation. The mask layout for multiple scanning mirrors in an array configuration, shown in Fig. 4.19, was realised in a thin aluminium sheet with side dimensions fitting the MEMS chip dimensions of 11 mm x 5.5 mm. The chip and mask were aligned manually using an optical microscope for exact positioning and were fixed relative to each other using Kapton tape around the circumference of the mask.

An overview of an optical profile of a coated array of scanning mirrors, taken by a white light interferometer scan, is shown in Fig. 4.20. A reduction of the coating thickness can be seen at the edges of the coated area due to shadowing effects from the mask suspended above the chip during coating. The surface profile of one of the gold coated mirrors, used for the 3-mirror laser cavity evaluation shown later, can be seen in Fig. 4.21(a) which shows a ROC of 0.22 m. The reduction of ROC from the uncoated value of 0.56 m, and therefore increase in curvature, is due to additional stresses from the gold and chromium coating layers, which generate a compressive stress during adsorption and cooling on the mirror surface.

To evaluate the changes to the mechanical resonance frequencies and movement angles induced by the coating, an FEM simulation similar to the one described earlier in this chapter was used with inclusion of the 240 nm gold layer. The order of resonance modes remained unchanged; however a drop of the resonance frequencies of about 4 % could be observed. For the two lowest movement modes this leads to a new simulated

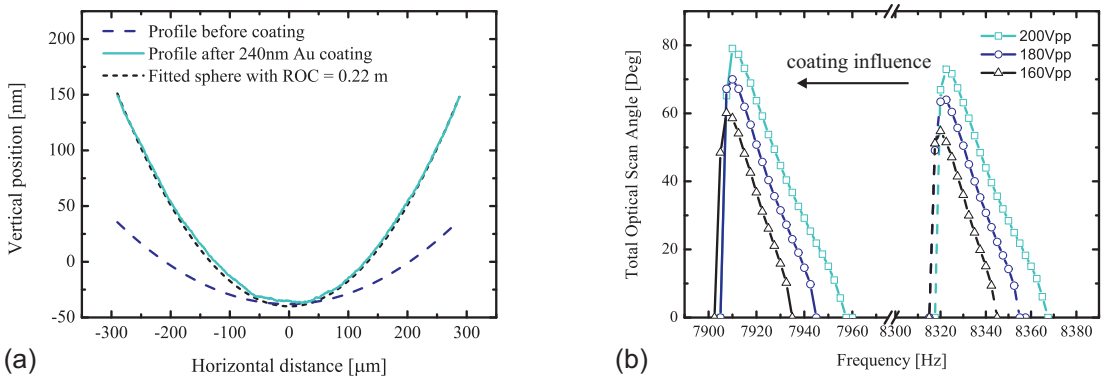

Figure 4.21: (a) Surface curvature and (b) frequency response of the gold coated micromirror used for the 3-mirror laser cavity.

resonance frequency of 5.621 kHz for the parasitic in-plane movement and of 7.858 kHz for the desired tilt movement. The experimental behaviour after coating was evaluated using the same projection setup as before with the results shown in Fig. 4.21(b). The actuation of only the harmonic excitation is displayed as the results from the uncoated chips showed a more than threefold increase of the angular scan range compared to the excitation with the fundamental frequency. As actuation signal a square-wave voltage signal was again used with peak to peak voltages of 160 V, 180 V and 200 V. The actuation limit of 200 V is set by the maximum available output of the signal generator and amplifier combination used for actuation. Higher actuation voltages can possibly be used, up to a voltage limit at which an in-plane pull-in of the comb-drives occurs. The highest scan angle for the 200 V actuation is 79.1° at a mechanical movement frequency of 7.910 kHz, which is equivalent to an excitation frequency of 15.820 kHz. The shape of the frequency response curve stayed nonlinear with a clearly visible spring softening behaviour, similar to the uncoated device. The drop in resonance frequency is in good agreement with the estimated frequency shift from the adapted FEM simulation.

The second gold coated mirror, used in this chapter for the 2-mirror laser cavity evaluation, showed a ROC of 0.35 m after coating (see Fig. 4.22(a)). The variation in the change of ROC due to the coating can be explained due to the non-uniform coating created through the shadow mask. The resonance frequency of this second gold mirror

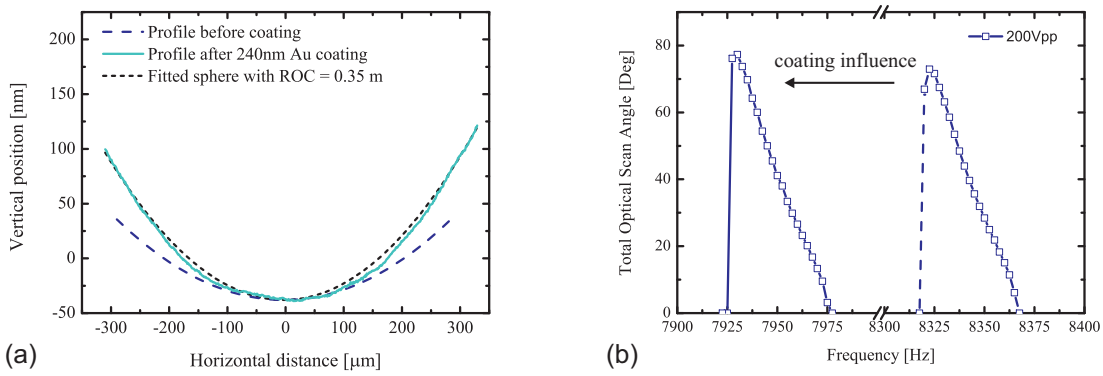

Figure 4.22: (a) Surface curvature and (b) frequency response of the gold coated micromirror used for the 2-mirror laser cavity.

also shifts to a lower frequency after coating with a peak at 7.93 kHz for the wanted tilt movement at 200 V actuation. The frequency response curve can be seen in Fig. 4.22(b) with a maximum scan angle of 77.3°. The variation of the resonance frequency of 20 Hz between the two used gold coated mirrors originates from manufacturing tolerances of the SOI chips and the already mentioned variance of the post fabrication coating layer thickness due to mask shadowing effects.

The measurement of the resulting reflectivity R at the lasing wavelength of 1064 nm of the Nd:YAG module was achieved by measuring the ratio of incoming and reflected optical power on a reference spot on the coated microscopy slide used for mounting the MEMS chip in the evaporation chamber. A 2 mirror laser cavity using conventional mirrors around the Nd:YAG module was used as a continuous wave (cw) probe beam for this purpose. With an incident laser power between 25 mW and 750 mW an average reflectivity of $R = 96\,\%$ was found at $\lambda = 1064$ nm.

When inserting the mirrors into a laser resonator, the non-reflected intra-cavity optical power will be absorbed in the gold coating and silicon mirror. This leads to heating of the overall mirror structure as heat conduction through the mirror torsion beams is in first approximation the only effect removing heat from the device. This temperature increase can lead to a change of the resonance frequency of the mirror (see also section 5.3.3), which will directly affect the mirror scan angle. Additionally the melting point

of the gold coating can be reached which will damage the coating and hinder further lasing actuation. To avoid damage to the coating and annihilation of the resonance movement, the average laser output power was limited to a level where a reduction of the scan line could be observed. For a laser cavity with an OC reflectivity of $R_{oc} = 80\,\%$ this limit was set at approximately 75 mW average output power.

4.5.2 Dielectric coatings

The usage of a stack of dielectric layers as HR coating allows the possibility to reach reflectivity values ideally higher than 99.5 % for a desired wavelength by using $\lambda/4$ layer thicknesses, with $\lambda = \lambda_0/n'$ being the desired HR wavelength in a medium with refractive index n'. This layer structure leads to constructive interference of the reflections at each refractive index change. A $\lambda/4$ thickness is necessary due to a phase shift of 180° for reflections at a refractive index boundary where the next medium has a higher refractive index. The amplitude of the reflection on each layer boundary is dependent on the difference between the two participating refractive indices, with a higher refractive index change leading to a higher reflection amplitude of the em wave. This leads to a desired material combination with high refractive indices difference to achieve HR coatings with as little as possible layers. Additional constrains for the material selection are a necessary transparency at the desired wavelength of 1064 nm and further necessary coating layer parameters specific for the coating task of thin micromirrors. These include low thin film stresses of the individual coating layers, with idealy a cancellation of the stresses by the two different material layers as well as a similar coefficient of thermal expansion in respect to the substrate material to avoid additional heat induced stresses during operation.

To achieve low stress HR coatings for thin micromirrors, a coating investigation with the company Helia Photonics Ltd based in Livingston, Scotland was initiated using electron beam deposition of the thin layer structures with evaluation of the resulting stresses and reflectivities undertaken at the University of Strathclyde. Possible material

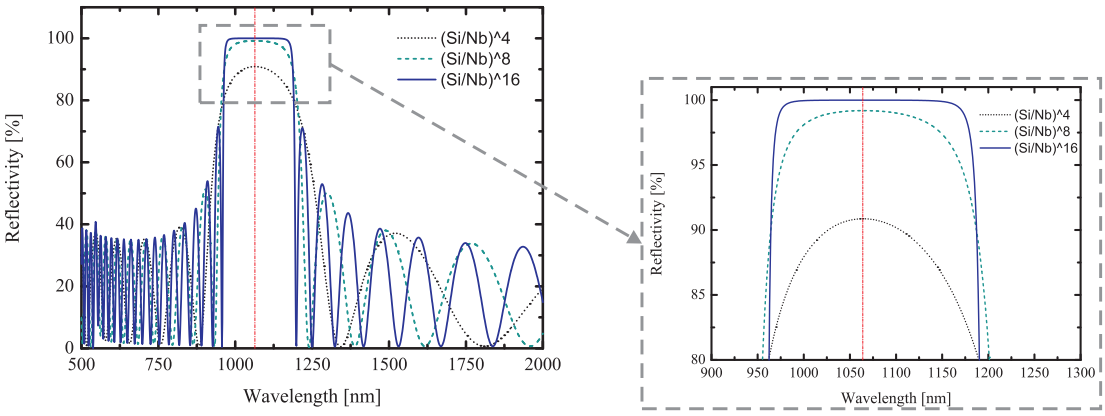

Figure 4.23: Simulated dielectric coating normal incident reflectivity behaviour with varying coating layer pairs (simulation carried out by Helia Photonics Ltd.).

combinations that were available lead to a selection of silica (SiO_2) and niobia (Nb_2O_5) as the layer combination (with the possible use of tantalum oxide (Ta_2O_5) as buffer layer). Silica is in this case the material with a lower refractive index of 1.45 at a wavelength of 1064 nm while niobia has the higher refractive index of 2.32 at this wavelength. This leads to the necessity of niobia being the top layer of a stack of alternating layers for achieving HR coatings. The estimated stress behaviour for thin coatings showed a tensile stress for SiO_2 and a compressive stress for Nb_2O_5. A tensile stress denotes a curvature change towards a further convex shape, while compressive stress leads the substrate to curl in a further concave direction. This single layer stress behaviour was experimentally confirmed by coating silicon micromirror samples with a $\lambda/4$ layer of the respective materials. For all dielectric coatings only the bondpads of the MEMS chips, used for creating the electrical connections, were masked during the coating. A HR coating layer is therefore also accessible on the plane substrate surrounding the mirror structures.

To estimate the number of layer pairs needed for reflectivity values above 99 %, a simulation of the reflection behaviour for normal incidence with varying wavelength was set up by Helia Photonics leading to the graph shown in Fig. 4.23. As can be seen in the inset, a reflectivity of above 99 % at 1064 nm can theoretically be reached with

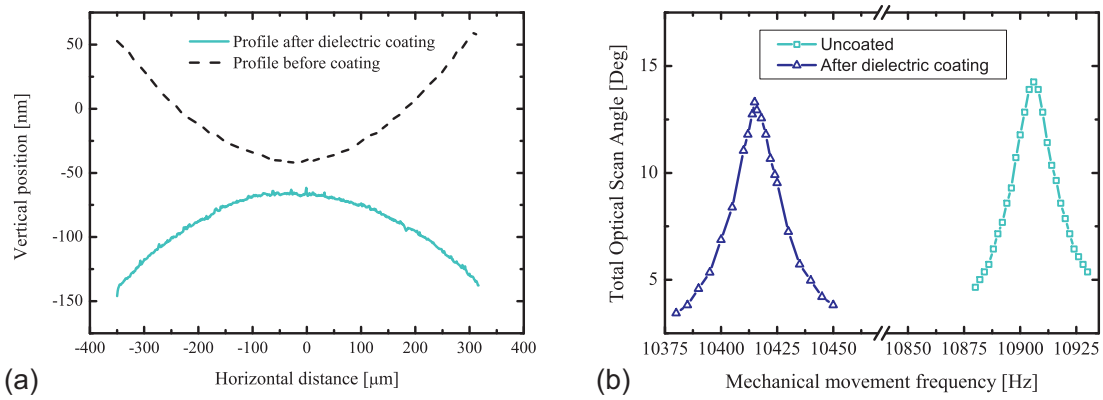

Figure 4.24: (a) Surface curvature of the dielectric coated micromirror and (b) frequency response after coating using square-wave excitation.

8 layer pairs of Niobia and Silica, while 16 pairs will lead in theory to a reflectivity of above 99.99 %.

The evaluation of the resulting curvatures of the 25 μm thick mirrors after coating was performed using a Veeco NT1100 white light interferometer, while the resulting reflectivities were measured using a 1064 nm probe laser beam and evaluating the ratio of incident and reflected power on the MEMS chip surface. At a current intermediate stage in the project, coatings with reflectivities up to $R = 97\,\%$ and a layer structur of 12 pairs of silica and niobia were evaluated on an aditional MEMS micromirror array test structure. This array was inserted in a 3-mirror cavity to create an active Q-switched laser output. The resulting surface stresses on the micromirrors due to the dielectric coatings tend to show a dependency on the underlying layer structure of previous coated layers, with a general tensile induced stress behaviour with resulting curvatures of convex shape and ROCs of −0.77 m for the used test structure (see Fig. 4.24(a)). This curvature change towards a convex shape has implications on the cavity setup of the laser. A 2-mirror cavity using a flat OC mirror does not remain stable over a wide range of thermal lens focal length values; therefore an additional optical element in the form of a folding mirror is required inside a laser cavity to achieve the desired stability range. The choice of using flat OCs was in this case taken due to the non-availability of curved OCs for the experiment.

The mirrors used for the currently most promising results (in respect of low stress and high reflectivity at 1064 nm) of the dielectric coating tests are similar to the devices used in chapter 3. The thickness of the devices used here is the only difference with a 25 μm thick device layer present for the dielectric coated devices. The frequency response after deposition of the dielectric coating can be seen in Fig. 4.24(b). The micromirror is actuated using a square-wave driving signal with 200 V peak-peak and an electrical excitation frequency matching the mechanical movement frequency. This was necessary as the first harmonic frequency of the mechanical tilt movement mode of the mirror was shifted towards the resonant frequency of a parasitic movement due to the coating. The maximum TOSA of the coated mirror is 13.3° at a movement frequency of 10.415 kHz, with a symmetric frequency response curve without visible nonlinearities.

The used dielectric coatings are only an intermediate step in the project initiated to develop low stress dielectric coatings for thin substrates like the micromirrors used here. Therefore their performance is still not at the intended level. A reflectivity of 97 % still leads to significant absorption of intra-cavity optical power and subsequent heating of the mirror, which therefore still poses a power handling limit. Additionally, the stresses induced by the coating are not at the desired level yet and limit the cavity setup, which therefore will include an additional folding mirror in the laser setup used for evaluation and discussed later in this chapter.

4.6 2-mirror cavity for short pulse durations

The gold coated chips were used to build up a 2-mirror laser cavity to evaluate the possible shortest pulse durations using the scanning micromirrors as active Q-switches for a Nd:YAG solid-state laser. Due to the mirror curvatures discussed in the previous section, only gold coated mirrors were used in this case as the convex curvature of the dielectric mirrors hinders the construction of a stable cavity for a wide enough variety of thermal lens values of the gain medium with using the available flat OC mirrors.

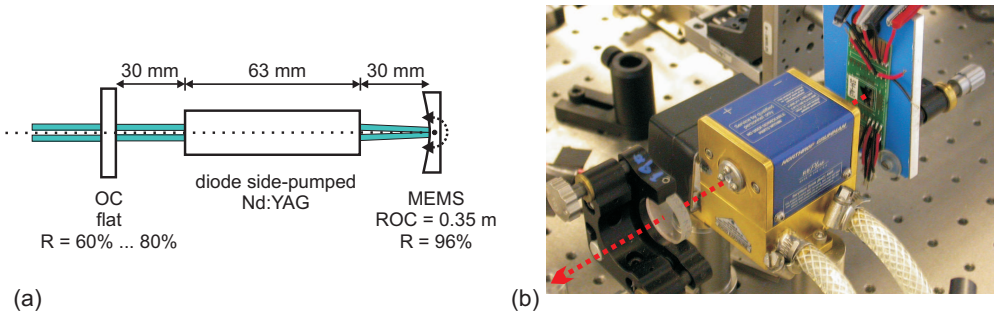

Figure 4.25: (a) 2-mirror Q-switch cavity schematic and (b) image of the assembled cavity in the laboratory.

4.6.1 Cavity setup

A schematic overview and an image of the 2-mirror cavity chosen for inclusion of the micromirror active Q-switch is shown in Fig. 4.25. The cavity is built around a side-pumped Nd:YAG laser module with a standard flat dielectric coated BK7 OC facing one end of the laser rod at a distance of 30 mm and the gold coated MEMS mirror facing the other end at the same distance. The Nd:YAG module is commercially available from Northrop Grumman under the description RBA30-1C2 and consists of a 63 mm long Nd:YAG laser rod with 3 mm diameter and three bars of laser diodes radially arranged around the rod for optical pumping. The laser rod has a Nd doping concentration of 0.6 % with two flat end facets that are anti-reflective coated at 1064 nm. The pump diodes allow continous wave (cw) pumping with a combined pump characteristic as shown in Fig. 4.26(a), where the input current is supplied by a Glassman LP35-35 DC power supply. The pump laser diodes have a threshold of 8.2 A and an overal output power slope of all three bars of 11.22 W/A. The diodes in the laser module are water cooled and run at a constant temperature of 22° C. During operation, the pump diodes will heat up the laser rod creating an optical pump power dependent thermal lens within the gain medium as specified by its focal length f'_{th} or focal power shown in Fig. 4.26(b). A linear dependency of the focal power on the pump diode drive current can be seen with an increased lensing effect for higher pump powers. This thermal lens needs to be considered for the evaluation of the stability of the designed laser cavities.

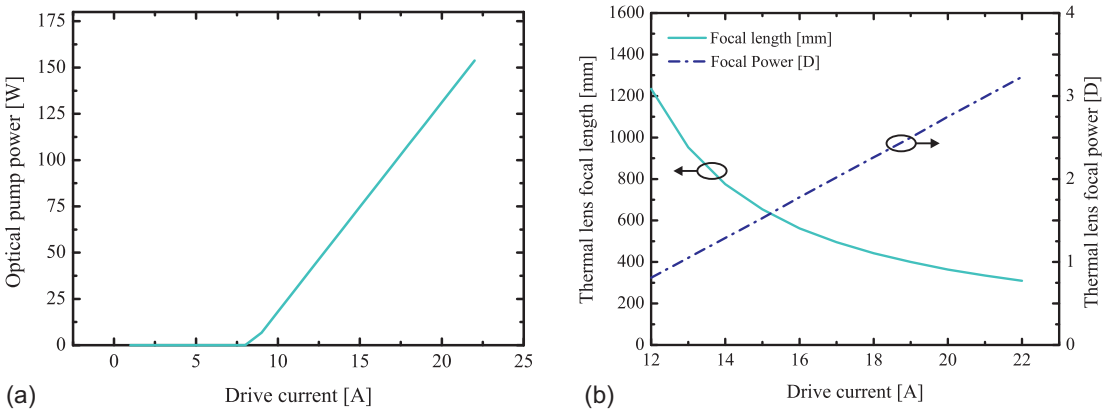

Figure 4.26: (a) Combined pump-diodes characteristic and (b) thermal lens focal length and focal power for the used Nd:YAG module (see Appendix C).

The simulation tool WinLase was used to evaluate the cavity stability and laser beam radius throughout the cavity. It is based on an ABCD matrix type Gaussian beam optics solver and enables the evaluation of the above mentioned parameters by building up a laser cavity with standard building blocks of freespace propagation, blocks of materials with constant refractive indices and lenses or curved mirrors. The cavity shown in the schematic in Fig. 4.25 was built-up resulting in a cavity stability diagram with varying f'_{th} as seen in Fig. 4.27(a). A cavity stability of 1 depicts in this case a perfect stable cavity while 0 depicts an unstable cavity. The thermal lens is included as a lens element between two blocks of Nd:YAG with a length of 31.5 mm each and refractive index of 1.8. For the relevant thermal lens focal length values between 1200 mm and 300 mm, as shown in Fig. 4.26(b), a cavity stability close to 1 is reached. A reduction of the stability will only appear when going to even lower focal lengths of the thermal lens below values of 200 mm. The Gaussian beam radius of the oscillating laser power for a thermal lens focal length of 800 mm, corresponding to a pump drive current of about 14 A, is shown in Fig. 4.27(b). The two vertical lines depict the end facets of the laser rod. The beam waist is located at the OC with a beam radius of 210 μm while the intra-cavity beam expands to a beam radius of 247 μm at the MEMS mirror. This results in a theoretical coverage of 50 % of the mirror surface area by the laser beam, which does not put any additional constraints on the cavity stability, as would be the

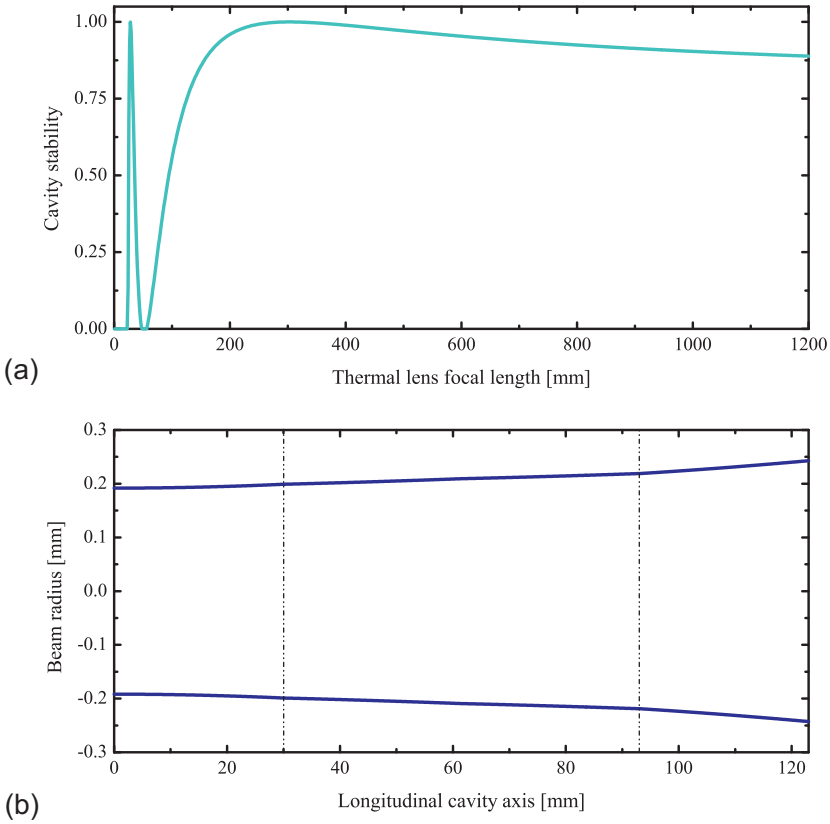

Figure 4.27: (a) Simulated 2-mirror cavity stability with varying f'_{th} and (b) beam radius evolution through the cavity with MEMS mirror at right hand side.

case for beam radi that would exceed the MEMS mirror radius.

To build-up the cavity, the PCB board with the mounted MEMS chip was fixed on a holder connected to a tip-tilt mirror mount for alignment purposes and an additional set of linear translation stages for lateral positioning of the initial MEMS mirror position. An initial cavity alignment was achieved by using a HeNe guidance laser entering the cavity through the OC side.

4.6.2 Pulsed output at threshold and at 25 mW

To generate Q-switch output pulses the scanning micromirror is actuated using a square-wave electrical driving signal with 200 V peak-to-peak voltage and an offset of 100 V at a drive frequency of $f_{el,1}$ = 15.87 kHz or $f_{el,2}$ = 15.90 kHz. These two frequencies

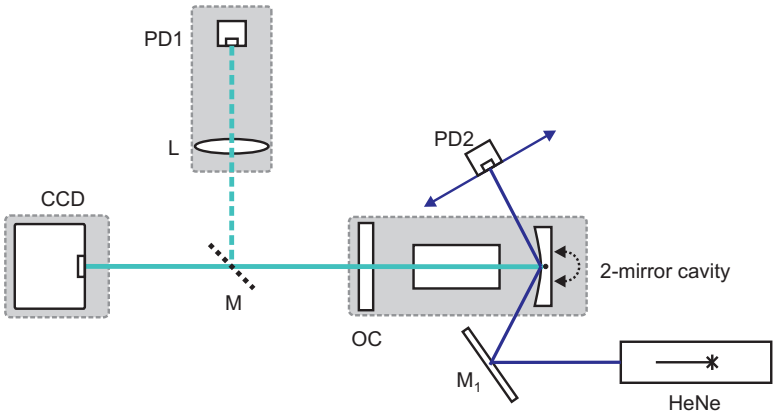

Figure 4.28: Measurement schematic for determination of the temporal and spatial output characteristic; M: HR mirror for switching between spatial and temporal measurement, CCD: CCD camera, L: focusing lens with $f' = 200\,\text{mm}$, PD1+2: photodiodes, OC: output coupler.

were chosen to evaluate the influence of the mirror midpoint speed, determined by the different maximum angular mirror response at both frequencies. From section 4.5.1 the values of the angular response of the mirror were $\theta_1 = 69.8°$ or $\theta_2 = 41.1°$. A $10\,\text{k}\Omega$ resistor is connected in series between the device and the voltage amplifier output to avoid damage to the comb-drive in the case of shorting between the moving and fixed combs.

The optical setup for measuring the temporal and spatial output characteristic of the Q-switched MEMS laser is shown in Fig. 4.28. The laser output through each selected OC is sequentially measured using a DataRay WinCamD-UC012-1310 CCD camera (CCD) for the spatial characteristics and a Hamamatsu S5973 1.5 GHz fast photodiode PD1 in combination with a lens with 200 mm focal length for the temporal characteristics. The lens was used to focus the output to avoid any truncation of the output characteristics over the full spatial beam width. The PD1 signal was amplified using a Femto DHPCA-100 amplifier and measured on an Agilent DSO6034A oscilloscope with a maximum temporal resolution of 0.5 ns. A HeNe probe laser combined with a second photodiode, PD2 (Hamamatsu S5973 with 1.5 GHz bandwidth), is included to determine the timing of the MEMS mirror midpoint crossing. PD2 is placed central in the scan line created by a reflection of the probe HeNe laser beam on the moving

micromirror. To achieve a best possible midpoint position, the pulse delay between successive pulses on PD2 is measured on the Agilent DSO6034A oscilloscope and the photodiode position adapted until all successive pulse delays have equal values.

An example of a temporal measurement of the laser output using both photodiodes is shown in Fig. 4.29. The cavity configuration in this case consisted of a 20 % OC with the MEMS driven at a frequency of 15.87 kHz and an average laser output power of 25 mW. The optical pump power for this case is ≈ 100 W. The Q-switch laser output has a pulse repetition frequency (PRF) of 15.87 kHz with pulse durations of about 50 ns, leading to pulse energies of 1.6 μJ and a pulse peak power of 32 W. The top trace in the figure shows the electrical driving signal of the mirror. The bottom trace is the measurement output of PD1, showing the pulse train with a PRF of 15.870 kHz. This is equal to double the mechanical movement frequency, as a pulse occurs on every passing through the mirror midpoint position with two passes per movement cycle. The individual output pulse has ideally a fast rise time and slower fall time (see lower inset of Fig. 4.29). With the rise time depending mainly on the initial population inversion and the fall time mostly on the empty cavity decay rate [178], shorter pulse durations for a specific cavity are expected to be generated with a pulse shape with even shorter rise times and longer fall times than shown. The middle trace originates from PD2 and shows the midpoint crossing of the MEMS mirror. Each midpoint crossing is close to the emission of a pulse, with the pulse depicted in the lower inset of Fig. 4.29 showing a time delay to the midpoint crossing. This leads to a pulse emission after the mirror has passed through the lowest loss alignment of the laser. The data analysis of the measurements related to the midpoint determination is done in the subsequent sections using Matlab. This is required as the PD2 signal representing the midpoint position is based on the physical position of the photodiode in the setup, which has an error margin translating to up to multiple tens of nanoseconds offset of the pulse delay time. The post-processing consisted of a determination of the peaks of the midpoint photodiode signal with an accuracy of 2 ns and a shift of the assumed midpoint positions to create

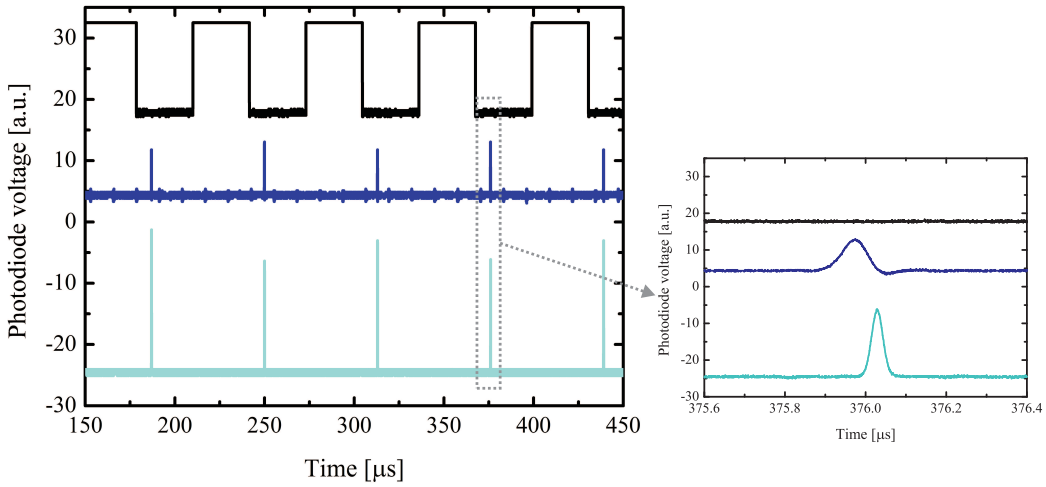

Figure 4.29: Example pulse trains for 25 mW average output power of R = 80 % OC cavity with 15.87 kHz actuation, top pulsetrain is the driving voltage, middle pulsetrain is the mirror midpoint position and bottom pulsetrain is the laser output.

a homogeneous time delay between each successive midpoint position. These adapted midpoint times were then used to evaluate the time delay between each laser pulse and respective mirror midpoint crossing.

Temporal output characteristics

The temporal output characteristics of the 2-mirror laser cavity were determined for three different OC mirrors with nominal reflectivities at 1064 nm of 60 %, 70 % and 80 %. The experimentally measured reflectivities of these three mirrors are 59 %, 71 % and 83 %. The cavity was aligned for each OC mirror configuration in order to gain an equal spaced output pulsetrain, with equal pulse delays for pulses originating from both movement directions of the mirror. During Q-switch actuation a measurement of the pulsetrain was taken just above the respective lasing threshold (with average output power < 1 mW) and at an average output power of 25 mW. The Q-switched laser output pulse shapes and pulse delays t_d in respect to the MEMS mirror midpoint crossing are shown in Fig. 4.30 for the actuation frequency of 15.87 kHz of the micromir-

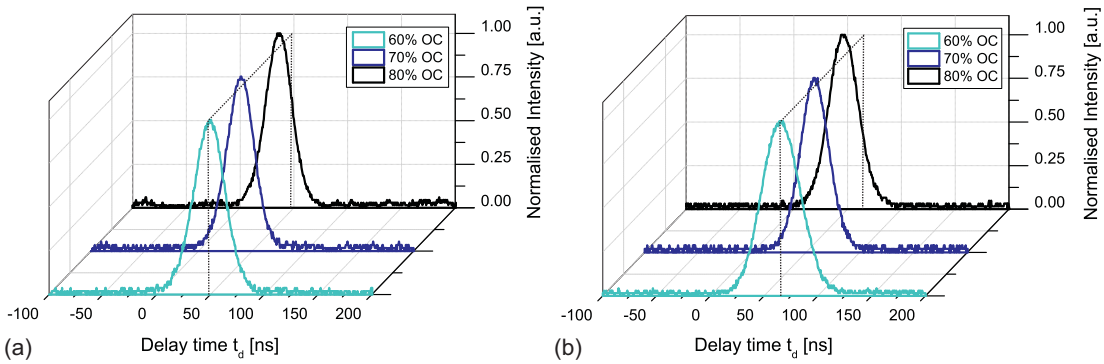

Figure 4.30: Pulseshapes of Q-switch output with 15.87 kHz MEMS actuation for varying OC reflectivities at (a) threshold and (b) 25 mW average output power.

ror. The pulse delays were determined as previously discussed with using PD2 while the amplitudes of the pulse intensities were normalised in order to create an easier comparison between all cavity configurations. Fig. 4.30(a) shows typical pulses for an output power around lasing threshold while Fig. 4.30(b) shows typical pulses for 25 mW average output power. In both cases the pulses originate from the micromirror movement direction leading to the highest pulse delay in the measurement. In both cases of Fig. 4.30 a shortest maximum pulse delay is visible for the cavity using the OC with 80 % reflectivity.

For the Q-switch output created with a MEMS actuation of 15.90 kHz, and therefore lower MEMS movement angle, the resulting pulse shapes and pulse delay times are shown in Fig. 4.31. Fig. 4.31(a) shows again the typical pulse outputs with an average output power around lasing threshold while Fig. 4.31(b) shows the outputs at an average output power of 25 mW. Similarly to the actuation with 15.87 kHz a lowest pulse delay can be seen for the cavity using the OC with 80 % reflectivity. Using the lower MEMS movement angle for generating the Q-switch output leads to a higher pulse delay with longer pulse durations compared to the outputs in Fig. 4.30.

A summary of the the pulse delay time measurements for all actuation cases is shown in Fig. 4.32. In all cases a split between the pulse delays of the two movement directions through the cavity alignment of each configuration is visible. The subscripts "max"

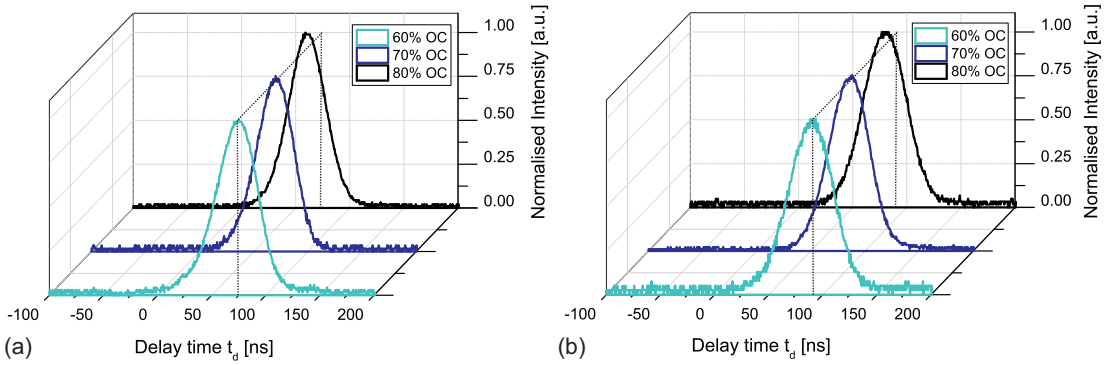

Figure 4.31: Pulseshapes of Q-switch actuation with 15.90 kHz MEMS actuation for varying OC reflectivities at (a) threshold and (b) 25 mW average output power.

show the pulse delays of the mirror movement direction corresponding to the longer delay, occurring for every second pulse in the measured pulse train as every second pulse coincides with the same movement direction of the MEMS mirror. The subscripts "min" represent accordingly the pulse delays of the second mirror movement direction corresponding with a shorter delay. The error bars in Fig. 4.32 correspond to the sample standard deviation of two measured pulses for each configuration. The origin of the different pulse delay times of the two mirror movement directions could be caused by an unbalanced cavity alignment, where the cavity axis is lateral shifted in respect to the gain medium axis. This would lead to different feedback times and therefore different delays. The pulse delay times for the 15.87 kHz actuation have in general lower values than the corresponding delay times for the 15.90 kHz actuation, showing a dependency of the delay times on the mirror movement speed.

The pulse delays for the 15.87 kHz actuation are between 67 ns and 32 ns for $R = 60\,\%$, 58 ns and 31 ns for $R = 70\,\%$ and 47 ns and 24 ns for $R = 80\,\%$. The positive pulse delay shows a non-optimum pump condition as the pulse build-up time is longer than the time required for the mirror to move through its midpoint position. An increase in pump power P_p with respect to the laser threshold power P_{th} should lead to a higher initial inversion density in the gain medium and, as shown in simulations in section 4.3.1, also to a reduction of the pulse delay time. The increase of pump power is

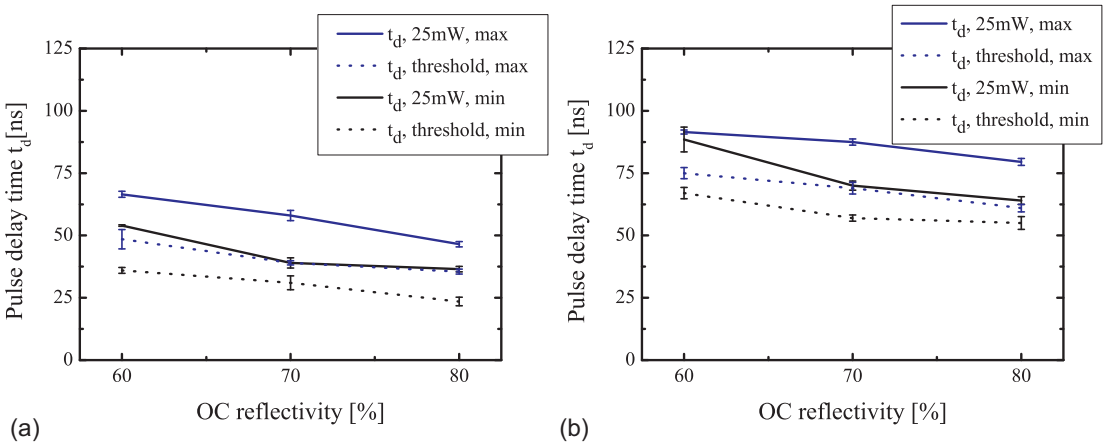

Figure 4.32: Summary of the measured pulse delays for all 2-mirror Q-switch actuation configurations with (a) MEMS mirror actuation with 15.87 kHz and (b) MEMS mirror actuation with 15.90 kHz.

nevertheless limited by the mirror coatings power handling capabilities. As a result no optimum pulse timing or even negative pulse delays were achieved. If negative pulse delays would occur these could be balanced by reducing the mirror movement speed to achieve optimum pulse timing. The reduced mirror speed would in this case increase the pulse delay time again without changes to the pump power. The trend in the measured pulse delay times showing a slight decrease with increasing OC reflectivity was expected to have the opposite direction, as a higher pump power is necessary to reach the laser threshold and output at 25 mW for lower OC reflectivities. Reasons for this deviating measured trend can lie in the necessary cavity realignment after changing the OC, with a high sensitivity of the cavity to small misalignments. Further future investigations are still necessary with higher quality mirror coatings, also in respect to results obtained from a 3-mirror cavity which show the expected pulse delay behaviour and are presented later in this chapter.

A summary of the pulse duration evaluation for all discussed actuation cases is shown in Fig. 4.33. For both the 15.87 kHz and 15.90 kHz actuation the pulse durations of the pulses emitted closer to the MEMS mirror midpoint position (denoted with "min") are by up to 10 ns shorter than the pulse durations from the opposite movement direction. The 15.87 kHz actuation shows in this case in general lower pulse durations, between

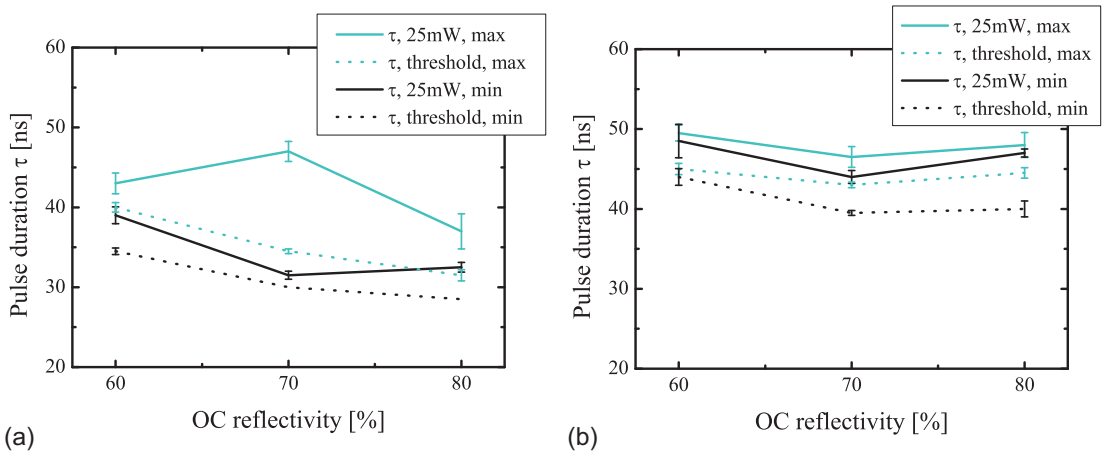

Figure 4.33: Summary of the measured pulse durations for all 2-mirror Q-switch actuation configurations with (a) MEMS mirror actuation with 15.87 kHz and (b) MEMS mirror actuation with 15.90 kHz.

25 ns to 45 ns, than the actuation with 15.90 kHz, which shows pulse durations between 40 ns and 50 ns. The error bars denote again the sample standard deviation mentioned in the paragraphs above. The variation in pulse durations shows a slight trend towards lower pulse durations for higher OC reflectivities for the 15.87 kHz actuation and no conclusive trend for the 15.90 kHz actuation. This is similar to the behaviour shown for the pulse delays, where an increase in the time values would be expected for higher OC reflectivities. Possible reasons for this deviation of the experimental trend from the expected behaviour are the same as already mentioned for the pulse delays, with loss variations between the cavities having different OCs having an influence due to the cavities sensitivity to alignment. Also changes to the mirror surface and coatings are more likely in this 2-mirror configuration as residual pump light of the gain medium close to the MEMS might create additional heating and changes on the mirrors depending on the pump power. Again further investigations are desirable with mirrors with increased coating quality.

The theoretical minimum pulse duration at threshold with different OC values can be estimated using [179]:

$$\tau_{min} \approx 8.1 \cdot \frac{\tau_r}{\ln(G')} \tag{4.23}$$

τ_r is the cavity round-trip time and G' the gain within the cavity. The minimum gain needed for laser actuation can be estimated using the reflectivities of the 2 mirrors as $G' = 1 + (1 - R_{oc} \cdot R_{mems})$, ignoring additional losses in the resonator. For the cavity configurations with $R = 60\,\%$, $70\,\%$ and $80\,\%$ this leads to cavity limited pulse durations of 27 ns, 34 ns and 47 ns, which is in the range of the measured minimum values. This estimation also shows the expected behaviour of increased cavity limited pulse durations with increased reflectivity of the OC, leading again to a possible reason of higher losses in the experimentally obtained pulse behaviour for the $R = 80\,\%$ OC.

Spatial output characteristics

The spatial characteristics of the laser output were measured for all cavity configurations during Q-switch actuation at a distance of 50 mm from the OC using a WinCamD CCD camera. From the temporal investigations discussed above, a spatial output consisting of two beam spots is expected, as a non zero pulse delay time leads to a different mirror position during pulse emission for the opposite mirror movement directions. The top row images of Fig. 4.34 show four examples of the measured beamprofile, each from the cavity using the $80\,\%$ reflectivity OC but with different MEMS mirror driving conditions and varying output power. In all four cases an output with two overlapping beam spots can be seen. The vertical stripes seen for both 25 mW outputs are smear from the CCD readout. The determination of the midpoint position of each beam and subsequently the midpoint beam separation d between both output beams was determined graphically. The accuracy of this determination is limited by the overlap between both spots and by the noise of the CCD camera measurement. Slight intensity fluctuations and minimal beam steering of the output can also lead to the noise seen in the output profiles. For the MEMS actuation with 15.87 kHz a midpoint beam separation between 250 μm and 450 μm was estimated at the measurement plane 50 mm from the OC, with no identifiable trend for varying OC reflectivities (see Fig. 4.34(a)). For the higher average output power of 25 mW a wider beam separation can be seen with in average 25 μm

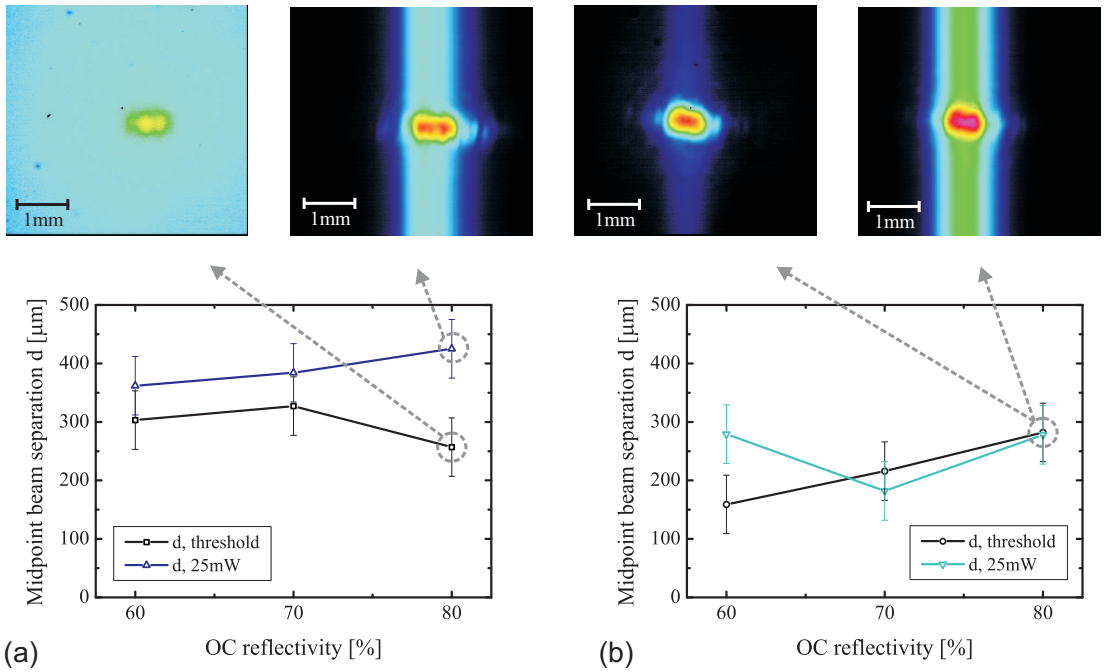

Figure 4.34: Summary of the measured midpoint beam separation of two successive pulses of the 2-mirror Q-switched output with (a) MEMS mirror actuation with 15.87 kHz and (b) MEMS mirror actuation with 15.90 kHz.

wider separation. With a measurement accuracy in the range of 50 μm this trend has to be treated carefully though. For the MEMS actuation with 15.90 kHz the midpoint beam separations were estimated between 150 μm and 300 μm (see Fig. 4.34(b)). Again due to the measurement accuracy already discussed for the other actuation case no conclusive trend can be identified for varying OC reflectivities.

The trend of a wider spatial separation between the output spots for the 25 mW measurements fits to the temporal pulse observation of longer pulse delays for these outputs compared to the measurements around laser threshold. The trend of an increase in pulse delay combined with a reduction of the spatial output spot separation when moving from the 15.87 kHz actuation to the 15.90 kHz actuation seems counter intuitive but occurs due to the change in the MEMS mirror movement speed. As the mirror moves slower an increase in the temporal delay of the pulses can still translate to a smaller spatial midpoint separation, which is present here.

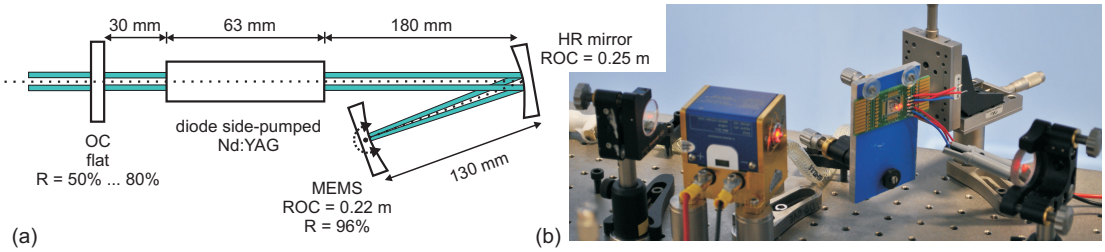

Figure 4.35: (a) 3-mirror Q-switch cavity schematic using a gold coated MEMS mirror and (b) image of the assembled cavity in the laboratory.

4.7 3-mirror cavity for double spot output evaluation

A 3-mirror cavity setup was investigated, in addition to the previously discussed 2-mirror cavity, to create a higher spatial separation between the two observable laser output spots while keeping a stable cavity. A more accurate measurement of the beam separation and the pulse build-up behaviour is therefore possible. A 3-mirror cavity is also used to evaluate the performance of a dielectric coated MEMS micromirror whose coating originates from an intermediate step in a project designed to create HR dielectric coatings with low stress for thin substrates. This coating and its influence was already discussed previously in this chapter.

4.7.1 Cavity setup for gold coated mirror

The 3-mirror laser cavity for using the second gold coated MEMS micromirror as active Q-switch is shown schematically in Fig. 4.35, including an image of the used physical setup. This gold coated micromirror with ROC of 220 mm and reflectivity of $R = 96\,\%$ at the lasing wavelength of 1064 nm is again used as cavity end-mirror. A HR dielectric coated mirror ($R > 99.5\,\%$) with a concave surface curvature with ROC of 250 mm is used as folding mirror at a distance of 130 mm from the MEMS micromirror. The Nd:YAG gain medium is placed in the intra-cavity arm between the flat OC (30 mm distance) and the folding mirror (180 mm distance) with the properties of the gain medium already described for the 2-mirror cavity setup. The cavity design was again constructed using the software WinLase with the aim of achieving a high cavity stability

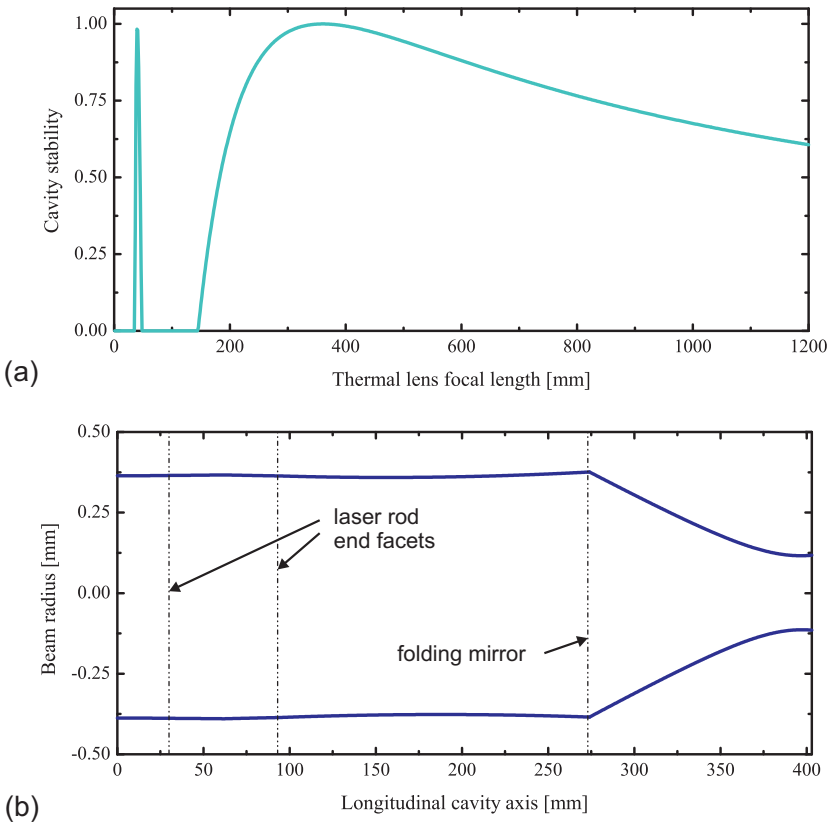

Figure 4.36: (a) Simulated 3-mirror cavity stability for varying thermal lens focal length and (b) laser beam radius evolution through the cavity with MEMS mirror at the right hand side.

throughout the possible range of thermal lensing values of the gain medium during laser operation. The resulting cavity stability diagram for varying thermal lens focal length values can be seen in Fig. 4.36(a), with the relevant thermal focal length range between 1200 mm (for a pump diode current of 12 A) and 300 mm (for a pump diode current at 22 A) showing cavity stabilities of $> 61\,\%$. The thermal lens values were again taken from the gain module data sheet (see Appendix C). When comparing the cavity stability with the diagram obtained for the previously used 2-mirror cavity a lower stability can be seen, especially towards higher thermal lens focal length values. This shows that the cavity is more susceptible to stability changes with cavity length or mirror focal power changes. Nevertheless it is still possible to build a stable laser cavity over the full usable range of the thermal lens focal length. The theoretical beam radius of the supported basic Gaussian mode of the intra-cavity laser field can be seen in Fig. 4.36(b)

for a thermal lens focal length value of 1200 mm, which corresponds to an optical side-pump power of 41 W. The theoretical beam diameter on the micromirror is in this case 235 μm with a beam widening towards the OC to a diameter of 728 μm. With the smaller beam radius on the MEMS a possible alignment over a wider transversal position of the micromirror can be achieved which allows an easier initial alignment.

4.7.2 Loss determination of cavity

The cavity losses are required as input to the simulation of the temporal output behaviour of the Q-switched laser using the rate equation model discussed previously. As the MEMS Q-switch falls into the category of slow Q-switching, it is not enough to measure the losses at perfect alignment but it is also required to determine the dependency of the cavity losses on the MEMS mirror rotation angle. To determine the round-trip losses inside a laser cavity two approaches are generally used. The first approach, widely referred to as the Findlay-Clay loss measurement due to the demonstration in their 1966 paper [180], determines the intrinsic losses inside the cavity using the pump power at laser threshold with varying OC reflectivities. The second approach was first used by Caird et al. in their investigation of a chromium doped gallium fluoride garnet laser [174], evaluating the cavity round-trip losses by measuring the slope efficiency η_s of the cw laser output with varying OC reflectivities. The slope efficiency of a laser is defined as the slope of the optical output power versus optical pump power graph. The slope efficiency relates to the cavity losses per pass in its most basic form for cw pumping with [174]

$$\eta_s = \frac{\lambda_p}{\lambda_o} \cdot \frac{O}{O+L}, \tag{4.24}$$

where λ_p and λ_0 are the pump and output laser wavelength, O describes the total output coupling fraction and L is the cavity loss per pass. Further loss factors like a nonunity pumping efficiency or excited state absorption have to be considered as well and can be included as additional efficiency factors. These factors can be combined with the quantum defect related factor λ_p/λ_o and lead to a limiting slope efficiency

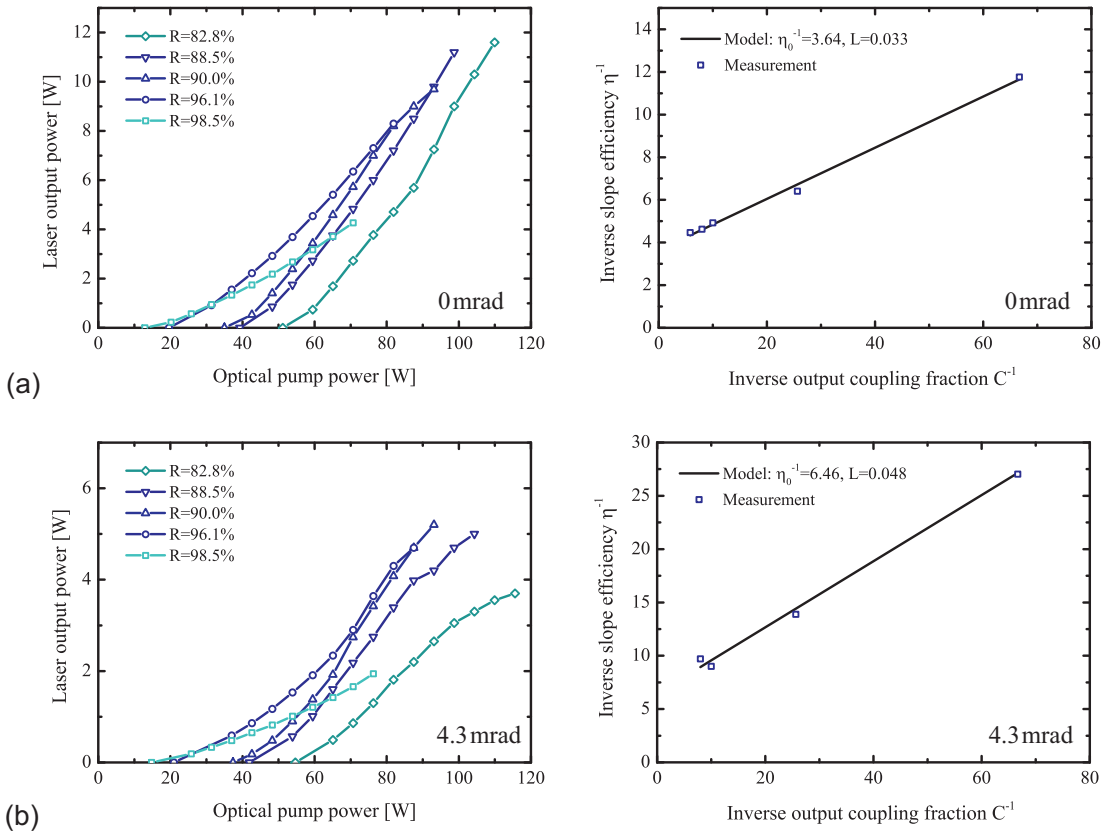

Figure 4.37: (a) Slope efficiency measurements and (b) loss calculation for the 3-mirror cavity for perfect alignment and (c) slope efficiency measurement and (d) loss calculation for a mirror tilt angle of 4.3 mrad; measurements were undertaken using an HR coated equivalent mirror.

for vanishing passive losses of η_0. Inverting this resulting equation leads to a linear relationship between the inverse slope efficiency η_s^{-1} and the inverse output coupling fraction O^{-1} as

$$\eta_s^{-1} = \eta_0^{-1}\left(1 + L \cdot O^{-1}\right). \tag{4.25}$$

Plotting therefore the inverse slope efficiency versus the inverse output coupling fraction and using a linear fit to this graph will allow the identification of the cavity losses L.

This second approach is used here, as the determination of the laser slope will occur through multiple laser output power measurement points and therefore does not rely only on a single threshold measurement point per OC configuration, which is the case for the Findlay-Clay analysis. To obtain the slope efficiency values, a CW output power

of up to several Watts is needed, hindering the use of the so far coated MEMS mirrors due to their current power handling limits. Therefore an equivalent mirror with similar ROC was used in the place of the MEMS for the loss measurement to experimentally model the MEMS mirror. The mirror consisted of a commercially available 25.4 mm BK7 substrate with a concave curvature with ROC of 250 mm and a HR dielectric coating with a reflectivity > 99.5 % at λ = 1064 nm. The mirror was placed inside a Newport U100-G gimbal mirror mount equipped with micrometre adjustment screws with 127 TPI (turns per inch). A full turn of one of the screws translates to a tilt of 5.73 mrad of the mirror in respect to the cavity axis. The cavity alignment was set to the centre of the HR mirror; therefore creating the similar movement possibility for the equivalent mirror as the aligned MEMS mirror has. No additional aperture was introduced in the cavity, with the limiting aperture therefore defined through the diameter of the gain medium.

To determine the angular dependent cavity losses, slope efficiency measurements were carried out for OC reflectivity values of 98.5 %, 96.1 %, 90 %, 88.5 % and 82.8 %. For each configuration the cavity was aligned for lowest midpoint threshold to measure the slope efficiency for the perfect aligned state, followed by slope efficiency measurements for 4 discrete angles of 1.43 mrad (0.082°), 2.87 mrad (0.164°), 4.30 mrad (0.246°) and 5.01 mrad (0.287°).

Fig. 4.37 shows exemplar measured laser power transfer curves and the resulting Caird analysis graphs for a MEMS angle of (a) 0 mrad, coinciding with a perfect midpoint alignment, and (b) 4.3 mrad. The power transfer curves show the expected behaviour of lower slope efficiencies with the angled mirror configuration, as consequence of a higher intra-cavity loss. It can also be seen that for the angled cavity configurations with higher output coupling (R = 82.8 % and R = 88.5 %) a saturation effect of the laser slopes is present at higher pump powers. This can be caused due to aperturing of the intra-cavity field at the edges of the gain medium combined with a larger laser spot size on the micromirror. Especially for the 82.8 % configuration it is difficult to determine where the

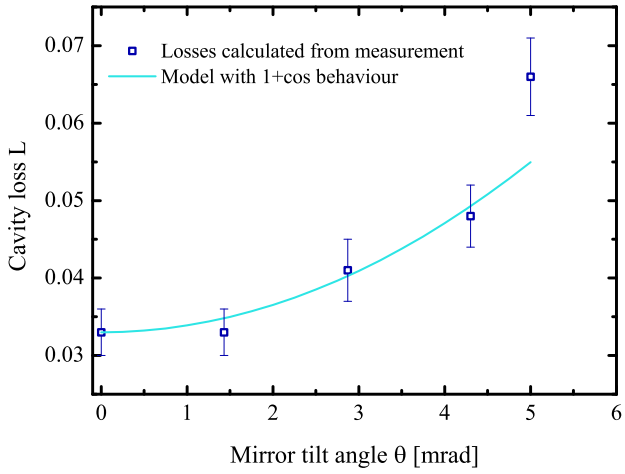

Figure 4.38: Angular dependent loss resulting from the individual Caird measurements including a model fit using a cosine dependency.

non-apertured slope is present, which lead to an omission of this data point in the further loss analysis. The inverse values of the fitted slope efficiencies for all configurations are plotted versus the inverse output coupling fraction. In accordance with the Caird analysis a linear fit is applied to the data points using the model equation (4.25), leading to an intra-cavity loss of 3.3 % for the 0 mrad alignment and 4.8 % for the 4.3 mrad tilted mirror alignment. The same procedure has been repeated for the measurements of the further tilt angles, resulting in an overall dependency of the losses on the mirror tilt angle shown in Fig. 4.38. To be able to use this angular loss dependency for the following rate equation simulations, a fit to the measured data was employed using the cosine dependency defined in equation (4.15). The parameters for the used fit are $A = 42$ and an offset of $\gamma_0^* = 0.033$, which is the midpoint loss γ_0 without taking the losses through the cavity-end mirror into account. A cosine fit was adopted following the approaches by [168, 172]. The fit shows good agreement for the angular values up to 4.3 mrad with the loss of the 5 mrad measurement being underestimated. It has to be noted, however, that at the higher mirror angle aperturing of the intra-cavity laser field at the edges of the gain medium can occur for higher output powers during the slope efficiency measurements, leading to a reduced output power which therefore overestimates the

losses that would occur for the Q-switched output. The fitted loss curve is therefore still considered adequate as simulation input.

4.7.3 Temporal and spatial intra-cavity simulation

The simulation of the time-dependent pulsed laser output behaviour was constructed in Matlab using the rate equation approach discussed in section 4.3.1. This simulation approach was not followed for the previously discussed 2-mirror cavity laser as no conclusive measurement of the angular dependent losses was possible. This loss determination is required for the description of the mirror behaviour in the simulation, which meant that only the presented 3-mirror cavity was simulated and the obtained laser output results compared with the experimentally obtained values for this case. The input parameters of the simulation are grouped into laser cavity dependent parameters and MEMS mirror dependent parameters. The necessary parameters from the laser cavity are the round-trip length of the cavity $l_c = 906.8\,\mathrm{mm}$, the length of the gain medium $l_a = 63\,\mathrm{mm}$, the stimulated emission cross-section $\sigma = 2.7 \cdot 10^{-23}\,\mathrm{m}^2$ and the pump power ratio for 25 mW average output power $P_p/P_{pc} = 1.15$ for an OC reflectivity of 50.6 % and $P_p/P_{pc} = 1.09$ for OC reflectivity values of 59.0 %, 70.6 % and 82.7 %. The input parameters of the MEMS mirror are needed to generate the time-dependent optical losses with the mirror movement frequency f, the maximum mechanical tilt angle $\theta_m = 319.4\,\mathrm{mrad}$ for $f = 7915\,\mathrm{Hz}$ and $\theta_m = 234.7\,\mathrm{mrad}$ for $f = 7925\,\mathrm{Hz}$ and the mirror reflectivity $R = 96\,\%$ which contributes towards the time-dependent loss function $\gamma(t)$. For the losses the parameters $\gamma_0 = 0.033$ and $A' = 42$ are used, determined from the experimental values in the previous section.

To match the experimental behaviour discussed below, an additional factor k' has to be included for the calculation of the initial inversion density n_0. This factor could be caused by thermal effects on the coated MEMS mirror surface, as it is dependent on the reflectivity of the OC, and therefore on the intra-cavity power incident on the MEMS. To obtain simulated output pulses with pulse delay times coinciding with the measurements

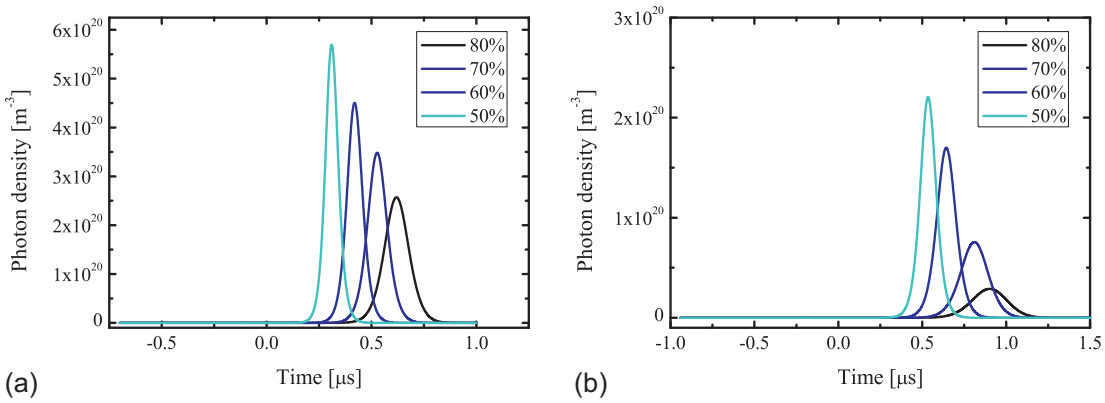

Figure 4.39: Simulated photon density inside the cavity (a) for 15.83 kHz actuation and (b) for 15.85 kHz actuation.

the factor takes the values 1.07, 1.16, 1.24 and 1.41 for 50.6 %, 59.0 %, 70.6 % and 82.7 % OC reflectivity respectively when actuating the MEMS with a frequency of 15.83 kHz. For the second driving frequency of 15.85 kHz, also used in the following experiments, the k' parameters needed to match the simulated laser output with the measurements are 1.11, 1.14, 1.20 and 1.34, respectively for the OC reflectivities mentioned before.

The simulated intra-cavity photon density development over time is shown in Fig. 4.39. The time origin is in both cases set to the micromirror midpoint pass through the cavity alignment. With rising OC reflectivity a longer pulse build-up time can be seen with a lower maximum photon density at the emission peak. The rising flank of the pulse has also a reduced slope steepness with rising OC reflectivity. These two trends can be explained due to the rise of losses inside the cavity for longer pulse delay times, originating from the mirror movement. Comparing the output for a mirror actuation with 15.83 kHz and 15.85 kHz, an increase of the delay time and at the same point a reduction of the maximum photon density can be seen for the higher actuation frequency. In this case, the reduction of the mirror scan angle for the higher actuation frequency leads to a slower movement speed through the alignment resulting in longer pulse delays for the output around lasing threshold.

A summary of the simulated pulse delay times t_d and pulse durations τ for varying actuation frequency and OC reflectivities is shown in Fig. 4.40. The pulse delay time

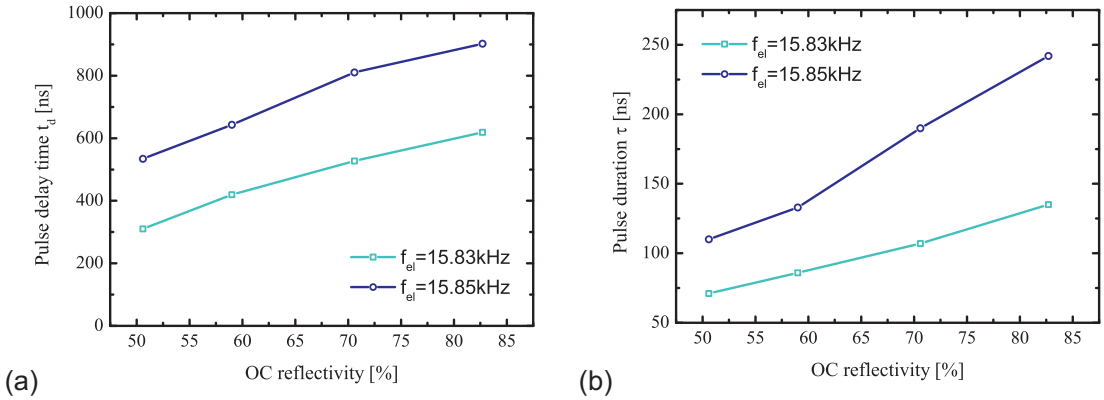

Figure 4.40: Simulated pulsed laser output values of (a) pulse delay time t_d and (b) pulse duration τ.

shows the already mentioned trend of increased delay times for rising OC reflectivity as well as lower mirror movement speed. For an actuation with 15.83 kHz pulse delays between 310 ns and 620 ns are simulated for 50.6 % and 82.7 % OC reflectivity respectively. These are in good agreement with the experimental values, which will be presented and discussed in the following section 4.7.4, due to the applied scaling factor. The pulse durations also show an increase with rising OC reflectivity and reduced mirror speed, which is again related to the increase in intra-cavity losses at the moment of laser emission. A comparison between these simulated values and the experimentally obtained results is given at the end of the following section 4.7.4 with a detailed discussion on the differences and their possible reasons.

4.7.4 Pulsed output at threshold and at 25 mW

The experimental measurement setup for determining the temporal and spatial Q-switched laser output characteristics of the 3-mirror cavity (see Fig. 4.41) is similar to the one used for the 2-mirror cavity described previously. Three photodiodes (PD1 - PD3) are used to determine the temporal characteristics of the laser pulse-train, including the pulse delay time in respect to the micromirror midpoint crossing. A scanning slit optical beam profiler (BP) is used to determine the spatial output at a distance of 50 mm from the OC.

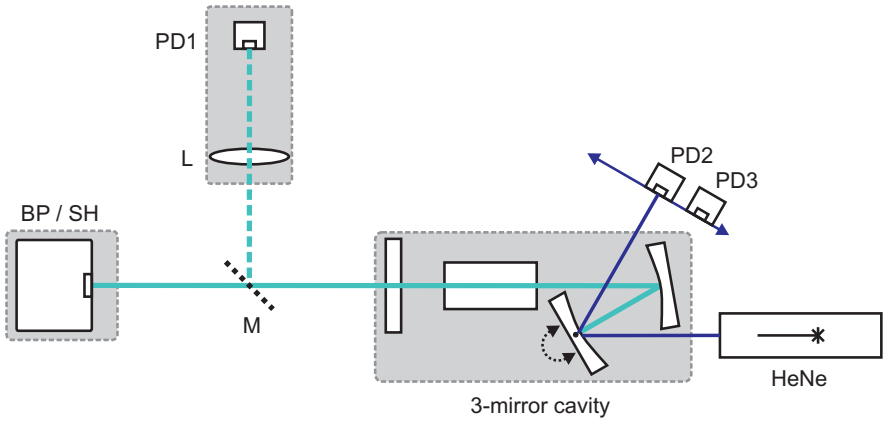

Figure 4.41: Measurement schematic for the 3-mirror temporal and spatial output behaviour, PD1-3: photodiodes, L: lens with $f' = 200\,\text{mm}$ focal length, BP: beam profiler, SH: Shack-Hartman wavefront sensor, M: HR mirror for switching between temporal and spatial measurements.

As a pulse delay between the mirror midpoint position and the emitted Q-switch pulse will translate to a wider spatial separation in the 3-mirror cavity than observed for the 2-mirror cavity, the spatial Q-switched laser output will show no overlap between the two output spots and therefore allows the determination of the deviation from parallelism of the two beams. This measurement is experimentally done using a Thorlabs WFS150-5C Shack-Hartmann wavefront sensor at the position of the BP. For alignment of the wavefront sensor no special procedures are required as only the opening angle between both laser output spots is of interest and not their individual angle in respect to the cavity axis. The wavefront sensor measures the distortion of the incoming optical wave in respect to an ideal plane wave by using a microlens array which divides the incoming beam and focuses each part on a sensor placed at the focal point of the microlens array. A distorted waveform will relate to a displacement of each individual lenslet focal point, which is used to calculate the waveform aberrations. These aberrations are quantified using Zernike polynomials in which two of the coefficients correspond to the tilt in x- and y-direction [181]. The experimental measurement results and corresponding calculation to gain the opening angle between the two output beams will be shown during the spatial output discussion.

To evaluate the intra- and extra-cavity independence of the two output spots (which

are also present in the 2-mirror cavity and whose presence in the here discussed cavity will be shown at the spatial behaviour below) a knife-edge (KE) was transversally moved through the intra- and extra-cavity laser field, with the resulting behaviour also presented in the spatial output characteristic discussion. An example pulse-train for the 3-mirror cavity is similar to the already shown pulse-train for the discussed 2-mirror cavity (see Fig. 4.29). One difference is the pulse delay as a potentially higher pulse delay is possible for the 3-mirror cavity.

Temporal output characteristics

The temporal output characteristics of the 3-mirror laser cavity using the previously described gold coated MEMS micromirror were determined using cavity configurations with four different OC mirrors with reflectivities at 1064 nm between 50 % and 80 %, which were presented in more details in the 2-mirror section. The added nominal 50 % OC had a measured reflectivity of 51 % and could be used in this case due to a lower laser threshold occuring for the 3-mirror laser cavity. The cavity was aligned for the lowest possible cw lasing threshold for each OC mirror before conducting the Q-switch measurements. Measurements of the Q-switch actuated laser output behaviour were, similar to before, taken at lasing threshold (average output power < 1 mW) and at an average output power of 25 mW. The pulse shapes and delays for the laser output with a MEMS micromirror actuation with 200 V and an electrical offset square-wave driving frequency of 15.83 kHz, translating to a movement frequency of 7.915 kHz and a TOSA of 73.2°, are shown in Fig. 4.42. For all four OC configurations the laser pulse build-up time is longer than the time interval needed by the moving mirror to cross its midpoint position, which leads to a positive delay time t_d. With rising OC transmission a lower delay time can be seen for both the threshold and 25 mW case. The rising OC transmission is related to a higher necessary pump power to reach the threshold condition and therefore a higher initial inversion density which is the reason for the reduced delay time. The pulse durations are visibly shorter for the lower OC

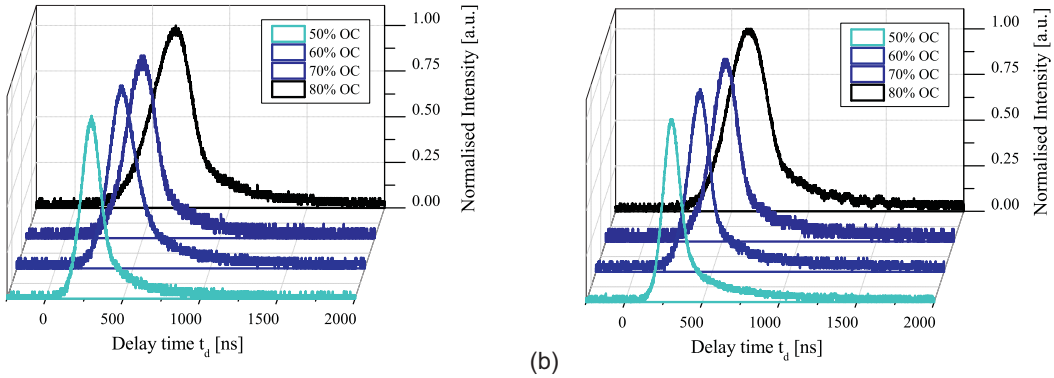

Figure 4.42: Pulse shapes for the 3-mirror cavity with Q-switched output of 15.83 kHz MEMS actuation for varying OC reflectivities for (a) threshold and (b) 25 mW average output power.

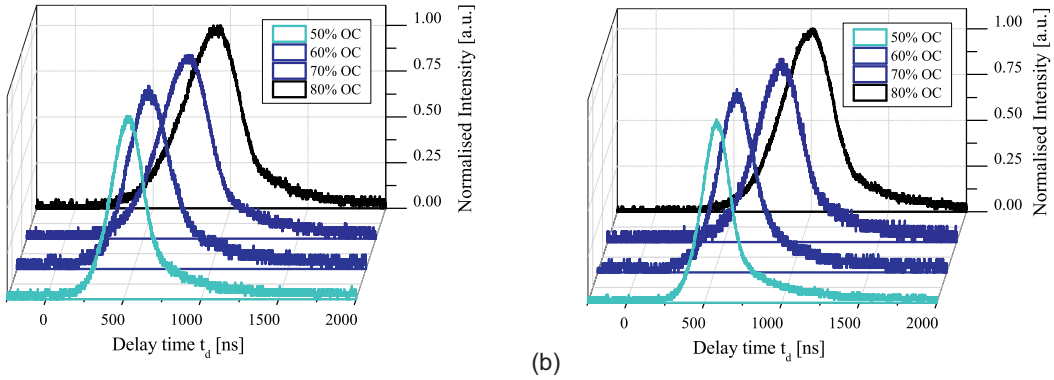

Figure 4.43: Pulse shapes for the 3-mirror cavity with Q-switched output of 15.85 kHz MEMS actuation for varying OC reflectivities for (a) threshold and (b) 25 mW average output power.

reflectivity value of 50 % compared to the 80 % OC cavity results. The elongation of the pulse can be mainly attributed to a longer pulse rise time originating from the lower initial inversion density present for the cavity with higher OC reflectivity.

For the pulse output originating from a MEMS actuation with a driving frequency of 15.85 kHz, leading to a TOSA of 53.8°, a similar behaviour can be seen in Fig. 4.43. The threshold and 25 mW graphs show again a close agreement. The pulse delay times and the increase of the pulse delay time with rising OC reflectivity are higher when comparing the pulses with the output from the 15.83 kHz actuation.

The summary of the measured pulse delay times for all investigated OC configurations

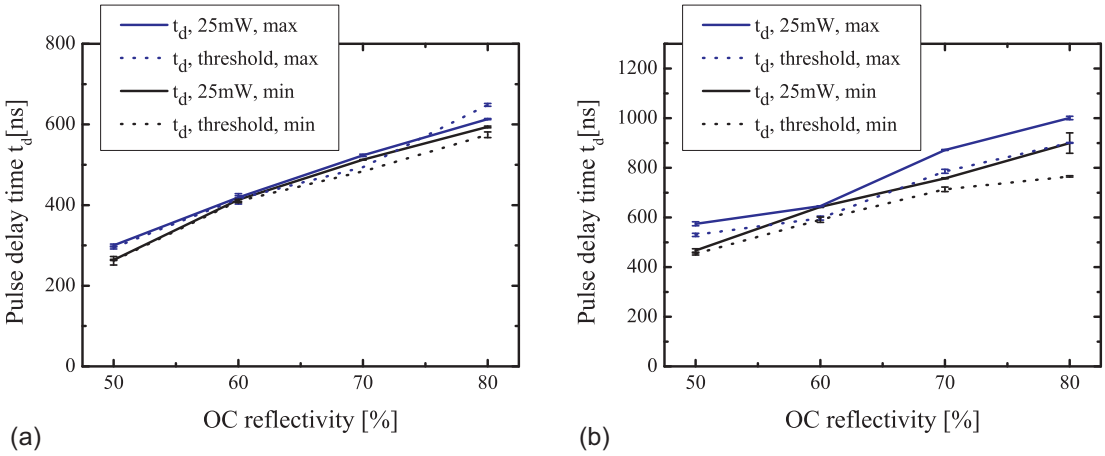

Figure 4.44: Summary of the measured pulse delays for all 3-mirror Q-switch actuation configurations using gold coated mirrors with (a) MEMS mirror actuation with 15.83 kHz and (b) MEMS mirror actuation with 15.85 kHz.

is shown in Fig. 4.44. The subscripts "min" and "max" are again used for distinguishing the pulses originating from the two movement directions, with small offsets possible due to alignment tolerances. For the actuation with f = 15.83 kHz the already mentioned increase of t_d with increasing OC reflectivity can be seen with delay times between 260 ns for the 50 % OC cavity and 650 ns for the 80 % OC cavity. The actuation with 15.85 kHz shows a similar trend with longer pulse delay times compared to the lower frequency actuation and up to 100 ns longer delay times for the output with 25 mW average power compared to the threshold condition. The pulse delays are between 450 ns for the 50 % OC configuration and 1 μs for the 80 % OC configuration in this case. The slower movement through the midpoint position for the higher frequency actuation leads to an increase of the delay time by almost a factor 2. The trend of lower pulse delays for lower OC reflectivities is following the expected behaviour due to an increase in the necessary inversion density for lower OC reflectivities. This increase is required to reach the laser threshold due to the added cavity losses by the higher outcoupling. The behaviour also matches the simulation results shown earlier.

The measured pulse durations for the discussed laser pulse outputs are shown in Fig. 4.45. The trend for both MEMS actuation frequencies shows a higher pulse duration τ for higher OC reflectivity values and matches the trend seen in the pulse delay

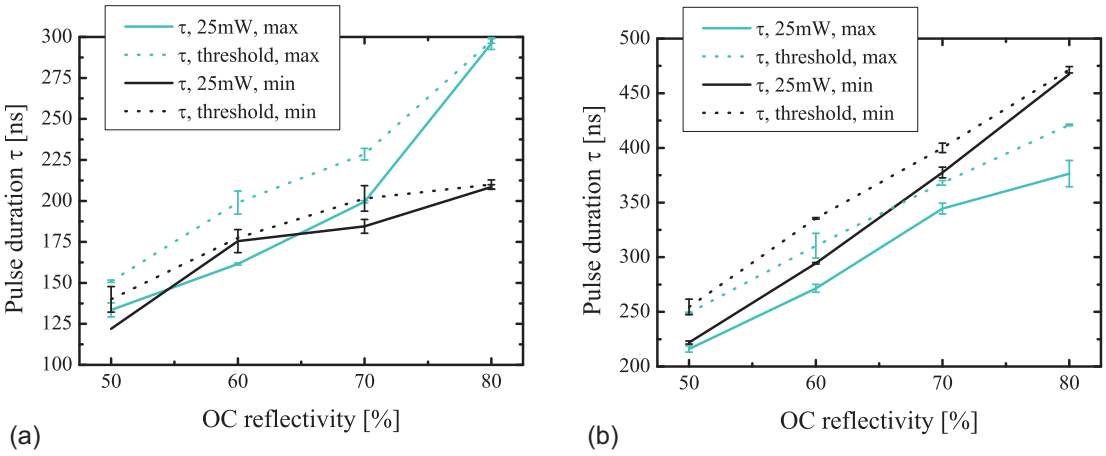

Figure 4.45: Summary of the measured pulse durations for all 3-mirror Q-switch actuation configurations using gold coatings with (a) MEMS mirror actuation with 15.83 kHz and (b) MEMS mirror actuation with 15.85 kHz.

measurements. Higher pulse delays lead to a further deviation from the optimum pulse timing and higher cavity losses at the time of pulse emission. A high offset between the pulse durations of the two scanner movement directions of up to 90 ns can be seen, especially when using an OC reflectivity of 80 %. The reason for this can be associated with the higher pulse delay time where the propagating field of the pulse within the laser cavity gets laterally shifted towards the physical boundary of the laser rod. A potential lateral shift of the inital alignment in respect to the cavity axis will then lead to a different proximity of the intra-cavity fields to the laser rod edges which can lead to a different effective loss and pulse duration between the pulses emitted from the two micromirror movement directions. The measured pulse durations for 15.83 kHz actuation are between 120 ns for the 50 % OC cavity and 300 ns for the 80 % OC cavity. For the actuation with 15.85 kHz the related longer pulse durations are measured to be between 220 ns for the 50 % OC and 470 ns for the 80 % OC. The trend of lower pulse durations with lower OC reflectivities is again expected due to the same reasons already mentioned for the pulse delays, with higher necessary initial inversion densities leading to lower pulse durations. At the end of this section the experimentally determined pulse duration values are compared with the simulation results and also set into context with the theoretical minimum obtainable pulse durations of the cavity.

Spatial output characteristics

The spatial output profile of the Q-switched 3-mirror laser cavity configurations is measured using a Thorlabs BP-104IR beam profiler at a distance of 50 mm from the OC. The dual-spot output present for the 2-mirror Q-switch laser outputs is again visible with a wider midpoint separation between the two spots, leading to a profile in which no overlap exists between them. The top row of Fig. 4.46 shows typical spatial output profiles for the cavities using the lowest OC reflectivity of 50 %, which has the shortest pulse delay for the measured 3-mirror cavities. For each threshold and 25 mW output condition the two spots can be distinguished. For the MEMS mirror actuation with 15.83 kHz the dependency of the midpoint beam separation d between both output spots on the OC reflectivity is shown in Fig. 4.46(a). The trend follows the pulse delay behaviour discussed in the previous section with a minimum d of 900 μm achieved for the 25 mW output with an OC of 50 % and a maximum measured d of 1.52 mm for the 25 mW output of the 80 % OC cavity. When looking at the mirror actuation with 15.85 kHz a similar minimum beam separation distance can be seen for the 50 % OC cavity with a separation value of 860 μm. The slope of the growing beam separation with increase of the OC reflectivity is nevertheless lower than the one at an actuation of 15.83 kHz and leads to a maximum d of 1.3 mm for the used cavity configurations. The reason behind this is the pulse delay behaviour, which also shows a lower slope for the slower mirror movement speed at the actuation frequency of 15.85 kHz and to which the spatial output behaviour is coupled.

To confirm the allocation of the spatial and temporal outputs, as well as to investigate the intra-cavity independence, a KE was mounted on a micrometre stage and was moved horizontally through the extra- and intra-cavity laser field. By moving the KE through the extra-cavity laser field at a distance of 20 mm from the OC, each of the output spots could be blocked individually, which matched with a disappearance of the corresponding laser output pulses of one of the mirror movement directions. By moving the KE through the intra-cavity field, a simultaneous annihilation of both output spots

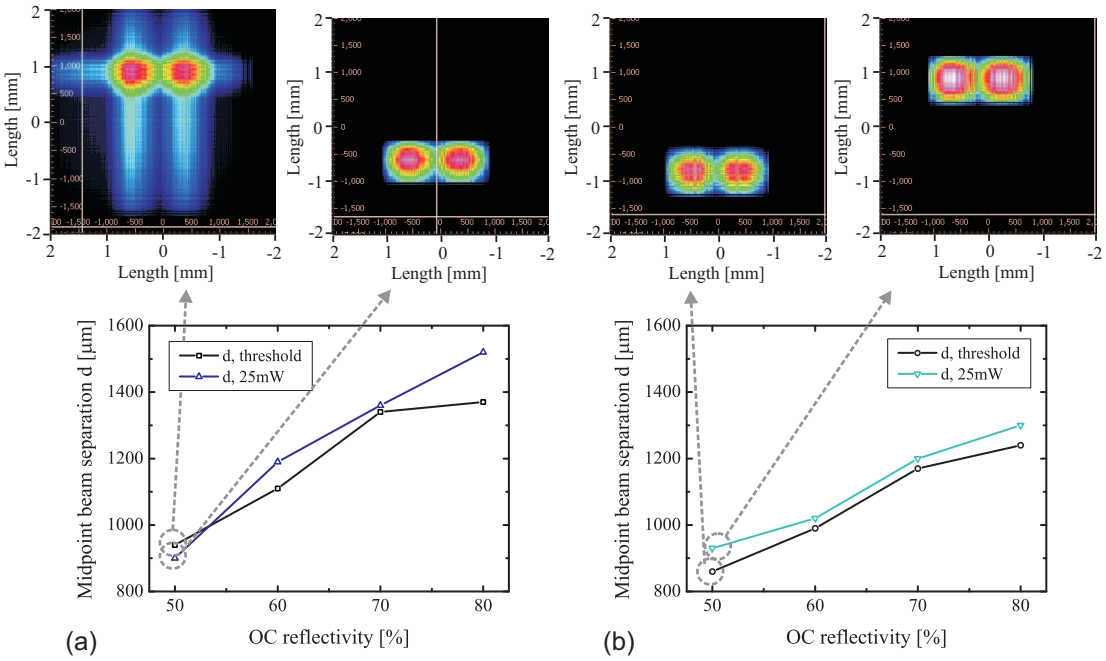

Figure 4.46: Summary of the measured midpoint beam separation of two successive pulses of the 3-mirror cavity using the gold coated micromirror for Q-switched output with (a) MEMS mirror actuation with 15.83 kHz and (b) MEMS mirror actuation with 15.85 kHz.

is observed. The reason for this is the needed intra-cavity round trips for building up of the laser pulse from spontaneous emission. These are delayed by the introduced KE which changes the cavity loss during the pulse build-up, up to the point where the time for which the moving mirror provides feedback through the cavity is too small to support the output of a laser pulse. As this time interval for pulse build-up is required for pulses originating from both micromirror movement directions both of the outputs vanish simultaneously when moving the KE through the intra-cavity alignment path.

With the Q-switched laser output spots being spatially separated a determination of the parallelism of the two output beams is possible by using the previously mentioned Thorlabs WFS150-5C Shack-Hartmann wavefront sensor. The measurement uses Zernike coefficient to describe the waveform deviation from an ideal plane wavefront. The first six Zernike coefficients, as defined for the wavefront sensor, are shown in Fig. 4.47 with the corresponding example wavefront distortion and a normalisation

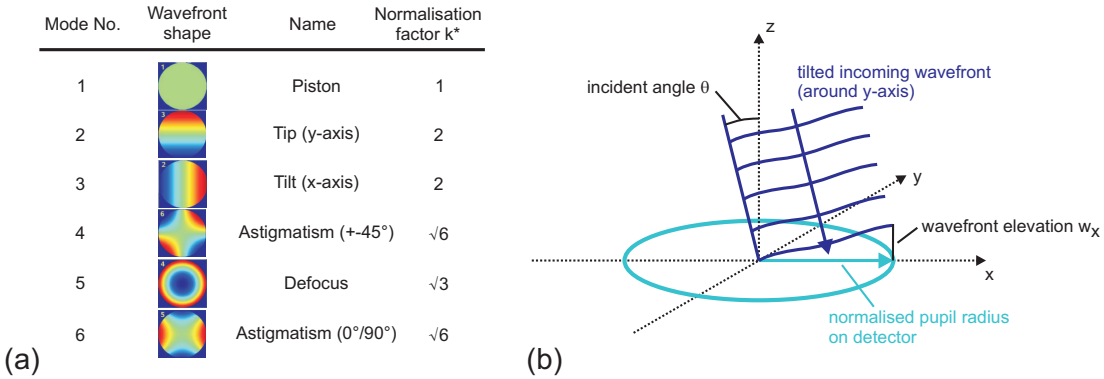

Figure 4.47: (a) List of the first six Zernike coefficients with the corresponding wavefront shape (from [182]), description and normalisation factor and (b) measurement schematic on the wavefront sensor for a tilt around y.

factor k^*, which is used in the measurement software to generate an orthonormal function set of the Zernike polynomials [181]. To obtain the individual waveform distortions of both laser output spots a pupil with diameter D is defined in the wavefront sensor measurement program which only encloses one of the output spots. From the measurement values the Zernike coefficient number 3, $c_{n,x}$, is used to determine the tilt angle of the individual beam in the x-axis as both output beams are offset only in this axis. To calculate the tilt angle θ from the given Zernike coefficient one can use trigonometric relationships according to the schematic on the right hand side of Fig. 4.47. A tilt around y gives a wavefront elevation of $w_x = k^* \cdot c_{n,x} \cdot 1 = 2 \cdot c_{n,x}$ on the sensor pupil. The factor 1 originates from the use of the normalised pupil radius as base for the elevation calculation. The incident angle θ can then be calculated using the pupil diameter D' defined for the measurement with:

$$\theta = \arctan\left(\frac{4 \cdot c_{n,x}}{D'}\right) \tag{4.26}$$

The wavefronts were measured for both output spots individually at a distance of 50 mm from the OC with an average output power of 500 μW to avoid saturation of the sensor. The relevant measured Zernike coefficient and the resulting divergence angle α_{rel} between the two output spots are shown in Table 4.2. The individual angles of each of the output beams are given in respect to the orientation of the wavefront sensor, which

Table 4.2: *Measured Zernike coefficients $c_{n,x}$ for x-axis tilt and resulting relative angles θ_{rel} between the output spots of the used 3-mirror cavities with* 15.83 kHz *actuation.*

OC	Position	$c_{n,x}[\mu m]$	D' [mm]	θ [mrad]	θ_{rel} [mrad]	θ_{calc} [mrad]
50 %	right	0.695	1.112	2.5	3.3	5.6
	left	-0.224	1.112	-0.8		
60 %	right	-0.579	1.312	-1.8	4.0	6.4
	left	-1.914	1.312	-5.8		
70 %	right	-1.319	1.312	-4.0	5.3	5.8
	left	-3.066	1.312	-9.3		
80 %	right	-3.481	1.312	-10.6	1	6.0
	left	-3.791	1.312	-11.6		

was aligned in the measurement system without special measures to generate a perfectly orthogonal orientation in respect to the cavity axis. As only the relative angle between the two output beams is of interest this was deemed to be an acceptable step. For all four cavity configurations no parallelism of the output beams was found, with all of them showing a convergence of the two beams at the measurement plane, with a relative opening angle between 1 mrad and 5.3 mrad. This behaviour was also modelled using the pulse delay time measurements obtained previously, in combination with the cavity geometry and thermal lens values for each laser driving condition of the selected OCs. This modelling was conducted using the ABCD matrix model discussed in section 4.3.2 by calculating the MEMS tilt angle corresponding to the respective pulse delay time and using this as input for the ABCD calculation. A converging behaviour between both beams was estimated at the measurement plane, with relative angles α_{calc} between both beams of 5.6 mrad, 6.4 mrad, 5.8 mrad and 6.0 mrad for the laser configurations using a 50 %, 60 %, 70 % and 80 % OC respectively. The fluctuation of the convergence angle originates from the combination of lower pulse delays for a cavity configuration with higher thermal lens focal power due to higher required pump power to reach the laser threshold. The measured relative angle between both beams is in the range of the calculated values, but still shows a deviation especially in the case of the 80 % reflective

OC. This deviation can originate for example from an offset of the beam position on the MEMS mirror, leading to an offset in the inital beam angle due to the concave surface curvature of the MEMS. The offset in the beam position on the MEMS can take place due to minimal horizontal misalignments of the mirror during cavity alignment or the resonance movement of the MEMS.

When comparing the simulated and experimental values for the laser output pulse duration, it can be seen that the simulation is underestimating the experimental pulse duration. While having the same trend, the experimental pulse durations are longer by about a factor of 2, with the simulated pulse duration at the 50.6 % OC reflectivity of about 70 ns and an experimental pulse duration of about 150 ns. Similarly for an OC reflectivity of 82.7 % at the actuation frequency of 15.85 kHz a simulated pulse duration of 240 ns is underestimating the measured pulse duration of about 450 ns.

This underestimation of the pulse duration in the simulation results can have its origin in the curvature of the MEMS mirror and the transverse distribution of the intra-cavity laser beam on the MEMS. As the mirror surface shows a concave curvature the normal vectors of the surface have an angular variation around the normal vector of the midpoint of the mirror. This combined with the intra-cavity laser spot size of 234 μm, which translates to a fill factor of 11 % of the micromirror, shows a possibility of an aligned cavity at mirror angles before and after the midpoint, which is also helped by the folding mirror of the cavity creating a wider acceptance angle for the mirror alignment than present in the 2-mirror cavity. This possibility of a transverse shift of the laser alignment around the mirror midpoint position could lead to an elongation of the pulse duration of the measured laser output, which can not be considered in the simulation. The reason for this is the chosen rate equation approach which does not consider a spatial varying profile along the transverse axis of the laser cavity and therefore can not account for the possibility of a movement of the laser alignment spot along the mirror. To include this possibility within a simulation of the Q-switched laser cavity a full field approach would be required, which is outside the scope of the work

presented here.

Comparing the measured pulse durations to the theoretical minimum obtainable Q-switch pulse durations according to equation (4.23) shows longer pulse durations in the experimentally observed case. The minimum theoretical pulse durations for the presented 3-mirror resonator with a cavity round-trip time of $\tau_r = 3.0\,\text{ns}$ are 58 ns, 69 ns, 86 ns and 116 ns for the cavity configurations using OC reflectivities of 50 %, 60 %, 70 % and 80 % respectively. This shows that the achievable pulse duration is for this cavity setup not limited by the cavity but by the scanning mirror. Reasons for this can be seen in the increased acceptance angle for alignments, compared to the previouly discussed 2-mirror cavity, due to the folding mirror and also due to the previously menioned possibility of alignments on varying positions of the curved micromirror surface.

4.7.5 Cavity setup for dielectric coated mirror

The dielectric coatings used for this investigation only form an intermediate step in the development of low stress HR coatings for thin substrates. The reflectivity of $R = 97\,\%$ and a convex surface curvature with ROC of $-0.77\,\text{m}$ of the test device are therefore not an ideal case for the application as cavity end-mirrors yet, but their behaviour was nevertheless investigated to gain preliminary insights. The micromirror on which the dielectric coatings were tested has the same driving principle as the previously discussed devices with a similar layout, which was also used for the investigations in chapter 3. A layout overview can be seen in Fig. 4.48(a) with the main difference to the previously used design being a wider torsion beam (18 μm instead of 12 μm) and the inclusion of a frame structure around the mirror surface. The device layer had the same thickness of 25 μm as the gold coated mirrors. The frequency response of the uncoated and dielectric coated micromirror is shown in Fig. 4.48(b) with an actuation and mechanical movement frequency of 10.418 kHz and a resulting TOSA of 13.3° after coating.

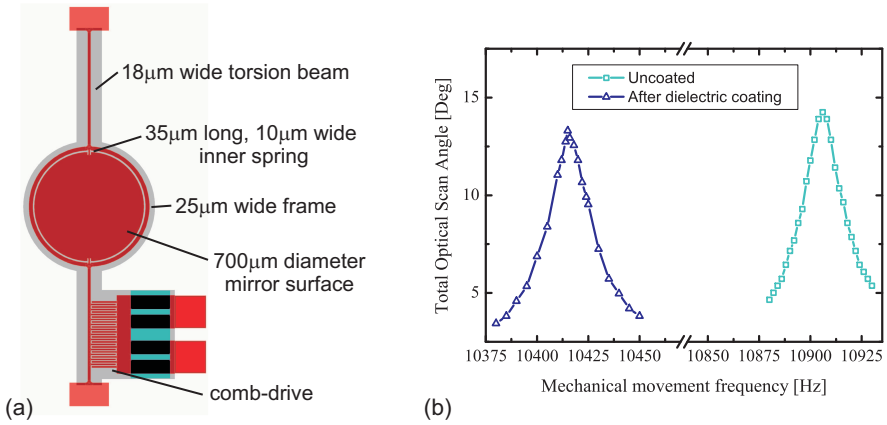

Figure 4.48: (a) Layout schematic of 700 μm diameter dielectric coated micromirror and (b) frequency response curves of the mirror before and after coating.

The convex surface curvature of the MEMS micromirror after coating hinders the build-up of a stable 2-mirror cavity that maintains its stability over the full range of possible thermal lens focal length values. Due to this, a longer 3-mirror cavity was chosen for the Q-switch investigations using a dielectric coated mirror. The constructed cavity is schematically shown in Fig. 4.49 using a HR folding mirror with a concave surface with ROC of 250 mm. The MEMS is again placed as cavity-end mirror in the cavity arm not containing the Nd:YAG gain medium, with a tilt angle of about 20° between the two cavity arms. The flat OC used had a nominal reflectivity of R = 80 % placed at a distance of 30 mm from the gain medium. The simulated cavity stability using WinLase is > 0.92 over the full range of possible thermal lens focal length values of the pumped gain medium. The resulting intra-cavity beam diameter on the micromirror varies between 250 μm for f'_{th} = 1200 mm and 300 μm for f'_{th} = 300 mm and does therefore fit comfortably on the 700 μm diameter mirror surface, but requiring exact lateral alignment to centre the mirror midpoint to the cavity axis.

4.7.6 Pulsed output at average output power of up to 500 mW

The experimental measurement setup for determining the temporal and spatial output behaviour of the Q-switched laser using the dielectric coated MEMS mirror is identical

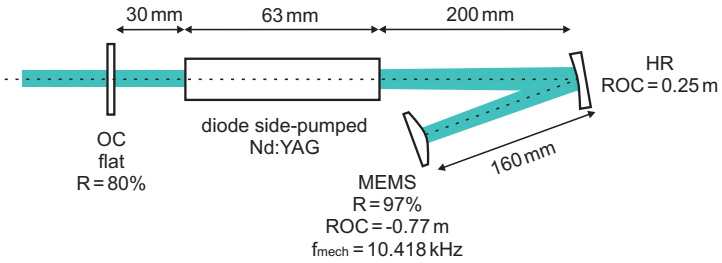

Figure 4.49: 3-mirror laser cavity setup used for Q-switching with dielectric coated MEMS mirror and 20% output coupler.

to the previously discussed 3-mirror cavity and shown in Fig. 4.35. Here the spatial output distribution was only measured using the scanning slit beam profiler (BP). The overall cavity length is 453 mm with this time a single chosen OC reflectivity of 80 % and the MEMS mirror acting again as second cavity end-mirror.

The laser cavity was aligned during pulsed operation to create an equal pulse duration for pulses emitted at both movement directions of the MEMS mirror and simultaneously a homogeneous pulse timing between subsequent pulses. This is necessary as small misalignments of the MEMS midpoint orientation in respect to the cavity axis will lead to an imbalanced pulse timing. Also small misalignments of the lasing axis in respect to the middle axis of the gain medium can lead to different pulse durations and pulse delays for pulses originating from the different movement directions of the mirror. A maximum average output power of 500 mW was achieved for Q-switch operation. For higher average output powers an imbalance in the intensity of the two output spots was visible as well as a change of the ROC of the MEMS, monitored by the HeNe beam used for the midpoint determination. This change occurred due to the absorbed intra-cavity power at the MEMS.

The laser output pulse train at an average output power of 500 mW and a representative single pulse are shown in Fig. 4.50. A homogeneous pulse train with PRF of 20.9 kHz can be seen with FWHM pulse durations of about 200 ns. This leads to a pulse energy of about 24 μJ and a peak power of 120 W. The increase of average output power compared to the output with using gold coated micromirrors is due to

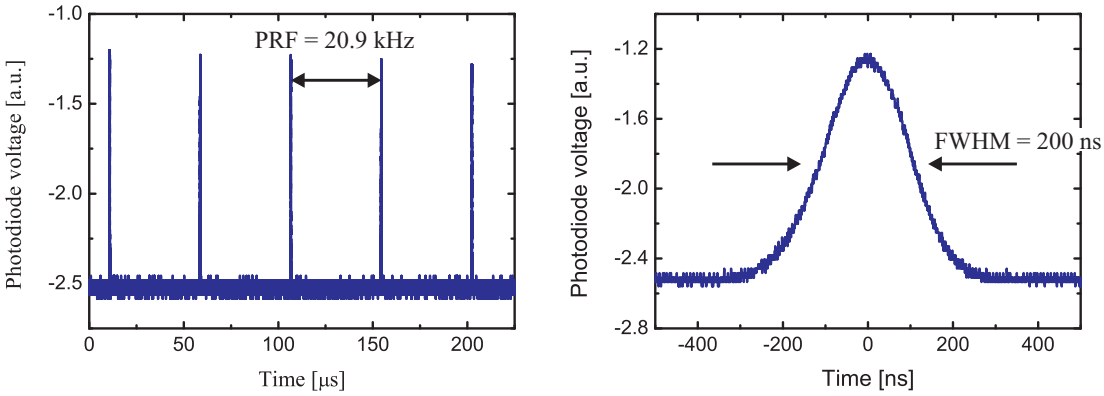

Figure 4.50: Q-switch laser output pulse train and exemplar pulse, for 500 mW average output power.

the increased damage limit of the coating and leads to higher pulse energies despite the present higher PRF. The peak power is lower than peak power values obtained for gold coated outputs shown in chapter 5.6.2 due to the longer pulse durations of 200 ns, compared to minimum pulse durations of about 30 ns achieved with gold coated mirrors as Q-switch.

To show the dependency of the pulse duration τ and pulse delay time t_d on the average output power, and therefore on the initial inversion density before pulse emission, measurements were taken at 100 mW, 250 mW and 500 mW average output power. The shape of the output pulses and their occurrence in respect to the micromirror midpoint position is shown in Fig. 4.51(a). Comparing the pulses at 100 mW and 500 mW one can see a longer pulse rise time for the lower power pulse, which is associated with the higher losses present at the pulse build-up as a higher pulse delay time is present. Fig. 4.51(b) and (c) show the measured pulse delay time and pulse duration for varying output power respectively. In both cases the average values for the outputs originating from the two movement directions of the MEMS are calculated separately, as a slight imbalance could not be avoided through the alignment. The error bars represent the sample standard deviation using 4 measured pulses. A decrease of the pulse delay time can be seen, as expected, for increasing average output power, with a pulse delay time of about 800 ns to 870 ns for 100 mW average output power decreasing to a pulse delay

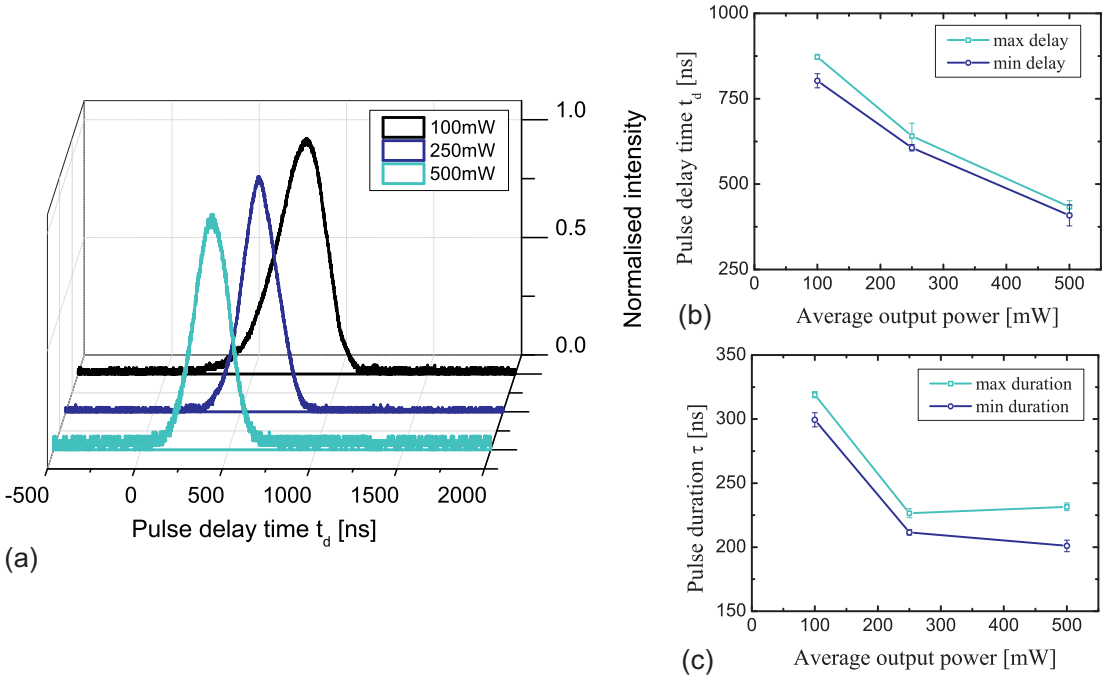

Figure 4.51: Temporal output measurements using the dielectric coated mirror with (a) pulse shapes, (b) pulse delay time evaluation and (c) pulse duration evaluation for varying average laser output powers.

time of about 430 ns to 410 ns for the maximum measured average output power of 500 mW. The pulse duration also decreases with increasing output power. At 100 mW average output power pulse durations between 300 ns and 320 ns are observed, which decrease to values between 200 ns and 230 ns for pulsed output with 500 mW average output power. At the output power limit of 500 mW no pulse emission at the mirror midpoint crossing, and therefore at the lowest cavity losses, could be achieved. The pulse duration could therefore still be further reduced when reaching the optimum pulse timing point.

The non-optimum pulse timing can also be seen when looking at the spatial output profile during Q-switch actuation. Fig. 4.52(a) shows the beam profile 50 mm after the OC for an average output power of 500 mW with the two spots originating from the two movement directions of the MEMS through the cavity alignment. The midpoint distance of the spots with varying output power is shown in Fig. 4.52(b) where the previously shown reduced pulse delay time for increased output power leads to a reduc-

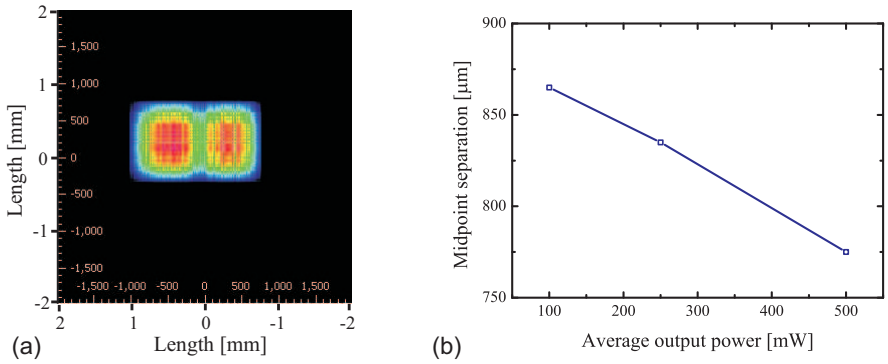

Figure 4.52: Spatial output characteristic using the dielectric coated MEMS with (a) beam profile for 500 mW average output power and (b) development of midpoint spot separation with varying output power.

tion of the spot midpoint separation. The midpoint distance decreases from 865 μm for 100 mW output to 775 μm for 500 mW average output power.

4.8 Conclusions

In this chapter the use of MEMS scanning micromirrors as intra-cavity active Q-switch element in a solid-state laser system was demonstrated and the performance using different laser cavity configurations evaluated and discussed.

The micromirrors were introduced together with the influence of their necessary coatings to increase the surface reflectivity, enabling an intra-cavity use of the silicon mirrors. The laser output power limitations arising from these coatings were additionally discussed as both the gold coatings and the tested dielectric coating have reflectivities below R = 97 % at the lasing wavelength. This leads to an absorption of intra-cavity optical power which can lead to thermal deformation of the mirror surface and even thermal damage in the case of the gold coatings. To overcome these limitations further improvements in dielectric coatings for the thin mirror structures are necessary as dielectric coatings have the possibility to reach reflectivities above 99 %.

For the use of gold coated micromirrors as active Q-switch two laser cavity configurations were investigated, a 2-mirror cavity with an overall cavity length of 123 mm

Table 4.3: *Summary of measured and simulated Q-switch characteristics, 25mW average output power with maximum measured delay and faster mirror driving (15.83kHz for 3-mirror and 15.87kHz for 2-mirror cavity).*

R	$\tau_{2-mirror}$	$t_{d,2-mirror}$	$\tau_{3-mirror}$	$t_{d,3-mirror}$	$\tau_{simulated}$	$t_{d,simulated}$
50.6 %	-	-	151 ns	295 ns	71 ns	310 ns
59.0 %	43 ns	67 ns	199 ns	416 ns	86 ns	420 ns
70.6 %	47 ns	58 ns	229 ns	494 ns	107 ns	527 ns
82.7 %	37 ns	47 ns	298 ns	649 ns	135 ns	619 ns

and a 3-mirror cavity including a folding mirror and overall cavity length of 403 mm. In both cases the Q-switch outputs were evaluated just above threshold and at an average output power of 25 mW in respect to the achievable pulse durations and pulse delay times towards the scanning mirror midpoint crossing, using different OC reflectivities. A summary of the achievable output pulse values is shown in Table 4.3. In all investigated configurations a positive pulse delay is present, leading to a pulse emission after the scanning mirror moved through its perfect alignment position and therefore leading to the observed double spot spatial output due to the bidirectional movement of the MEMS mirror. For the 2-mirror cavity pulse durations similar to the theoretical minimum pulse durations due to the cavity parameters were obtained, with minimum pulse durations around 40 ns and pulse delays between 25 ns and 75 ns. The investigated 3-mirror cavity does not lead to cavity limited pulse durations, with minimum experimentally observed pulse durations around 150 ns and minimum pulse delay times around 300 ns, while the theoretical minimum cavity limited pulse durations are around 60 ns. Possible reasons for this deviation were identified as well as a possibility to move towards optimum pulse timing by increasing the pump power and therefore the resulting initial population inversion density in the gain medium. This was not possible to be implemented using the presented gold coated devices due to the imposed power limit by the coatings thermal damage limits.

The use of a dielectric coated mirror showed an improvement of the output power, which was nevertheless still limited due to a coating reflectivity of 97 %. The micromir-

ror had in this case a lower angular movement speed through the alignment compared to the mirrors with gold coatings, which lead to longer pulse durations of about 200 ns for the maximum investigated output power and showed the influence of the mirror speed on the Q-switch behaviour.

To model the laser behaviour a simulation approach using the rate equations of the laser actuation was shown in this chapter. This approach is based on previously reported models for slow Q-switching [170] but also considers the bidirectional movement with varying instantaneous velocity of the scanning micromirror present as Q-switch in this work. This novel simulation part requires the determination of a scan angle dependent loss introduced by the micromirror, which was only possible to be measured for the 3-mirror gold cavity with a high enough accuracy to be used as simulation input. The simulation approach showed in this case a good agreement with the measured pulse delays. The introduction of a scaling factor for the initial inversion density was required which has its possible origins in a heat induced change of the coating and the possibility of a transversal movement of the used laser beam spot on the micromirror. The pulse durations were underestimated in the simulation with the possible reasons already mentioned and also relating to a possible beam wander on the micromirror during the aligned part of the scanning mirror movement cycle.

Overall stable Q-switch pulse outputs were reached for all shown laser cavities, with a possible way forward through improvements to the used dielectric coatings. This can lead to further power scaling of the outputs and therefore a possibility to reach optimum pulse timing. If a point is reached where a negative pulse delay occurs, which means pulses being emitted before the scanning mirror reaches its midpoint position, optimum pulse timing can still be created by adjusting the mirror movement speed through a change in the actuation frequency or actuation voltage. An additional possibility for reaching a single spot output and optimum pulse timing could be the inclusion of an intra-cavity pinhole which constraints the intra-cavity beam propagation but also generates additional losses. In the following chapter 5 the advantage of the small feature

size of the MEMS scanning micromirrors used as Q-switches is used to create multiple individual controlled Q-switched laser outputs through a single gain medium by using an array of micromirrors similar to the ones discussed in this chapter.

5 MEMS array laser

5.1 Introduction

To use the unique properties of MEMS micromirrors for adding functionality to a MEMS Q-switched solid-state laser, a micromirror array is used in this chapter to create multiple individually controllable Q-switched laser outputs through a single gain medium. This could allow new concepts for applications in laser range finding, industrial applications, e.g. marking, or medical applications. Laser arrays produced from a single gain medium have been shown previously for semiconductor lasers, where VCSEL (Vertical Cavity Surface Emitting Laser) arrays have been realised with application prospects for pumping solid-state lasers [183–185]. Commercially available array output powers of up to 18 W average power for an end-pumped Nd:YAG laser module are available for this laser category [186] and cw VCSEL arrays with output powers of up to 100 W at λ = 975 nm [187]. These arrays have nevertheless the inherent low beam quality of VCSELs combined with no individual controllability of the array pixel. For lower power VCSEL arrays, with mW cw output power, wavelength variation over the array outputs was demonstrated, with the individual wavelength depending on the varied layer thickness of the VCSEL array pixel [188], or on the variation of high contrast gratings used as top side output coupler of each array pixel [189]. Nevertheless no wavelength controllability during operation was presented in both cases.

VECSEL (Vertical External Cavity Surface Emitting Laser) arrays have also been

reported using diamond microlens arrays [190, 191]. VECSEL arrays show currently an output power limit in the mW range due to "thermal rollover" in the gain structure, with both semiconductor array lasers not having the prospects of reaching laser pulse energies in the "mJ" range. By using a solid-state laser gain medium to create an array laser output the potential for high output powers with average powers in the Watts range combined with good beam qualities is possible. A multi-beam output through a common solid-state laser medium has been used previously to generate variably spaced pulses by combining multiple cavities [192]. This has been done using multiple electro-optic modulators (EOM) and an intra-cavity prism to combine the multiple beams, leading to a large footprint of the laser cavities and necessary individual driving equipment for all EOMs. With the approach of using a MEMS array a greatly reduced laser cavity footprint is possible, combined with tighter packaging due to the sub-millimetre to millimetre size of the MEMS array mirrors and reduced driving equipment for the Q-switch.

In section 5.2, the design of the micromirror array is presented followed by its characterisation and the characteristics of a deposited surface gold coating in section 5.3. The laser cavity used for creating a dual-beam output through the MEMS array is presented in section 5.4 followed by the experimental characterisation of the laser output above threshold in section 5.5 and at the highest so far demonstrated average output power of 125 mW in section 5.6.

5.2 Micromirror array design

The MEMS scanning micromirror array used as intra-cavity end mirror to achieve a dual laser output consists of four electrostatic comb-drive actuated micromirrors similar to the ones described in chapter 4 (see Fig. 5.1). Each mirror has a circular reflective surface with a diameter of 700 μm, a single-sided comb-drive with 10 interdigitated comb-pairs and rectangular torsion beams acting as springs. The comb-pairs used as

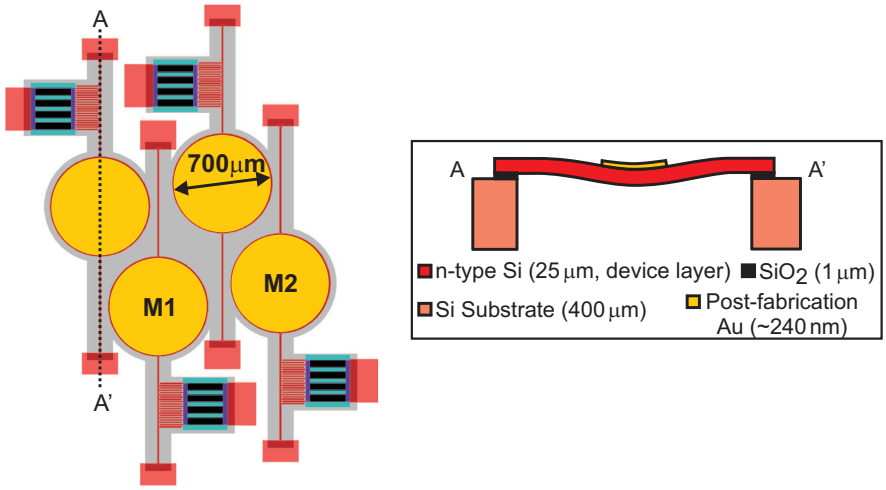

Figure 5.1: Layout and layer structure of the MEMS scanning mirror array used for the dual output Q-switch. Mirrors M1 and M2 are used for the laser output.

actuators have a comb length of 160 μm and width of 10 μm for both the moving and fixed combs, with a lateral gap of 6 μm between them and an overlap length of 152 μm. The torsion beams for each mirror are designed with different width and length to create a difference in the mechanical tilt resonance eigenfrequency of the mirrors in order to avoid possible coupling between two neighbouring mirrors. This coupling could occur due to a shared air cavity between the array mirrors. The length of the torsion beams of both mirrors M1 and M2, used in the laser cavity, are 750 μm, with mirrors M3 and M4 (which are the top right and top left mirrors in Fig. 5.1 respectively) having a torsion beam length of 750 μm and 675 μm respectively. The width of each torsion beam is from mirror M1 to M4: 12 μm, 13 μm, 11 μm and 10 μm. The mirrors and their actuators are placed to have a midpoint separation of less than 900 μm between two neighbouring mirrors.

The commercially available SOIMUMPs multi-user process provided by the company MEMSCAP, and previously described in chapter 3.2, is used as the fabrication process for the micromirror array. A tilted SEM image of the fabricated chip is shown in Fig. 5.2. The chip consists of a 400 μm thick silicon substrate, a 1 μm oxide layer for isolation and a 25 μm thick phosphor doped single crystal silicon device layer in which all the

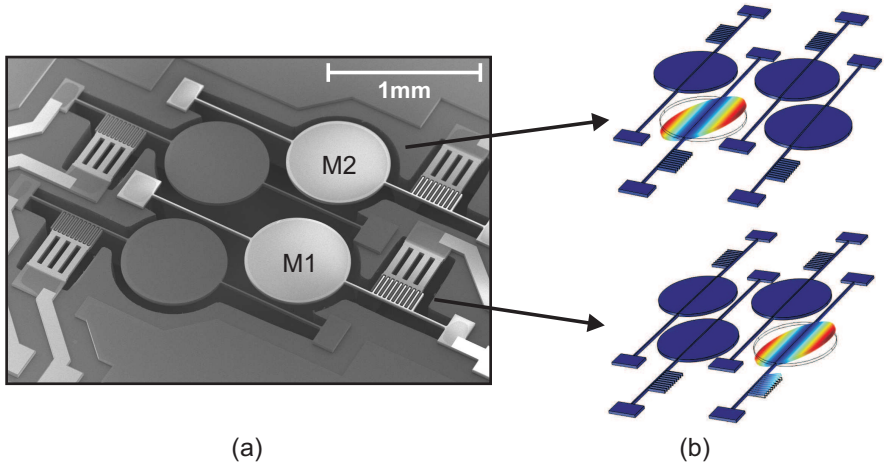

Figure 5.2: (a) SEM image of the fabricated micromirror array including (b) FEM simulations of the desired movement mode for both actuated array mirrors.

functional parts of the array are defined. The array mirrors are moving, when actuated, in a common air cavity created by a full release using a backside etch step through the substrate layer. The mirror surfaces have a concave curvature, similar to the previously used scanning micromirrors, due to the intrinsic stress created by a non-homogeneous doping profile in the device layer after the backside release. The resulting curvatures and their behaviour after coating will be characterised in detail in the next section 5.3.

A modal FEM simulation was conducted for each of the mirrors in COMSOL Multiphysics, considering the first six mechanical resonant eigenfrequencies of each layout. The material properties and orientations discussed in chapter 4.4 are again used for these simulations. The 3D mesh for the simulation is constructed in this case using a swept mesh with three layers through the thickness by considering four individual areas of each mirror. These areas are the anchor pads, the torsion springs, the mirror surface and the moving combs. The movement mode of interest is similar to before the tilt resonance mode around the anchor connections, which is the second eigenmode with simulated resonance frequencies of 8243 Hz, 9049 Hz, 7451 Hz and 7043 Hz for mirrors M1, M2, M3 and M4 respectively. For the two mirrors M1 and M2 used in the experimental laser work in this chapter, this leads to a resonance movement frequency offset of 806 Hz, which shows a wide enough separation to hinder any resonance coupling

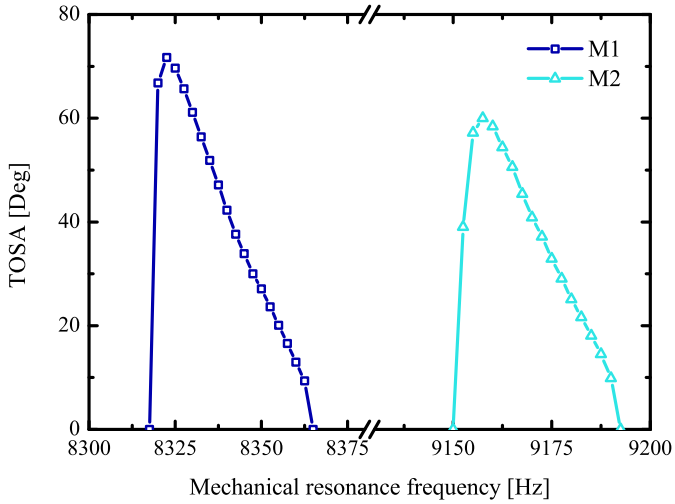

Figure 5.3: Frequency response curves of the two uncoated array mirrors used as basis for the dual output Q-switched laser.

between both mirrors and also has the advantage of having a simple way of distinguishing the laser output pulse trains originating from each mirror during the dual-output Q-switching.

5.3 Mirror characteristics

5.3.1 Uncoated array

The fabricated mirror array was characterised prior to any applied coatings through its resonance movement behaviour and surface curvature. A full characterisation is only done for the marked mirrors M1 and M2 as these are used for creating two simultaneous laser output beams. To evaluate the tilt resonance movement behaviours of the two mirrors M1 and M2 used for the laser operation, the measurement methodology and setup described in section 4.4.1 is used. The total optical scan angle (TOSA) of each mirror during its resonant actuation is measured using the reflection of a HeNe probe laser beam on a screen. All mirrors are electrically actuated using a square-wave

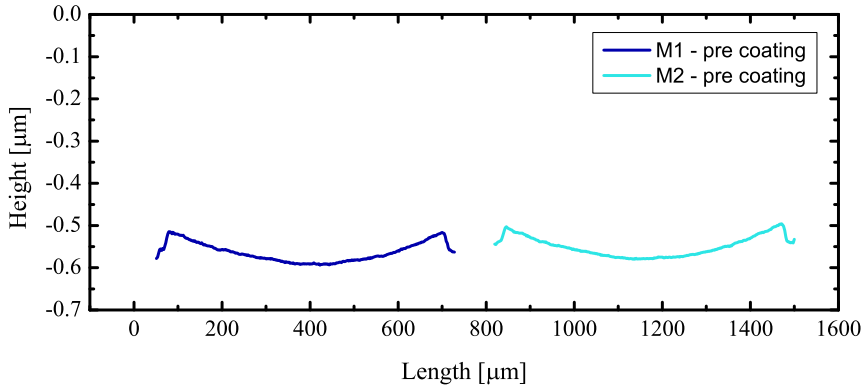

Figure 5.4: Measured surface curvature profiles of the uncoated array mirrors.

voltage driving signal with an excitation frequency of double the mechanical movement frequencies of the mirror. This sub-harmonic driving has already been shown in chapter 4 to generate higher TOSA responses compared to actuation with the fundamental frequency. The actuation signal has a peak-to-peak voltage of 200 V and is created using an Agilent 33250A signal generator in combination with a x20 FLC A400 voltage amplifier. A 10 kΩ series resistor is connected between the amplifier output and the PCB holding the MEMS chip with the array mirrors. In this way, the mirror actuators are protected from any accidental shorting created between the moving and fixed combs (see also section 2.4.2).

The frequency response curves using the described square-wave actuation signal for the two mirrors M1 and M2 show a nonlinear spring softening behaviour with a jump discontinuity below the resonance frequency peak (see Fig. 5.3). The graphs were in this case taken using a frequency down-sweep. The maximum TOSA of mirror M1 is found at a mechanical resonance frequency of 8323 Hz with a value of 72°. For mirror M2 the resonance peak is at 9158 Hz with a TOSA of 60°. The higher resonance frequency is due to the wider torsion beam, which is stiffer and therefore also lowers the TOSA. Despite the nonlinear shape of the frequency response curve a Q-factor for both resonances can be calculated using the definitions in [193], which leads to a Q-factor of 480 for M1 and of 500 for M2 when we assume a linear damping of the mirror movement. The

Table 5.1: *Micromirror properties of array mirrors M1 and M2.*

Mirror	Torsion beam length L / width w	f_{sim}	f_{meas}	ROC
M1	750 μm/12 μm	8243 Hz	8323 Hz	0.52 m
M2	750 μm/13 μm	9049 Hz	9158 Hz	0.52 m

measured resonance frequencies are higher than the simulated values by about 0.9 % for M1 and 1.2 % for M2. This mismatch can occur due to the thickness uncertainty originating from the fabrication process of the MEMS chips.

The surface curvatures of both mirrors were measured using the Veeco NT1100 optical white light interferometer introduced in the previous chapters. The profiles of both mirror surfaces are displayed in Fig. 5.4 where both profiles were placed close to each other to show the co-directionality of the mirror surface normal vectors. The surfaces of both mirrors have a radius of curvature of 0.52 m after fabrication, originating from the already mentioned intrinsic stresses in the silicon device layer. The positive sign denotes hereby a concave surface shape. A summary of the uncoated mirror properties is shown in Table 5.1

5.3.2 Gold coating

To increase the reflectivity R of the micromirror surfaces at the desired lasing wavelength of λ = 1064 nm, a gold coating was deposited using thermal evaporation. The used coating for the arrays was already introduced in chapter 4.5.1 and was deposited by a colleague at the Centre for Ultrasonic Engineering of the University of Strathclyde. The coating deposited through a metal shadow mask (see Fig. 4.19) has a measured thickness of 240 nm, which was determined by using a contact stylus profiler on the microscopy slide used as sample holder during coating. The reflectivity R of the devices was measured on this microscopy slide, leading to a value of R = 96 % at the lasing wavelength. For this measurement, a laser cavity using two bulk dielectric coated laser mirrors was built-up, with its laser output directed on the coating surface. The incident

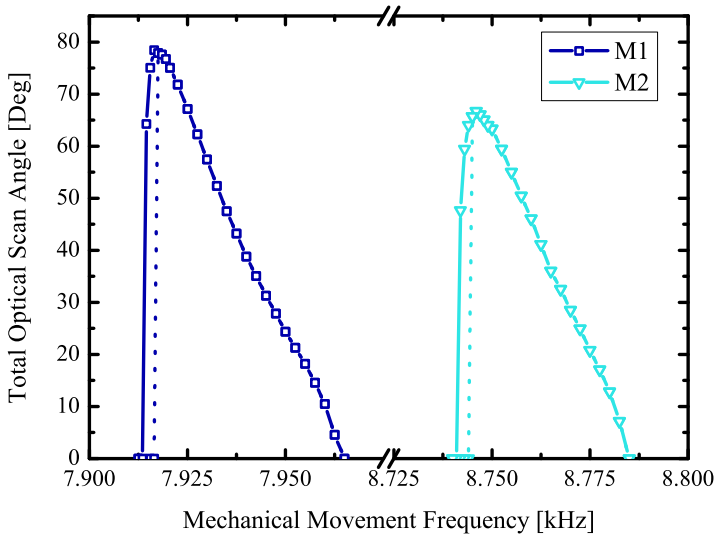

Figure 5.5: Frequency response curve of gold coated array mirrors used for dual output Q-switching; solid lines originate from the frequency down-sweep while dotted lines originate from the frequency up-sweep, showing a slight hysteresis.

and reflected laser power was measured at an incident angle of smaller than 10° on the coating and the resulting reflectivity was calculated. A mask edging effect was visible for the coating (see Fig. 4.20) which is introduced by the thickness of the metal mask and the offset between mask and chip. This effect together with a manual positioning of the mask leads to a non-homogeneous coating as seen in the figure.

The coating introduces an additional mass to the mirror structure and therefore shifts the mirror resonance movement frequencies to lower values. This shift is predicted by a modification of the previously mentioned FEM simulations by adding a gold layer of 240 nm thickness to the FEM layout. This gold layer has just been applied to the mirror surface and not the torsion springs of the model; therefore only modelling the influence of the added mass on the device resonance frequency. The second factor influencing the resonance frequency could be a change of the torsional stiffness due to an added thickness of the torsion springs coated with gold, which is not considered in the FEM. The predicted frequency shift for the mirrors used here is then −4.7 % of the original uncoated mirror resonance frequency. The tilt resonance peaks after coating were

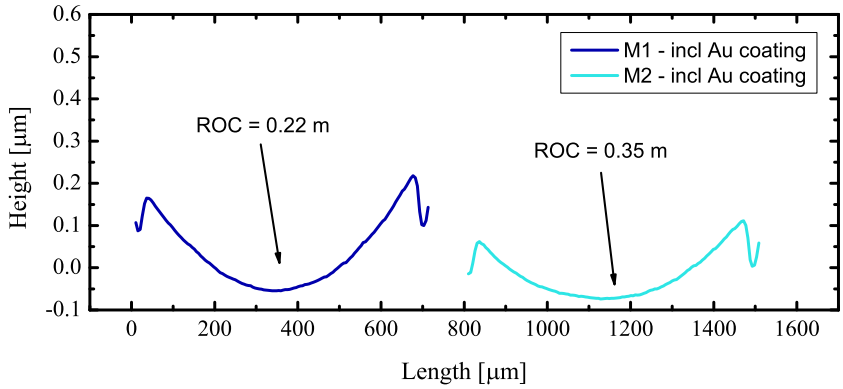

Figure 5.6: Surface curvatures of the coated array mirrors used for the laser output.

measured as 7916 Hz for mirror M1 and 8748 Hz for mirror M2 (see Fig. 5.5), showing in good agreement with the FEM the predicted shift of −4.9 % for M1 and −4.5 % for M2. This also shows that the added mass of the gold layer is the dominating factor for the frequency shift. The measured frequency shift is about 410 Hz for both mirrors, with achieving similar TOSA values. For the mirror M1 the maximum TOSA is hereby 78° after coating and for the mirror M2 it is 67°. In both cases the nonlinear spring softening effect is visible in the frequency response curves, with a slight hysteresis of below 0.05 % of the resonance frequency. The built-up and decay times of the resonance movement from a static mirror position were measured to be approximately 200 ms to reach the full angular movement. This gives the maximum build-up time for a stable Q-switch operation.

The curvatures of the two array mirrors, resulting from the additional stress of the gold coatings, are shown in Fig. 5.6. The ROC values for mirror M1 and mirror M2 differ hereby through the already mentioned non-homogeneity of the coating resulting from the in-house shadow mask process. For mirror M1 a post coating ROC of 0.22 m is shown while mirror M2 has a post coating ROC of 0.35 m. The parallelism of both mirrors in their respective rest-position is not influenced, as can be seen by the profiles in Fig. 5.6. Both ROCs will allow the build-up of a stable 2-mirror laser cavity around the Nd:YAG gain medium used in this thesis.

5.3.3 Heat influence on mirror behaviour

With the mirrors being used as intra-cavity elements of a Nd:YAG laser cavity, heating of the micromirrors will be introduced by absorption of intra-cavity optical power through the non-perfectly reflective coatings. The optical power will be absorbed in the gold coating and not the silicon mirror due to an absorption coefficient of $8.69 \cdot 10^5\,\mathrm{cm}^{-1}$ for gold at a wavelength of 1064 nm [194]. This will create heat which is transferred to the silicon mirror. The coating and mirror temperature will rise until a balance between the incident optical power and the heat transfer from the micromirror is achieved. The main heat transfer principle from the micromirrors is heat conduction through the torsion beams, which leads to an increase in temperature in these. For dielectric coatings the absorption would not take place in the coating layers but only in the silicon mirror surface, which has an absorption coefficient of $9.7\,\mathrm{cm}^{-1}$ at the here present lasing wavelength of 1064 nm. If a wavelength of 1550 nm would be used by using the MEMS Q-switch with a different laser gain medium like Er:Glass, this heating problem would be avoided as the absorption coefficient would reduce to $9.2 \cdot 10^{-2}\,\mathrm{cm}^{-1}$ leading to negligible absorption.

The influence of the temperature increase in the whole micromirror structure creates multiple effects. First, it leads to a curvature change of the mirror surface due to a bimorph effect created between the metal and silicon as these layers have different thermal expansion coefficient. An initial concave curvature of the mirrors of $ROC = 0.22\,\mathrm{m}$ or $ROC = 0.35\,\mathrm{m}$ will be increased, leading to lower ROC values (e.g. $ROC = 0.1\,\mathrm{m}$) due to the increased temperature. Second, the thermal expansion combined with thermal variant material properties also leads to a change in resonance frequency of the device, which can be in the range of tens of Hertz for the scanning micromirrors discussed in this chapter. With the thermal elongation of the torsion beams the resonance peak frequency will hereby shift to lower values. A third effect created by the temperature increase can be a buckling in the torsion beams due to the thermal expansion [195, Chapter 8 - p.379], which can create unstable resonance movements with a parasitic in-plane

component leading to pull-in failure of the comb-drive. A further effect of the temperature increase of the micromirror can also be thermal damage to the coating when the gold melting point is reached.

To avoid thermal induced changes, the laser output power is limited. In the case of the dual-beam Q-switched output presented in this chapter a limit of 150 mW average laser output power was set. This limit resulted from on-line monitoring of the array mirror resonance movement during laser operation. The monitoring was hereby conducted using a low power (< 5 mW) probe HeNe laser directed on the front mirror surfaces and evaluation of the resulting scan line on a screen. The power limit was set when a distinct reduction of the angular range of the mirrors could be observed.

To overcome the power limit a reduction of the absorbed optical power in the mirror coating is required which can be achieved by dielectric coatings, as discussed in chapter 4.5.2. As conventionally used dielectric coatings with high damage limit introduce stresses on the thin mirror structures, leading to curvature changes that render the mirrors non-usable in the here discussed laser cavities, a custom coating process is required which can create low stress coatings with reflectivities above 99 % and the additional requirement of balanced thermal expansion coefficients to avoid curvature changes under heating. An increase in reflectivity to a value of for example $R = 99.5\,\%$ would lead to an average output power limit of 1.2 W if a similar absorbed power limit for the mirrors is assumed as for the gold coatings. Further power scaling of the output power can be expected for this case as dielectric coatings also exhibit a higher damage limit than gold coatings. Currently the requirements of high reflectivity combined with low induced stress and negligible thermal induced stress are not met for the thin substrates by commercially available standard coating technologies like electron-beam or ion-beam sputtering. The research group of Talghader et al. [196, 197] has achieved the requirements in the visible spectrum by using plasma enhanced chemical vapour deposition (PECVD) coatings, which is expensive to run and not as useful for commercial exploitation as sputter coating based approaches. The investigation in creating a

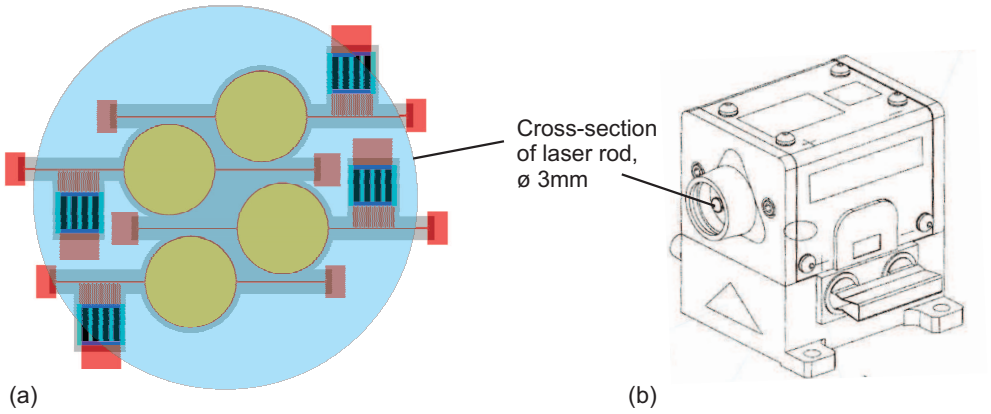

Figure 5.7: (a) Micromirror array schematic with cross-section overlap of Nd:YAG laser rod and (b) schematic of the used Nd:YAG gain module (see Appendix C).

scalable coating process of this type is ongoing work, with applications to reach further power scaling potentials for MEMS active Q-switch laser outputs being part of the future work.

5.4 Laser cavity setup

The laser cavity using the micromirror array as simultaneous Q-switch and cavity-end mirror is again built around a Northrop Grumman Nd:YAG laser module with a laser crystal rod with 3 mm diameter, a length of 63 mm and a neodymium concentration of 0.6 % (for pump characteristics and the thermal lens characteristic see chapter 4.6). The size and respective position of the array mirrors was chosen to enable an overlap between all array mirrors and the cross-section of the gain medium (see Fig. 5.7).

A 2-mirror laser cavity is constructed with an overall cavity length of 123 mm and spacings of 30 mm between the bulk BK7 output coupler (OC) and the laser rod on one side and the MEMS array as cavity-end mirror and the laser rod on the other side (see Fig. 5.8). The spacing was chosen to allow the monitoring of the array mirror movements during laser operation with the previously described HeNe probe laser, while simultaneously keeping the cavity length short to enable alignment of two array mirrors even if they would have minimal directional offsets. The OC is a 25.4 mm diameter

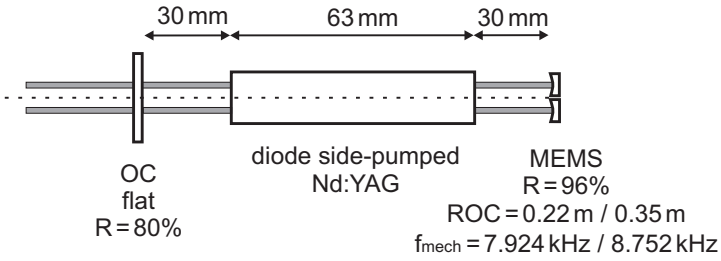

Figure 5.8: Laser cavity setup for creating dual-output Q-switching with the MEMS array.

dielectric coated BK7 mirror with a nominal reflectivity of 80 % at the lasing wavelength of 1064 nm. The two array mirrors M1 and M2, used for the dual-output investigation, are initially aligned without actuation of the micromirrors in continuous wave (cw) lasing mode, with the target of creating an identical lasing threshold for the laser outputs originating from both mirrors. To achieve this, the two mirrors are centred around the laser cavity axis using a two-axis linear micrometre translation stage in addition to a tip-tilt mirror mount. To obtain a Q-switched output regime, both mirrors are actuated with an electrical voltage signal with an actuation frequency above the respective double of each of their peak resonance frequencies to avoid resonance movement breakdown through temperature shifts. This could occur as the resonance frequency curves for both mirrors show a jump discontinuity about 4 Hz below the peak. The movement breakdown would lead to a cw-lasing case of the respective mirror and therefore a possible overheating of the gold coating as the laser has a lower lasing threshold for cw than for Q-switch operation and therefore a higher optical power incident on the mirror surface. The chosen actuation frequencies are f_{M1} = 15.848 kHz and f_{M2} = 17.504 kHz which lead to mechanical movement frequencies of 7.924 kHz and 8.752 kHz. These were chosen to create similar scan angles for both actuated array mirrors. A similar effect can also be achieved by adapting the actuation voltage of the mirrors. A variation of the frequency was chosen so as to not include an additional frequency shift induced by electrostatic nonlinearities when changing the actuation voltage, which could lead to actuation closer to the jump observed in the frequency response curves of the mirrors.

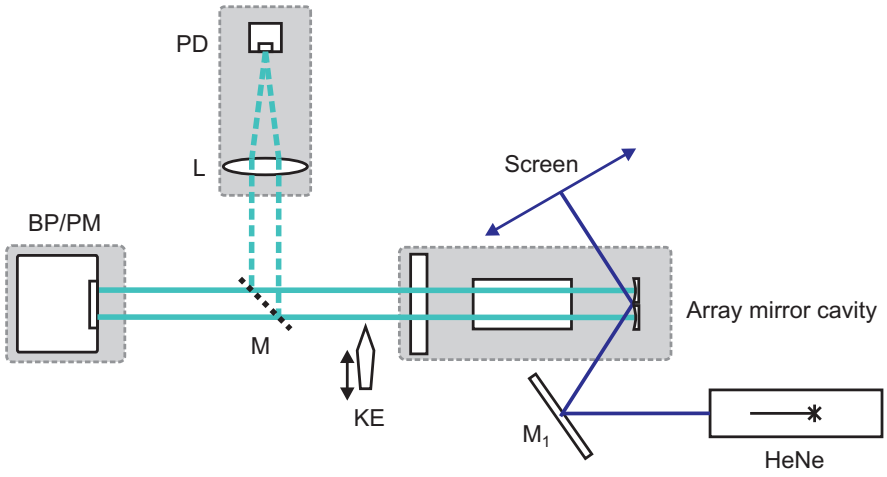

Figure 5.9: Measurement setup for determining the temporal and spatial laser output of the dual-output Q-switch, BP: beam profiler, PM: power meter, PD: photodiode, L: focusing lens, M: HR mirror to select temporal or spatial measurement, KE: knife edge, M1: HeNe guidance mirror.

5.5 Dual laser output above threshold

To gain Q-switch laser output through both aligned array mirrors, both M1 and M2 are actuated simultaneously at their respective driving frequencies. An Agilent 33250A signal generator and times twenty amplifier combination together with a 10 kΩ series resistor is used. The measurement setup to determine the spatial and temporal Q-switch laser output characteristics of both outputs simultaneously is shown in Fig. 5.9. The setup is similar to the previously shown measurement setup in Fig. 4.28, with both outputs being focused on a 1.5 GHz photodiode (PD) for the temporal measurement, as well as both output beams incident on the Thorlabs BP104-IR beamprofiler (BP) for the spatial measurement or on a Gentec Solo PE powermeter (PM). A knife edge (KE) is mounted on a linear micrometre translation stage to block each of the output beams individually and therefore enable the determination of the individual pulse trains and output powers.

The Q-switch operation has a higher laser threshold level than the cw-case used for the original alignment; therefore an increase in pump power is required when both scanning mirrors M1 and M2 are actuated. The pump power was increased to 90 W

optical power for the Nd:YAG gain module, leading to a stable pulse train output for both mirrors with a total average optical output power of 30 mW. The transverse position of the MEMS chip was adapted minimally through the two translation-stages on the mirror holder to get a balanced average output power for both individual beams. The individual average powers were in this case confirmed by using the KE placed after the OC to sequentially block each of the output beams.

5.5.1 Spatial output behaviour

The spatial output profile from both mirrors is shown for a total average output power of 30 mW in Fig. 5.10. The beamprofiler was hereby placed 50 mm after the OC. Both output beams, originating from mirror M1 and M2, show a fundamental Gaussian beam distribution in both the horizontal and vertical axis, indicating a TEM_{00} spatial output during Q-switching for each individual beam. The measurement speed and principle of the scanning slit beam profiler leads to an averaging over multiple laser output pulses to create the 2D beam profile. The beam pointing stability of the outputs is therefore confirmed over the averaging times of the detector, which were up to two minutes. In contrast to the Q-switched spatial laser outputs observed in chapter 4 only a single output spot is visible per actuated mirror. This is a result from the chosen alignment to generate Q-switched laser output from both mirrors, together with a minimal orthogonal tilt in respect to the scanning movement of each mirror during their resonance movement. The orthogonal tilt was measured to be around 0.015° between every successive pass through the laser alignment. This minimal unbalanced movement is believed to originate from the non-symmetric actuation point of the electrostatic force due to the single side comb-drive used for the mirror actuation. The alignment chosen for creating a simultaneous Q-switched output of both actuated mirrors M1 and M2 with a balanced average output power results in a beam position on the MEMS mirrors towards their edge. The observed orthogonal tilt during the scanning motion can in this case lead to an alignment and laser pulse output at only one of the mirror

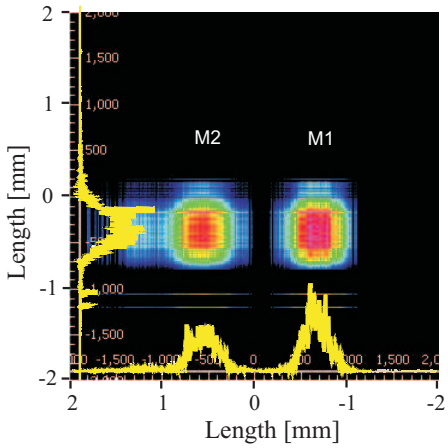

Figure 5.10: Spatial output profile of the dual output Q-switch with average power of 30mW.

movement directions, especially as the laser output power was limited to operation close to threshold. This leads to the observed single temporal and spatial output per beam and mirror movement cycle. The midpoint distance between the Q-switch output beams originating from the actuated mirrors M1 and M2 was measured to be 1.25 mm at the measurement plane located 50 mm from the OC.

5.5.2 Temporal output behaviour

The time dependent laser output was first evaluated with both output spots incident on the photodiode , as shown in the measurement setup. The actuation conditions are unchanged to get a total average output power of 30 mW. The pulse train has a varying time delay between two subsequent pulses (see Fig. 5.11(a)). This is created due to the movement frequency offset of the two mirrors used as active Q-switches. The offset of 828 Hz will lead to the shown varying time spacing between the pulses originating from mirror M1 and the pulses originating from mirror M2. The pulses are mapped in Fig. 5.11 to the pulse trains of the two individual output beams, showing that every alternate pulse can be associated with one of them respectively.

The individual outputs were measured by blocking the output beam from mirror M1 (Fig. 5.11(b)) or mirror M2 (Fig. 5.11(c)) with the mentioned KE. The resulting

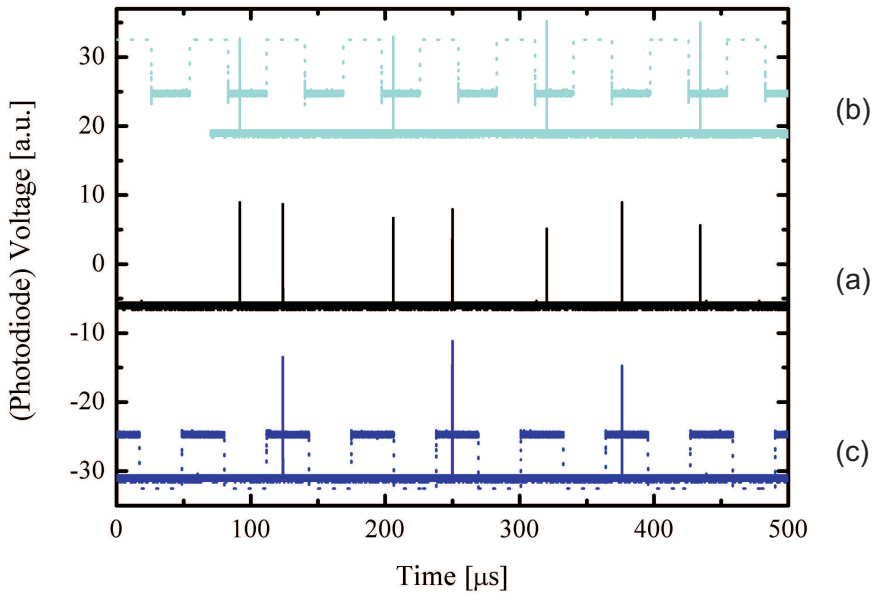

Figure 5.11: Measured time dependent laser output with (a) pulse train of both outputs, (b) pulse train and electrical actuation signal of M2 and (c) pulse train and electrical actuation signal of M1.

individual pulse trains show then a homogeneous pulse repetition frequency (PRF) of 7.924 kHz for the laser output from M1 and 8.752 kHz for the laser output for M2. Both individual output pulse trains in Fig. 5.11 also include the respective electrical square-wave driving signals with an amplitude of 200 V, with a laser pulse output visible for every second electrical actuation cycle. This corresponds to one pulse per mechanical movement cycle as the mirrors are actuated with sub-harmonic frequency driving as mentioned earlier in this chapter. The electrical driving signal for M1 (Fig. 5.11(c)) is in the shown graph inverted in respect to the driving signal of M2, due to an inverted channel setting during data acquisition.

Typical pulses of the two individual controlled output beams are shown in Fig. 5.12, with measured full width half maximum (FWHM) pulse durations of 40 ns for the output of M1 and 33 ns for the output of M2. This variation in the pulse duration can be associated with a non-homogeneous gold coating and possible minimal variations in the reflectivity of each mirror. A similar behaviour of lower pulse durations for the output of M2 is also shown later for the maximum achieved combined average output

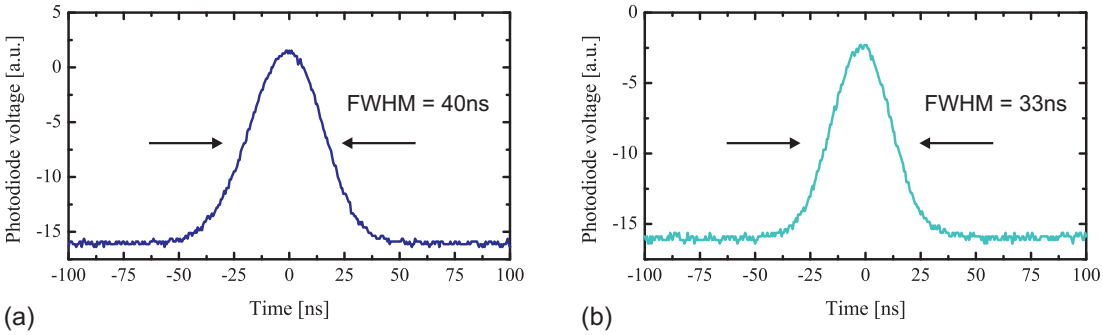

Figure 5.12: Individual Q-switch output pulses for the output originating from (a) mirror M1 and (b) mirror M2.

power of 125 mW. The pulse peak powers and pulse energies for both output beams can be calculated, as the average output power for both outputs was measured to be equal. The individual pulse energy can then be calculated through the ratio of the average output power of each output divided by the PRF, as both outputs show a regular pulse train. For the output pulses originating from M1 a pulse energy of 1.9 μJ is therefore present and for pulses originating from M2 a pulse energy of 1.7 μJ. The peak power for each output is then possible to be calculated by the ratio of the obtained pulse energy divided by the respective pulse duration. For the output using M1 this leads to a peak power of 48 W and for the output using M2 a peak power of 52 W.

5.6 Dual laser output with 125 mW average power

The average output power of the combined Q-switch laser output was further increased until a point close to the defined limit of thermal induced changes to the mirror movement or surface curvature is reached. For the micromirror array, with the previously described gold coating, this maximum limit was set to an overall average output power below 150 mW. The output characteristics of a dual Q-switched output with a combined average output power of 125 mW is therefore presented in this section. The corresponding optical pump power of the side-pump diode-stacks is 100 W in this case.

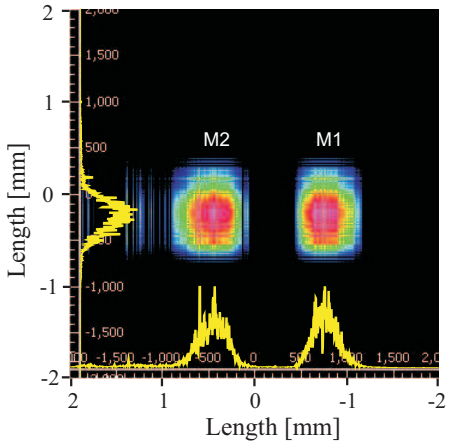

Figure 5.13: Spatial laser output profile of the dual output Q-switch with average power of 150mW.

5.6.1 Spatial output behaviour

The measurement setup for the spatial output behaviour is identical to the previously described setup, with the resulting 2D beamprofile at a distance of 50 mm from the OC shown in Fig. 5.13. The two output spots originating from the Q-switched outputs of the laser cavities using mirror M1 and M2 show both again a fundamental Gaussian beam distribution in both axes. The midpoint separation between both spots is in this case 1.2 mm. The combined and individual average output powers of both Q-switch outputs were measured using the KE to sequentially block each individual beam. The individual output power of each beam originating from one of the actuated array mirrors is in this case about 63 mW. The KE was after this moved to an intra-cavity position, to allow blocking the resonating laser field of each output sequentially inside the cavity. When blocking one of the outputs no change in output power and output characteristics of the respective other output beam was observed, showing that no gain competition exists in this case between both output beams.

To confirm the spatial fundamental mode output of both beams the beam profiler setup was used to experimentally determine the beam quality factor M^2 of each output. The output beams are individually focused through a lens and the resulting beam radius is measured in both transversal axes throughout the focal range by moving the beam

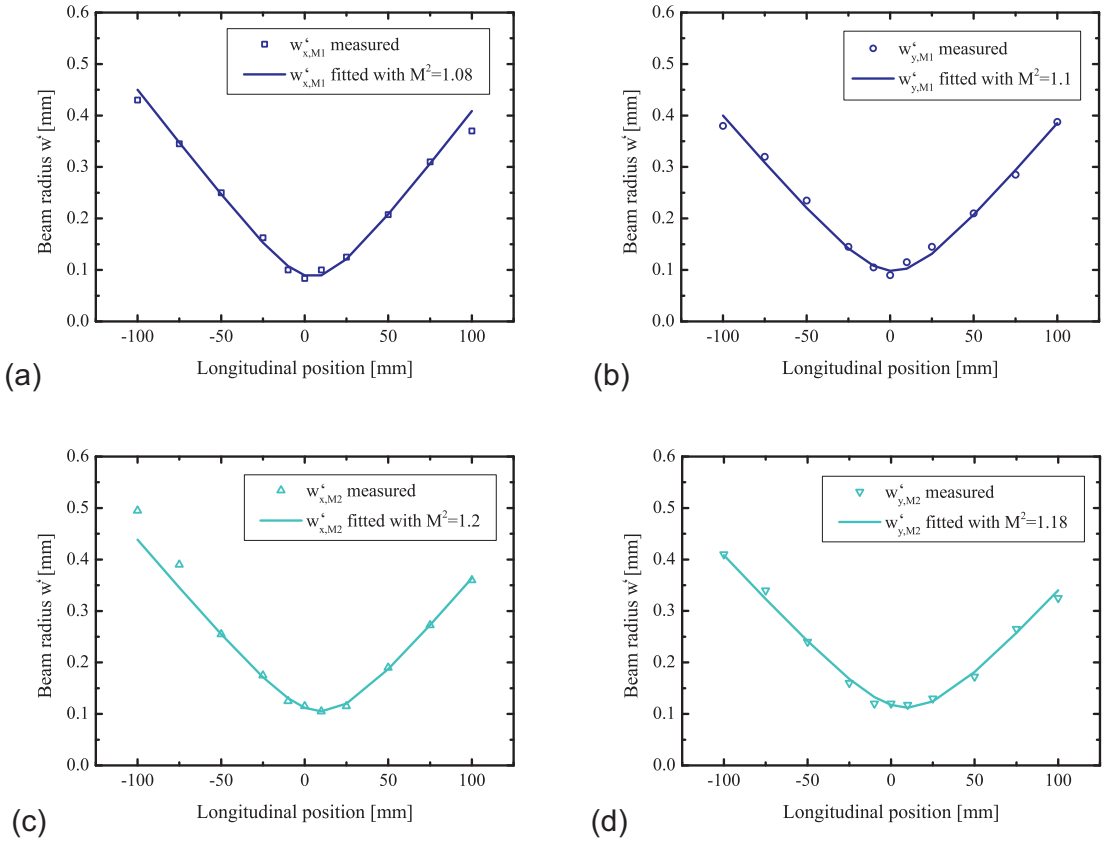

Figure 5.14: Beam radii measurements to determine the beam quality factor M^2 for (a+b) the output from M1 and (c+d) the output from M2.

profiler longitudinally along the laser output. The resulting distributions for the beam radii for both axes of the output originating from mirror M1 and from mirror M2 are shown in Fig. 5.14. A manual fit to the experimentally obtained data points is used to obtain a value for M^2 using three fit parameters: the beam radius at the beam waist w'_0, the beam quality factor M^2 and the beam waist position z'_0. The spatial beam distribution is assumed to be Gaussian, including possible higher order transversal modes. The equation of the fitted curve for a theoretical beam radius distribution $w'_{calculated}$ can then be used for each axis with [167]:

$$w'_{calculated} = w'_0 \cdot \sqrt{1 + \left(\frac{M^2 \cdot \lambda}{\pi \cdot w'^2_0} (z' - z'_0) \right)^2}. \tag{5.1}$$

The wavelength λ is in this case 1064 nm, the beam position z' is the longitudinal

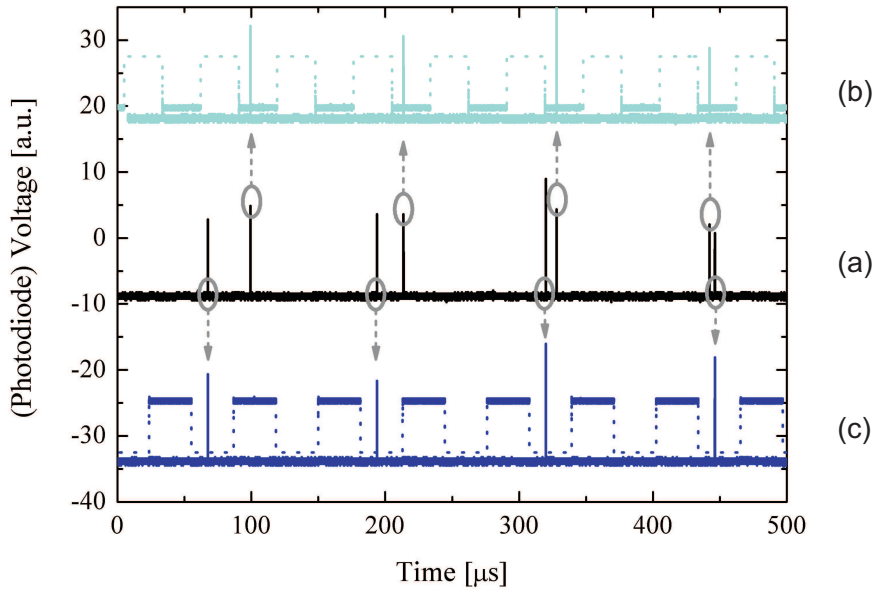

Figure 5.15: Measured time dependent laser output with (a) pulse train of both outputs combined, (b) pulse train and electrical actuation signal of M2 and (c) pulse train and electrical actuation signal of M1.

position and z'_0 is the position of the beam waist. The beam radius w'_0 is set to the minimum measured beam radius as starting point for the fit, with then adaptations to the M^2 value, w'_0 and z'_0 conducted until a good fit between the measured and calculated longitudinal beam distribution is achieved. For the Q-switched output beam originating from mirror M1 the fit shown in Fig. 5.14(a) leads to beam quality factors of $M^2_{M1,x}$ = 1.08 and $M^2_{M1,y}$ = 1.1, with a beam radius at the waist of $w'_{0,M1,x}$ = 87 μm and $w'_{0,M1,y}$ = 98 μm respectively. Likewise, the fit to the Q-switch output beam originating from mirror M2 (see Fig. 5.14(b)) leads to beam quality factors of $M^2_{M2,x}$ = 1.2 and $M^2_{M2,y}$ = 1.18, with a beam radius at the waist of $w'_{0,M2,x}$ = 105 μm and $w'_{0,M2,y}$ = 112 μm respectively. The beam quality factors of both mirrors show that both Q-switched laser outputs have excellent beam quality with a confirmed TEM_{00} spatial output behaviour.

5.6.2 Temporal output behaviour

The temporal behaviour of the Q-switched laser outputs with a total average power of 125 mW was measured using again the same setup as described earlier. The measured

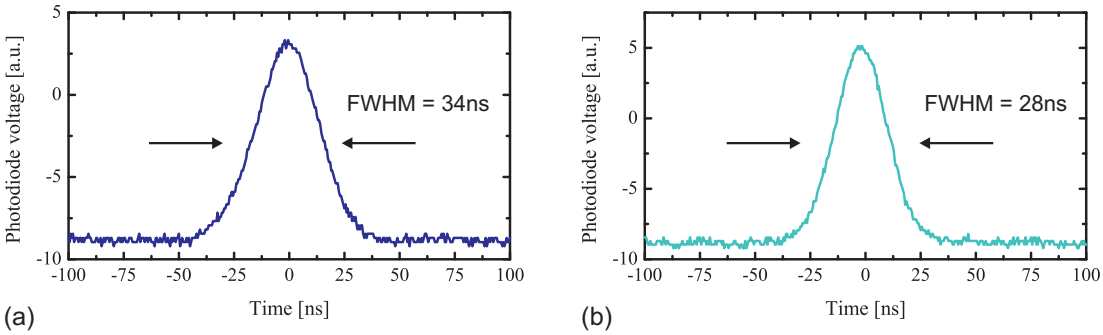

Figure 5.16: Individual Q-switch output pulses for the average output power of 125mW for (a) the output from M1 and (b) the output from M2.

pulse trains for the combined output and each individual output beam are shown in Fig. 5.15 (a), (b) and (c) respectively. The pulse train of the combined output shows, identical to the measurement with 30 mW average output power, a variable pulse spacing between two successive pulses. The individual outputs show a regular pulse train with a PRF of 7.929 Hz for the output using M1 and 8.752 Hz for the output using M2. The allocation of the individual pulses in the combined pulse train is again visible in Fig. 5.15, confirming the presence of output pulses originating from both actuated mirrors. The pulse train shows a pulse peak power variation of about maximum 45 %, which can originate due to operation close to the set damage limit of the mirror gold coatings.

Individual pulses from both Q-switch outputs are shown in Fig. 5.16, with again the pulses originating from the cavity using M1 having longer pulse durations than the pulses originating from the cavity using M2 as Q-switch. This could be caused by variations in the mirror surface reflectivity due to the inhomogeneous coating of the array mirrors (see chapter 4.5). The respective FWHM pulse durations are 34 ns and 28 ns for the output from M1 and M2. The average output powers for each output beam were again measured to be equal, which leads to a calculation of the individual pulse energies of 7.9 μJ for the output from M1 and 7.1 μJ for the output from M2, according to the average power and PRF ratios introduced for the 30 mW output. The corresponding pulse peak powers are 232 W and 253 W respectively.

To experimentally evaluate the influence of the mirror movement speed on the pulse duration, the excitation frequency for both actuated micromirrors was varied with minimal adaptation to the pump power to keep a Q-switch total average output power of 125 mW. A change in the mirror excitation frequency will change the mechanical movement frequency and the TOSA; therefore leading to a change in the maximum angular velocity of the mirror during the pass through the laser cavity alignment. With the knowledge of the TOSA θ and movement frequency f_{mech} the maximum angular velocity through the mirror rest-position ω_{max} can be calculated with

$$\omega_{max} = 2\pi f \cdot \sin\frac{\theta}{4}. \tag{5.2}$$

The actuation frequencies of both mirror M1 and M2 were changed from their original actuation points for the above presented Q-switch results to higher frequencies. For the mirror M1 the actuation frequency was changed from 15.848 kHz up to 15.905 kHz, leading to angular speeds from $1.53{\cdot}10^4$ rad/s to $4.6{\cdot}10^3$ rad/s with the angular response changing as shown previously in Fig. 5.5. The resulting Q-switch pulse durations τ for these mirror speeds are shown in Fig. 5.17. The pulse duration of 34 ns of the initial driving conditions stays constant when the angular speed of the scanning mirror is decreased down to a maximum angular speed of about $1 \cdot 10^4$ rad/s. The pulse duration rises for Q-switch actuation with maximum angular speeds of the mirror below this value, with a maximum measured pulse duration of 54 ns at the lowest used mirror speed of $4.6 \cdot 10^3$ rad/s. A similar behaviour is present for the Q-switch pulse output originating from M2 when its actuation frequency is increased. The actuation frequency was hereby increased from 17.504 kHz to 17.540 kHz leading to maximum angular speeds between $1.41{\cdot}10^4$ rad/s and $6.8{\cdot}10^3$ rad/s. The resulting Q-switch pulse durations are also shown in Fig. 5.17 with an increase in the pulse duration visible for maximum angular mirror movement speeds below around $1.2{\cdot}10^4$ rad/s. The pulse duration of 28 ns of the initial driving conditions is hereby increased to a value of 41 ns for a maximum angular velocity of $6.8 \cdot 10^3$ rad/s.

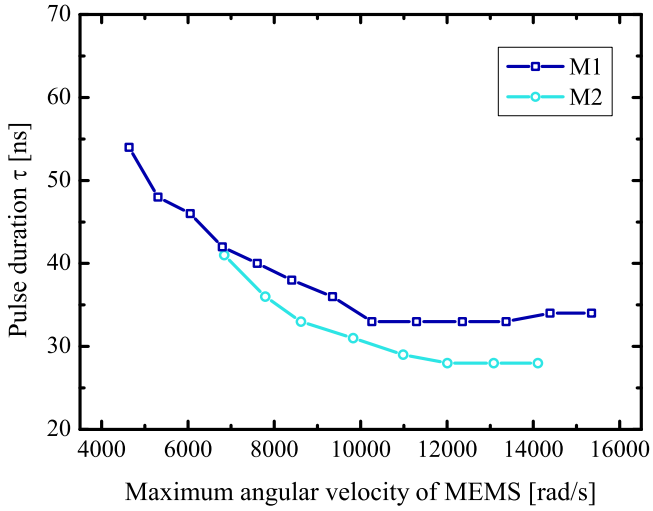

Figure 5.17: Experimentally measured Q-switch pulse duration dependency on the MEMS angular velocity through the cavity alignment for an average output power of 125mW.

For both Q-switch outputs a regime of constant pulse duration is possible with varying mirror movement speed, in which the minimum pulse duration is limited by the laser cavity to about 30 ns, as will be discussed in section 5.7. Below a maximum angular mirror movement speed of about $1.0 \cdot 10^4$ rad/s to $1.2 \cdot 10^4$ rad/s the Q-switch pulse duration increases, leading to the pulse duration being limited by the mirror movement speed rather than the laser cavity itself.

5.7 Conclusions of pulsed array laser output

A dual output with two individual controllable Q-switch laser outputs generated from a common Nd:YAG solid-state laser gain medium was presented in this chapter. The outputs were created using two scanning mirror of a silicon MEMS micromirror array, leading to a combined maximum average output power of 125 mW, maximum pulse energies of $E_{pulse} = 7.9\,\mu$J and minimum pulse durations of 28 ns. The individual pulse durations of both output beams are shorter for the higher average output power of

125 mW compared to the behaviour at 30 mW. This can be expected as the increased pump power will lead to a higher initial inversion density of the laser gain medium and therefore to a lower pulse duration.

Both Q-switch laser outputs for the 125 mW average output power case show pulse durations limited by the cavity, as can be shown by using equation (4.23) [179] already introduced in section 4.6.2. This relates the minimum theoretical pulse duration τ_{min} to the cavity round-trip time τ_r and the gain G present in the cavity. For the cavity used in this case a round-trip time of 0.82 ns was calculated and an unsaturated round trip gain of $G = 1.24$ was estimated through the minimum gain necessary to overcome losses through the reflectivities of the OC and MEMS. This leads to a theoretical minimum pulse duration of $\tau_{min} \approx 30$ ns. Both measured pulse durations of 28 ns and 34 ns of the two outputs are close to this value, with possible small deviations due to the non-homogeneous gold coating mentioned previously.

These cavity limited pulse durations were experimentally shown to be present for micromirror angular velocities through the alignment of above $\approx 1.2 \cdot 10^4$ rad/s. For slower scanning speeds an elongation of the pulse is measured, leading to a case where the pulse duration is not limited by the cavity setup but by the micromirror speed. With this it was also shown that the array mirrors used for the dual laser output were fast enough to generate Q-switch pulses with similar durations to acousto-optic or electro-optic modulators whose outputs are also limited by the laser cavity [179].

Their spatial beam quality was measured, showing an excellent beam quality with beam quality factors M^2 below 1.2 for the Q-switch outputs with pulse energies up to 7.9 μJ. The laser outputs from each of the two used array mirrors have a single output spot, in contrast to the results shown in chapter 4 with similar scanning mirrors. This behaviour is explained due to a minimal orthogonal tilt of the mirror surfaces on every successive pass through the laser alignment combined with the overall necessary cavity alignment chosen to generate two balanced outputs from two neighbouring array mirrors. With the alignment placing the laser spots on the edge of the mirrors, only one

of the movement directions of the mirror creates a cavity alignment with low enough losses to enable pulsed laser output due to the orthogonal tilt. Therefore a single pulse output per movement cycle is obtained and only a single spot, as the previously shown dual spot behaviour in chapter 4 originates from the two movement directions of the scanning mirror.

The limitations of the currently used devices were also shown in this chapter, which have their origin due to heat generation in the gold coatings used to improve the reflectivity of the silicon micromirrors. This heat is created through absorption of intra-cavity optical power and leads to changes of the mirror surface curvature, the movement of the mirror and ultimately thermal destruction of the gold coating above certain temperature limits.

To overcome these limitations and achieve further power scaling of the laser output dielectric optical coatings are a desired way forward, with preliminary tests in this direction already mentioned and investigated in the previous chapter 4. A further improvement for future work can also be seen in a reduction of the size of the scanning micromirror, with a further reduction of the mirror diameter leading to the possibility of a denser packaging and the possibility for an increase in the number of simultaneous Q-switched laser outputs which are individual controllable through individual MEMS array mirrors.

6 Overall conclusions and future work

The work presented in this thesis investigates MEMS electrostatic scanning micromirrors and their application as intra-cavity elements in solid-state laser systems. The category of angled vertical offset comb-drives (AVC) was investigated in respect of the influence of the actuator initial conditions on the resonant movement behaviour, using an analytical hybrid simulation model and experimental data. The integration in a Nd:YAG laser system was done as cavity end-mirror and Q-switch. The performance of a single scanning MEMS mirror is in this case investigated as well as the use of an array of micromirrors to create novel individual controllable multiple laser outputs through a common gain medium.

6.1 Overall conclusions

MEMS scanning micromirrors with an AVC actuator geometry were theoretically and experimentally investigated, with particular focus on the influence of the initial AVC geometry on the dynamic resonant movement behaviour of the mirror. For the theoretical investigation a simulation approach was presented, combining FEM calculations of the electrical field distribution of the AVC actuator with an analytical solution of the governing ODE motion equations of the mirror. The 2D FEM simulation was created to model a comb-drive unit cell and its capacitance changes for varying vertical comb-offsets by including electrical fringe fields. This distribution was used as one of

the inputs for the analytic ODE motion equation description in Matlab to simulate the frequency response curve of the AVC MEMS scanning micromirror. The model does not include an analytical description of the air damping acting on the micromirror and therefore requires the prior knowledge or estimation of the damping coefficient of the motion equation as the only experimentally obtained input variable for the initial model. The AVC initial offset, device geometry and applied driving voltage are the further necessary input parameters. The generated model was validated with excellent agreement using experimental data from an example scanning micromirror, exhibiting movement angles of maximum 13.3° at a resonance frequency of 26.4 kHz with no observed non-linearities. The agreement between the simulation and measurement was in this case within 5 % with excellent agreement of the Q-factor.

The influence of an AVC actuator initial offset on the dynamic resonant movement was experimentally investigated using a scanning micromirror with a novel comb-drive actuator geometry, allowing an electrically controllable continuous variation of the initial comb offset. This continuous variation is achieved using an electrothermal actuator built in the fixed comb anchor of the AVC. The variation of the vertical offset between moving and fixed combs is limited by the thermal damage limit of the actuator, leading to achievable offsets between 10.4 μm and 4.9 μm. The frequency response curves of the scanning micromirror were investigated for varying initial offsets using this thermal displacement actuation, as well as through employing a mechanical displacement of the fixed part of the AVC using a mechanical needle prober. This mechanical displacement allowed initial comb offsets close to an in-plane configuration, as well as negative initial offsets. Negative initial offsets means in this case the tip of the fixed combs being initially vertically placed below the moving combs. For both initial offset actuation principles the torsional resonance of the same device was generated, using an offset square-wave voltage signal with 80 V and 120 V amplitude. The frequency response around the 6.0 kHz torsional resonance was evaluated using maximum vertical comb-offsets of 10.4 μm, 8.0 μm, 5.6 μm and 4.9 μm for electrical offsets as well as

0.5 μm and −1.7 μm for mechanical offsets. The frequency response of the investigated device showed no observable nonlinear behaviour in the form of hysteresis and spring hardening or softening in the investigated cases. Lower initial comb-offset magnitudes resulted in lower measured optical scan angles at resonance, confirming that the initial AVC geometry not only influences the static tilt behaviour of a MEMS mirror (which has been studied by other international researchers), but also its dynamics and achievable angular response at resonance.

In the second part of the thesis, the above presented micromirrors were then used as intra-cavity Q-switches of a Nd:YAG solid-state laser. The MEMS mirrors were investigated as end-mirrors of several laser cavity configurations, showing Q-switched laser output with possible shortest pulse durations, limited by the parameters of a 2-mirror laser cavity and not the mirror movement dynamics. Therefore, the possibility was shown to employ this Q-switch type as an alternative to commonly used crystal modulators without any impact on the laser performance. For all single MEMS mirror lasers investigated, the pulsed laser outputs presented a dual spot spatial output, originating from the bi-directional scanner movement combined with a temporal laser pulse emission delay in respect to the perfect mirror alignment. This delay time and spatial laser output were investigated for varying output coupler reflectivities of the laser cavity, leading to a variation in the pump power and subsequently a variation of the initial inversion density which influences the laser pulse build-up time. For the three experimental cavity configurations, consisting of one 2-mirror and one 3-mirror cavity using a gold coated MEMS as well as a 3-mirror cavity using a dielectric coated MEMS, clear trends of lower laser pulse delay times with increased pump power was shown for the 3-mirror cavities. For the gold coated devices with limited maximum average output power of 25 mW, the pulse delay reduced from 600 ns to 300 ns by using a 50 % reflective output coupler (OC) rather than a 80 % OC. A similar trend was shown for the dielectric coated devices by increasing the average output power through increased pumping. Coupled to the reduced delay time was also the reduction of the pulse dura-

tion due to laser cavity losses at the point of the pulse emision. With these trends it is expected that an optimum pulse timing at the lowest cavity losses can be achieved by an increase in the pump power to threshold power ratio. This would correspond to a pulse emission at the lowest laser cavity losses, creating highest possible output pulse energies. In the experimental work optimum pulse timing was not achieved due to output power limitations introduced by the optical coatings of the mirror surface. Gold coatings and a test dielectric coating were used with a maximum reflectivity of 97 %, leading to thermal changes and damage above about 75 mW average output power for gold coatings and 500 mW average output power for the dielectric coatings. A simulation model for the Q-switch laser behaviour was additionally presented, matching the experimentally obtained data. The model is based on the laser rate equations, including the time dependent description of the losses introduced by the mechanical mirror movement through the cavity alignment. As this model is only considering the temporal laser behaviour, an ABCD matrix description was introduced to simulate the matching spatial output behaviour.

To build on the miniaturisation advantages of the MEMS micromirrors, an array of scanning micromirrors was used to generate, for the first time, multiple individual controllable Q-switched laser outputs through a single gain medium using MEMS as active Q-switches. The designed array consisted of four electrostatic comb-drive actuated 700 μm diameter mirrors with midpoint distances below 1 mm. However only two of the array mirrors were used to create simultaneous pulsed outputs as the gold coatings used for the mirror surfaces lead to high laser threshold powers for alignments of multiple mirrors, not reaching Q-switched output for alignment of more than two array mirrors in the presented cavity configurations. The mechanical resonance frequencies correspond in this case with the achieved pulse repetition frequency (PRF), with all array mirrors having a slight variation in their resonance frequency between 7.0 kHz and 9.0 kHz to avoid coupling and cross-talk. Simultaneous pulsed laser outputs were achieved using two adjacent gold coated array mirrors, with both output beams exhibit-

ing pulse durations of 28 ns and 34 ns, limited by the chosen 2-mirror cavity. Excellent spatial beam quality was measured for both, with beam-quality factors of M_1^2 = 1.1 and M_2^2 = 1.2. The output power was again limited due to the gold coatings, leading to maximum pulse energies of about 8 μJ per beam with a total average output power of 125 mW.

When putting these results into context with further MEMS Q-switched lasers introduced in chapter 1.3.3, higher pulse energies have been achieved with excellent laser beam quality and prospects of further power scaling. The power scaling possibility by using the presented silicon scanning micromirrors is also seen to be more promising than using thin metallic membrane or cantilever mirrors, as seen by the power limits encountered with gold coatings used in the here presented work. The demonstrated possibility of using multiple outputs through the same gain medium also shares these power scaling possibilities.

6.2 Future work

Regarding the investigation of the basic behaviour of AVC scanning micromirror, further work can be undertaken on the simulative part, with the possibility of developing an analytical description of the damping behaviour. This would be desired to remove the requirement of experimental data or estimations of the resonance Q-factor used as input for the current simulation model as described in section 2.1. With the interaction of several damping mechanisms in the form of squeeze-film damping and drag damping, an analytic description to model these influences has not been shown yet for theoretical models of the resonant dynamics of comb-drive actuated scanning micromirror. For scanning mirror showing higher nonlinear behaviour of the frequency response curve than the investigated devices, an FEM based description of the nonlinear spring constant would be an additional necessary inclusion to the presented model.

Further investigations on the influence of the initial AVC offset on the scanning mirror

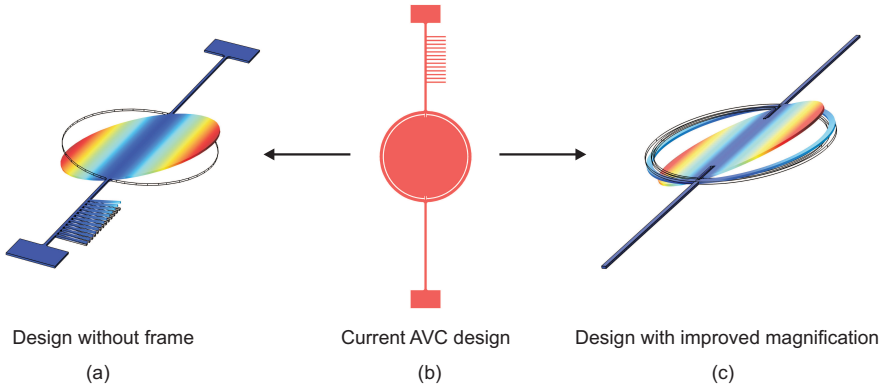

Figure 6.1: Further design improvement possibilities for the presented AVC scanning micromirror, with (a) mode shape of an adapted design without frame structure, (b) current design and (c) mode shape of an adapted design with increased magnification.

resonance behaviour can include the creation of higher initial offsets than possible with the device investigated here, to find the offset angles corresponding to a maximum angular frequency response. An improvement of the overlap accuracy between the model and experimental results can possibly be achieved by using a non-framed mirror structure (see Fig. 6.1 (left)). This results from the minimal angular tilt magnification which a framed mirror would exhibit in respect to the frame, which was not considered in the theoretical model used here. A comparison of this framed and rigid scanning mirrors could also allow the investigation of the estimation of an accurate damping coefficient for coupled torsional scanning systems, when only a single frequency response is experimentally obtainable. To increase the accuracy of this possible investigation an AVC scanning mirror with improved magnification between the frame and central mirror structure could be used (see Fig. 6.1 (right)).

Future work on the integration of MEMS scanning mirror as active Q-switch elements in solid-state lasers could focus on the development of high reflective low stress dielectric coatings, to enable further power scaling of the laser output. This will possibly also lead to an improvement of the pulse train homogeneity, as well as enable laser operation with perfect timed pulse emission coinciding with the lowest cavity loss point. Employing MEMS Q-switches in laser systems with an output wavelength around 1.5 μm using low

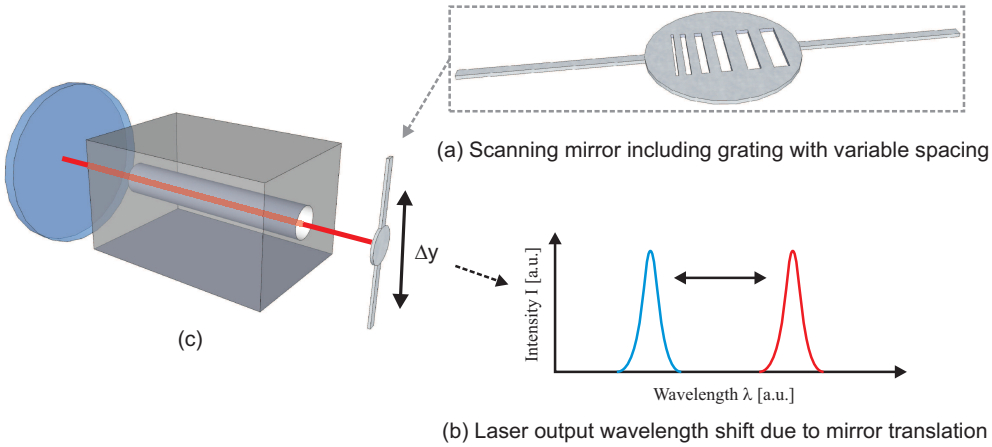

Figure 6.2: Future added functionality possibilities of MEMS in solid-state laser systems by integrating a high contrast grating to a scanning micromirror for laser output wavelength selectivity; (a) possible grating, (b) spectral laser output and (c) mirror movement to achieve the spectral tuning.

loss dielectric coatings can also allow higher power scaling possibilities, as the absorption coefficient of silicon reduces by two orders of magnitude between the used 1.064 μm output and operation at 1.5 μm. Therefore the optical heat power on the mirror can be reduced, which enables higher optical intra-cavity powers. Further work can also include the investigation of a full electro-magnetic field simulation of the MEMS Q-switched laser cavity, obtaining a comparison to the rate equation simulation approach used in the work presented here. Additionally this model would generate a complete analysis of the spatial variable field behaviour inside the cavity during pulse build-up using both scanning mirror movement directions. The integration of additional functionalities to the laser systems by using further MEMS devices is also a future possibility, with ideas of integrating a grating structure to achieve wavelength selectivity next to the temporal control achieved through the scanning movement (see Fig. 6.2) if a gain medium with large gain bandwidth is used.

Further work on creating multiple individual controllable laser outputs through an array of MEMS micromirror also includes the improvement of the dielectric coating processes. An improved coating reflectivity will lead to lower laser threshold levels, which will possibly enable an increase in the number of laser outputs due to less stringent

alignment tolerances and higher possible output power levels of each individual output. Additional possibilities for future work also include modifications to the scanning mirror arrays, using smaller mirrors and a resulting tighter packaging to also increase the number of individual controllable outputs. Investigations of integrating additional spectral or spatial control, next to the temporal Q-switch control, are also possible with long term goals of creating fully configurable outputs through multiple active MEMS devices within the laser cavity.

References

[1] Yole Developpement, "Status of the MEMS industry." `http://goo.gl/vAfRX`. [Online; accessed 19-May-2013].

[2] M. Esashi, "Revolution of Sensors in Micro-Electromechanical Systems," *Japanese Journal of Applied Physics*, vol. 51, p. 080001, July 2012.

[3] L. Baumgartel, A. Vafanejad, S.-J. Chen, and E. S. Kim, "Resonance-Enhanced Piezoelectric Microphone Array for Broadband or Prefiltered Acoustic Sensing," *Journal of Microelectromechanical Systems*, vol. 22, pp. 107–114, Feb. 2013.

[4] Y. Takaki, H. Takenaka, Y. Morimoto, O. Konuma, and K. Hirabayashi, "Multi-view display module employing MEMS projector array," *Optics Express*, vol. 20, pp. 28257–66, Dec. 2012.

[5] W. Lubeigt, J. Gomes, G. Brown, A. Kelly, V. Savitski, D. Uttamchandani, and D. Burns, "Control of solid-state lasers using an intra-cavity MEMS micromirror," *Optics Express*, vol. 19, pp. 2456–2465, Jan. 2011.

[6] S. R. Samuelson and B. S. Sorg, "A 2.8-mm Imaging Probe Based On a High-Fill-Factor MEMS Mirror and Wire-Bonding-Free Packaging for Endoscopic Optical Coherence Tomography," *Journal of Microelectromechanical Systems*, vol. 21, pp. 1291–1302, Dec. 2012.

[7] L. Li, R. Bauer, G. Brown, and D. Uttamchandani, "A symmetric hybrid MEMS scanner with electrothermal and electrostatic actuators," in *16th International Conference on Optical MEMS and Nanophotonics*, pp. 163–164, IEEE, Aug. 2011.

[8] X. Mu, W. Sun, H. Feng, A. Yu, K. W. S. Chen, C. Y. Fu, and M. Olivo, "MEMS micromirror integrated endoscopic probe for optical coherence tomography bioimaging," *Sensors and Actuators A: Physical*, vol. 168, pp. 202–212, July 2011.

[9] M. Freeman, M. Champion, and S. Madhavan, "Scanned Laser Pico-Projectors: Seeing the Big Picture (with a Small Device)," *Optics and Photonics News*, vol. 20, p. 28, May 2009.

[10] H. Schenk, T. Sandner, C. Drabe, T. Klose, and H. Conrad, "Single crystal silicon micro mirrors," *Physica Status Solidi C*, vol. 6, no. 3, pp. 728– 735, 2009.

[11] J. W. Judy, "Microelectromechanical systems (MEMS): fabrication, design and applications," *Smart Materials and Structures*, vol. 10, pp. 1115–1134, Dec. 2001.

[12] C. K. Malek and V. Saile, "Applications of LIGA technology to precision manufacturing of high-aspect-ratio micro-components and -systems: a review," *Microelectronics Journal*, vol. 35, pp. 131–143, Feb. 2004.

[13] C. Liu, "Recent Developments in Polymer MEMS," *Advanced Materials*, vol. 19, pp. 3783–3790, Nov. 2007.

[14] M. A. Hopcroft, W. D. Nix, and T. W. Kenny, "What is the Young's Modulus of Silicon?," *Journal of Microelectromechanical Systems*, vol. 19, pp. 229–238, Apr. 2010.

[15] K. Petersen, "Silicon as a mechanical material," *Proceedings of the IEEE*, vol. 70, no. 5, pp. 420–457, 1982.

[16] J. Bustillo, R. Howe, and R. Muller, "Surface micromachining for microelectromechanical systems," *Proceedings of the IEEE*, vol. 86, no. 8, pp. 1552–1574, 1998.

[17] V. Cimalla, J. Pezoldt, and O. Ambacher, "Group III nitride and SiC based MEMS and NEMS: materials properties, technology and applications," *Journal of Physics D: Applied Physics*, vol. 40, pp. 6386–6434, Oct. 2007.

[18] A. Kaushik, H. Kahn, and A. H. Heuer, "Wafer-level mechanical characterization of silicon nitride MEMS," *Journal of Microelectromechanical Systems*, vol. 14, pp. 359–367, Apr. 2005.

[19] E. J. Boyd and D. Uttamchandani, "Measurement of the Anisotropy of Young's Modulus in Single-Crystal Silicon," *Journal of Microelectromechanical Systems*, vol. 21, pp. 243–249, Feb. 2012.

[20] Y. Zhao, X. Li, J. Liang, and Z. Jiang, "Design, fabrication and experiment of a MEMS piezoresistive high-g accelerometer," *Journal of Mechanical Science and Technology*, vol. 27, pp. 831–836, Mar. 2013.

[21] D. J. Young, M. A. Zurcher, M. Semaan, C. A. Megerian, and W. H. Ko, "MEMS capacitive accelerometer-based middle ear microphone," *IEEE Transactions on Biomedical Engineering*, vol. 59, pp. 3283–92, Dec. 2012.

[22] H. V. Estrada, "A MEMS-SOI 3D-magnetic field sensor," *2011 IEEE 24th International Conference on Micro Electro Mechanical Systems*, pp. 664–667, Jan. 2011.

[23] M. Li, V. T. Rouf, M. J. Thompson, and D. A. Horsley, "Three-Axis Lorentz-Force Magnetic Sensor for Electronic Compass Applications," *Journal of Microelectromechanical Systems*, vol. 21, pp. 1002–1010, Aug. 2012.

[24] Z. Vobecka, R. Blue, F. Vilela, P. Skabara, and D. Uttamchandani, "Microelectrode sensor utilising nitro-sensitive polymers for application in explosives detection," *Micro & Nano Letters*, vol. 7, no. 9, p. 962, 2012.

[25] J. C. Belmonte, J. Manzano, J. Arbiol, A. Cirera, J. Puigcorbé, A. Vilà, N. Sabaté, I. Gràcia, C. Cané, and J. R. Morante, "Micromachined twin gas sensor for CO and O2 quantification based on catalytically modified nano-SnO2," *Sensors and*

Actuators B: Chemical, vol. 114, pp. 881–892, Apr. 2006.

[26] N. Levit, D. Pestov, and G. Tepper, "High surface area polymer coatings for SAW-based chemical sensor applications," *Sensors and Actuators B: Chemical*, vol. 82, pp. 241–249, Feb. 2002.

[27] C. A. Gutierrez and E. Meng, "Parylene-Based Electrochemical-MEMS Transducers," *Journal of Microelectromechanical Systems*, vol. 19, pp. 1352–1361, Dec. 2010.

[28] Y. Kim, E. Hwang, S. Yoon, and S. Park, "MEMS-Based Biosensor," *Encyclopedia of Microfluidics and Nanofluidics: SpringerReference*, 2008.

[29] X. Feng, Y. Huang, and A. J. Rosakis, "On the Stoney Formula for a Thin Film/-Substrate System With Nonuniform Substrate Thickness," *Journal of Applied Mechanics*, vol. 74, no. 6, p. 1276, 2007.

[30] K. E. Petersen, "Silicon Torsional Scanning Mirror," *IBM Journal of Research and Development*, vol. 24, no. 5, pp. 631–637, 1980.

[31] W. O. Davis, R. Sprague, and J. Miller, "MEMS-based pico projector display," *2008 IEEE/LEOS International Conference on Optical MEMs and Nanophotonics*, vol. 1, pp. 31–32, Aug. 2008.

[32] J. Chong, S. He, and R. Ben Mrad, "Development of a Vector Display System Based on a Surface-Micromachined Micromirror," *IEEE Transactions on Industrial Electronics*, vol. 59, pp. 4863–4870, Dec. 2012.

[33] A. Yalcinkaya, H. Urey, D. Brown, T. Montague, and R. Sprague, "Two-Axis Electromagnetic Microscanner for High Resolution Displays," *Journal of Microelectromechanical Systems*, vol. 15, pp. 786–794, Aug. 2006.

[34] L. Li, V. Stankovic, L. Stankovic, L. Li, S. Cheng, and D. Uttamchandani, "Single pixel optical imaging using a scanning MEMS mirror," *Journal of Micromechanics and Microengineering*, vol. 21, p. 025022, Feb. 2011.

[35] J. Sun, S. Guo, L. Wu, L. Liu, S.-W. Choe, B. S. Sorg, and H. Xie, "3D In Vivo optical coherence tomography based on a low-voltage, large-scan-range 2D MEMS mirror," *Optics Express*, vol. 18, p. 12065, May 2010.

[36] H. Ra, W. Piyawattanametha, M. J. Mandella, P.-l. Hsiung, J. Hardy, T. D. Wang, C. H. Contag, G. S. Kino, and O. Solgaard, "Three-dimensional in vivo imaging by a handheld dual-axes confocal microscope," *Optics Express*, vol. 16, no. 10, pp. 7224–7232, 2008.

[37] C. L. Arrasmith, D. L. Dickensheets, and A. Mahadevan-Jansen, "MEMS-based handheld confocal microscope for in-vivo skin imaging," *Optics Express*, vol. 18, pp. 3805–3819, Feb. 2010.

[38] W. Piyawattanametha, E. D. Cocker, L. D. Burns, R. P. J. Barretto, J. C. Jung, H. Ra, O. Solgaard, and M. J. Schnitzer, "In vivo brain imaging using a portable 2.9 g two-photon microscope based on a microelectromechanical systems scanning

mirror," *Optics Letters*, vol. 34, no. 15, pp. 2309–2311, 2009.

[39] W. Jung, S. Tang, D. T. Mccormic, T. Xie, Y.-C. Ahn, J. Su, I. V. Tomov, T. B. Krasieva, B. J. Tromberg, and Z. Chen, "Miniaturized probe based on a microelectromechanical system mirror for multiphoton microscopy," *Optics Letters*, vol. 33, no. 12, pp. 1324–1326, 2008.

[40] Y. Watanabe, Y. Takahashi, Y. Abe, S. Iwamatsu, T. Yahagi, S. Kobayashi, S. Konno, and T. Sato, "Electromagnetically dual-axis driven MEMS grating and its application to 3D profiling with near-infrared low-coherence interferometry," *Electronics and Communications in Japan*, vol. 96, pp. 9–15, Feb. 2013.

[41] K. H. Koh, Y. Qian, and C. Lee, "Design and characterization of a 3D MEMS VOA driven by hybrid electromagnetic and electrothermal actuation mechanisms," *Journal of Micromechanics and Microengineering*, vol. 22, p. 105031, Oct. 2012.

[42] W. Riethmuller and W. Benecke, "Thermally excited silicon microactuators," *IEEE Transactions on Electron Devices*, vol. 35, pp. 758–763, June 1988.

[43] L. Li and D. Uttamchandani, "Dynamic response modelling and characterization of a vertical electrothermal actuator," *Journal of Micromechanics and Microengineering*, vol. 19, no. 7, p. 075014, 2009.

[44] Q.-A. Huang and N. K. S. Lee, "Analytical modeling and optimization for a laterally-driven polysilicon thermal actuator," *Microsystem Technologies*, vol. 5, pp. 133–137, Feb. 1999.

[45] D. H. Kim, Y. C. Park, and S. Park, "Design and fabrication of twisting-type thermal actuation mechanism for micromirrors," *Sensors and Actuators A: Physical*, vol. 159, pp. 79–87, Apr. 2010.

[46] A. Jain, A. Kopa, Y. Pan, G. Fedder, and H. Xie, "A Two-Axis Electrothermal Micromirror for Endoscopic Optical Coherence Tomography," *IEEE Journal of Selected Topics in Quantum Electronics*, vol. 10, pp. 636–642, May 2004.

[47] J. Singh, T. Gan, A. Agarwal, and S. Liw, "3D free space thermally actuated micromirror device," *Sensors and Actuators A*, vol. 123-124, pp. 468–475, 2005.

[48] S. T. Todd, A. Jain, H. Qu, and H. Xie, "A multi-degree-of-freedom micromirror utilizing inverted-series-connected bimorph actuators," *Journal of Optics A: Pure and Applied Optics*, vol. 8, pp. S352–S359, July 2006.

[49] A. Atre, "Analysis of out-of-plane thermal microactuators," *Journal of Micromechanics and Microengineering*, vol. 16, pp. 205–213, Feb. 2006.

[50] W.-C. Chen, C.-C. Chu, J. Hsieh, and W. Fang, "A reliable single-layer out-of-plane micromachined thermal actuator," *Sensors and Actuators A: Physical*, vol. 103, pp. 48–58, Jan. 2003.

[51] D. Yan, A. Khajepour, and R. Mansour, "Design and modeling of a MEMS bidirectional vertical thermal actuator," *Journal of Micromechanics and Microengineering*, vol. 14, pp. 841–850, July 2004.

[52] K. Jia, S. Pal, and H. Xie, "An Electrothermal TipTiltPiston Micromirror Based on Folded Dual S-Shaped Bimorphs," *Journal of Microelectromechanical Systems*, vol. 18, pp. 1004–1015, Oct. 2009.

[53] L. Wu and H. Xie, "124 Deg Rotation Angle Electrothermal Micromirror With Integrated Platinum Heater," *IEEE Journal of Selected Topics in Quantum Electronics*, vol. 13, no. 2, pp. 316–321, 2007.

[54] S. Pal and H. Xie, "Distributed and lumped element models for a bimorph-actuated micromirror," *Journal of Micromechanics and Microengineering*, vol. 20, p. 045020, Apr. 2010.

[55] A. Jain and H. Xie, "A single-crystal silicon micromirror for large bi-directional 2D scanning applications," *Sensors and Actuators A: Physical*, vol. 130-131, pp. 454–460, Aug. 2006.

[56] K. Palmer, S. Lotfi, M. Berglund, G. Thornell, and H. Kratz, "A micromachined dual-axis beam steering actuator for use in a miniaturized optical space communication system," *Journal of Micromechanics and Microengineering*, vol. 20, p. 105007, Oct. 2010.

[57] J. Singh and T. Selvaratnam, "Two-Axis Gimbal-Less Electrothermal Micromirror for Large-Angle Circumferential Scanning," *IEEE Journal of Selected Topics in Quantum Electronics*, vol. 15, no. 5, pp. 1432–1438, 2009.

[58] K. H. Koh and C. Lee, "A Two-Dimensional MEMS Scanning Mirror Using Hybrid Actuation Mechanisms With Low Operation Voltage," *Journal of Microelectromechanical Systems*, vol. 21, pp. 1124–1135, Oct. 2012.

[59] Y. Eun, H. Na, B. Jeong, J.-I. Lee, and J. Kim, "Bidirectional electrothermal electromagnetic torsional microactuators for large angular motion at dc mode and high frequency resonance mode operation," *Journal of Micromechanics and Microengineering*, vol. 19, p. 065023, June 2009.

[60] R. A. Miller, "Micromachined electromagnetic scanning mirrors," *Optical Engineering*, vol. 36, no. 5, p. 1399, 1997.

[61] J. J. Bernstein, S. Member, W. P. Taylor, J. D. Brazzle, C. J. Corcoran, G. Kirkos, J. E. Odhner, A. Pareek, M. Waelti, and M. Zai, "Electromagnetically Actuated Mirror Arrays for Use in 3-D Optical Switching Applications," *Journal of Microelectromechanical Systems*, vol. 13, no. 3, pp. 526–535, 2004.

[62] T. Mitsui, Y. Takahashi, and Y. Watanabe, "A 2-axis optical scanner driven nonresonantly by electromagnetic force for OCT imaging," *Journal of Micromechanics and Microengineering*, vol. 16, pp. 2482–2487, Nov. 2006.

[63] Y. Watanabe, Y. Abe, S. Iwamatsu, S. Kobayashi, Y. Takahashi, and T. Sato, "Electromagnetically driven two-axis optical beam steering MEMS mirror and its dependence of actuation on magnetic field," *Electronics and Communications in Japan*, vol. 94, pp. 24–31, Nov. 2011.

[64] T.-L. Tang, C.-P. Hsu, W.-C. Chen, and W. Fang, "Design and implementation

of a torque-enhancement 2-axis magnetostatic SOI optical scanner," *Journal of Micromechanics and Microengineering*, vol. 20, no. 2, p. 025020, 2010.

[65] H.-A. Yang, T.-L. Tang, S. T. Lee, and W. Fang, "A Novel Coilless Scanning Mirror Using Eddy Current Lorentz Force and Magnetostatic Force," *Journal of Microelectromechanical Systems*, vol. 16, pp. 511–520, June 2007.

[66] B. Wagner, M. Kreutzer, and W. Benecke, "Electromagnetic microactuators with multiple degrees of freedom," in *TRANSDUCERS '91: 1991 International Conference on Solid-State Sensors and Actuators. Digest of Technical Papers*, pp. 614–617, IEEE, 1991.

[67] A. Debray, A. Ludwig, T. Bourouina, A. Asaoka, N. Tiercelin, G. Reyne, T. Oki, E. Quandt, H. Muro, and H. Fujita, "Application of a Multilayered Magnetostrictive Film to a Micromachined 2-D Optical Scanner," *Journal of Microelectromechanical Systems*, vol. 13, pp. 264–271, Apr. 2004.

[68] A. D. Yalcinkaya, H. Urey, and S. Holmstrom, "NiFe Plated Biaxial MEMS Scanner for 2-D Imaging," *IEEE Photonics Technology Letters*, vol. 19, no. 5, pp. 330–332, 2007.

[69] S. Isikman and H. Urey, "Dynamic Modeling of Soft Magnetic Film Actuated Scanners," *IEEE Transactions on Magnetics*, vol. 45, pp. 2912–2919, July 2009.

[70] H. Miyajima, N. Asaoka, T. Isokawa, M. Ogata, Y. Aoki, M. Imai, O. Fujimori, M. Katashiro, and K. Matsumoto, "A mems electromagnetic optical scanner for a commercial confocal laser scanning microscope," *Journal of Microelectromechanical Systems*, vol. 12, pp. 243–251, June 2003.

[71] C. Mu, F. Zhang, L. Lu, and Y. Wu, "A novel electromagnetically actuated resonant MEMS scanning mirror with large deflection," *2008 3rd IEEE International Conference on Nano/Micro Engineered and Molecular Systems*, pp. 600–604, 2008.

[72] H. Urey, S. Holmstrom, and A. D. Yalcinkaya, "Electromagnetically Actuated FR4 Scanners," *IEEE Photonics Technology Letters*, vol. 20, pp. 30–32, Jan. 2008.

[73] T. Fujita, K. Maenaka, and Y. Takayama, "Dual-axis MEMS mirror for large deflection-angle using SU-8 soft torsion beam," *Sensors and Actuators A: Physical*, vol. 121, no. 1, pp. 16–21, 2005.

[74] L. C. M. Oliveira, P. R. Barbaroto, L. O. S. Ferreira, and I. Doi, "A novel Si micromachined moving-coil induction actuated mm-sized resonant scanner," *Journal of Micromechanics and Microengineering*, vol. 16, pp. 165–172, Jan. 2006.

[75] A. Selvakumar, K. Najafi, W. Juan, and S. Pang, "Vertical comb array microactuators," in *Proceedings IEEE Micro Electro Mechanical Systems*, pp. 43–48, IEEE, 1995.

[76] H. Toshiyoshi, W. Piyawattanametha, and M. Wu, "Linearization of electrostatically actuated surface micromachined 2-D optical scanner," *Journal of Microelectromechanical Systems*, vol. 10, pp. 205–214, June 2001.

[77] H. Camon and F. Larnaudie, "Fabrication, simulation and experiment of a rotating electrostatic silicon mirror with large angular deflection," in *Proceedings IEEE Thirteenth Annual International Conference on Micro Electro Mechanical Systems (Cat. No.00CH36308)*, pp. 645–650, IEEE, 2000.

[78] Y. Ma, S. Islam, and Y.-J. Pan, "Electrostatic Torsional Micromirror With Enhanced Tilting Angle Using Active Control Methods," *IEEE/ASME Transactions on Mechatronics*, vol. 16, pp. 994–1001, Dec. 2011.

[79] C. Agudelo, M. Packirisamy, and L. Saydy, "Nonlinear Control of an Electrostatic Micromirror Beyond Pull-In With Experimental Validation," *Journal of Microelectromechanical Systems*, vol. 18, pp. 914–923, Aug. 2009.

[80] Y. S. Yoon, K. D. Bae, J. H. Kim, H. Choi, and B. C. Koh, "A low voltage actuated micromirror with an extra vertical electrode for 90 rotation," *Journal of Micromechanics and Microengineering*, vol. 13, pp. 922–926, Nov. 2003.

[81] B. Wingfield, M. Whitley, J. Brooks, and J. Hammer, "A design methodology for a bulk-micromachined two-dimensional electrostatic torsion micromirror," *Journal of Microelectromechanical Systems*, vol. 12, pp. 692–701, Oct. 2003.

[82] Y. Bai, J. T. W. Yeow, and B. C. Wilson, "Design and fabrication of 22 and 44 biaxial micromirror array," in *2010 International Symposium on Optomechatronic Technologies*, vol. 2, pp. 1–5, IEEE, Oct. 2010.

[83] Y. Zhao, F. E. Tay, F. S. Chau, and G. Zhou, "Linearization of the scanning field for 2D torsional micromirror by RBF neural network," *Sensors and Actuators A: Physical*, vol. 121, pp. 230–236, May 2005.

[84] Y. Zhao, F. E. H. Tay, F. S. Chau, and G. Zhou, "Stabilization of dual-axis micromirrors beyond the pull-in point by integral sliding mode control," *Journal of Micromechanics and Microengineering*, vol. 16, pp. 1242–1250, July 2006.

[85] M. Dokmeci, A. Pareek, S. Bakshi, M. Waelti, C. Fung, K. Heng, and C. Mastrangelo, "Two-Axis Single-Crystal Silicon Micromirror Arrays," *Journal of Microelectromechanical Systems*, vol. 13, pp. 1006–1017, Dec. 2004.

[86] J. T. W. Yeow, V. X. D. Yang, A. Chahwan, M. L. Gordon, B. Qi, I. A. Vitkin, B. C. Wilson, and A. A. Goldenberg, "Micromachined 2-D scanner for 3-D optical coherence tomography," *Sensors and Actuators A: Physical*, vol. 117, pp. 331–340, Jan. 2005.

[87] Y. Bai, J. T. W. Yeow, and B. C. Wilson, "Design, Fabrication, and Characteristics of a MEMS Micromirror With Sidewall Electrodes," *Journal of Microelectromechanical Systems*, vol. 19, pp. 619–631, June 2010.

[88] A. Molfese, A. Nannini, and F. Pieri, "Reduced-order modelling of the bending of an array of torsional micromirrors," *Analog Integrated Circuits and Signal Processing*, vol. 53, pp. 137–143, Dec. 2006.

[89] W. Piyawattanametha, P. Patterson, D. Hah, H. Toshiyoshi, and M. Wu, "Surface- and bulk- micromachined two-dimensional scanner driven by angular vertical

comb actuators," *Journal of Microelectromechanical Systems*, vol. 14, pp. 1329–1338, Dec. 2005.

[90] A. Arslan, D. Brown, W. O. Davis, S. Holmström, S. K. Gokce, and H. Urey, "Comb-Actuated Resonant Torsional Microscanner With Mechanical Amplification," *Journal of Microelectromechanical Systems*, vol. 19, no. 4, pp. 936–943, 2010.

[91] W. C. Tang, T.-C. H. Nguyen, and R. T. Howe, "Laterally Driven Polysilicon Resonant Microstructures," *Sensors and Actuators*, vol. 20, pp. 25–32, Nov. 1989.

[92] Y. Du, G. Zhou, K. L. Cheo, Q. Zhang, H. Feng, and F. S. Chau, "Double-Layered Vibratory Grating Scanners for High-Speed High-Resolution Laser Scanning," *Journal of Microelectromechanical Systems*, vol. 19, pp. 1186–1196, Oct. 2010.

[93] H. Schenk, D. Kunze, H. Lakner, H. Kueck, and P. Duerr, "A resonantly excited 2D-micro-scanning-mirror with large deflection," *Sensors And Actuators A*, vol. 89, pp. 104–111, 2001.

[94] T. Klose, H. Conrad, T. Sandner, and H. Schenk, "Fluidmechanical Damping Analysis of Resonant Micromirrors with Out-of-plane Comb Drive," in *COMSOL*, (Hannover), 2008.

[95] A. Tortschanoff, M. Lenzhofer, A. Frank, M. Wildenhain, T. Sandner, H. Schenk, W. Scherf, and A. Kenda, "Position encoding and phase control of resonant MOEMS mirrors," *Sensors and Actuators A: Physical*, vol. 162, pp. 235–240, Aug. 2010.

[96] S. Hsu, T. Klose, C. Drabe, and H. Schenk, "Fabrication and characterization of a dynamically flat high resolution micro-scanner," *Journal of Optics A*, vol. 10, pp. 1–8, 2008.

[97] S. K. Gokce, S. Holmstrom, C. Hibert, S. Olcer, D. Bowman, and H. Urey, "Two-Dimensional MEMS Stage Integrated With Microlens Arrays for Laser Beam Steering," *Journal of Microelectromechanical Systems*, vol. 20, pp. 15–17, Feb. 2011.

[98] Y. Du, G. Zhou, K. K. Cheo, Q. Zhang, H. Feng, B. Yang, and F. S. Chau, "High speed laser scanning using MEMS driven in-plane vibratory grating: Design, modeling and fabrication," *Sensors and Actuators A: Physical*, vol. 156, pp. 134–144, Nov. 2009.

[99] Y. Du, G. Zhou, K. Koon, L. Cheo, and Q. Zhang, "A high-speed MEMS grating laser scanner with a backside thinned grating platform fabricated using a single mask delay etching technique," *Journal of Micromechanics and Microengineering*, vol. 20, no. 11, p. 115028, 2010.

[100] H. Schenk, P. Durr, T. Haase, D. Kunze, U. Sobe, H. Lakner, and H. Kuck, "Large deflection micromechanical scanning mirrors for linear scans and pattern generation," *IEEE Journal of Selected Topics in Quantum Electronics*, vol. 6,

pp. 715–722, Sept. 2000.

[101] W. Ma, H.-Y. Chan, C. C. Wong, Y. C. Chan, C.-J. Tsai, and F. C. S. Lee, "Design optimization of MEMS 2D scanning mirrors with high resonant frequencies," *2010 IEEE 23rd International Conference on Micro Electro Mechanical Systems (MEMS)*, pp. 823–826, Jan. 2010.

[102] H. Schenk, T. Sandner, C. Drabe, M. Scholles, K. Frommhagen, C. Gerwig, and H. Lakner, "Ultra Compact Laser Based Projectors and Imagers," *Human-Coumputer Interaction*, pp. 501–510, 2009.

[103] E. Gallagher, W. Moussa, and M. McDermott, "A review of fabrication processes for vertical comb drives," *Microsystem Technologies*, vol. 18, pp. 381–397, Jan. 2012.

[104] D. Hah, S.-Y. Huang, J.-C. Tsai, H. Toshiyoshi, and M. Wu, "Low-Voltage, Large-Scan Angle MEMS Analog Micromirror Arrays With Hidden Vertical Comb-Drive Actuators," *Journal of Microelectromechanical Systems*, vol. 13, pp. 279–289, Apr. 2004.

[105] J.-C. Tsai and M. Wu, "Design, Fabrication, and Characterization of a High Fill-Factor, Large Scan-Angle, Two-Axis Scanner Array Driven by a Leverage Mechanism," *Journal of Microelectromechanical Systems*, vol. 15, pp. 1209–1213, Oct. 2006.

[106] J.-I. Lee, S. Park, Y. Eun, B. Jeong, and J. Kim, "Resonant Frequency Tuning of Torsional Microscanner by Mechanical Restriction using MEMS Actuator," *2009 IEEE 22nd International Conference on Micro Electro Mechanical Systems*, pp. 164–167, Jan. 2009.

[107] J.-W. Jeong, S. Kim, and O. Solgaard, "Split-Frame Gimbaled Two-Dimensional MEMS Scanner for Miniature Dual-Axis Confocal Microendoscopes Fabricated by Front-Side Processing," *Journal of Microelectromechanical Systems*, vol. 21, pp. 308–315, Apr. 2012.

[108] V. Milanovic, S. Kwon, and L. Lee, "High Aspect Ratio Micromirrors With Large Static Rotation and Piston Actuation," *IEEE Photonics Technology Letters*, vol. 16, pp. 1891–1893, Aug. 2004.

[109] U. Krishnamoorthy and O. Solgaard, "Self-aligned vertical electrostatic combdrives for micromirror actuation," *Journal of Microelectromechanical Systems*, vol. 12, pp. 458–464, Aug. 2003.

[110] D. Lee, U. Krishnamoorthy, K. Yu, and O. Solgaard, "Single-crystalline silicon micromirrors actuated by self-aligned vertical electrostatic combdrives with piston-motion and rotation capability," *Sensors and Actuators A: Physical*, vol. 114, pp. 423–428, Sept. 2004.

[111] H. M. Chu, J. Mizuno, K. Hane, and T. Takagi, "Compact slanted comb two-axis micro-mirror scanner fabricated by silicon-on-insulator micromachining," *Journal of Vacuum Science & Technology B: Microelectronics and Nanometer Structures*,

vol. 29, no. 4, p. 042001, 2011.

[112] T. Sasaki and K. Hane, "Varifocal Micromirror Integrated With Comb-Drive Scanner on Silicon-on-Insulator Wafer," *Journal of Microelectromechanical Systems*, vol. 21, pp. 971–980, Aug. 2012.

[113] H. M. Chu and K. Hane, "Design, fabrication and vacuum operation characteristics of two-dimensional comb-drive micro-scanner," *Sensors and Actuators A: Physical*, vol. 165, pp. 422–430, Feb. 2011.

[114] R. Syms, "Self-assembled 3-D silicon microscanners with self-assembled electrostatic drives," *IEEE Photonics Technology Letters*, vol. 12, no. 11, pp. 1519–1521, 2000.

[115] Y. K. Hong and R. R. A. Syms, "Dynamic Response Modeling of MEMS Micromirror Corner Cube Reflectors With Angular Vertical Combdrives," *Journal of Lightwave Technology*, vol. 25, pp. 472–480, Feb. 2007.

[116] Y. Eun, H. Na, J. Choi, J.-i. Lee, and J. Kim, "Angular vertical comb actuators assembled on-chip using in-plane electrothermal actuators and latching mechanisms," *Sensors and Actuators A: Physical*, vol. 165, pp. 94–100, Jan. 2011.

[117] J. Kim, H. Choo, L. Lin, and R. Muller, "Microfabricated Torsional Actuators Using Self-Aligned Plastic Deformation of Silicon," *Journal of Microelectromechanical Systems*, vol. 15, pp. 553–562, June 2006.

[118] P. Patterson, H. Toshiyoshi, and M. Wu, "A scanning micromirror with angular comb drive actuation," in *Technical Digest. MEMS 2002 IEEE International Conference. Fifteenth IEEE International Conference on Micro Electro Mechanical Systems (Cat. No.02CH37266)*, pp. 544–547, IEEE, 2002.

[119] D. Hah, P. Patterson, H. Nguyen, H. Toshiyoshi, and M. Wu, "Theory and Experiments of Angular Vertical Comb-Drive Actuators for Scanning Micromirrors," *IEEE Journal of Selected Topics in Quantum Electronics*, vol. 10, pp. 505–513, May 2004.

[120] M. Fujino, P. Patterson, H. Nguyen, W. Piyawattanametha, and M. Wu, "Monolithically Cascaded Micromirror Pair Driven by Angular Vertical Combs for Two-Axis Scanning," *IEEE Journal of Selected Topics in Quantum Electronics*, vol. 10, pp. 492–497, May 2004.

[121] K. Isamoto, K. Totsuka, T. S. Tooru Sakai, A. Morosawa, C. Chong, H. Fujita, and H. Toshiyoshi, "A high speed MEMS scanner for 140-kHz SS-OCT," in *16th International Conference on Optical MEMS and Nanophotonics*, pp. 73–74, IEEE, Aug. 2011.

[122] T. Sandner, D. Jung, D. Kallweit, T. Grasshoff, and H. Schenk, "Microscanner with vertical out of plane combdrive," in *16th International Conference on Optical MEMS and Nanophotonics*, pp. 33–34, IEEE, Aug. 2011.

[123] H. Xie, Y. Pan, and G. Fedder, "A CMOS-MEMS mirror with curled-hinge comb drives," *Journal of Microelectromechanical Systems*, vol. 12, pp. 450–457, Aug.

2003.

[124] P. Qu and H. Qu, "A Novel CMOS-MEMS Scanning Micro-mirror Using Vertical Comb Drives," in *Optical Mems and Nanophotonics 2012*, vol. 1, pp. 63–64, 2012.

[125] M. D. Williams, B. a. Griffin, T. N. Reagan, J. R. Underbrink, and M. Sheplak, "An AlN MEMS Piezoelectric Microphone for Aeroacoustic Applications," *Journal of Microelectromechanical Systems*, vol. 21, pp. 270–283, Apr. 2012.

[126] T. Iseki, M. Okumura, T. Sugawara, and M. K. Kurosawa, "Deflection properties of a MEMS optical scanner with four torsion beams and L-shaped arms," *Sensors and Actuators A: Physical*, vol. 178, pp. 154–163, May 2012.

[127] U. Baran, D. Brown, S. Holmstrom, D. Balma, W. O. Davis, P. Muralt, and H. Urey, "Resonant PZT MEMS Scanner for High-Resolution Displays," *Journal of Microelectromechanical Systems*, vol. 21, pp. 1303–1310, Dec. 2012.

[128] M. Tani, M. Akamatsu, Y. Yasuda, H. Fujita, and H. Toshiyoshi, "A Combination of Fast Resonant Mode and Slow Static Deflection of SOI-PZT Actuators for MEMS Image Projection Display," in *IEEE/LEOS International Conference on Optical MEMS and Their Applications Conference, 2006.*, pp. 25–26, IEEE, 2006.

[129] J.-H. Park, Y. Kawakami, M. Suzuki, and J. Akedo, "Fabrication and Characterization of Optical Micro-Electro-Mechanical System Scanning Devices Using BaTiO _{3} -Based Lead-Free Piezoelectric-Coated Substrate Sheet by Aerosol Deposition," *Japanese Journal of Applied Physics*, vol. 50, p. 09ND19, Sept. 2011.

[130] T. Kobayashi, J. Tsaur, and R. Maeda, "Fabrication of Optical Micro Scanner Driven by PZT Actuators," *Japanese Journal of Applied Physics*, vol. 44, pp. 7078–7082, Sept. 2005.

[131] K. H. Koh, T. Kobayashi, J. Xie, A. Yu, and C. Lee, "Novel piezoelectric actuation mechanism for a gimbal-less mirror in 2D raster scanning applications," *Journal of Micromechanics and Microengineering*, vol. 21, p. 075001, July 2011.

[132] C. Chang-Hasnain, "Tunable VCSEL," *IEEE Journal of Selected Topics in Quantum Electronics*, vol. 6, pp. 978–987, Nov. 2000.

[133] M. Wu, E. Vail, G. Li, W. Yuen, and C. Chang-Hasnain, "Tunable micromachined vertical cavity surface emitting laser," *Electronics Letters*, vol. 31, no. 19, pp. 1671–1672, 1995.

[134] S. Schilt, K. Zogal, B. Kögel, P. Meissner, M. Maute, R. Protasio, and M.-C. Amann, "Spectral and modulation properties of a largely tunable MEMS-VCSEL in view of gas phase spectroscopy applications," *Applied Physics B*, vol. 100, pp. 321–329, Feb. 2010.

[135] A. Daly, C. Gierl, T. Grundl, C. Grasse, K. Zogal, D. Carey, P. Townsend, M.-C. Amann, P. Meissner, and B. Corbett, "10 Gbit/s transmission over 50 km of SMF using MEMS tunable VCSEL," *Electronics Letters*, vol. 48, no. 7, pp. 394–395, 2012.

[136] M. Nakahama, H. Sano, N. Nakata, A. Matsutani, and F. Koyama, "Electrothermal tuning of MEMS VCSEL with giant wavelength-temperature dependence," *IEICE Electronics Express*, vol. 9, no. 5, pp. 416–421, 2012.

[137] A. Q. Liu and X. M. Zhang, "A review of MEMS external-cavity tunable lasers," *Journal of Micromechanics and Microengineering*, vol. 17, no. 1, pp. R1–R13, 2007.

[138] X. M. Zhang, A. Q. Liu, D. Y. Tang, and C. Lu, "Discrete wavelength tunable laser using microelectromechanical systems technology," *Applied Physics Letters*, vol. 84, no. 3, pp. 329–331, 2004.

[139] D. Zhang, J. Zhao, Q. Yang, W. Liu, Y. Fu, C. Li, M. Luo, S. Hu, Q. Hu, and L. Wang, "Compact MEMS external cavity tunable laser with ultra-narrow linewidth for coherent detection," *Optics Express*, vol. 20, p. 19670, Aug. 2012.

[140] D. Michel, F. Xiao, and K. Alameh, "MEMS-Based Tunable Linear-Cavity Fiber Laser," *IEEE Photonics Journal*, vol. 4, pp. 895–902, June 2012.

[141] J. Masson, R. St-Gelais, A. Poulin, and Y.-a. Peter, "Tunable Fiber Laser Using a MEMS-Based in Plane Fabry-Pérot Filter," *IEEE Journal of Quantum Electronics*, vol. 46, pp. 1313–1319, Sept. 2010.

[142] OKOFlexibleOptical, "OKO Flexible Optical B.V.." `http://www.okotech.com/`. [Online, accessed 12-June-2013].

[143] L. Zhu, P.-C. Sun, D.-U. Bartsch, W. R. Freeman, and Y. Fainman, "Adaptive Control of a Micromachined Continuous-Membrane Deformable Mirror for Aberration Compensation," *Applied Optics*, vol. 38, p. 168, Jan. 1999.

[144] W. Lubeigt, G. Valentine, J. Girkin, E. Bente, and D. Burns, "Active transverse mode control and optimisation of an all-solid-state laser using an intracavity adaptive-optic mirror," *Optics Express*, vol. 10, no. 13, pp. 550–555, 2002.

[145] S. Verpoort, P. Rausch, and U. Wittrock, "Characterization of a miniaturized unimorph deformable mirror for high power CW-solid state lasers," in *Proc. SPIE 8253, MEMS Adaptive Optics VI* (S. S. Olivier, T. G. Bifano, and J. Kubby, eds.), vol. 8253, pp. 825309–825309–12, Feb. 2012.

[146] P. Léna, "Adaptive optics: a breakthrough in astronomy," *Experimental Astronomy*, vol. 26, pp. 35–48, Mar. 2009.

[147] J. M. Girkin, S. Poland, and A. J. Wright, "Adaptive optics for deeper imaging of biological samples," *Current Opinion in Biotechnology*, vol. 20, pp. 106–10, Feb. 2009.

[148] G. Vdovin and V. Kiyko, "Intracavity control of a 200-W continuous-wave Nd:YAG laser by a micromachined deformable mirror," *Optics Letters*, vol. 26, pp. 798–800, June 2001.

[149] A. Inoue, T. Komikado, K. Kinoshita, J. Hayashi, and S. Umegaki, "Deformable Mirror for Mechanical Q-Switching of Laser-Diode-Pumped Microchip Laser,"

Japanese Journal of Applied Physics, vol. 46, pp. L1016–L1018, Oct. 2007.

[150] V. Couderc, A. Crunteanu, M. Fabert, F. Doutre, F. El Bassri, D. Pagnoux, and A. Jalocha, "Picosecond pulse generation in a hybrid Q-switched laser source by using a microelectromechanical mirror," *Optics Express*, vol. 20, p. 5524, Feb. 2012.

[151] Y.-A. Peter, H. P. Herzig, E. Rochat, R. Dandliker, C. Marxer, and N. F. de Rooij, "Pulsed fiber laser using micro-electro-mechanical mirrors," *Optical Engineering SPIE*, vol. 38, no. 4, pp. 636–640, 1999.

[152] D. Bouyge, A. Crunteanu, V. Couderc, D. Sabourdy, and P. Blondy, "Synchronized Tunable Q -Switched Fiber Lasers Using Deformable Achromatic Microelectromechanical Mirror," *IEEE Photonics Technology Letters*, vol. 20, no. 12, pp. 991–993, 2008.

[153] M. Fabert, A. Desfarges-Berthelemot, V. Kermène, A. Crunteanu, D. Bouyge, and P. Blondy, "Ytterbium-doped fibre laser Q-switched by a cantilever-type micro-mirror," *Optics Express*, vol. 16, no. 26, pp. 22064–22071, 2008.

[154] M. Fabert, A. Desfarges-Berthelemot, V. Kermène, and A. Crunteanu, "Temporal synchronization and spectral combining of pulses from fiber lasers Q-switched by independent MEMS micro-mirrors," *Optics Express*, vol. 20, p. 22895, Sept. 2012.

[155] M. Fabert, V. Kermène, A. Desfarges-Berthelemot, P. Blondy, and A. Crunteanu, "Actively mode-locked fiber laser using a deformable micromirror," *Optics Letters*, vol. 36, p. 2191, June 2011.

[156] D. Miller, B. Boyce, M. Dugger, T. Buchheit, and K. Gall, "Characteristics of a commercially available silicon-on-insulator MEMS material," *Sensors and Actuators A: Physical*, vol. 138, pp. 130–144, July 2007.

[157] J.-L. Yeh, C.-Y. Hui, and N. Tien, "Electrostatic model for an asymmetric combdrive," *Journal of Microelectromechanical Systems*, vol. 9, pp. 126–135, Mar. 2000.

[158] A. H. Nayfeh and D. T. Mook, *Nonlinear Oscillations*. New York: Wiley, 1979.

[159] Y. K. Hong, R. R. A. Syms, K. S. J. Pister, and L. X. Zhou, "Design, fabrication and test of self-assembled optical corner cube reflectors," *Journal of Micromechanics and Microengineering*, vol. 15, pp. 663–672, Mar. 2005.

[160] A. M. Elshurafa, K. Khirallah, H. H. Tawfik, A. Emira, A. K. S. Abdel Aziz, and S. M. Sedky, "Nonlinear Dynamics of Spring Softening and Hardening in Folded-MEMS Comb Drive Resonators," *Journal of Microelectromechanical Systems*, vol. 20, pp. 943–958, Aug. 2011.

[161] V. Kaajakari, T. Mattila, a. Oja, and H. Seppa, "Nonlinear Limits for Single-Crystal Silicon Microresonators," *Journal of Microelectromechanical Systems*, vol. 13, pp. 715–724, Oct. 2004.

[162] M. Palaniapan and L. Khine, "Nonlinear behavior of SOI free-free micromechanical beam resonator," *Sensors and Actuators A: Physical*, vol. 142, pp. 203–210,

Mar. 2008.

[163] COMSOL, "Capacitive 3D Comb Drive solved with COMSOL Multiphysics." `http://www.comsol.com/model/download/34131/comb_drive_3d_sbs.pdf`. [Online; accessed 21-Aug-2013].

[164] L. Li, R. Li, W. Lubeigt, and D. Uttamchandani, "Design, Simulation, and Characterization of a Bimorph Varifocal Micromirror and Its Application in an Optical Imaging System," *Journal of Microelectromechanical Systems*, vol. 22, no. 2, pp. 285–294, 2013.

[165] P. W. Roth, A. J. Maclean, D. Burns, and A. J. Kemp, "Direct diode-laser pumping of a mode-locked Ti:sapphire laser.," *Optics Letters*, vol. 36, pp. 304–6, Jan. 2011.

[166] M. Vainio, M. Merimaa, L. Halonen, and K. Vodopyanov, "Degenerate 1 GHz repetition rate femtosecond optical parametric oscillator.," *Optics Letters*, vol. 37, pp. 4561–3, Nov. 2012.

[167] O. Svelto, *Principles of Lasers*. Boston, MA: Springer US, 5th ed., 2010.

[168] W. Koechner, *Solid-State Laser Engineering*. Berlin Heidelberg: Springer-Verlag, 4th ed., 1996.

[169] H. Kogelnik and T. Li, "Laser beams and resonators," *Applied Optics*, vol. 54, no. 10, pp. 1312–1329, 1966.

[170] M. Lukac, "Output energy characteristics of optimally pumped rotating mirror Q-switch lasers," *IEEE Journal of Quantum Electronics*, vol. 27, no. 9, pp. 2094–2097, 1991.

[171] A. Bizjak, K. Nemeš, and J. Možina, "Rotating-Mirror Q-Switched Er:YAG Laser for Optodynamic Studies," *Strojniški vestnik Journal of Mechanical Engineering*, vol. 57, pp. 3–10, Jan. 2011.

[172] J. E. Midwinter, "The theory of Q-switching applied to slow switching and pulse shaping for solid state lasers," *British Journal of Applied Physics*, vol. 16, pp. 1125–1133, Aug. 1965.

[173] M. Marincek and M. Lukac, "Development of EM field in lasers with rotating mirror Q-switch," *IEEE Journal of Quantum Electronics*, vol. 29, no. 8, pp. 2405–2412, 1993.

[174] J. Caird, S. Payne, P. Staber, A. Ramponi, L. Chase, and W. Krupke, "Quantum electronic properties of the Na3Ga2Li3F12:Cr3+ laser," *IEEE Journal of Quantum Electronics*, vol. 24, pp. 1077–1099, June 1988.

[175] A. Crunteanu, D. Bouyge, D. Sabourdy, P. Blondy, V. Couderc, L. Grossard, P. H. Pioger, and A. Barthelemy, "Deformable micro-electro-mechanical mirror integration in a fibre laser Q-switch system," *Journal of Optics A*, vol. 8, pp. 347–351, 2006.

[176] R. Bauer, W. Lubeigt, and D. Uttamchandani, "Q-switching of Nd : YAG solid-

state laser with intra-cavity MEMS resonant scanning mirror," in *2012 International Conference on Optical MEMS and Nanophotonics*, vol. 10, pp. 81–82, 2012.

[177] Thorlabs, "Thorlabs Protected Gold Mirrors." `http://www.thorlabs.de/NewGroupPage9.cfm?ObjectGroup_ID=744`, 2013. [Online; accessed 22-Jan-2013].

[178] A. E. Siegman, *Lasers*. Mill Valey, CA: University Science Books, 1986.

[179] J. J. Zayhowski, "Microchip lasers," *Optical Materials*, vol. 11, pp. 255–267, Jan. 1999.

[180] D. Findlay and R. Clay, "The measurement of internal losses in 4-level lasers," *Physics Letters*, vol. 20, pp. 277–278, Feb. 1966.

[181] Thorlabs, "Thorlabs WFS Series Operation Manual." `http://www.thorlabs.de/Thorcat/19900/WFS150-5C-Manual.pdf`, 2012. [Online; accessed 13-Jan-2013].

[182] J. Ruoff and M. Totzeck, "Orientation Zernike polynomials: a useful way to describe the polarization effects of optical imaging systems," *Journal of Micro / Nanolithography, MEMS and MOEMS*, vol. 8, no. 3, p. 031404, 2009.

[183] L. Goldberg, C. McIntosh, and B. Cole, "VCSEL end-pumped passively Q-switched Nd:YAG laser with adjustable pulse energy," *Optics Express*, vol. 19, pp. 4261–4267, Feb. 2011.

[184] D. Liu, Y. Ning, Y. Zeng, L. Qin, Y. Liu, X. Zhang, L. Zhang, J. Zhang, C. Tong, and L. Wang, "High-Power-Density High-Efficiency Bottom-Emitting Vertical-Cavity Surface-Emitting Laser Array," *Applied Physics Express*, vol. 4, p. 052104, May 2011.

[185] E. Lamothe, L. D. A. Lundeberg, and E. Kapon, "Eigenmode analysis of phased-coupled VCSEL arrays using spatial coherence measurements," *Optics Letters*, vol. 36, pp. 2916–8, Aug. 2011.

[186] R. Van Leeuwen, Y. Xiong, J.-F. Seurin, G. Xu, A. Miglo, Q. Wang, B. Xu, W.-X. Zou, D. Li, J. D. Wynn, V. Khalfin, and C. L. Ghosh, "High-power vertical-cavity surface-emitting lasers for diode pumped solid-state lasers," in *Laser Technology for Defense and Security VIII*, pp. 83810I–83810I–7, May 2012.

[187] PrincetonOptronics, "100W CW 975nm VCSEL Array Submodule." `http://www.princetonoptronics.com/pdfs/PCW-CS1-100-W0975.pdf`. [Online; accessed 31-May-2013].

[188] W. Yuen, G. S. Li, and C. Chang-Hasnain, "Multiple-wavelength vertical-cavity surface-emitting laser arrays," *IEEE Journal of Selected Topics in Quantum Electronics*, vol. 3, pp. 422–428, Apr. 1997.

[189] Y. Rao, C. Chase, and C. J. Chang-Hasnain, "Multiwavelength HCG-VCSEL array," in *22nd IEEE International Semiconductor Laser Conference*, pp. 11–12, IEEE, Sept. 2010.

[190] J. Hastie, L. Morton, S. Calvez, M. Dawson, T. Leinonen, M. Pessa, G. Gibson, and M. Padgett, "Red microchip VECSEL array," *Optics Express*, vol. 13, pp. 7209–14, Sept. 2005.

[191] N. Laurand, C.-L. Lee, E. Gu, J. E. Hastie, A. J. Kemp, S. Calvez, and M. D. Dawson, "Array-Format Microchip Semiconductor Disk Lasers," *IEEE Journal of Quantum Electronics*, vol. 44, pp. 1096–1103, Nov. 2008.

[192] M. J. Landry, "Variably Spaced Giant Pulses From Multiple Laser Cavities in a Single Lasing Medium," *Applied Physics Letters*, vol. 18, no. 11, pp. 494–496, 1971.

[193] W. O. Davis, "Measuring Quality Factor From a Nonlinear Frequency Response With Jump Discontinuities," *Journal of Microelectromechanical Systems*, vol. 20, pp. 968–975, Aug. 2011.

[194] RefractiveIndex.info, "Refractive index database." `http://refractiveindex.info/`, 2013. [Online, accessed 02-June-2013].

[195] C. T. Leondes, ed., *MEMS/NEMS*. Boston, MA: Springer US, 2006.

[196] K. Cao, W. Liu, and J. Talghader, "Curvature compensation in micromirrors with high-reflectivity optical coatings," *Journal of Microelectromechanical Systems*, vol. 10, no. 3, pp. 409–417, 2001.

[197] W. Liu and J. J. Talghader, "Thermally invariant dielectric coatings for micromirrors.," *Applied Optics*, vol. 41, pp. 3285–93, June 2002.

Publications

Journal publications

R. Bauer, L. Li, and D. Uttamchandani, "*Dynamic properties of angular vertical comb-drive scanning micromirrors with electrothermal controllable variable initial offset*", in preparation, to be submitted to IEEE Journal of Microelectromechanical Systems.

L. Ran, R. Bauer, and W. Lubeigt, "*Continuous-Wave Nd:YVO4 self-Raman lasers operating at 1109nm, 1158nm and 1231nm*", Optics Express, vol. 21, no. 15, pp. 17745-17750, July 2013.

R. Bauer, W. Lubeigt, and D. Uttamchandani, "*Dual Q-switched laser outputs from a single lasing medium using an intra-cavity MEMS micromirror array*", Optics Letters, vol. 37, no. 17, pp. 3567-3569, September 2012.

R. Bauer, G. Brown, and D. Uttamchandani, *"Comparison of the curvature homogeneity and dynamic behavior of framed and frameless electrostatic X/Y scanning micromirrors"*, Micro Nano Letters, vol. 6, no. 6, pp. 425-428, June 2011.

Conference publciations

R. Bauer, W. Lubeigt, C. Clark, E. McBrearty, and D. Uttamchandani, *"Multi-output Q-switched solid-state laser using an intra-cavity MEMS micromirror array"*, SPIE Photonics West 2013, San Francisco, USA, 2-7 February 2013. **(talk)**

G. Brown, R. Bauer, L. Li, W. Lubeigt, and D. Uttamchandani, *"SOI based electromagnetic MEMS scanners and applications in laser systems"*, SPIE Photonics West 2013, San Francisco, USA, 2-7 February 2013. **(talk)**

R. Bauer, G. Brown, L. Li, and D. Uttamchandani, *"A novel continuously variable angular vertical comb-drive with application in scanning micromirror"*, IEEE MEMS 2013, Taipei, Taiwan, 20-24 January 20013.

R. Bauer, W. Lubeigt, and D. Uttamchandani, *"Active Q-switched Nd:YAG laser using MEMS micromirrors"*, Photon 12, Durham, UK, 3-6 September 2012. **(talk)**

R. Bauer, W. Lubeigt, and D. Uttamchandani, *"Q-Switching of Nd:YAG Solid-State Laser with Intra-Cavity MEMS Resonant Scanning Mirror"*, IEEE Optical MEMS & Nanophotonics, Banff, Canada, 6-9 August 2012.

L. Li, R. Bauer, G. Brown, and D. Uttamchandani, *"A 2D MEMS Scanning Micromirror with Electrothermal and Electrostatic Actuators"*, IEEE Optical MEMS & Nanophotonics, Banff, Canada, 6-9 August 2012.

R. Bauer, W. Lubeigt, and D. Uttamchandani, *"Q-switched Nd:YAG laser using a resonantly actuated intra-cavity MEMS micromirror",* IONS-11, Paris, France, 22-25 February 2012. **(talk)**

R. Bauer, G. Brown, and D. Uttamchandani, *"Hysteresis comparison of framed and frameless electrostatic X/Y scanning micromirrors",* IEEE Optical MEMS & Nanophotonics, Istanbul, Turkey, August 2011.

L. Li, R. Bauer, G. Brown, and D. Uttamchandani, *"A symmetric hybrid MEMS scanner with electrothermal and electrostatic actuators",* IEEE Optical MEMS & Nanophotonics, Istanbul, Turkey, August 2011.

R. Engelbrecht, A. Siekiera, R. Bauer, R. Neumann, and B. Schmauss, *"Characterization of Short PM Raman Fiber Lasers with a Small Spectral Bandwidth",* in Optical Fiber Communication Conference (OFC), paper OMQ2, Los Angeles, USA, 6-10 March 2011.

G. Brown, L. Li, R.Bauer, J. Liu, and D. Uttamchandani, *"A two-axis hybrid MEMS scanner incorporating electrothermal and electrostatic actuators",* IEEE Optical MEMS & Nanophotonics, Sapporo, Japan, 9-12 August 2010.

Appendix A - MEMS model Matlab files

```
%--------------------------
% CapacitanceCalculation_inclFringeFields.m
%
% Matlab-Code to calculate the angular dependent Capacitance and ...
    differential Capacitance
% for a single defined set of initial comb-offset values
%--------------------------

clear all

%Input variables:
N=26; %number of comb-finger gaps
l1 = 153e-6; %comb-finger length of overlap area
ltot = 169e-6; %comb-finger length of moving finger including ...
    distance to rotation axis
h1 = 10.4e-6; %comb-offset at open-end of fixed-combs
h2 = 6.1e-6; % comb-offset at anchor-end of fixed-combs
t = 10e-6; %thickness of mirror
dBase2 = 9e-6; %half-width of torsion beam
V0 = 80; %Voltage used in COMSOL to calculate We (electrical field ...
    distribution), value was 80V


thetai=atan((h1-h2)/l1);

j=0; k=0;
%define loop to calculate C between +-22.5Deg
for theta=(-22.5*3.14159/180):0.001:(+22.5*3.14159/180)
    j=j+1;

    %coefficients from 8th order fourier fit to COMSOL We(h) simulation
       a0 =  2.422e-008;
       a1 =  2.598e-008;
       b1 =  3.821e-024;
       a2 =  1.403e-008;
       b2 = -1.242e-024;
       a3 =  8.506e-009;
       b3 =   1.91e-024;
       a4 =  4.681e-009;
       b4 = -5.731e-025;
       a5 =  2.683e-009;
       b5 =  1.004e-040;
       a6 =   1.34e-009 ;
       b6 = -1.146e-024;
       a7 =  7.181e-010;
       b7 =  2.674e-024 ;
       a8 =  2.933e-010;
       b8 = -6.492e-025;
```

```
46          w =  4.189e+004;
47
48      %h = @(l) (l*sin(theta-thetai)+h1+sin(theta)*(ltot-l1)); %heigth ...
            depending on l value
49
50      We = @(l) a0 + ...
            a1*cos((l*sin(theta-thetai)+h1+sin(theta)*(ltot-l1))*w) + ...
51          b1*sin((l*sin(theta-thetai)+h1+sin(theta)*(ltot-l1))*w) + ...
52        a2*cos(2*(l*sin(theta-thetai)+h1+sin(theta)*(ltot-l1))*w) + ...
53        b2*sin(2*(l*sin(theta-thetai)+h1+sin(theta)*(ltot-l1))*w) + ...
54        a3*cos(3*(l*sin(theta-thetai)+h1+sin(theta)*(ltot-l1))*w) + ...
55        b3*sin(3*(l*sin(theta-thetai)+h1+sin(theta)*(ltot-l1))*w) + ...
56        a4*cos(4*(l*sin(theta-thetai)+h1+sin(theta)*(ltot-l1))*w) + ...
57        b4*sin(4*(l*sin(theta-thetai)+h1+sin(theta)*(ltot-l1))*w) + ...
58        a5*cos(5*(l*sin(theta-thetai)+h1+sin(theta)*(ltot-l1))*w) + ...
59        b5*sin(5*(l*sin(theta-thetai)+h1+sin(theta)*(ltot-l1))*w) + ...
60        a6*cos(6*(l*sin(theta-thetai)+h1+sin(theta)*(ltot-l1))*w) + ...
61        b6*sin(6*(l*sin(theta-thetai)+h1+sin(theta)*(ltot-l1))*w) + ...
62        a7*cos(7*(l*sin(theta-thetai)+h1+sin(theta)*(ltot-l1))*w) + ...
63        b7*sin(7*(l*sin(theta-thetai)+h1+sin(theta)*(ltot-l1))*w) + ...
64        a8*cos(8*(l*sin(theta-thetai)+h1+sin(theta)*(ltot-l1))*w) + ...
65        b8*sin(8*(l*sin(theta-thetai)+h1+sin(theta)*(ltot-l1))*w);
66        %We from COMSOL fitted with 8th order fourier in CFTool to get ...
              coefficients
67
68      We_int = quad(We,0,l1);
69
70      C(j) = N * 2 / V0^2 * We_int;
71      angle(j)=theta;
72
73  end
74
75  dC(1)=0;
76  for k=1:(j-1)
77      k=k+1;
78      dC(k) = (C(k)-C(k-1))/(angle(k)-angle(k-1));
79  end
80
81  angleDeg=angle*180/3.14159;
82
83  figure
84  subplot(2,1,1)
85  plot(angle, C,'red')
86  xlabel('Rotation angle [Rad]')
87  ylabel('Capacitance [F]')
88  subplot(2,1,2)
89  plot(angle, dC, 'blue')
90  xlabel('Rotation angle [Rad]')
91  ylabel('Differential Capacitance [F/Rad]')
```

```
%--------------------------------
% FourierFitToDifferentialCapacitance.m
%
% Program to run and evaluate Fourier Series fit to C and dC
% Function Fseries and Fseriesval from : ...
% http://www.mathworks.co.uk/matlabcentral/fileexchange/ ...
% 31013-simple-real-fourier-series-approximation
%
%--------------------------------

function [a,b] = main(angle,dC)
%needs import of calculated C-vs-theta to enable fit!!

[a1,b1]=Fseries(angle,dC,20); %20th order fourier fit to dataset
a=a1';
b=b1';

j=0;
for i= (-22.5*3.14159/180):0.001:(22.5*3.14159/180)
    j=j+1;

    theta1(j)=i;

       dC1(j)=b(1)*sin(theta1(j)*8)+a(2)*cos(theta1(j)*8)...
            +b(2)*sin(theta1(j)*8*2)+a(3)*cos(theta1(j)*8*2)...
            +b(3)*sin(theta1(j)*8*3)+a(4)*cos(theta1(j)*8*3)...
            +b(4)*sin(theta1(j)*8*4)+a(5)*cos(theta1(j)*8*4)...
            +b(5)*sin(theta1(j)*8*5)+a(6)*cos(theta1(j)*8*5)...
            +b(6)*sin(theta1(j)*8*6)+a(7)*cos(theta1(j)*8*6)...
            +b(7)*sin(theta1(j)*8*7)+a(8)*cos(theta1(j)*8*7)...
            +b(8)*sin(theta1(j)*8*8)+a(9)*cos(theta1(j)*8*8)...
            +b(9)*sin(theta1(j)*8*9)+a(10)*cos(theta1(j)*8*9)...
            +b(10)*sin(theta1(j)*8*10)+a(11)*cos(theta1(j)*8*10)...
            +b(11)*sin(theta1(j)*8*11)+a(12)*cos(theta1(j)*8*11)...
            +b(12)*sin(theta1(j)*8*12)+a(13)*cos(theta1(j)*8*12)...
            +b(13)*sin(theta1(j)*8*13)+a(14)*cos(theta1(j)*8*13)...
            +b(14)*sin(theta1(j)*8*14)+a(15)*cos(theta1(j)*8*14)...
            +b(15)*sin(theta1(j)*8*15)+a(16)*cos(theta1(j)*8*15)...
            +b(16)*sin(theta1(j)*8*16)+a(17)*cos(theta1(j)*8*16)...
            +b(17)*sin(theta1(j)*8*17)+a(18)*cos(theta1(j)*8*17)...
            +b(18)*sin(theta1(j)*8*18)+a(19)*cos(theta1(j)*8*18)...
            +b(19)*sin(theta1(j)*8*19)+a(20)*cos(theta1(j)*8*19)...
            +b(20)*sin(theta1(j)*8*20)+a(21)*cos(theta1(j)*8*20)+a(1)/2;
end

figure
plot(theta1,dC1,angle,dC)

end
```

```
%-----------------------------
%
% MotionEquation_inclFringeFields.m
%
% Fourier coefficients from fit to dC(theta) originating from Matlab ...
    program
% using electrical energy density We from COMSOL fringe field simulation
%-----------------------------

function [frequency, TOSA] = main(volt)

%Variables
I_i = 2.947E-16; %torsional moment of inertia of inner part
I_o = 1.016E-16; %torsional moment of inertia of frame/outer part
I=I_i+I_o; %overall torsional moment of inertia of mirror S38
V0 = volt; %actuation voltage
chi=30E-4; %damping coefficient from Q-factor measurements

k = 5.61E-7; %spring constant, from COMSOL frequency 5987Hz , ...
    I=3.963E-16;
b_t = 2* chi * sqrt(k / I); %damping factor

k_2 = 0.33; % nonlinear spring constant to balance NL behaviour ...
    introduced by E-field

i=0;
xSt=0;
vSt=0;

% loop to calculate maximum scan angle for each actuation frequency point
for f=6120:-5:5920
    i=i+1;

    options = odeset('RelTol',1e-3);
    [t,theta] = ode45(@motionEqu, [0,0.2], [xSt vSt], options, f, I, ...
        V0, b_t, k, k_2);
    thetaD = theta(:,1)*180/3.14159 *2; %optical scan angle in degree ...
        of mirror

    frequ(i)=f;
    maxAngle(i)=max(thetaD(length(thetaD)-200:length(thetaD),1));
    minAngle(i)=min(thetaD(length(thetaD)-200:length(thetaD),1));
    ScanAngle(i)=maxAngle(i)-minAngle(i);

    %figure
    plot(t,thetaD(:,1),'red')
    xSt=theta(length(theta),1);
    vSt=theta(length(theta),2);
end

figure(2)
plot(frequ,ScanAngle,'blue')

frequency = frequ;
TOSA = ScanAngle;

```

```
52 %function definition for ODE solver
53 function dtheta = motionEqu(t, theta, f, I, V0, b_t, k, k_2)
54
55     a = [-5.84036596151532e-14, -1.30418468661294e-13, ...
          -1.20975075544607e-13, -7.53943971000068e-14, ...
          -4.19904363514037e-14, -1.81801827163762e-14, ...
          -7.48890148551746e-15, -9.75358597698473e-16, ...
          -3.19194904307977e-16, 2.79035206337273e-16, ...
          -2.69950855764030e-16, 2.61006889418562e-16, ...
          -2.53415194260764e-16, 2.47167296038075e-16, ...
          -2.42045609643612e-16, 2.37826817879094e-16, ...
          -2.34324674906412e-16, 2.31392487762061e-16, ...
          -2.28916580562092e-16, 2.26808979557159e-16, ...
          -2.25001272898397e-16];
56     b = [-1.83305493731570e-13, -4.94083772227064e-14, ...
          -3.06147156377665e-14, 1.01551366385046e-14, ...
          -3.01248865881671e-15, 9.23808817728841e-15, ...
          -4.72268161671609e-15, 4.68104345485444e-15, ...
          -4.17415397793106e-15, 3.76571834910926e-15, ...
          -3.42797976372623e-15, 3.14494338125658e-15, ...
          -2.90461358046485e-15, 2.69812063676891e-15, ...
          -2.51884135460813e-15, 2.36175425174029e-15, ...
          -2.22299191283005e-15, 2.09953122425440e-15, ...
          -1.98897664847382e-15, 1.88940629127840e-15];
57
58     a=a';
59     b=b';
60     %a and b copied from Fourier fit of ...
           FourierFitToDifferentialCapacitance.m
61
62     theta1=theta(1); %angular position of mirror
63     theta2=theta(2); %angular velocity of mirror
64
65     %V2 = V0^2/2*(1+cos(2*2*3.14159*f*t)); %sin-wave driving squared
66     V2 = (0.5* V0 * (1 + square(2*3.14159*f * t)))^2; %square-wave ...
           driving signal
67     %V2 = (0.5*V0*(1+cos(2*3.14150*f*t)))^2; %offset sin-wave driving ...
           signal
68
69     dC=b(1)*sin(theta1*8)+a(2)*cos(theta1*8)...
70             +b(2)*sin(theta1*8*2)+a(3)*cos(theta1*8*2)...
71             +b(3)*sin(theta1*8*3)+a(4)*cos(theta1*8*3)...
72             +b(4)*sin(theta1*8*4)+a(5)*cos(theta1*8*4)...
73             +b(5)*sin(theta1*8*5)+a(6)*cos(theta1*8*5)...
74             +b(6)*sin(theta1*8*6)+a(7)*cos(theta1*8*6)...
75             +b(7)*sin(theta1*8*7)+a(8)*cos(theta1*8*7)...
76             +b(8)*sin(theta1*8*8)+a(9)*cos(theta1*8*8)...
77             +b(9)*sin(theta1*8*9)+a(10)*cos(theta1*8*9)...
78             +b(10)*sin(theta1*8*10)+a(11)*cos(theta1*8*10)...
79             +b(11)*sin(theta1*8*11)+a(12)*cos(theta1*8*11)...
80             +b(12)*sin(theta1*8*12)+a(13)*cos(theta1*8*12)...
81             +b(13)*sin(theta1*8*13)+a(14)*cos(theta1*8*13)...
82             +b(14)*sin(theta1*8*14)+a(15)*cos(theta1*8*14)...
83             +b(15)*sin(theta1*8*15)+a(16)*cos(theta1*8*15)...
84             +b(16)*sin(theta1*8*16)+a(17)*cos(theta1*8*16)...
85             +b(17)*sin(theta1*8*17)+a(18)*cos(theta1*8*17)...
86             +b(18)*sin(theta1*8*18)+a(19)*cos(theta1*8*18)...
```

```
87              +b(19)*sin(theta1*8*19)+a(20)*cos(theta1*8*19)...
88              +b(20)*sin(theta1*8*20)+a(21)*cos(theta1*8*20)+a(1)/2;
89      %differentialCapacitance defined through fourier fit parameters
90
91      k_t = k * (1 + k_2*(theta1)^2); %inclusion of nonlinear spring ...
            constant
92
93      %Motion equation of scanner:
94      dtheta(1)=theta2;
95      dtheta(2)= -b_t *theta2 - k_t/I *theta1 + 0.5*V2*dC /I;
96
97      dtheta = dtheta';
98  end
99
100 end
```

Appendix B - MEMS Q-switch laser Matlab files

```
%-----------------------------
%
% LaserRateEquation.m
%
% Runge-Kutta solver for Rate-equations of scanning mirror laser
% Approximation of loss over mirror angle with "inconclusive" ...
    Findlay-Clay measurements
%-----------------------------
function [n_Out, phi_Out, t, gamma] = main()

%---------  Definitions ----------------------------------
sigma = 2.7e-23; %[m^2] stimulated emission cross-section
c = 3e8; %[m/s] speed of light
l = 2*(0.03+1.8*0.063+0.03); %[m] optical resonator length
lg = 2*0.063; %[m] length of gain medium
tr = l/c; %[s] cavity round-trip time
fr = 8000; %[Hz] resonant frequency of MEMS mirror
t_end = (1/(4*fr))+2e-6; %[s] end time of calculation
t_start = (1/(4*fr))-2e-6; %[s] start time of calculation
theta_max = 40 / 4 *3.14159/180; %[rad] maximum MEMS scan angle

R=0.8; % reflectivity of OC
gamma_0 = 0.01; % loss factor for intrinsic losses (incl MEMS ...
    reflectivity)
A= 1/2e-2; % [1/rad] scaling factor for time dependent losses ...
    (determined from cos fit to loss-vs-angle measurements)
k=1; % factor to gain match between experimental and theoretical data


%---------- Start values for ODE ----------------------
n_0 = (gamma_0 + log(1/R))/(sigma * 2 * 0.063)*1.75*k; %[m^-3] ...
    attempted calculation with Svelto, factor 1.205 through threshold ...
    difference for cw and q-sw
phi_0 = 1; %[m^-3] initial photon density (calculation possible?)


%-------- Calculate angle/time-dependent loss ------
gammat = linspace(t_start, t_end, 1000); % generate time vector for gamma
theta = theta_max * cos(2*3.14159*fr * gammat);
for j=1:length(theta)
    if abs(theta(j)) < 8e-3
        gamma(j) = log(1/R) + (cos(A*theta(j) + 3.14159) + 1) + gamma_0;
    else
        gamma(j) = 1;
    end
    j=j+1;
end
```

```
43
44 %-------- Run ODE with output of time t and vector n (population ...
       inversion density and photon density) -------
45 options1 = odeset('RelTol',1e-3);
46 [t,n] = ode45(@RateEqn, [t_start:0.5e-9:t_end], [n_0, phi_0], ...
       options1 , c, sigma, gammat, gamma, tr, l, lg);
47
48 %------- Format outputs --------------------------------
49 n_Out = n(:,1);
50 phi_Out = n(:,2);
51 gamma = interp1(gammat, gamma, t);
52 t=t-(1/(4*fr));
53
54 %------- ODE function ----------------------------------
55     function dndt = RateEqn(t, n, c, sigma, gammat, gamma, tr, l, lg)
56
57         gamma1 = interp1(gammat, gamma, t); % interpolate ...
               time-dependent gamma function at times t
58
59         dndt(1) = - c * sigma * n(1) * n(2);
60         dndt(2) = n(2) * (c * sigma * n(1) * (lg/l) - gamma1/tr);
61
62         dndt = dndt';
63     end
64
65 end
```

```
%------------------------
%
% ABCDspatialLaser.m
% ABCD matrix calculation of laser beam separation
% Origin of spatial simulation at MEMS mirror midpoint
%------------------------
clear all

%parameters
lend = 0.05; %[m] distance measurement plane - OC
toc = 0.006; %[m] thickness OC
l2 = 0.03; %[m] distance OC - gain medium
la = 0.063; %[m] length of gain medium
l1 = 0.03; %[m] distance gain medium - MEMS
fth = 0.6; %[m] thermal lens in gain medium
nBK7 = 1.51; % refractive index of BK7 glass at 1064nm
nYAG = 1.8; % refractive index of Nd:YAG at 1064nm

xin = 0; %[m] transversal position of beam on MEMS mirror
thetain = 4.32e-3; %[rad] angular position of MEMS mirror

Xin=[xin; thetain];

%calculation

Xout = [1 lend; 0 1]*[1 0; 0 nBK7]*[1 toc; 0 1]*[1 0; 0 1/nBK7]*[1 ...
    l2; 0 1]*[1 0; 0 nYAG]* ...
    [1 la/2; 0 1]*[1 0; -1/fth 1]*[1 la/2; 0 1]*[1 0; 0 1/nYAG]*[1 ...
        l1; 0 1]*Xin;

xout = Xout(1)
thetaout = Xout(2)

xgainMEMS = [1 l1; 0 1]*Xin;
xgainMiddle = [1 la/2; 0 1]*[1 0; 0 1/nYAG]*[1 l1; 0 1]*Xin;
xgainOC = [1 0; 0 nYAG]*[1 la/2; 0 1]*[1 0; -1/fth 1]*[1 la/2; 0 ...
    1]*[1 0; 0 1/nYAG]*[1 l1; 0 1]*Xin;
xOCin = [1 l2; 0 1]*[1 0; 0 nYAG]*[1 la/2; 0 1]*[1 0; -1/fth 1]*[1 ...
    la/2; 0 1]*[1 0; 0 1/nYAG]*[1 l1; 0 1]*Xin;
xOCout = [1 0; 0 nBK7]*[1 toc; 0 1]*[1 0; 0 1/nBK7]*[1 l2; 0 1]*[1 0; ...
    0 nYAG]*[1 la/2; 0 1]*[1 0; -1/fth 1]*[1 la/2; 0 1]*[1 0; 0 ...
    1/nYAG]*[1 l1; 0 1]*Xin;

ProfileL = [0, l1, l1+(la/2), l1+la, l1+la+l2, l1+la+l2+toc, ...
    l1+la+l2+toc+lend];
ProfileX = [xin, xgainMEMS(1), xgainMiddle(1), xgainOC(1), xOCin(1), ...
    xOCout(1), xout];

plot(ProfileL, ProfileX, '-r+', 'LineWidth',2, 'MarkerSize', 10)
xlabel('Distance from MEMS [m]')
ylabel('Transverse position from cavity axis [m]')
```

Appendix C - Laser module data sheets

Pumpdiode characteristic of one of the three stacks of the laser module

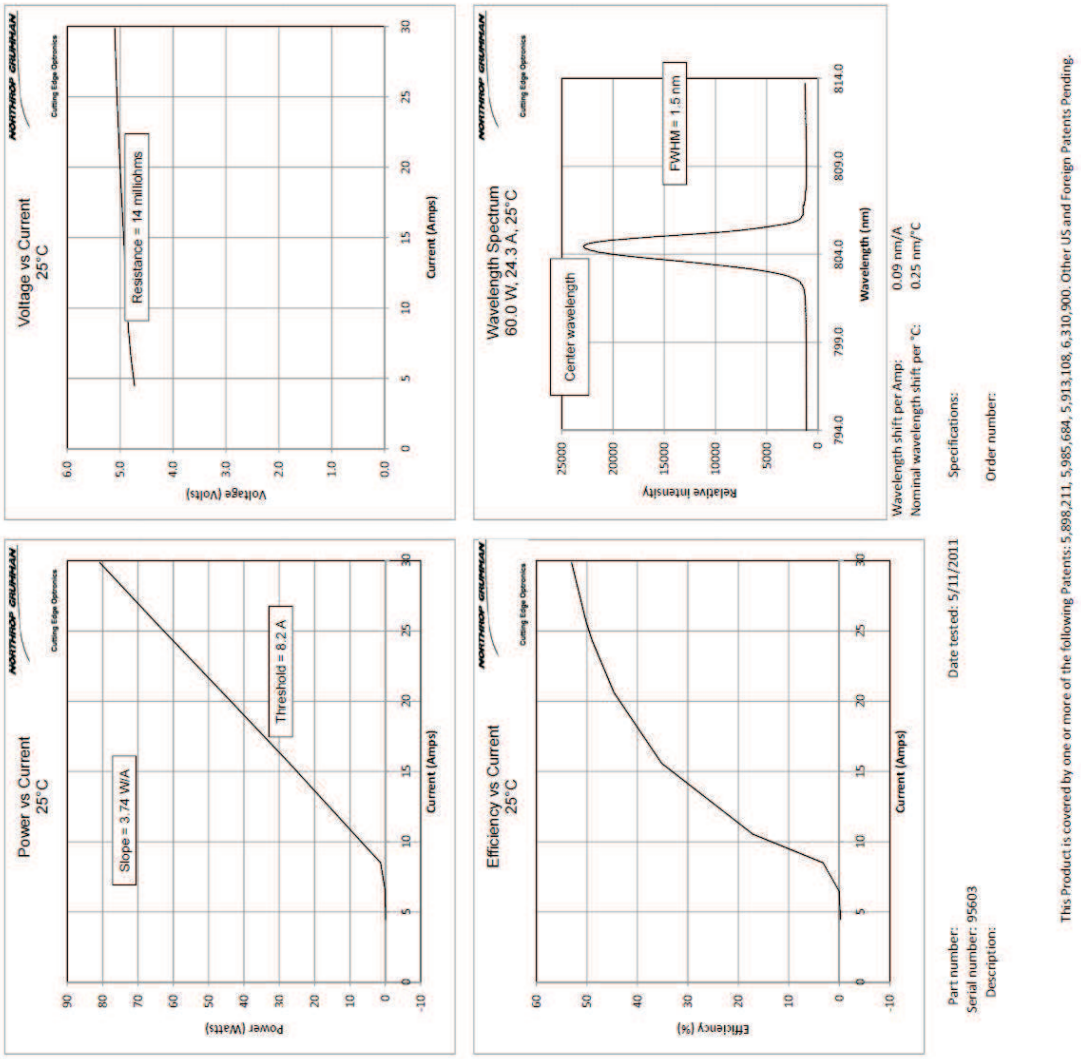

NORTHROP GRUMMAN

RB Plus

Product Overview
DPSS Nd:YAG Laser Modules

Product Definition
The RB Plus Series is the improved version of the RB Series. It is the ideal OEM building block for the development or production of new state of the art laser systems. The RB Plus Series is a highly reliable, sealed module. It is extremely compact, rugged, and efficient.

Pump Symmetry

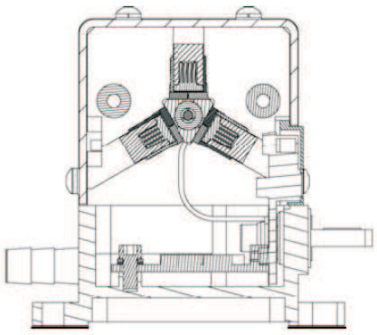

Relay Image of Fluorescence

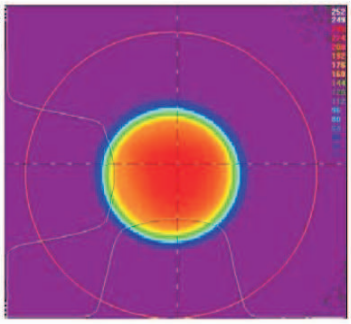

2mm x 63 mm rod, 0.6% doped Nd:YAG

20 Point West Blvd. • St. Charles, MO 63301 • 636-916-4900 • 636-916-4994 (fax) http://www.as.northropgrumman.com/ceolaser

Rev 5-7-10

NORTHROP GRUMMAN

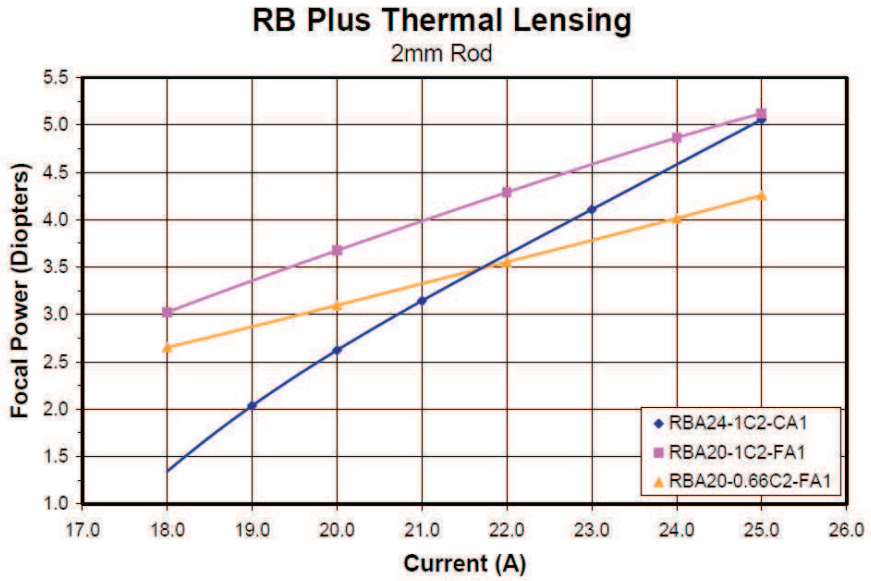

Note: All curves are typical beginning of life performance curves. Data obtained with a Shack Hartmann wavefront sensor.

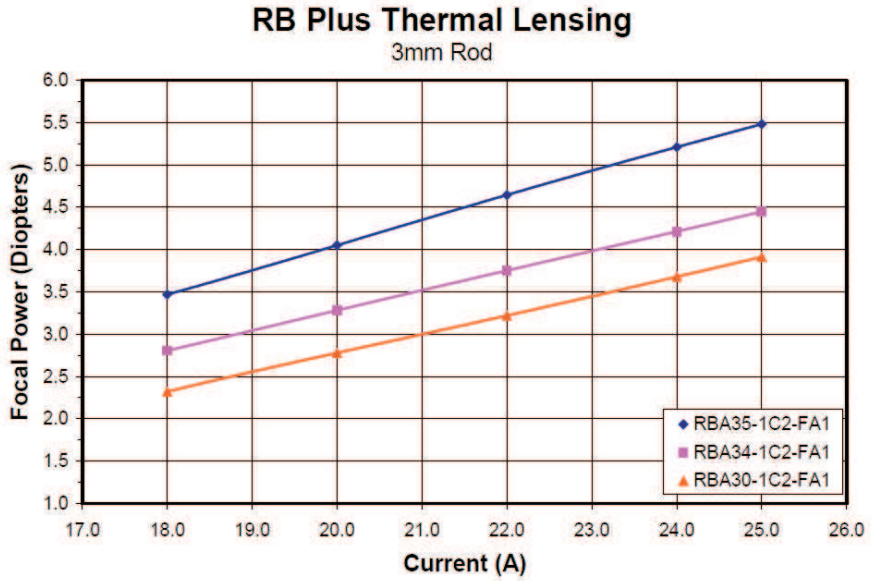

Note: All curves are typical beginning of life performance curves. Data obtained with a Shack Hartmann wavefront sensor.

20 Point West Blvd. • St. Charles, MO 63301 • 636-916-4900 • 636-916-4994 (fax) http://www.as.northropgrumman.com/ceolaser

Rev 5-7-10

NORTHROP GRUMMAN

Cutting Edge Optronics
20 Point West Blvd
St Charles, MO 63301
636.916.4900

FINAL TEST REPORT

RBA30-1C2-FA1-1013 **S/N 110619**

Specifications

Threshold Current	11.7 A
Operating Voltage	15.50 V
Maximum Current (beginning of life**)	22.6A
Operating Temperature	22 °C
Maximum Flow Rate Obtained	1.4 GPM

Module Details

Array 1 Serial Number	95597
Array 2 Serial Number	95603
Array 3 Serial number	95628
Rod Part Number	CEOROD_30
Rod Serial Number	380897
Rod Manufacturer	Synoptics

Test Conditions

☑ Pass ☐ Fail

Cavity Length	165mm±5mm
HR Mirror	0.75mCC
Output Coupler	80%
Power Specification	50 W

Performance Details

Current, A	Power, W
10	0
11	0
12	0.8
13	4.2
14	8.6
15	13.2
16	18.2
17	23.5
18	28.9
19	34.6
20	40.1
21	45.9
22	51.6

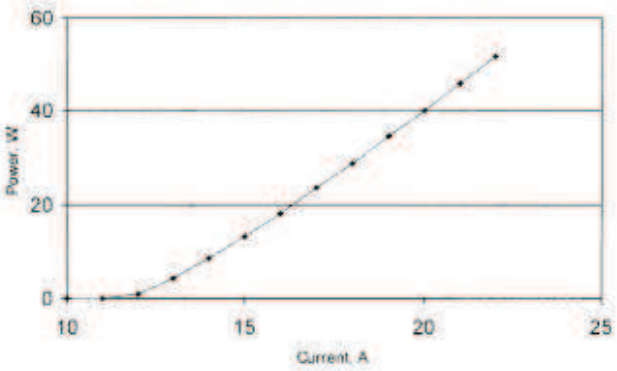

* Recommended Temperature is the temperature that is recommended by Cutting Edge Optronics due to the wavelength of the laser diodes and the cavity configuration used for testing at Cutting Edge Optronics. This recommended temperature may or may not match the optimum temperature of a temperature excursion is performed.
** Beginning of Life Current is the current required to meet specification in the standard Cutting Edge Optronics cavity. This current should not be exceeded at the beginning of life of the diodes. If current is exceeded in the beginning of the life, diode degradation will be accelerated.

Production Details

- ☑ Wiring Check
- ☑ Continuity Check
- ☑ Coolant Leak Check
- ☑ Visual Inspection
- ☑ Rod Surface Inspection (prior to shipping)

Built For: Photonics Solutions

Internal Work Order: RX12670

Test Station Used: Production 2

Test Date: 5/12/2011 9:34:19 AM

Technician: Kaci Stuekerjuergen

NORTHROP GRUMMAN

Cutting Edge Optronics
20 Point West Blvd
St. Charles, MO 63301
636.916.4900

RBA SERIES LABELS CHECKLIST

MODEL NO:
SERIAL NO:
DATE:

✓ ID Label

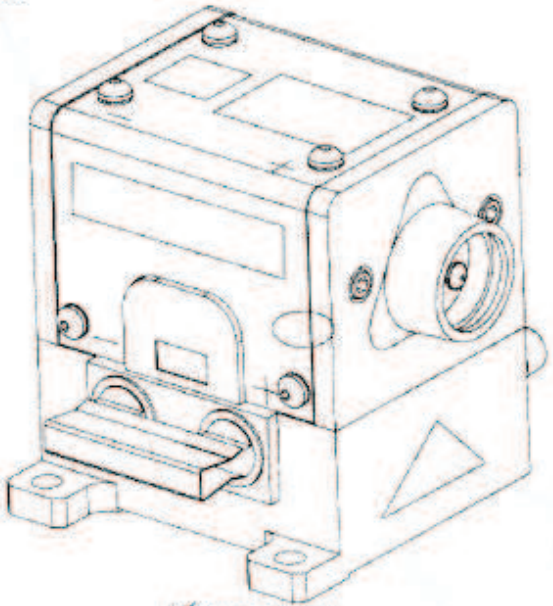

✓ Warranty Void Label

Warranty Void
If Removed

✓ Laser Emission Label (both ends)

✓ China RoHS Label (on bottom)

Technician: 5-1241
Date

Quality Assurance: 5-1241
Date